# Bubble Dynamics in Polymeric Foams

Sally Louise Everitt

Submitted in accordance with the requirements for the degree of Doctor of Philosophy

The University of Leeds

Department of Applied Mathematics

April 2004

# Abstract

The effects of fluid viscoelasticity on the expansion of gas bubbles in polymer foams for both non-reactive and reactive polymers are investigated. Polymer foams are used extensively in consumer products, from car parts to upholstery. They are produced either by injection moulding (of non-reactive polymeric fluids) or reaction injection moulding.

We use standard rheological models (Oldroyd B and Pompom) to investigate bubble growth driven by gas diffusion as a model for injection moulding. To model reaction injection moulding, we develop a new fluid model based on existing linear theory for a gelling liquid. In this case gas is produced as a by-product of the polymer reaction.

At small bubble volume fractions gas bubbles remain spherical and isolated from neighbouring bubbles during expansion. In this regime we demonstrate the effects of rheology and gelation on the bubble growth.

At high bubble volume fractions neighbouring bubbles compete for the available gas and become distorted in shape. The effects of viscoelasticity on the expansion of gas bubbles arranged in a two-dimensional hexagonal array in a non-reacting polymeric fluid are investigated. In addition to a full finite element calculation of the two-dimensional flow, two one-dimensional approximations valid in the limits of small and large gas area fractions are presented. We show that these approximations give accurate predictions of the evolution of the bubble area, but give less accurate predictions of the bubble shape.

Finally we consider how bubbles of different sizes evolve in an expanding foam. We illustrate how the surface tension driven phenomenon known as Ostwald Ripening causes large bubbles to grow at the expense of smaller ones. For the case of bubbles of two different sizes we examine the effects of viscoelasticity on the shapes of the bubbles within the structure and show that viscoelasticity has a different effect on the bubble size distribution depending upon the initial geometry.

For Eleanor

# Acknowledgements

Sally Everitt would like to thank her husband, Chris, for his faith, love and encouragement, and Eleanors grandparents for all their childcare, without whom none of this would have been possible. She would also like to thank her supervisors, Dr Oliver Harlen and Dr Helen Wilson, for their continued support and encouragement throughout the period of study as well as Dr Daniel Read for his ideas on the reacting fluid model. Sally would like to acknowledge the EPSRC and Huntsman Polyurethanes (an international business of Huntsman International LLC) for their financial support. She would also like to thank Don Jones for many useful discussions and acknowledge Tim Nicholson for use of FLOWDIS.

# Contents

# List of figures

# List of tables

# Chapter 1

# Introduction

## 1.1 Polymeric Liquids

Polymeric liquids are liquids containing very large molecules. Due to the freedom of rotation of the molecular bonds, these molecules are highly flexible and their configuration can be deformed by velocity gradients within the fluid. However, random collisions with other molecules will try to return the configuration distribution to the equilibrium state. This competition between deformation by the fluid velocity gradient and entropic relaxation causes these liquids to display viscoelastic and other non-Newtonian fluid properties. Here we describe some of the key non-Newtonian flow phenomena of polymeric liquids, more details can be found in reference [5].

Polymeric fluids display non-linear resistance to flow. For Newtonian fluids the rate of volume flow down a pipe is proportional to the applied pressure gradient. In polymeric liquids the flux depends non-linearly on the pressure gradient. Since the long polymer molecules become elongated in the direction of the flow and reduced in the gradient direction shear-thinning behaviour is observed in which the volume flow rate more than doubles when the applied pressure gradient doubles.

Polymeric liquids resist extension allowing them to be drawn into long filaments where equivalent Newtonian filaments would break up under capillary instabilities, see figure

1.1. The extensional resistance of a polymeric liquid increases with strain, so that the thinnest sections of the filament provide the greatest resistance to further extension.
In shear flows polymeric liquids possess normal stress differences that are absent in Newtonian flows. In a Newtonian fluid the diagonal components of the stress tensor in a shear flow $\mathbf{q} = (\dot{\gamma}y, 0, 0)$ are all equal. However, in a polymeric liquid the first normal stress difference, the difference between the normal stresses in the flow direction and gradient direction, is positive. This can be thought of as a tension in the streamlines. If a Newtonian liquid is stirred with a rotating rod the fluid level dips slightly near the rod due to centripetal acceleration. However, in polymeric liquids the streamline tension produces a force towards the rod that causes the fluid level to rise there. This phenomenon is known as **rod climbing** or the **Weissenberg effect** and is illustrated in figure 1.2. The streamline tension is also responsible for keeping sedimenting rods vertical and drives particles suspended in polymeric liquids together into chains - see figures 1.3 (a) and (b).

Polymeric liquids display elastic as well as viscous behaviour. When stirring is ceased in liquid such as bubble bath a small recoil effect is seen. A polymeric liquid will recoil back into its original container if the fluid is cut with a pair of scissors as it is being poured out. This experiment is illustrated in figure 1.4. Elastic effects also contribute to **die swell**: when a viscoelastic liquid is forced through a small die the jet of liquid swells in an attempt to recover its 'remembered' width upstream of the die, see figure 1.5.

## 1.2 Polymeric Foams

Polymeric foams are foams consisting of either gas bubbles embedded in a polymeric solid, or a bi-continuous structure of air and solid polymer like a sponge. They are used in a vast range of applications from car steering wheels and shoe soles to furniture upholstery and cavity wall insulation due to their low weight, sound- and shock-absorbing, and thermal insulation properties. The properties of the foam are

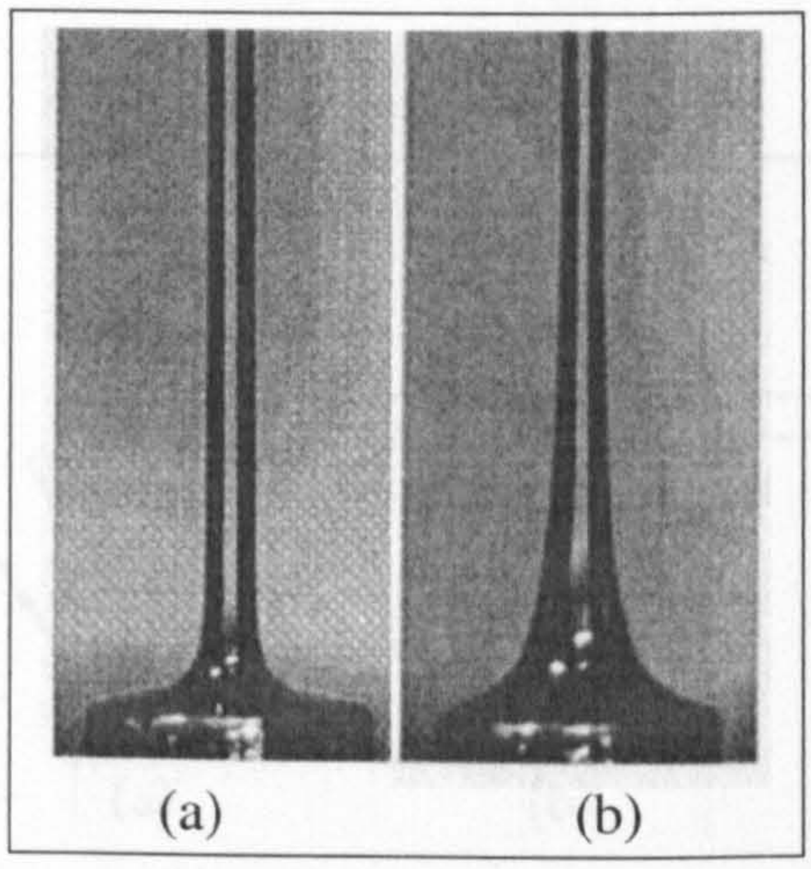


Figure 1.1: Comparison of the shape of a filament drawn from a polymeric liquid (a) and a Newtonian liquid (b). The polymeric filament has a more uniform cross section and smaller foot region near the plate. Picture taken from [49].

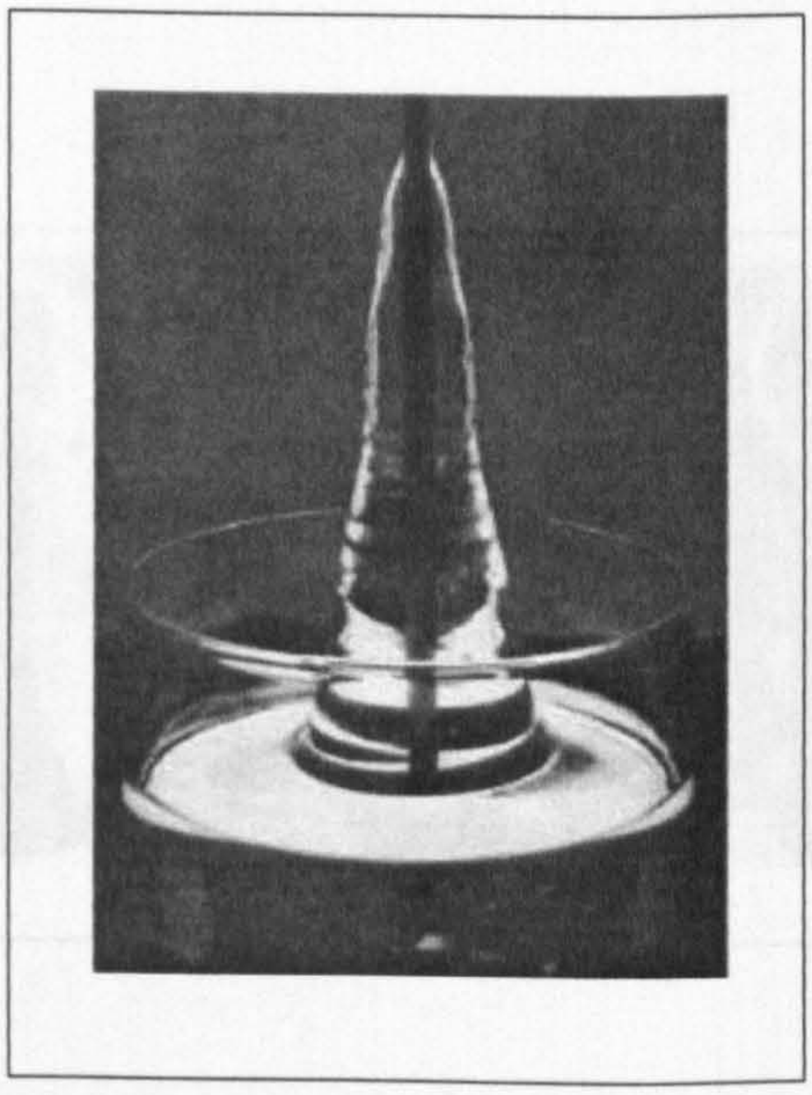

Figure 1.2: The rod climbing or Weissenberg effect observed when a polymeric liquid is stirred with a rotating rod. Picture taken from [9].

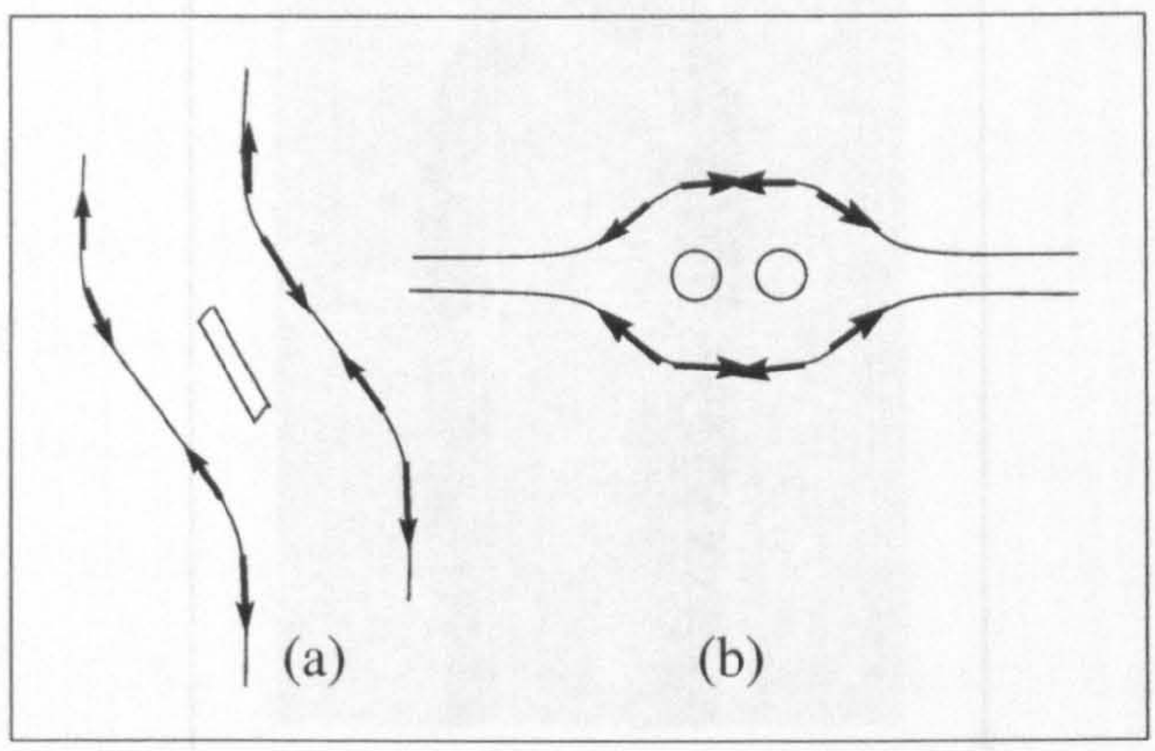


Figure 1.3: Diagram showing how the streamline tension due the first normal stress difference (a) rotates a sedimenting rod to the vertical, and (b) drives particles towards each other.

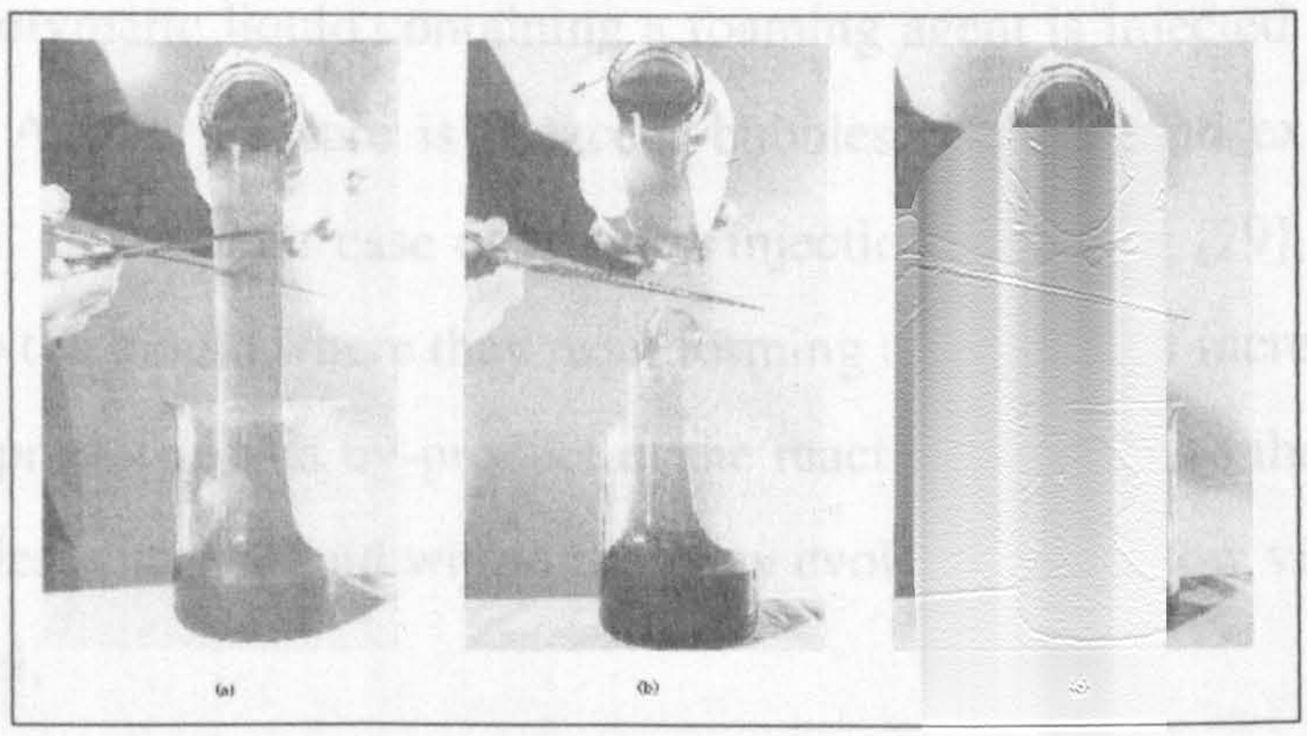

Figure 1.4: Polymeric liquid showing elastic recoil as the flow from one container to another is cut. Picture taken from [9].

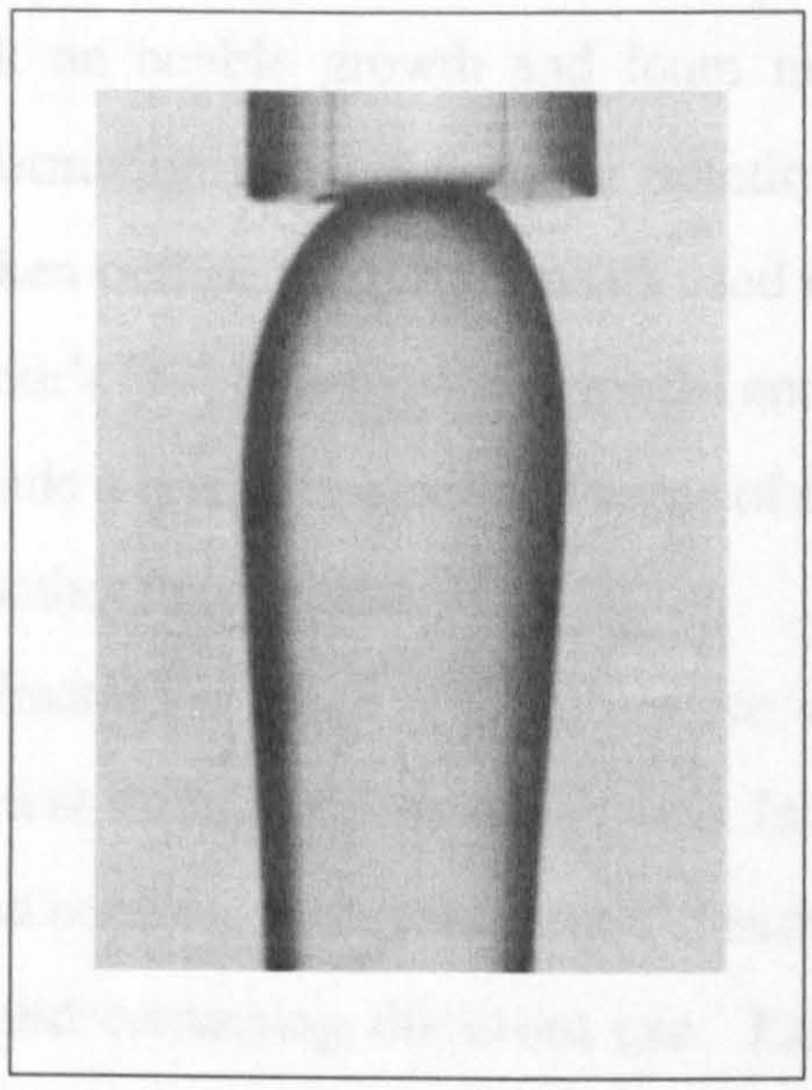

Figure 1.5: Die swell of a polymeric liquid exiting a convergent die. Picture taken from [9].

highly dependent on the size, distribution, and density of the bubbles and on whether the bubbles remain whole (closed cell foams) or whether the windows separating them break forming open cell foams. There are two distinct methods of production depending on whether the polymer is synthesised prior to, or during, the moulding process. In the former case a polymeric liquid containing a foaming agent is injected at high pressure into a mould. As the pressure is reduced, bubbles nucleate and expand forming a polymeric foam. In the latter case of reaction injection moulding [29], liquid reactants are injected into the mould where they react forming a polymer of increasing molecular weight. Gas is produced as a by-product of the reaction, leading to the nucleation and growth of bubbles within a fluid whose rheology evolves from a low viscosity liquid to a viscoelastic gel.

Our aim is to provide a better understanding, firstly of the growth of isolated bubbles, and secondly of the deformation of the liquid windows between neighbouring bubbles, that could be applied to these two processes.

We begin in this chapter by describing the production processes and the background chemistry involved in reaction injection moulding in more detail. We also review

some of the existing work on bubble growth and foam models. In chapter 2 we give some background information about the tensor notation used in this thesis and linear viscoelasticity. We then outline the fluid models used including a description of Rubinstein, Colby and Gilmor's [43] linear reacting model and our non-linear extension to it. In this section we include a brief description of some of the percolation theory that is used as a basis for the reacting fluid model.

When the bubble volume fraction is small the bubbles are sufficiently far from their neighbours to remain spherical throughout the expansion. In chapter 3 we analyse the growth of individual isolated bubbles, by considering a spherical bubble surrounded by a spherical envelope of liquid containing dissolved gas. Expansion is driven by the pressure difference between the pressure inside the bubble and an ambient pressure outside the liquid layer. In order to model the two different production processes we employ a number of constitutive models for the liquid layer. In the case of thermoplastic injection moulding the liquid rheology does not change during the expansion and so we use Oldroyd B and Pompom models for the liquid phase. In order to model foaming in reaction injection moulding, we apply the reacting fluid model described in chapter 2 in which the fluid viscoelasticity increases as the reaction proceeds and gas is produced that then diffuses into the bubble.

When the bubble volume fraction is large, bubbles are affected by the proximity of their neighbours and the assumption of spherical symmetry breaks down. In chapter 4 we analyse the growth of identical bubbles in a two-dimensional hexagonal array of bubbles and liquid. In this chapter we study the size and shape of bubbles as the fluid films separating them thin by analysing a small region of the fluid window, equal to 1/12 of a hexagonal cell. Here we adapt an existing simulation developed by Harlen [22] to include the effects of gas diffusion. Comparisons are made between the full two-dimensional, finite-element solution and two approximations. When the liquid layer becomes very thin we can assume that velocity gradients and polymer stresses are independent of fluid depth and so we are able to construct a one-dimensional, planar, approximation. In the opposite limit we assume that the bubble remains circular

throughout the expansion. Due to the geometric differences between two and three dimensions we also present axisymmetric models for the strut in an open cell foam and a circularly symmetric section of the window between two bubbles in a closed cell foam. In reality foams are not made up of identical bubbles. The competition between bubbles of different sizes for the available gas gives rise to the surface tension driven phenomenon known as **Ostwald Ripening**. This causes small bubbles to shrink while large bubbles continue to expand. In chapter 5 we use an approximate model for a distribution of spherical bubbles of varying sizes to investigate the effect of fluid rheology on Ostwald ripening and the final bubble size distribution in a dilute suspension of bubbles. We then extend the two-dimensional hexagonal geometry of chapter 4 to include bubbles of two different sizes to investigate higher volume fractions. We solve the full two-dimensional problem for bubbles expanding in an Oldroyd B liquid and make comparisons with a circular approximation in which gas diffusion is instantaneous. In this way we are able to predict the final bubble sizes and the shape of the gas-liquid interface at various stages of the expansion. Chapter 6 provides discussion and conclusions of the work presented in chapters 3 to 5.

The fluid constitutive models referred to in the following sections will be described fully in chapter 2.

## 1.3 The Reaction Injection Moulding Process

The major development of reaction injection moulding technology was pushed by the needs of the U.S. automotive industry following a 1972 Congress mandate that bumpers on all cars sold in the U.S. should withstand a 5 mile per hour impact without damage. Reaction injection moulding production in the U.S. grew from 2000 tons in 1974 to 17 000 tons in 1978, by 1987 production had risen dramatically again and included application to interior car parts, furniture, construction items such as window frames, appliances and recreational equipment.

In conventional thermoplastic injection moulding, the polymer is heated until its viscosity is low enough that it can injected into moulds. The mould is then cooled, the polymer solidifies, and the product is turned out. During this process there is no chemical change in the material but very high temperatures are often required so that cooling can be a relatively lengthy process.

Reaction injection moulding is a method for rapid production of complex plastic parts directly from low viscosity monomers. The liquid reactants are combined by impingement mixing as they enter the mould. Mixing activates the reaction and solid polymer forms by cross-linking or phase separation so that parts can often be removed from the mould in less than a minute. Bubble density gradients occur in the final part in the direction of the flow. These can be caused by bubbles at the flow front having longer to grow and experiencing lower pressures, coalescence of bubbles near the front, and temperature gradients in the mould walls affecting the rate at which the reaction progresses to gelation.

The viscosity of materials entering a reaction injection mould are of the order 0.1 – 1Pas compared to $10^2$ – $10^5$Pas for thermoplastic injected materials. This has the advantage that large parts with complex shapes can be made relatively easily and cheaply. However, a disadvantage of using low viscosity liquids is that if the flow into the mould is too rapid air may be entrained and large bubbles appear in the final part. This is the greatest source of scrap production in reaction injection moulding. In addition, the liquid reactants are highly dangerous and often carcinogenic.

Mould pressures are typically very low in the reaction injection moulding process, resulting in lighter weight and lower cost moulds than in thermoplastic injection moulding.

Since reaction injection moulding uses polymerisation rather than cooling to set the part shape the temperature of the mould walls is much closer to the temperature of the material than in thermoplastic injection moulding. Typically there might be a difference of 30°$C$ between mould walls and materials compared to a difference of 175°$C$ between thermoplastic mould walls and materials. Other processes use polymerisation to set the

part shape but employ hot mould walls to activate the reaction.

More detail regarding reaction injection moulding can be obtained from 'The Fundamentals of Reaction Injection Moulding' [29].

## 1.4 Reaction Chemistry of Polyurethane

The main polymer used in foam manufacture is polyurethane. Polyurethane is made by reacting two groups of reactants: molecules with isocyanate end groups (NCO); and polyols, low molecular weight polymers containing OH end groups. There are two reactions involved in making polyurethane foam. In the first molecules containing isocyanate end groups react with water generating carbamic acid. This compound is unstable and degenerates into amine and carbon dioxide. The carbon dioxide causes foaming and the amine reacts again with a second isocyanate group to form a urea bond. Figure 1.6 shows this reaction diagrammatically. Thus one complete reaction involves two isocyanate groups and one water molecule. In the second reaction polyol molecules react with isocyanate groups to produce urethane groups (see figure 1.7). Most molecules contain either two OH groups or two NCO groups, one at each end, so that these reactions lead to the synthesis of linear polymers. However branching may be introduced by adding a few molecules with functionality greater than two. The ratio of NCO groups to OH groups (in the water and polyol) is called the **stoichiometric ratio.** In practice the foaming process is more complicated as other elements are added to control the properties of the cured foam and the foaming reaction. For example, volatile compounds are added as blowing agents and surfactants are often used to stabilise the bubbles. Different molecules with isocyanate end groups can be used by changing the 'R' part of the molecule. The NCO+$H_2O$ segments are referred to as **hard block** segments with the water molecules playing the role of **chain extender.** The long polyol molecules are referred to as **soft block** segments because of the presence of a flexible alkane chain between the OH groups. The resulting polymer is therefore a block

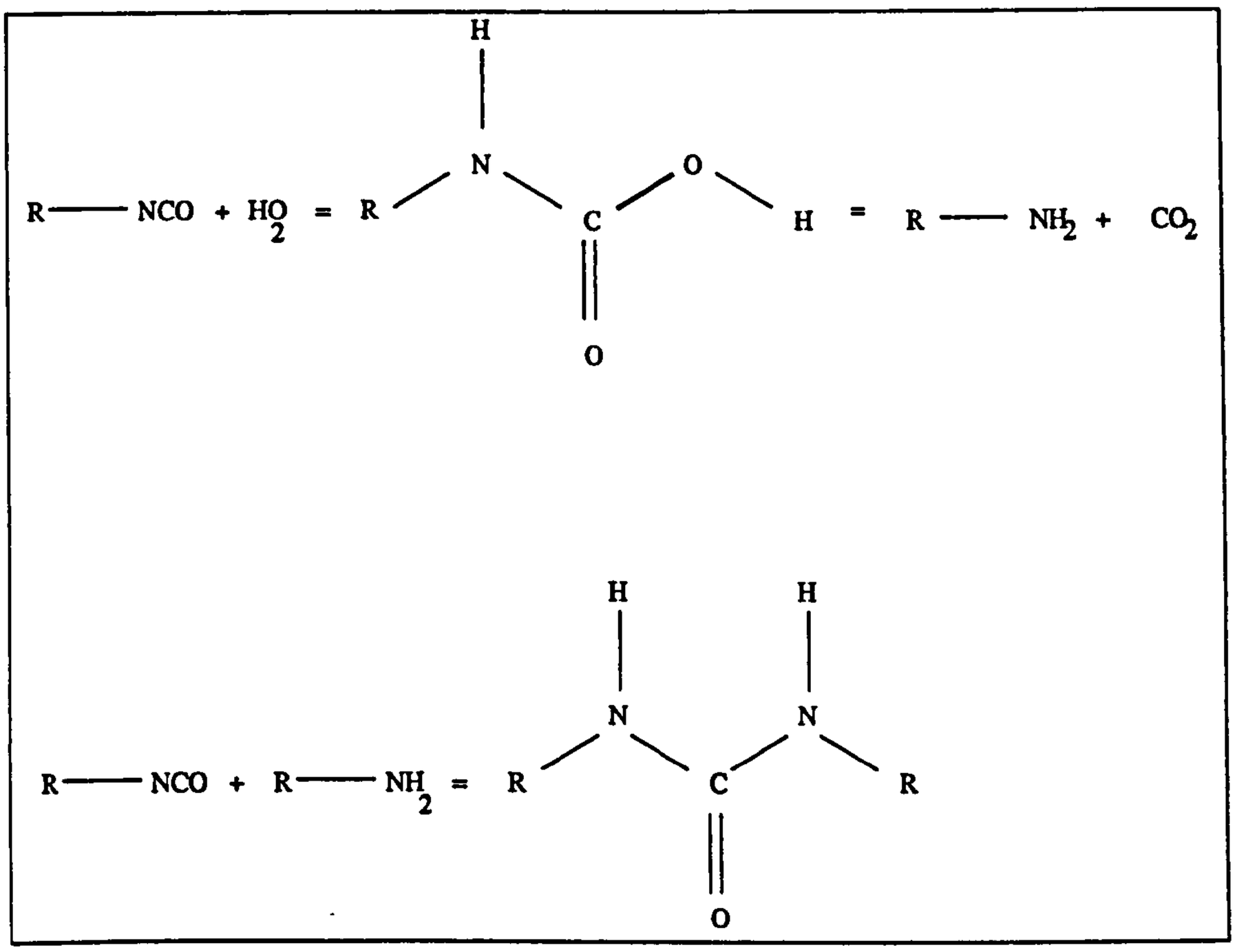


Figure 1.6: Isocyanate and water reaction, resulting in hard block segments.

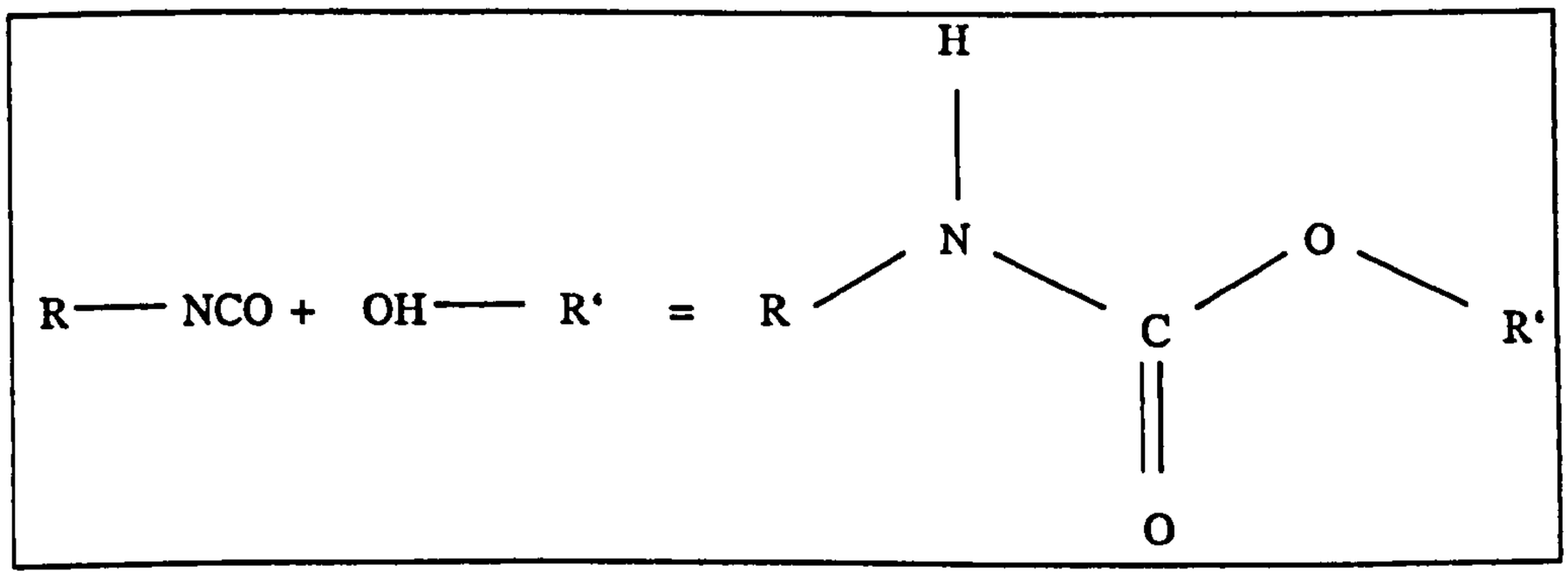


Figure 1.7: Isocyante and polyol reaction, resulting in soft block segments.

copolymer consisting of hard and soft block segments. It is observed that the ratio of hard to soft block segments affects the level of cell opening.

In reaction injection moulding the moulded part is usually removed from the mould while hot (the reactions are highly exothermic) to speed up the process, so the liquid must have gelled and cured sufficiently to hold the required shape. Gelation occurs through a combination of two mechanisms. The inclusion of isocyanate molecules with functionalities greater than two produces branching during polymerisation and the formation of a gel held by chemical bonds. In addition, as the temperature decreases phase separation occurs between the soft and hard block phases. This phase separation forms a physical gel as hard block segments of different molecules are held together.

## 1.5 Bubble Growth in Newtonian and Viscoelastic Liquids

For small bubble volume fractions bubbles remain isolated, and so remain spherical during the expansion. Several studies are available on bubble growth where expansion is driven by gas diffusing from the surrounding liquid. Here we present a brief summary of previous work on bubbles expanding in Newtonian and viscoelastic fluids. The assumption of spherical symmetry breaks down as the bubble volume fraction increases and bubble growth is affected by the presence of neighbouring bubbles. Few studies of the effects of proximity of neighbouring bubbles have been reported in the literature though we review two that study two-dimensional bubble expansion.

### 1.5.1 Growth of Isolated, Spherical, Bubbles

There have been a number of studies of the expansion of a spherical gas bubble due to diffusion of gas from the surrounding liquid.

Amon and Denson [1] introduce the idea of a 'cell model' - a spherical bubble

surrounded by a spherical envelope of fluid which contains a limited supply of gas. The volume of fluid is dictated by the number of bubbles per unit volume in the cured foam. Arafmanesh and Advani [3] describe a model for bubble growth in a Newtonian fluid driven by gas diffusion. Their model takes account of heat transfer and inertia and couples bubble growth to the changing foam density.

Street [52] was one of the first to study the effects of viscoelasticity on bubble growth rate using the Oldroyd B fluid model. When compared to bubbles expanding in Newtonian liquids he found that bubbles expanding in a viscoelastic liquid with the same zero shear rate viscosity have a higher initial growth rate followed by a cessation of growth as bubbles interact to form thin liquid films. Tanasawa and Yang [54] and Ting [55] also studied bubble growth in an Oldroyd B fluid and, like Street, assumed that all available gas was inside the bubble at nucleation. Han and Yoo [21] provide experimental results showing the effects of various parameters. At low injection pressure the growth mechanism is controlled by diffusion, whereas at high injection pressure there is an initial phase of slower growth rate before the growth rate approaches that of the diffusion controlled case. Melt viscoelasticity was again found to enhance the initial growth rate compared to a Newtonian liquid with the same zero shear rate viscosity while increasing the melt viscosity reduces the initial growth rate. Ramesh, Rasmusen and Campbell [41] give a comparison of experimental results with their own model for bubble growth in a power law fluid and the model of Arafmanesh and Advani [2] in which gas diffuses into the bubble from a limited supply dissolved in an Oldroyd B fluid. They concluded that the Oldroyd B model is better able to fit the experimental data capturing both the rapid initial phase followed by a slower growth phase and the equilibrium bubble radius. The two viscous models show large deviations during the initial stages of growth and, since these models assume a limitless supply of gas, do not predict an equilibrium bubble radius.

Koopmans et al [26] model foam growth in a thermoplastic polymer by analysing an isolated spherical bubble expanding in a generalised Newtonian fluid. The temperature dependent viscosity accounts for the cooling effect of the blowing agent in addition to

the cooling of the polymer.

### 1.5.2 Foam Windows

At higher volume fractions the bubbles become non-spherical with thin fluid windows separating neighbouring bubbles. Schwartz and Roy [45] study the effects of closely packed gas bubbles on a gelling liquid using a lubrication approximation for the flow in the liquid films. In their model bubble expansion is driven by a known rate of gas production imposing a deformation rate on the liquid. The fluid is modelled as a generalised Newtonian fluid whose viscosity increases at a rate dependent on the **drying time**. For times larger than the drying time the viscosity is assumed infinite and a final fluid profile is obtained. Their model includes the effects of surfactant molecules on the fluid-gas interface. Surfactant concentration affects the interface dynamics in two ways: Marangoni stress, caused by surface tension gradients, hardens the liquid-gas interface and thickens windows while the surfactant locally reduces the surface tension. When sections of the film become very thin a **disjoining pressure** caused by Van der Waals and other molecular forces tends to prevent window breakage.

Pozrikidis [35] considered the expansion of two dimensional bubbles surrounded by a Newtonian liquid, in square and hexagonal arrays, for a specified areal flow rate. Here the long time structure of the foam is a strong function of the capillary number and the thickness of the liquid films decreases in time according to a power law relation with film rupture occurring at infinite time.

In the event that the liquid windows break, all the liquid is found in struts that stretch and deform as the foam continues to expand. These stretching struts have similarities with stretching filaments that have been described in numerous papers. Szabo [53] provides a detailed analysis of the forces on a filament with circular cross section attached to horizontal moving plates. He analyses the model to ascertain the importance of inertia, gravity and surface tension with various viscoelastic fluid models. These calculations were done specifically for use with filament stretching rheometers to ensure

that measurements are appropriately corrected. Entov and Hinch [15] use a FENEcr constitutive model to describe the behaviour of a uniform cylindrical column of fluid which is squeezed by surface tension. The resulting extension is divided into three regions: early viscous times before elastic stress becomes significant; middle elastic times in which the strain-rate drops in order not to stretch the elastic stress beyond the capillary pressure and the way in which the radius decreases is dependent on the spectrum of relaxation times and could not be represented by a single model; and late times limited by the finite extension of the FENE model. These filament stretching models provide a useful qualitative comparison of elastic effects for our axisymmetric model of the liquid struts in an open cell foam (section 4.3).

### 1.5.3 Nucleation

The expansion of a foam is dependent on the formation of clusters of gas molecules that are able to nucleate and expand into bubbles. The calculation of the size of cluster that is able to nucleate and the rate at which clusters are able to overcome the nucleation threshold is highly complex and has been the subject of much investigation. The simplest form of nucleation is **homogeneous nucleation** which is generally used as a basis for describing other forms of nucleation such as **heterogeneous nucleation** (in which bubbles nucleate on the surface of impurities in the liquid phase) and **crystallisation** from solutions and melts. While there are a number of theories on the subject they are largely divided into two categories: classical theory dating back to the 1930's and 40's and, more recently, kinetic theories.

Nucleation occurs when a cluster of gas molecules is larger than a **critical cluster.** The free energy of formation of the critical cluster can be thought of as a free energy barrier to nucleation. A decrease in size of the critical cluster increases the likelihood of nucleation. As the amount of gas dissolved in the liquid increases the size of the critical cluster, and hence the energy barrier, is reduced and the probability of nucleation increases. The calculation of the nucleation rate involves the free energy associated

with the surface of the critical cluster, which is difficult to obtain. In the classical theory a capillarity approximation allows the free energy of formation of a cluster to be calculated from bulk thermodynamics. Validity of this assumption is questionable because of the high surface curvature of clusters involved. There have been numerous attempts to correct this - a review is given in [23]. A kinetic theory developed by Ruckenstein et al (eg. [44]) and later applied to the formation of gas bubbles by Shen and Debenedetti [48] avoids the capillarity approximation by deriving a balance between the rates of dissociation (the rate at which molecules on the surface of a cluster leave the surface layer by overcoming a potential energy barrier) and condensation (rate at which molecules diffuse from the external field).

The main difficulty arising in applying these theories to bubble growth and foam formation is that these are microscopic theories and the bubble growth models are macroscopic. Shafi et al [46] and [47] divide foam expansion in Newtonian liquids into two phases - a nucleation phase and a bubble growth phase. In the nucleation phase the bubble growth and gas diffusion equations are solved locally in the neighbourhood of each bubble. An 'influence volume' is assigned to each bubble by setting the outer radius of a spherical shell of liquid to be that at which the gas concentration falls below the nucleation threshold. As the bubbles grow and the gas concentration in the bulk decreases the influence volumes increase in size. Outside the influence volumes the gas concentration is higher than the nucleation threshold and new bubbles are able to nucleate. Eventually all the liquid is assigned to influence volumes and the nucleation phase ends with a distribution of bubble volumes, each surrounded by a spherical shell of liquid containing a fixed mass of gas. Final bubble volumes are calculated via a mass balance on each cell. They found that decreasing the nucleation rate or increasing the bubble growth rate resulted in fewer bubbles being formed.

Due to the complex nature of the nucleation process we will study the expansion of bubbles from the end of the nucleation phase.

## 1.6 Numerical Methods

Much of the work in this thesis concerns the solution of partial differential equations with variations in space and time. In this section we describe the main numerical methods employed in this thesis to solve these equations.

### 1.6.1 Spatial Variations

In chapter 3 and part of chapter 4 the geometry and assumptions made reduce the governing equations to a one-dimensional set. In chapter 3 a spherical geometry allows the spherical layer of liquid surrounding a spherical gas bubble to be discretized into a series of spherical shells as shown in figure 1.8. In chapter 4 the liquid film between two bubbles is pulled into a long, thin, filament and we make assumptions that, again, reduce the problem to one dimension and allow us to discretize the computational domain into a series of trapezia as shown in figure 1.9. Since spatial variations are restricted to one dimension we can use **finite difference methods** to discretize derivatives. Since the nodes are not equally spaced we use

$$\frac{\partial c}{\partial x} = \frac{c_{i+1} - c_i}{x_{i+1} - x_i}$$

for first derivatives and

$$\begin{aligned} \frac{\partial^2 c}{\partial x^2} &= \frac{\frac{\partial c_i}{\partial x} - \frac{\partial c_{i-1}}{\partial x}}{\frac{1}{2}(x_{i+1} - x_{i-1})} \\ &= 2\left(\frac{c_{i+1} - c_i}{(x_{i+1} - x_i)(x_{i+1} - x_{i-1})} - \frac{c_i - c_{i-1}}{(x_i - x_{i-1})(x_{i+1} - x_{i-1})}\right) \end{aligned}$$

for second derivatives. However, when the simplifying assumptions that reduce the solution space to one dimension are not made we require methods to solve the two-dimensional forms of the equations. Finite difference methods can also be used in multiple dimensions by solving the equations on an orthogonal grid. However, the complex shape of the fluid domain makes it difficult to apply the boundary conditions.

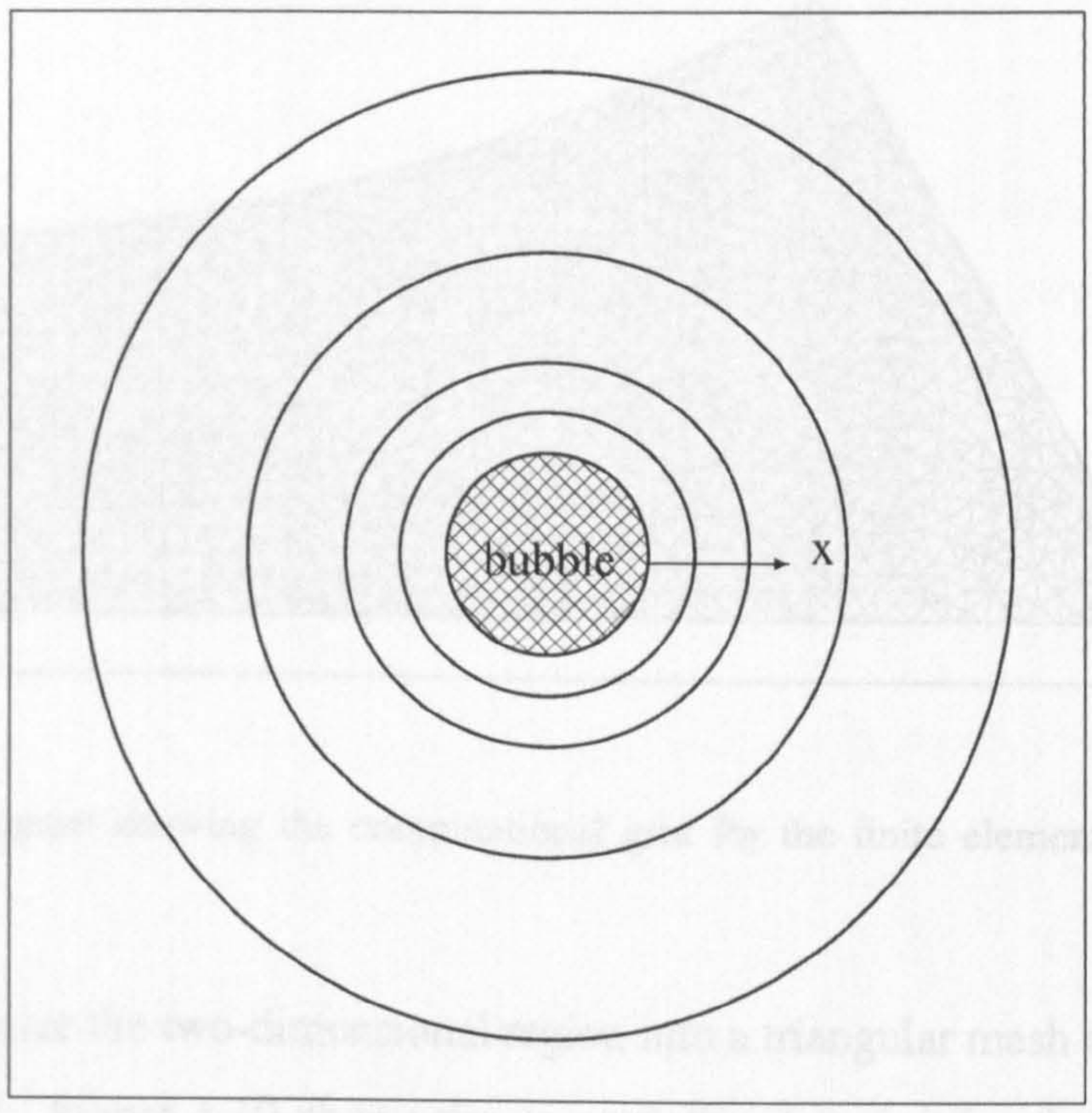


Figure 1.8: Schematic diagram showing the computational grid for chapter 3.

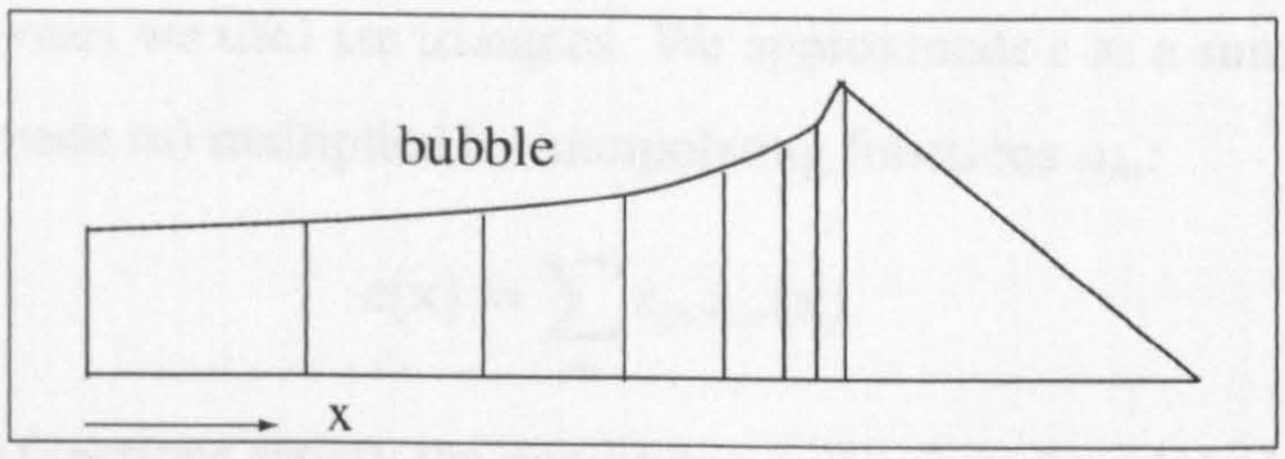


Figure 1.9: Schematic diagram showing the computational grid for the finite difference calculations in chapter 4.

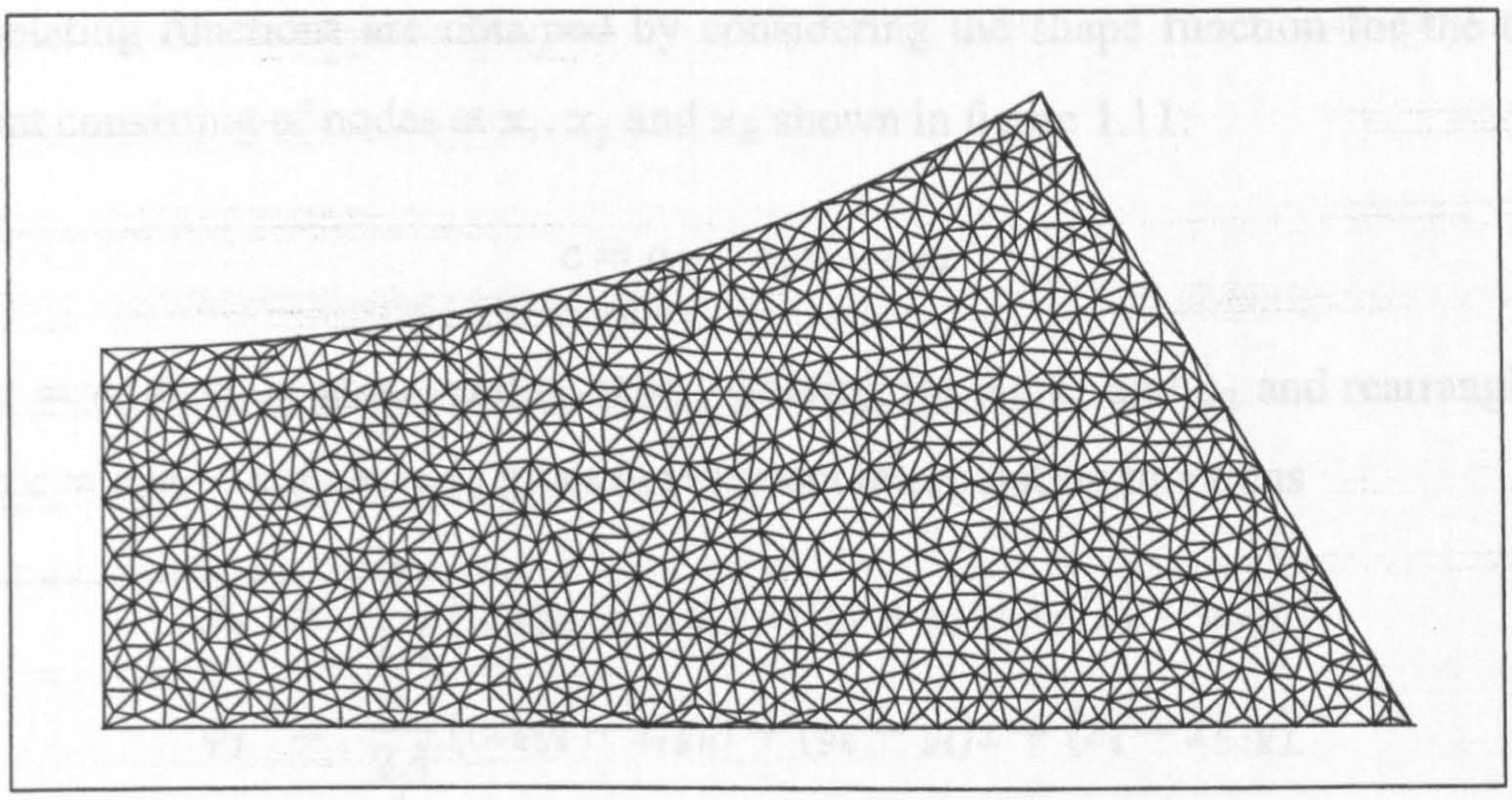

Figure 1.10: Diagram showing the computational grid for the finite element calculations in chapter 4.

Instead we discretize the two-dimensional region into a triangular mesh and use a **finite element method**. Figure 1.10 shows the computational region for the finite element calculations in chapter 4. Details of finite element methods can be found in numerous books, however [7] gives a clear introduction while [11] and [24] give more detailed explanations. Here we outline the theory applied to the two dimensional Laplace equation, $\nabla^2 c = 0$.

The domain is discretized into a series of elements that can be of any shape, however the simplest (and the ones we use) are triangles. We approximate $c$ as a sum of discrete $c_m$ (the value of $c$ at node $m$) multiplied by interpolating functions $\phi_m$:

$$c(\mathbf{x}) = \sum_m c_m \phi_m(\mathbf{x}). \tag{1.1}$$

The interpolating functions satisfy the conditions $\phi_m(\mathbf{x}_m) = 1$ and $\phi_m(\mathbf{x}_s) = 0$ where $s \neq m$. $\phi_m$ is only non-zero in elements which include node $m$. For triangles with nodes at the vertices the interpolating functions are linear. However, more complex elements use interpolating functions that are quadratic or higher order polynomials. In particular, spectral element methods use small numbers of elements with high order polynomial interpolation within each element. For the linear triangular element

interpolating functions are obtained by considering the shape function for the single element consisting of nodes at $\mathbf{x}_i$, $\mathbf{x}_j$ and $\mathbf{x}_k$ shown in figure 1.11:

$$c = a_0 + a_1 x + a_2 y$$

with $c = c_i$ at $\mathbf{x}_i$, $c_j$ at $\mathbf{x}_j$, and $c_k$ at $\mathbf{x}_k$. Solving for $a_0$, $a_1$ and $a_2$ and rearranging to obtain $c = c_i\phi_i + c_j\phi_j + c_k\phi_k$ gives the element interpolating functions

$$\begin{aligned}
\phi_i &= \frac{1}{2A}\left((x_j y_k - x_k y_j) + (y_j - y_k)x + (x_k - x_j)y\right) \\
\phi_j &= \frac{1}{2A}\left((x_k y_i - x_i y_k) + (y_k - y_i)x + (x_i - x_k)y\right) \\
\phi_k &= \frac{1}{2A}\left((x_i y_j - x_j y_i) + (y_i - y_j)x + (x_j - x_i)y\right)
\end{aligned}$$

where $A$ is the area of the triangle. The interpolating function $\phi_m$ is then obtained by

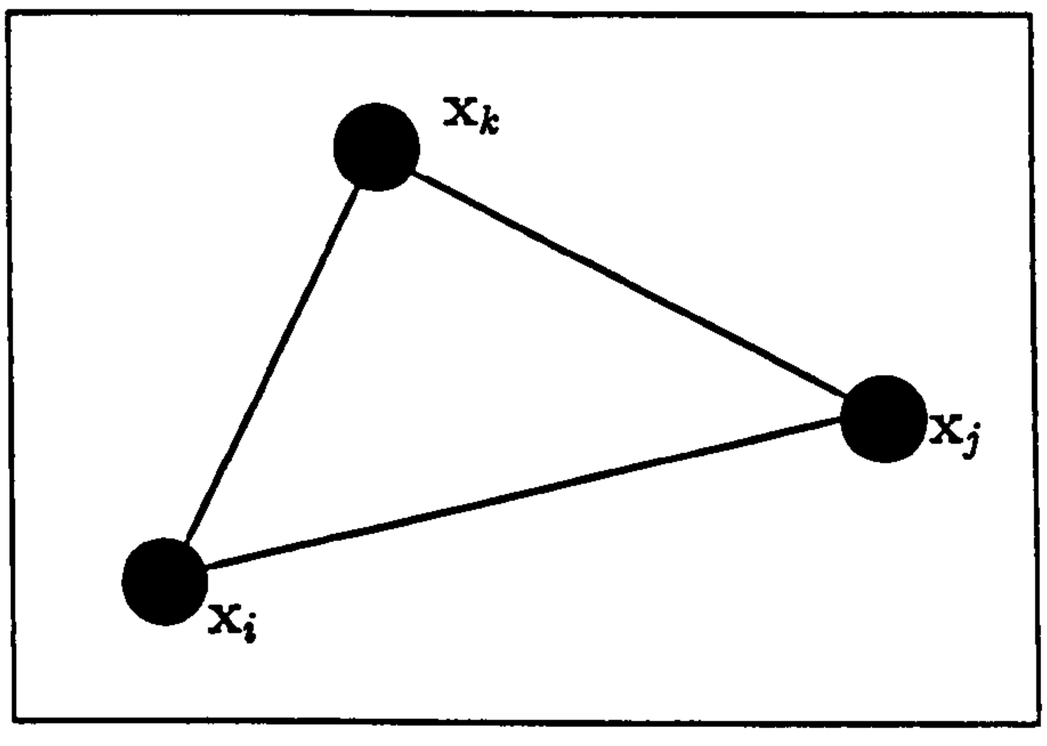


Figure 1.11: Schematic diagram showing a triangular element with nodes $\mathbf{x}_i$, $\mathbf{x}_j$ and $\mathbf{x}_k$.

summing the element interpolation functions for each element including the node at $\mathbf{x}_m$. Substituting the approximate solution 1.1 into Laplace's equation gives a residual, $R$:

$$\sum_m c_m \nabla^2 \phi_m = R.$$

The method of **weighted residuals** minimises this by multiplying by a weighting function and integrating over the fluid volume, $V$, to give

$$\int_V R w_k dV = 0,$$

where $w_k$ are the weighting functions associated with node $k$. **Galerkin's method** uses the interpolating functions as the weighting functions, thus

$$\sum_m c_m \int_V \phi_k \nabla^2 \phi_m dV = 0.$$

By integration by parts we can obtain two integrals: one over the fluid volume and one over the surface bounding the fluid volume,

$$\sum_m c_m \int_V \nabla\phi_k \nabla\phi_m dV = \int_S \nabla c.\hat{\mathbf{n}}\phi_k dS,$$

$$\sum_m c_m M_{mk} = \int_S \nabla c.\hat{\mathbf{n}}\phi_k dS, \tag{1.2}$$

where the matrix $M_{mk} = \int_V \nabla\phi_k \nabla\phi_m dV$. $\nabla\phi_i$ can be calculated for the element consisting of nodes at $\mathbf{x}_i$, $\mathbf{x}_j$ and $\mathbf{x}_k$ as

$$\begin{aligned} \nabla\phi_i &= \left(\frac{\partial\phi_i}{\partial x}, \frac{\partial\phi_i}{\partial y}\right) \\ &= \frac{1}{2A}\left((y_j - y_k), (x_k - x_j)\right). \end{aligned}$$

Thus the element containing nodes $i$, $j$, and $k$ contributes to the following coefficients of M:

$$\begin{matrix} ii & ij & ik \\ ji & jj & jk \\ ki & kj & kk. \end{matrix}$$

Since $\nabla\phi$ is constant over triangles, the contributions to M from this element are

$$\mathrm{M} = \frac{1}{4A}\begin{pmatrix} (y_j - y_k)^2 + (x_k - x_j)^2 & (y_j - y_k)(y_k - y_i) + (x_k - x_j)(x_i - x_k) & (y_j - y_k)(y_i - y_j) + (x_k - x_j)(x_j - x_i) \\ (y_k - y_i)(y_j - y_k) + (x_i - x_k)(x_k - x_i) & (y_k - y_i)^2 + (x_i - x_k)^2 & (y_k - y_i)(y_i - y_j) + (x_i - x_k)(x_j - x_i) \\ (y_i - y_j)(y_j - y_k) + (x_j - x_i)(x_k - x_j) & (y_i - y_j)(y_k - y_i) + (x_i - x_k)(x_j - x_i) & (y_i - y_j)^2 + (x_j - x_i)^2 \end{pmatrix}.$$

Thus M is constructed by summing contributions from each element. The surface integral on the left hand side of 1.2 is obtained from boundary conditions. For Dirichlet boundary conditions the integral is zero since $\phi_k = 0$ for all unknown $c_k$. For Neumann boundary conditions the surface integral can be calculated directly from the boundary conditions. The discretization leads to a matrix equation of the form $\mathbf{Mc} = \mathbf{r}$ for the vector of $c_m$ coefficients **c**.

### Conjugate Gradient Method

The system $\mathbf{Mc} = \mathbf{r}$ is solved for the symmetric, positive definite matrix M, using a **conjugate gradient method**. Solving $\mathbf{Mc} - \mathbf{r} = 0$ is equivalent to finding the minimum value of the function $\Phi = \frac{1}{2}\mathbf{c}^T\mathbf{Mc} - \mathbf{c}^T\mathbf{r}$. One way to do this would be by the method of **steepest descents**. Here $\Phi$ represents a surface and $\mathbf{c}_0$ is a starting point on the surface. In order to find an improved estimate of the true value of **c** we first find the steepest gradient given by

$$-\nabla\Phi(\mathbf{c}_0) = \mathbf{r} - \mathbf{Mc}_0 = \mathbf{p}_0.$$

Then the new estimate, $\mathbf{c}_1$ is given by the minimum of $\Phi$ in the direction of $\mathbf{p}_0$. Let

$$\mathbf{c}_1 = \mathbf{c}_0 + \alpha_0\mathbf{p}_0$$

then for a stationay point $d\Phi/d\alpha_0 = 0$ so that

$$\alpha_0 = \frac{\mathbf{p}_0^T\mathbf{p}_0}{\mathbf{p}_0^T\mathbf{Mp}_0}.$$

From the point $\mathbf{c}_1$ we move in the new direction of steepest gradient until we reach $\mathbf{c}_2$, the minimum in this direction, and so on.

The conjugate gradient method allows us to minimise $\Phi$ in a number of directions simultaneously. When the matrix M is positive definite the minimum value that is the true solution, **c**, lies at the centre of the elliptical level curves $\Phi(\mathbf{c}_i)$. Thus, we find $\mathbf{c}_1$ as above but then choose a new search direction, $\mathbf{p}_1$, that points to the centre of the level

curve through $\mathbf{c}_1$. In this way the new direction, $\mathbf{p}_1$, is in a conjugate direction to $\mathbf{p}_0$ satisfying the condition that

$$\mathbf{p}_0^T \mathbf{M} \mathbf{p}_1 = 0 \tag{1.3}$$

In order to find $\mathbf{p}_1$ we let

$$\mathbf{p}_1 = \mathbf{n}_1 - \beta_1 \mathbf{p}_0$$

where $\mathbf{n}_1$ is the normal to the level curve through $\mathbf{c}_1$ at the point $\mathbf{c}_1$. Substituting this into 1.3 gives

$$\beta_1 = \frac{\mathbf{p}_0^T \mathbf{M} \mathbf{n}_1}{\mathbf{p}_0^T \mathbf{M} \mathbf{p}_0}.$$

Then we search for $\mathbf{c}_2$ by finding the minimum value of $\Phi(\mathbf{c}_1 + \alpha_1 \mathbf{p}_1)$ in the direction $\mathbf{p}_1$.

The algorithm for finding $\mathbf{c}_i$ is:

$$\begin{aligned}
\alpha_i &= \frac{\mathbf{p}_i^T \mathbf{n}_i}{\mathbf{p}_i^T \mathbf{M} \mathbf{p}_i} \\
\mathbf{c}_{i+1} &= \mathbf{c}_i + \alpha_i \mathbf{p}_i \\
\mathbf{n}_{i+1} &= \mathbf{n}_i - \alpha_i \mathbf{M} \mathbf{p}_i \\
\beta_i &= \frac{\mathbf{n}_{i+1}^T \mathbf{M} \mathbf{p}_i}{\mathbf{p}_i^T \mathbf{M} \mathbf{p}_i} \\
\mathbf{p}_{i+1} &= \mathbf{n}_{i+1} - \beta_i \mathbf{p}_i.
\end{aligned}$$

Provided that $\mathbf{M}$ is non-singular the search directions $\mathbf{p}_i$ are linearly independent and, with exact arithmetic, the conjugate gradient method converges exactly when the number of iterations equals the size of the matrix. However, due to round off errors, the numerical algorithm is in practice iterative. The rate of convergence depends on the ratio of largest to smallest eigenvalues of $\mathbf{M}$.

In order to further improve efficiency the basic method is preconditioned, that is it is replaced with a problem with the same solution but with a smaller ratio of eigenvalues. This is done by multiplying the original equation by a preconditioner matrix that is an approximate inverse of $\mathbf{M}$. In order to preserve the symmetry of the system we solve

$$\tilde{\mathbf{L}}^{-1} \mathbf{M} \tilde{\mathbf{L}}^{-1} \tilde{\mathbf{L}} \mathbf{c} = \tilde{\mathbf{L}}^{-1} \mathbf{r},$$

where the preconditioner, $\tilde{\mathbf{L}}^{-1}$, is obtained from an incomplete Cholesky factorisation of M. The complete Cholesky factorisation of M is a lower triangular matrix, L, such that $\mathbf{M} = \mathbf{L}\mathbf{L}^T$. The matrix $\tilde{\mathbf{L}}$ is formed using the same algorithm as the complete factorisation but only has non-zero entries if the corresponding element of M is non-zero. Consequently $\tilde{\mathbf{L}}\tilde{\mathbf{L}}^T$ gives an approximate factorisation of M, so that $\tilde{\mathbf{L}}\mathbf{M}\tilde{\mathbf{L}}$ has a lower ratio of eigenvalues.

Further details of these methods are to be found in [17] and [36].

### 1.6.2 Time Integration

There are numerous methods for stepping through time and considerations of stability, accuracy and efficiency dictate the appropriate choice. The simplest, first order scheme, is a **forward Euler method** in which $\frac{\partial c}{\partial t}$ is calculated at the current time and the new $c$ is calculated by

$$c^{n+1} = c^n + \frac{\partial c}{\partial t}\Delta t.$$

The true value of $c^{n+1}$ could be expressed as an infinite series

$$c^{n+1} = c^n + \frac{\partial c}{\partial t}\Delta t + \frac{\partial^2 c}{\partial t^2}\frac{\Delta t^2}{2!} + \frac{\partial^3 c}{\partial t^3}\frac{\Delta t^3}{3!} + \ldots$$

which is truncated after the order $\Delta t$ term, thus each step involves errors of order $\Delta t^2$, so that this scheme produces errors of order $\Delta t$. Higher order methods are available by using multiple calculations in each time step such as Runge Kutta methods.

Applying this, and other forward methods, to the gas diffusion equation, $\partial c/\partial t = D\nabla^2 c$, produces an unstable scheme in which errors escalate if the time step $\Delta t > (\Delta x^2)/2D$ [36]. This critical time step can be thought of as time scale for gas to diffuse over one spatial step $\Delta x$. This instability can be overcome by using either a backwards method in which the $\nabla^2$ term is calculated at the new time,

$$c^{n+1} - c^n = D\Delta t\nabla^2 c^{n+1},$$

or by a **Crank-Nicolson** method which calculates the $\nabla^2$ term as an average of the value at the current time and at the new time

$$c^{n+1} - c^n = \frac{D\Delta t}{2}\left(\nabla^2 c^{n+1} + \nabla^2 c^n\right).$$

The Crank-Nicolson method has the advantage of being second order accurate in time. Whether one uses a finite difference or finite element method to express the $\nabla^2$ term spacially, the solution of an equation of the form $\mathbf{cM} = \mathbf{r}$ is required. In the case of the finite difference method $\mathbf{M}$ is a band-diagonal matrix that can be solved using standard numerical recipes [36] routines to construct and solve an LU decomposition. In the finite element case it is a sparse symmetric matrix that is, again, solved using the preconditioned conjugate gradient method described above.

# Chapter 2

# Fluid models

In this chapter we present the Oldroyd B and Pompom constitutive equations that are used to model the non-reacting polymer. The results of bubble expansion in these fluids are reported in subsequent chapters. We also include a brief description of the Rouse model. Although we do not apply this model directly to the bubble expansion flow, it is the starting point for the derivation of the reacting fluid model. We detail results from percolation theory before going on to present the derivation and linear viscoelastic behaviour of the model of a reacting fluid used in chapters 3 and 4.

## 2.1 Stress, Constitutive Equations and Tensor Notation

Before discussing specific fluid models we introduce the concepts of stress and constitutive equations in general terms. When a force is applied to a Newtonian liquid the liquid deforms and remains in this deformed state when the force is removed. However, when a force is applied to an elastic solid it deforms but returns to its original shape when the force is released. Polymeric liquids display a complex combination of these two types of behaviour.

The **stress** in a material is defined as the force per unit area acting across a plane of unit

normal $\mathbf{n}$, such that the force density, $\mathbf{f}$

$$\mathbf{f} = \boldsymbol{\sigma} \cdot \mathbf{n}.$$

The stress, $\boldsymbol{\sigma}$, is therefore a tensor field with component $\sigma_{ij}$. In an incompressible material part of the stress is an isotropic pressure required to maintain conservation of volume. It is therefore useful to express the stress, $\boldsymbol{\sigma}$ in the form

$$\boldsymbol{\sigma} = -p\mathbf{I} + \mathbf{S}, \tag{2.1}$$

where $p$ is the isotropic pressure and $\mathbf{S}$ is the extra stress which depends on the deformation and deformation rate of the material. It should be noted that, unlike the case of Newtonian fluids, the extra stress in many viscoelastic fluid models is not traceless.
The rate of deformation of the material can be obtained from the gradient of the velocity field, $\mathbf{q}(\mathbf{x})$ written as $\nabla\mathbf{q}$ where $[\nabla\mathbf{q}]_{ij} = \frac{\partial q_j}{\partial x_i}$. However only the symmetric part of this tensor, $\mathbf{E} = \frac{1}{2}(\nabla\mathbf{q} + \nabla\mathbf{q}^T)$, describes deformation as the antisymmetric part, $\Omega = \frac{1}{2}(\nabla\mathbf{q} - \nabla\mathbf{q}^T)$, represents a solid body rotation. The concept of **strain** is introduced by comparing the length of a fluid element at the current time to that in a reference configuration. The tensor $\mathbf{F}$ is defined by $F_{ij} = \frac{\partial x_i}{\partial x'_j}$ where $\mathbf{x}$ is the current position of the particle at time $t$ and $\mathbf{x}'$ is the position in a reference configuration. The current length of a fluid element, $dx$, is

$$d\mathbf{x}^2 = d\mathbf{x} \cdot d\mathbf{x} = \mathbf{F}^T\mathbf{F} : d\mathbf{x}'d\mathbf{x}'$$

The tensor $\mathbf{C} = \mathbf{F}^T\mathbf{F}$ is the Cauchy-Green tensor.
Two examples of constitutive equations are those of a Newtonian liquid in which the non-isotropic part of the stress is proportional to the deformation rate

$$\mathbf{S} = 2\mu\mathbf{E};$$

and a neo-Hookean rubber where the non-isotropic part of the stress is proportional to the deformation

$$\mathbf{S} = G\mathbf{B}$$

where $\mathbf{B} = \mathbf{F}\mathbf{F}^T$ is the Finger strain tensor. Further details can be found in 'Understanding Viscoelasticity' [34].

## 2.2 Viscoelasticity

A non-Newtonian fluid is any fluid not governed by the Newtonian constitutive equation, $\mathbf{S} = 2\mu\mathbf{E}$. Non-Newtonian effects can be classified into two groups: non-linear effects associated with the non-linearity of the constitutive relation (effects such as shear dependent viscosity, normal stress differences and high extensional resistance); and viscoelasticity, the extent to which the stress is dependent on the strain history rather than just the current strain-rate. Most non-Newtonian fluids have a characteristic time scale $\tau$. In a flow with characteristic shear-rate $\dot{\gamma}$ and time $T$ we can define two dimensionless numbers, the **Deborah number**, $De = \tau/T$, and the **Weissenberg number**, $Wi = \tau\dot{\gamma}$ [34]. The Deborah number measures the transient nature of the flow relative to the fluid time scale and characterises the memory effect associated with viscoelasticity. If the flow time scale is large compared to the relaxation time the material responds like a fluid, if it is small compared to the relaxation time the response is like an elastic solid. Thus in the limit $De = 0$ we have a visocus liquid and in the opposite limit, $De = \infty$, we have an elastic solid.

The Weissenberg number measures the nonlinearity of the stress strain-rate relationship. For example, in shear flow it gives a measure of the ratio of the first normal stress difference to the shear stress.

In a Newtonian fluid stress is linearly dependent on current strain-rate so that $De = Wi = 0$. In viscometric flows where the time scale for the flow is infinite (steady shear flows), $De = 0$ while $Wi > 0$. Conversely in small amplitude oscillatory flows the stress strain-rate relation is linear but time dependent, so that the relation is $Wi = 0$ but $De > 0$. This latter flow regime is referred to as linear viscoelasticity. Figure 2.1 shows a Pipkin diagram from [34] that maps all possible flow types in terms of Deborah and Weissenberg numbers. In general flows both the Deborah number and Weissenberg number are non-zero.

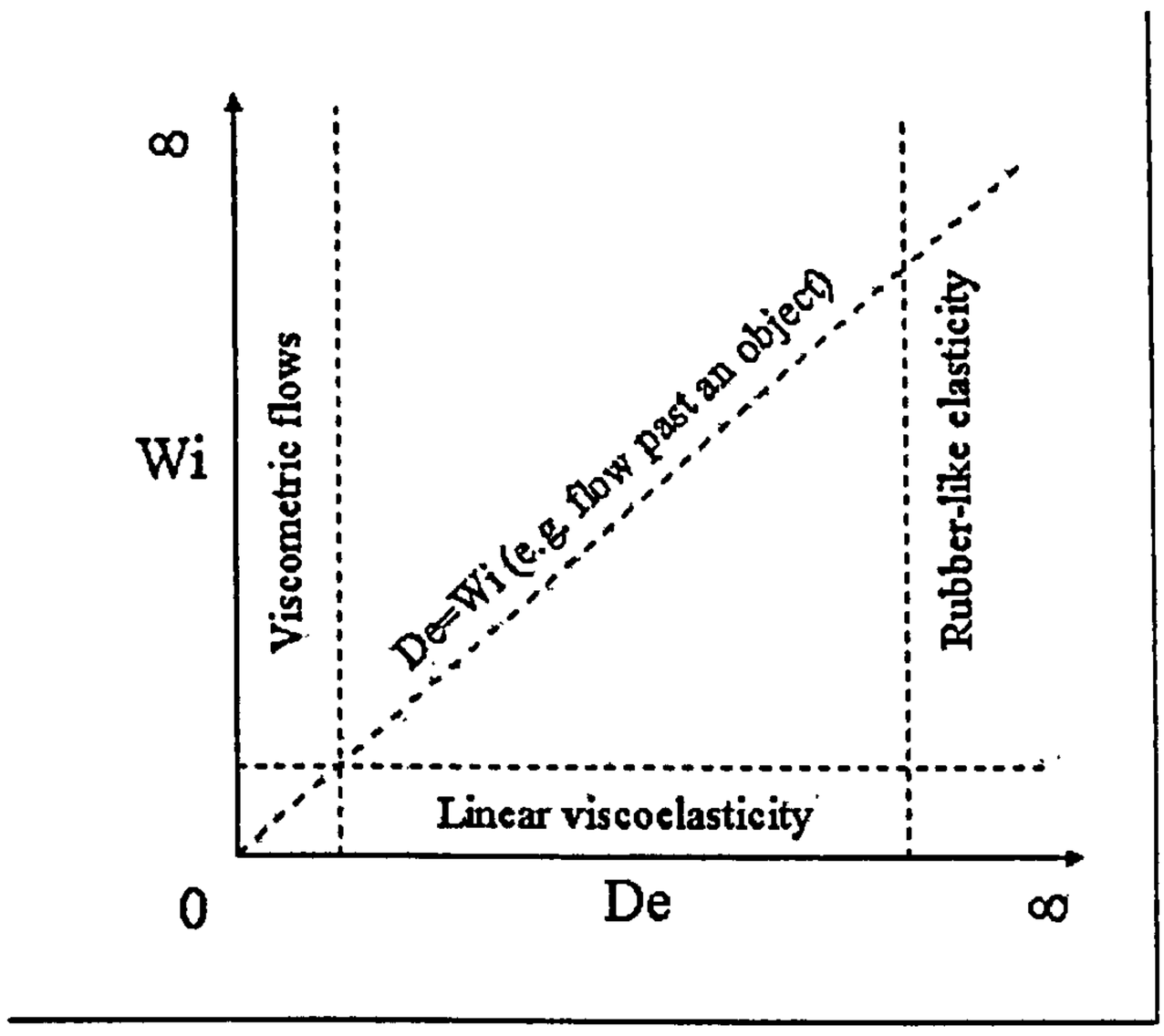


Figure 2.1: Schematic diagram mapping all possible flow types in terms of Deborah number and Weissenberg number.

### 2.2.1 Linear Viscoelasticity

In the linear viscoelastic regime (small strain amplitude) the extra stress, **S**, is a linear function of deformation rate and so can be written

$$\mathbf{S} = 2\int_{-\infty}^{t} G(t-t')\mathbf{E}(t')dt'. \tag{2.2}$$

Here it is assumed that no aging occurs i.e. the experiment yields the same results today and tomorrow, and that stress does not depend on future deformation. Equation 2.2 is known as Boltzman's constitutive equation. He was the first to quantify the memory effect in viscoelasticity and proposed this equation in 1874. $G$ is a function which depends on all past times, relating stress to strain history. If $G$ is constant this reduces to an elastic solid - a material with infinite memory so that it 'remembers' its initial configuration and resists deformation. In the opposite limit of a Newtonian viscous liquid we have $G(t-t') = \mu\delta(t-t')$. Here the stress depends only on the deformation rate at the current time and resists deformation rate. In a viscoelastic liquid the stress

depends on a combination of deformation and deformation rate.

There are a number of rheological experiments available to measure the properties of a fluid in the linear regime. The first of these is a step-strain where a constant strain is applied instantaneously to a sample of fluid and the shear stress is then measured as a function of time. In a step-strain $2E_{xy} = \dot{\gamma}(t') = \gamma\delta(t')$ so that

$$S_{xy} = \gamma G(t).$$

In the elastic solid limit where $G$ is constant, a constant stress needs to be applied to maintain a constant strain. In the Newtonian liquid limit, stress is only non-zero at $t = 0$, thus no stress is required to maintain a constant strain since all the stress is instantaneously relaxed. Between these limits, stress relaxes with a characteristic relaxation time $\tau$ (see figure 2.2).

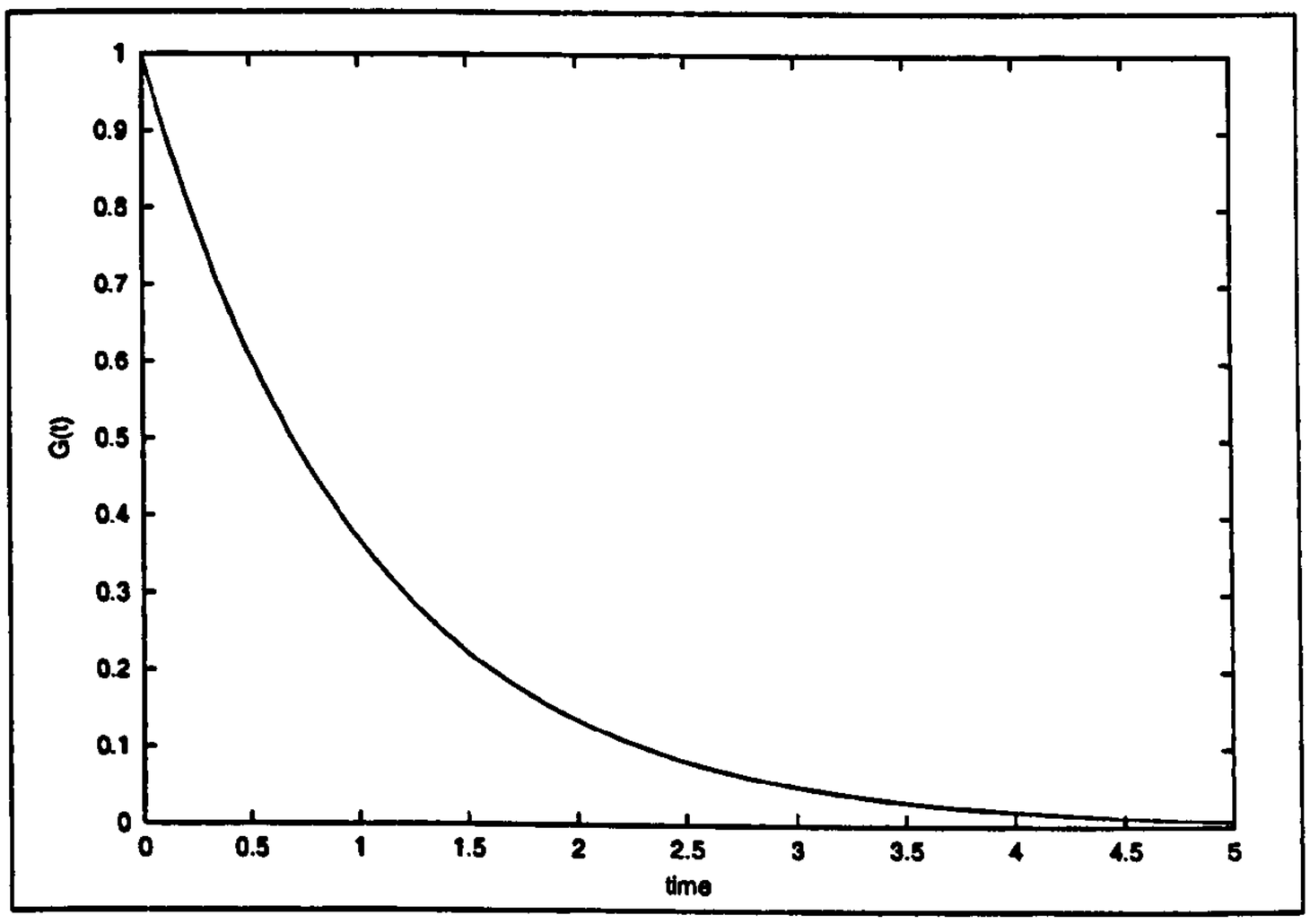


Figure 2.2: Schematic of $G(t)$ for a viscoelastic fluid. $G(t)$ for a Newtonian fluid is zero except when $t = 0$ and $G(t)$ for an elastic solid is constant (equal to the elastic modulus). Here the elastic modulus $G = 1$ and the characteristic relaxation time $\tau = 1$.

Another commonly used experiment is that of small amplitude oscillations, used to measure the elastic and viscous responses of the fluid. An oscillatory strain is applied so that

$$E_{xy} = \gamma(t) = \epsilon Re[e^{i\omega t}]$$

so that,

$$\dot{\gamma}(t) = \epsilon Re[i\omega e^{i\omega t}].$$

The shear stress is therefore

$$S_{xy} = \int_0^\infty i\omega\epsilon e^{i\omega(t-s)} G(s) ds$$

where $s = t - t'$. This can be represented in two ways:

$$S_{xy} = G^\star(\omega)\gamma \quad \text{where} \quad G^\star(\omega) = G'(\omega) + iG''(\omega) = \int_0^\infty i\omega e^{-i\omega s} G(s) ds$$
$$\text{or} \quad S_{xy} = \eta^\star(\omega)\dot{\gamma} \quad \text{where} \quad \eta^\star(\omega) = \eta'(\omega) + i\eta''(\omega) = \int_0^\infty e^{-i\omega s} G(s) ds.$$

$G^\star(\omega)$ is called the **complex elastic modulus** whereas $\eta^\star(\omega)$ is called the **complex viscosity.** The **storage modulus,** $G'(\omega)$, the real part of $G^\star(\omega)$, is in phase with $\gamma$ and measures the elastic response of the liquid, $G' = -\omega\eta''$. The imaginary part of $G^\star(\omega)$, the **loss modulus,** $G''(\omega) = \omega\eta'(\omega)$, is in phase with $\dot{\gamma}$ and measures the viscous response.

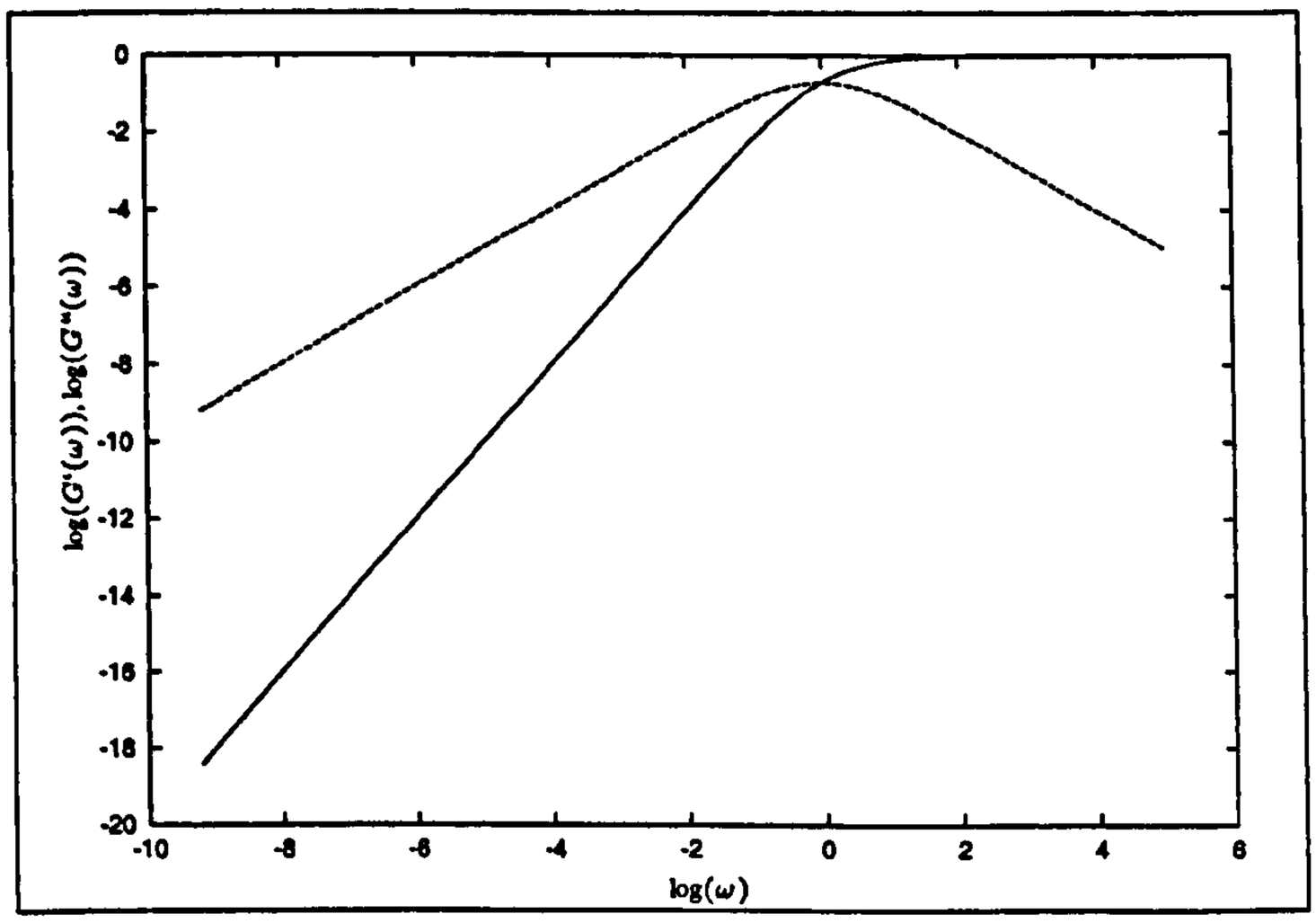


Figure 2.3: Schematic of $\log(G'(\omega))$ and $\log(G''(\omega))$ against $\log(\omega)$ are shown as solid and dashed lines respectively. An elastic solid with the same elastic modulus has $\log(G') = 0$ and a Newtonian fluid with the same zero shear rate viscosity has $\log(G'') = \log(\omega) + \log(\mu)$.

### 2.2.2 Viscosity Measurements

In order to measure the viscosity of the fluid a constant deformation rate is applied to a sample, $E_{xy} = \dot{\gamma}$ so that

$$S_{xy} = \dot{\gamma} \int_{-\infty}^{t} G(t - t')dt'.$$

Changing the variable of integration gives

$$\eta = \frac{\sigma}{\dot{\gamma}} = \int_{0}^{\infty} G(T)dT$$

When $G(t)$ is constant we see that the viscosity for an elastic solid is infinite while $G(t) \propto \delta(t)$ gives a constant viscosity for a Newtonian liquid. Since a constant strain rate is being applied, the magnitude of the strain eventually gets large enough so that we may see non-linear effects if the shear-rate is large enough. We may then see shear thickening or, more commonly, shear thinning (figure 2.4 shows a schematic diagram). Most polymeric liquids show shear thinning behaviour because, as the shear rate is increased, the long polymer molecule becomes elongated in the direction of the flow and reduced in size in the gradient direction which reduces the viscosity. However, the Oldroyd B model (which is introduced in the next section), does not show shear thinning because the extension of a linear elastic dumbbell in the gradient direction remains constant so that the viscosity is not reduced.

## 2.3 Constitutive Equations For Non-Reacting Viscoelastic Liquids

In order to capture the viscoelastic effects in the liquid surrounding the bubbles we use the Oldroyd B and Pompom models to describe the fluid. The Oldroyd B model is the simplest constitutive equation for a polymeric fluid that can be derived from a microscopic model. It is most appropriate for dilute polymer solutions at moderate strains as it does not include entanglement effects or finite extensibility. The Pompom

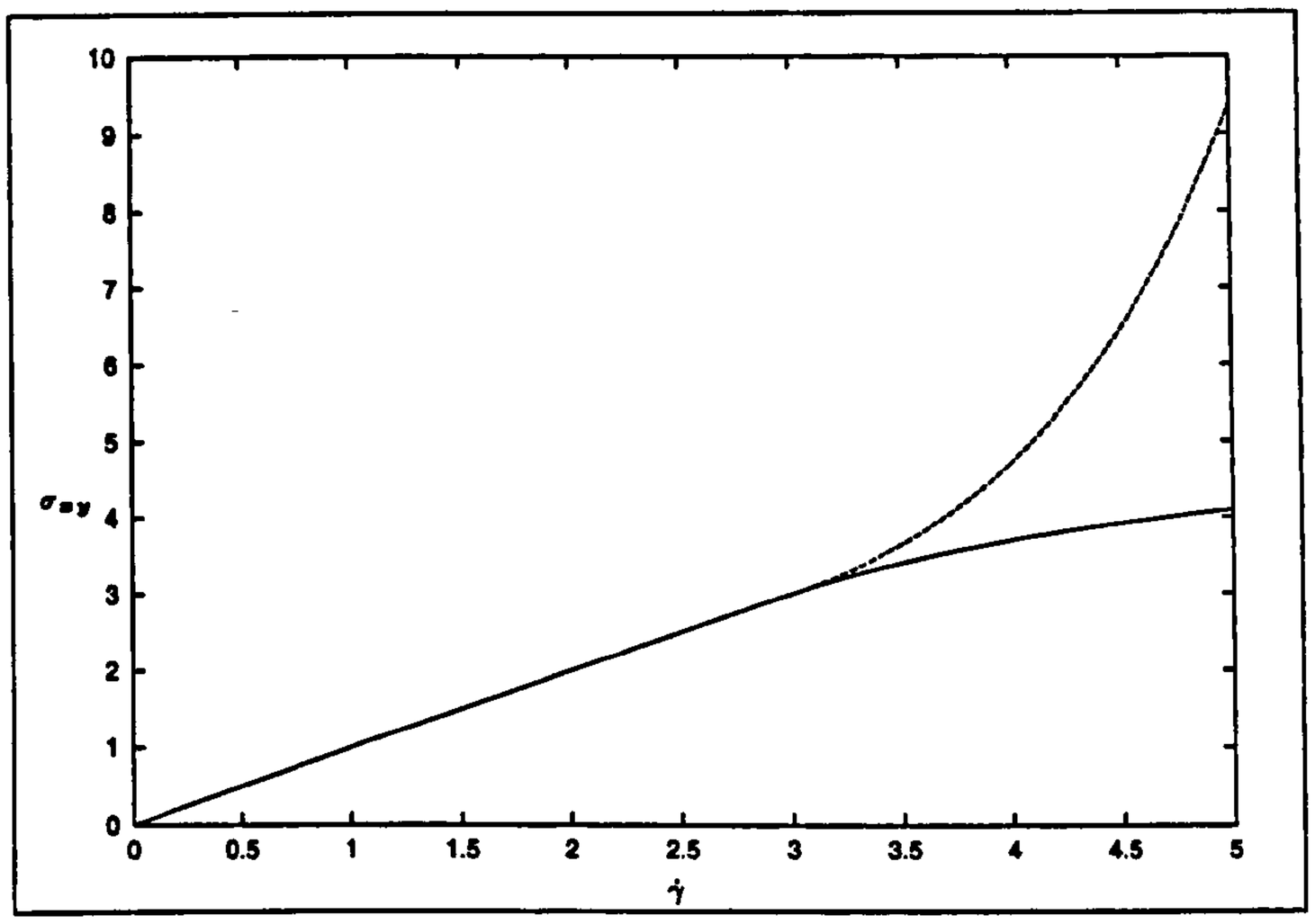


Figure 2.4: Schematic diagram showing constant viscosity in the linear regime, here the slope $\frac{\sigma_{xy}}{\dot{\gamma}} = \eta$. Shear thinning (solid line), and shear thickening (dashed line) are shown in the nonlinear regime with smaller and larger gradients respectively.

model of McLeish and Larson [30] is appropriate for entangled long chain branched polymers. Qualitative differences arise from the separation of the stretch and orientation in the Pompom model. The Oldroyd B fluid does not predict shear thinning whereas the Pompom model does, however, the bubble expansion flow does not contain any shear. Both models capture extension hardening with strain. References [30] and [6] give descriptions of the equations required by the Pompom model and reference [25] describes the properties of the model in shear and extensional flows.

### 2.3.1 Oldroyd B Model

The Oldroyd B model may be derived by representing the gross distortion of a polymer molecule by the extension of a dumbbell consisting of two beads joined by a linear spring. For a solution of dumbbells the stress is defined as

$$\boldsymbol{\sigma} = -p\mathbf{I} + 2\mu\mathbf{E} + \boldsymbol{\sigma}^p \tag{2.3}$$

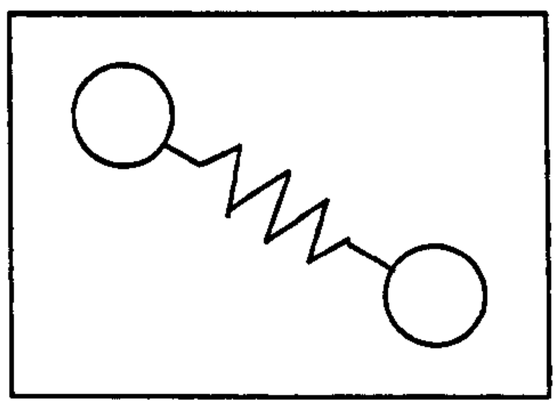

Figure 2.5: Oldroyd B model - beads and spring.

where $\boldsymbol{\sigma}^p$ is the extra stress contributed by the dumbbells. The force exerted by the dumbbells across a surface is obtained by counting the number of dumbbells intersecting the surface (see figure 2.6). Molecules with end to end vector $\mathbf{R}$ intersect a surface with normal $\mathbf{n}$ if they lie within a distance $\mathbf{R} \cdot \mathbf{n}$ of the surface. Each of these molecules contributes its entropic force $\mathbf{F}$ to the polymer stress, $\boldsymbol{\sigma}^p$. The number of molecules with end-to-end vector $\mathbf{R}$ is given by $\nu\psi$ where $\nu$ is the total number of molecules per unit volume and $\psi$ is the probability distribution function for the dumbbell orientations. Thus the force density is given by

$$\boldsymbol{\sigma}^p \cdot \mathbf{n} = -\nu \int \psi \mathbf{F}\mathbf{R} \cdot \mathbf{n} d^3\mathbf{R}.$$

In the Oldroyd B model the entropic spring is assumed to be Hookean with $\mathbf{F} = -\kappa\mathbf{R}$

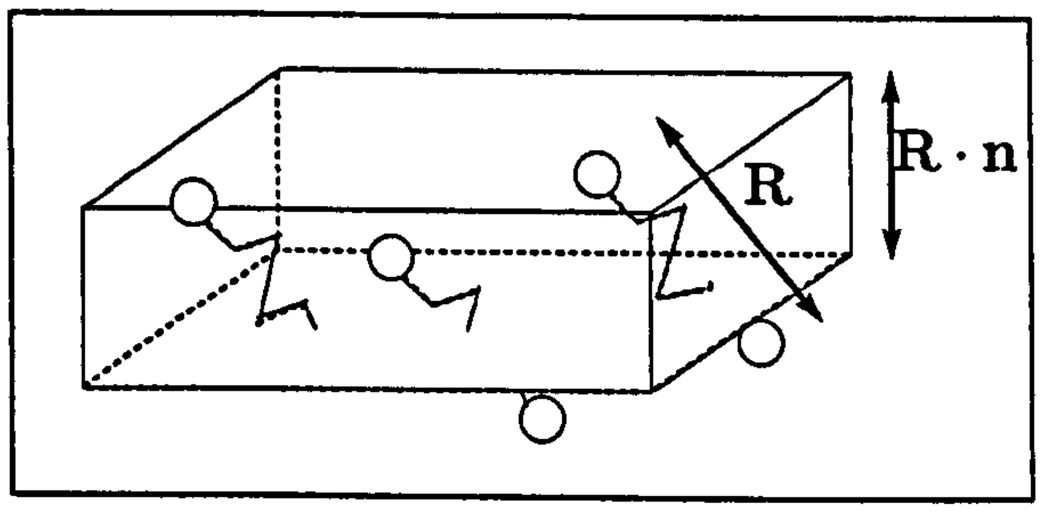


Figure 2.6: Oldroyd B model - stress generation.

so that the stress is given by

$$\boldsymbol{\sigma}^p = \nu\kappa \int \psi \mathbf{R}\mathbf{R} d^3\mathbf{R}.$$

The equation of motion for the second bead relative to the first is then given by

$$\xi(\dot{\mathbf{R}} - \mathbf{R} \cdot \nabla\mathbf{q}) = -\kappa\mathbf{R},$$

where $\xi$ is the friction coefficient between the beads and fluid and $\mathbf{q}$ is the fluid velocity field. The Fokker-Plank equation for conservation of dumbbells is

$$\frac{\partial \psi}{\partial t} + \nabla_{\mathbf{x}} \cdot \mathbf{q}\psi + \nabla_{\mathbf{R}} \cdot \left( \dot{\mathbf{R}}\psi - D\frac{\partial \psi}{\partial \mathbf{R}} \right) = 0. \tag{2.4}$$

The second term here is the advection of dumbbells by the flow, and $\nabla_R$ represents the gradient with respect to dumbbell orientation so that the third term is the divergence of the flux of dumbbells in orientation space due to stretch and diffusion ($D = k_B T/\xi$ is the diffusion coefficient). Substituting for $\dot{\mathbf{R}}$, multiplying by $\mathbf{RR}$ and integrating gives a closed equation for the second moment

$$\frac{D\mathbf{A}}{Dt} = \mathbf{A} \cdot \nabla \mathbf{q} + (\nabla \mathbf{q})^T \cdot \mathbf{A} - \frac{1}{\tau}(\mathbf{A} - \mathbf{I}), \tag{2.5}$$

where $\mathbf{A} = \int \frac{\psi \kappa}{k_B T} \mathbf{RR} d^3\mathbf{R}$ and $\tau = \frac{\xi}{2\kappa}$. The time derivative $\overset{\nabla}{A} = \frac{D\mathbf{A}}{Dt} - \mathbf{A}.\nabla \mathbf{q} - (\nabla \mathbf{q})^T.\mathbf{A}$ is the upper convected derivative which describes the rate of change of $\mathbf{A}$ in a frame that is moving and deforming with the fluid. The term $\frac{1}{\tau}(\mathbf{A} - \mathbf{I})$ represents the relaxation of the polymer towards its equilibrium configuration. The extra stress contributed by the polymer is $\boldsymbol{\sigma}^p = G(\mathbf{A} - \mathbf{I})$, where $G = \nu k_B T$ is an elastic modulus.

By substituting the expression for $\boldsymbol{\sigma}^p$ into equation (2.5) we get the more common version of the Oldroyd B constitutive equation, in which $\boldsymbol{\sigma}^p$ satisfies the Upper Convected Maxwell equation

$$\overset{\nabla}{\boldsymbol{\sigma}}^p + \frac{1}{\tau}\boldsymbol{\sigma}^p = 2G\mathbf{E} \tag{2.6}$$

In the limit of small Deborah number $|\nabla \mathbf{q}|\tau \ll 1$, $|\overset{\nabla}{\boldsymbol{\sigma}}^p|\tau \ll \boldsymbol{\sigma}^p$ so that to leading order $\boldsymbol{\sigma}^p = 2G\tau\mathbf{E}$. Thus in this limit the polymer contributes an extra Newtonian viscosity $G\tau$. In the opposite limit, $|\nabla \mathbf{q}|\tau \gg 1$, the model behaves as an incompressible elastic solid with shear modulus $G$. This can be seen by considering the Finger strain tensor $\mathbf{B}$. For a rubber $\boldsymbol{\sigma}^p = G(\mathbf{B} - \mathbf{I})$. Applying the upper convected derivative gives $\overset{\nabla}{\boldsymbol{\sigma}}^p = 2G\mathbf{E}$ (since $\overset{\nabla}{\mathbf{B}} = 0$) in agreement with equation 2.6. The model is able to capture the entire range of behaviour from a viscous fluid to an elastic solid.

In the linear regime of small strains (section 2.2.1) $\mathbf{A} = \mathbf{I} + \mathbf{a}$ where $|\mathbf{a}| \ll 1$, equation

2.5 becomes

$$\dot{\mathbf{a}} - (\nabla\mathbf{q} + \nabla\mathbf{q}^T) = -\frac{1}{\tau}\mathbf{a}$$

to leading order. This yields the solution

$$\mathbf{a} = 2\int_{-\infty}^{t} e^{-\frac{(t-t')}{\tau}}\mathbf{E}(t')dt'.$$

Hence, for the Oldroyd B fluid in the linear regime, the relaxation modulus is $G(t) = \mu\delta(t) + Ge^{-\frac{t}{\tau}}$ where $\delta(t)$ is the Dirac delta function. The response of an Oldroyd B fluid to oscillatory strain is given by

$$\begin{aligned} G^*(\omega) &= \int_0^\infty i\omega e^{-i\omega s}(\mu\delta(s) + Ge^{-\frac{s}{\tau}})ds \\ &= i\omega\mu + \frac{G}{1+\omega^2\tau^2}\left(\omega^2\tau^2 + i\omega\tau\right). \end{aligned}$$

Thus at low frequency $G'(\omega) = G\omega^2$ and $G''(\omega) = \omega(\mu + G\tau)$.

We can calculate the orientation tensor, **A**, analytically for simple non-linear flows such as simple shear and planar extension. In the start-up of shear flow

$$\nabla\mathbf{q} = \begin{pmatrix} 0 & 0 & 0 \\ \dot{\gamma} & 0 & 0 \\ 0 & 0 & 0 \end{pmatrix} \text{ for } t > 0.$$

Substituting this into (2.5) yields

$$\mathbf{A} = \begin{pmatrix} 2\dot{\gamma}^2\tau(\tau - te^{-t/\tau} - \tau e^{-t/\tau}) + 1 & \dot{\gamma}\tau(1 - e^{-t/\tau}) & 0 \\ \dot{\gamma}\tau(1 - e^{-t/\tau}) & 1 & 0 \\ 0 & 0 & 1 \end{pmatrix}.$$

The transient shear viscosity is given by $\sigma_{xy}/\dot{\gamma} = \mu + G\tau(1 - e^{-t/\tau})$ which is independent of $\dot{\gamma}$ and tends to $\mu + G\tau$ for $t \gg \tau$. Thus the Oldroyd B fluid has a constant shear viscosity. In steady shear flow the orientation tensor becomes

$$\mathbf{A} = \begin{pmatrix} 1 + 2\dot{\gamma}^2\tau^2 & \dot{\gamma}\tau & 0 \\ \dot{\gamma}\tau & 1 & 0 \\ 0 & 0 & 1 \end{pmatrix}.$$

Thus there is a positive first normal stress difference, $\sigma_{xx} - \sigma_{yy} = 2G\dot{\gamma}^2\tau^2$ as is observed experimentally in polymeric liquids, and which is responsible for flow phenomena such as rod climbing and die swell, but the second normal stress difference is zero.

In the startup of planar extension flow

$$\nabla \mathbf{q} = \dot{\epsilon} \begin{pmatrix} 1 & 0 & 0 \\ 0 & -1 & 0 \\ 0 & 0 & 0 \end{pmatrix} \text{ for } t > 0$$

where $\dot{\epsilon}$ is the extension rate. This yields

$$\mathbf{A} = \begin{pmatrix} \dfrac{1 - 2\tau\dot{\epsilon}e^{-t(1-2\tau\dot{\epsilon})/\tau}}{1 - 2\tau\dot{\epsilon}} & 0 & 0 \\ 0 & \dfrac{1 + 2\tau\dot{\epsilon}e^{-t(1+2\tau\dot{\epsilon})/\tau}}{1 + 2\tau\dot{\epsilon}} & 0 \\ 0 & 0 & 1 \end{pmatrix}.$$

Thus the transient extensional viscosity is given by

$$\frac{\sigma_{xx} - \sigma_{yy}}{\dot{\epsilon}} = 4\mu + 2G\tau \left( \frac{2}{(1 - 2\tau\dot{\epsilon})(1 + 2\tau\dot{\epsilon})} - \frac{e^{-t(1-2\tau\dot{\epsilon})/\tau}}{1 - 2\tau\dot{\epsilon}} - \frac{e^{-t(1+2\tau\dot{\epsilon})/\tau}}{1 + 2\tau\dot{\epsilon}} \right)$$

and is strongly dependent on the extension rate $\dot{\epsilon}\tau$. In particular for $\dot{\epsilon}\tau > 1/2$ the extensional stress grows exponentially without bound due to the absence of finite extensibility [40]. However, provided that we restrict our considerations to flows with finite extension strain the Oldroyd B model captures the extension hardening found in the filament stretching experiment.

### 2.3.2 Rouse Model

Although the Oldroyd B model captures the competition between stretching by velocity gradient and entropic relaxation it is a rather crude representation of a polymer and does not capture the linear viscoelastic spectrum. In the Rouse model the molecule is represented by a random walk of $N$ steps. Each step is modelled as beads connected by a spring as in the Oldroyd B model. In this way the drag on the molecule from the fluid

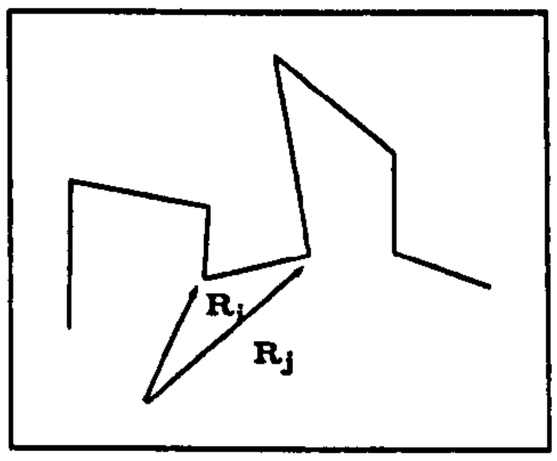


Figure 2.7: Rouse model - random walk made up of beads and springs.

is now distributed at points along the chain. By a similar argument to the previous the polymer stress is obtained by summing the contributions from each link in the chain so that

$$\sigma^p = \nu\kappa \sum_{n=0}^{N-1} \langle (\mathbf{R}^{n+1} - \mathbf{R}^n)(\mathbf{R}^{n+1} - \mathbf{R}^n) \rangle.$$

where $\kappa$ is the entropic spring constant, and $\mathbf{R}^n$ is the position vector of bead $n$. The net force acting on bead $n$ is $-\kappa(\mathbf{R}^{n+1} - 2\mathbf{R}^n + \mathbf{R}^{n-1})$ except for the two end beads $n = 0$ and $n = N$. Thus the equation of motion of the bead with position vector $\mathbf{R}^n$ in the absence of flow is

$$\xi \frac{\partial \mathbf{R}^n}{\partial t} = -\kappa(-\mathbf{R}^{n+1} + 2\mathbf{R}^n - \mathbf{R}^{n-1}) + \mathbf{f}^n; \quad n = 1, ..., N-1$$

$$\xi \frac{\partial \mathbf{R}^0}{\partial t} = -\kappa(\mathbf{R}^1 - \mathbf{R}^0) + \mathbf{f}^0;$$

$$\xi \frac{\partial \mathbf{R}^N}{\partial t} = -\kappa(\mathbf{R}^{N-1} - \mathbf{R}^N) + \mathbf{f}^N;$$

where $\xi$ is the friction coefficient between the beads and the fluid. The Rouse model ignores hydrodynamic and excluded volume interactions between different points on the chains, so that $\xi$ is constant. $\mathbf{f}^n$ is the random force on bead $n$ due to Brownian motion. The forces on each bead are uncorrelated so that $\langle \mathbf{f}^i \mathbf{f}^j \rangle = 0$ for $i \neq j$.

Since the equations of motion for all the beads in the chain are coupled, we define **normal coordinates** by taking the Fourier series

$$\mathbf{X}^k = \frac{1}{N} \sum_0^N \cos\left(\frac{k\pi n}{N}\right) \mathbf{R}^n(t) dn.$$

The equations of motion uncouple to give

$$\xi^k \frac{\partial \mathbf{X}^k}{\partial t} = -c^k \mathbf{X}^k + \mathbf{f}^{\star k}$$

where

$$c^k = \frac{2\pi^2 \kappa}{N} k^2, \qquad k = 0, 1, 2, ...$$

$$\xi^0 = N\xi; \qquad \xi^k = 2N\xi, \qquad k = 1, 2, ....$$

and

$$\mathbf{f}^{\star k} = \frac{\xi^k}{\xi N} \sum_0^N \cos\left(\frac{k\pi n}{N}\right) \mathbf{f}^n$$

are the random forces in Fourier space which remain uncorrelated. Taking the inverse transform and differentiating with respect to $n$ gives an expression for the stress in terms of the normal modes:

$$\boldsymbol{\sigma}^p = \nu \sum_k c^k \langle \mathbf{X}^k(t) \mathbf{X}^k(t) \rangle.$$

Including the effect of a flow the equation of motion becomes

$$\frac{D\mathbf{X}^k}{Dt} = -\frac{c^k}{\xi^k} \mathbf{X}^k + \frac{1}{\xi^k} \mathbf{f}^k + \mathbf{X}^k \cdot \nabla \mathbf{q}.$$

As for the dumbbell model, we define a Fokker-Plank equation for the probability distribution associated with the normal modes, multiply by $\mathbf{X}^k \mathbf{X}^k$ and integrate to get

$$\frac{D}{Dt} \langle X_i^k X_j^k \rangle = \frac{1}{\xi^k} \left( 2k_B T \delta_{ij} - 2c^k \langle X_i^k X_j^k \rangle \right) + [\nabla_\mu \mathbf{q}_i] \langle X_\mu^k X_j^k \rangle + \langle X_\mu^k X_i^k \rangle [\nabla_j \mathbf{q}_\mu]$$

Defining $\mathbf{A}^k = k_B T \langle \mathbf{X}^k \mathbf{X}^k \rangle / c_k$ gives an equivalent of equation 2.5

$$\frac{D\mathbf{A}^k}{Dt} = (\nabla \mathbf{q})^T . \mathbf{A}^k + \mathbf{A}^k . \nabla \mathbf{q} - \frac{1}{\tau^k} (\mathbf{A}^k - \mathbf{I})$$

for each mode, $k$, where $\tau^k = \xi N^2 / 2\pi^2 \kappa k^2 = \tau_R / k^2$. Stress is then obtained by summing the contributions from each mode

$$\boldsymbol{\sigma}^p = G \sum_{k=0}^N \mathbf{A}^k$$

where the elastic modulus $G = \nu k_B T$.

Thus for linear Rouse chains we have a spectrum of modes with relaxation times $\tau^k = \tau_R/k^2$. Other bead chain models give spectrums of the general form $\tau^k = \tau_R/k^\upsilon$ for a suitable choice of the index $\upsilon$. For example, the Zimm model [14] includes hydrodynamic interactions to give $\upsilon = 3/2$. For branched polymers $\upsilon$ depends on the fractal dimension $d_f$, of the molecule with $\upsilon = \frac{2}{d_f} + 1$ [43].

Since the Rouse model is in effect a superposition of Maxwell models, the linear viscoelastic results for the Rouse model are a straightforward extension of the Oldroyd B model. Results for the Rouse model are obtained by summing contributions from each of the $k$ modes. Thus the steady shear viscosity is given by

$$\frac{\sigma_{xy}}{\dot{\gamma}} = G\sum_{k=1}^{N}\tau^k.$$

This is dominated by the modes with the largest relaxation times and, for large $N$

$$\eta \simeq G\tau_R\sum_{k=1}^{\infty}\frac{1}{k^2} = \frac{G\tau_R\pi^2}{6}.$$

The relaxation modulus, $G(t)$, is given by

$$G(t) = G\sum_{k=1}^{N}e^{-\frac{t}{\tau^k}} = G\sum_{k=1}^{N}e^{-\frac{k^2t}{\tau_R}}.$$

We can also obtain expressions for the storage and loss moduli, $G'(\omega)$ and $G''(\omega)$, from the Rouse model:

$$\begin{aligned} G^\star &= \int_0^\infty i\omega G\sum_{k=1}^{\infty}e^{\left(-\frac{k^2s}{\tau_R}-i\omega s\right)}\,ds \\ &= G\sum_{k=1}^{\infty}\frac{i\omega\tau_R}{k^2+i\omega\tau_R} \\ &= G\sum_{k=1}^{\infty}\left(\frac{\omega^2\tau_R^2}{k^4+\omega^2\tau_R^2}+i\frac{k^2\omega\tau_R}{k^4+\omega^2\tau_R^2}\right). \end{aligned}$$

Thus for small frequencies, $\omega \ll 1/\tau_R$, $G'(\omega) \propto \omega^2$ and $G''(\omega) \propto \omega$. For large frequencies, $\omega \gg 1/\tau_R$ many of the modes contribute and we can approximate the

sum as an integral so that

$$G'(\omega) \simeq G \int_1^\infty \frac{\omega^2 \tau_R^2}{k^4 + \omega^2 \tau_R^2}\, dk$$

and

$$G'(\omega) \simeq G \int_1^\infty \frac{k^2 \omega \tau_R}{k^4 + \omega^2 \tau_R^2}\, dk.$$

Changing the variable of integration from $k$ to $X = k/\sqrt{\omega \tau_R}$ we obtain

$$G'(\omega) = G\sqrt{\omega \tau_R} \int_0^\infty \frac{1}{X^4 + 1}\, dX \propto \omega^{\frac{1}{2}}$$

$$G''(\omega) = G\sqrt{\omega \tau_R} \int_0^\infty \frac{X^2}{X^4 + 1}\, dX \propto \omega^{\frac{1}{2}}.$$

Figure 2.8 shows a plot of $\log(G')$ and $\log(G'')$ against $\log(\omega)$.

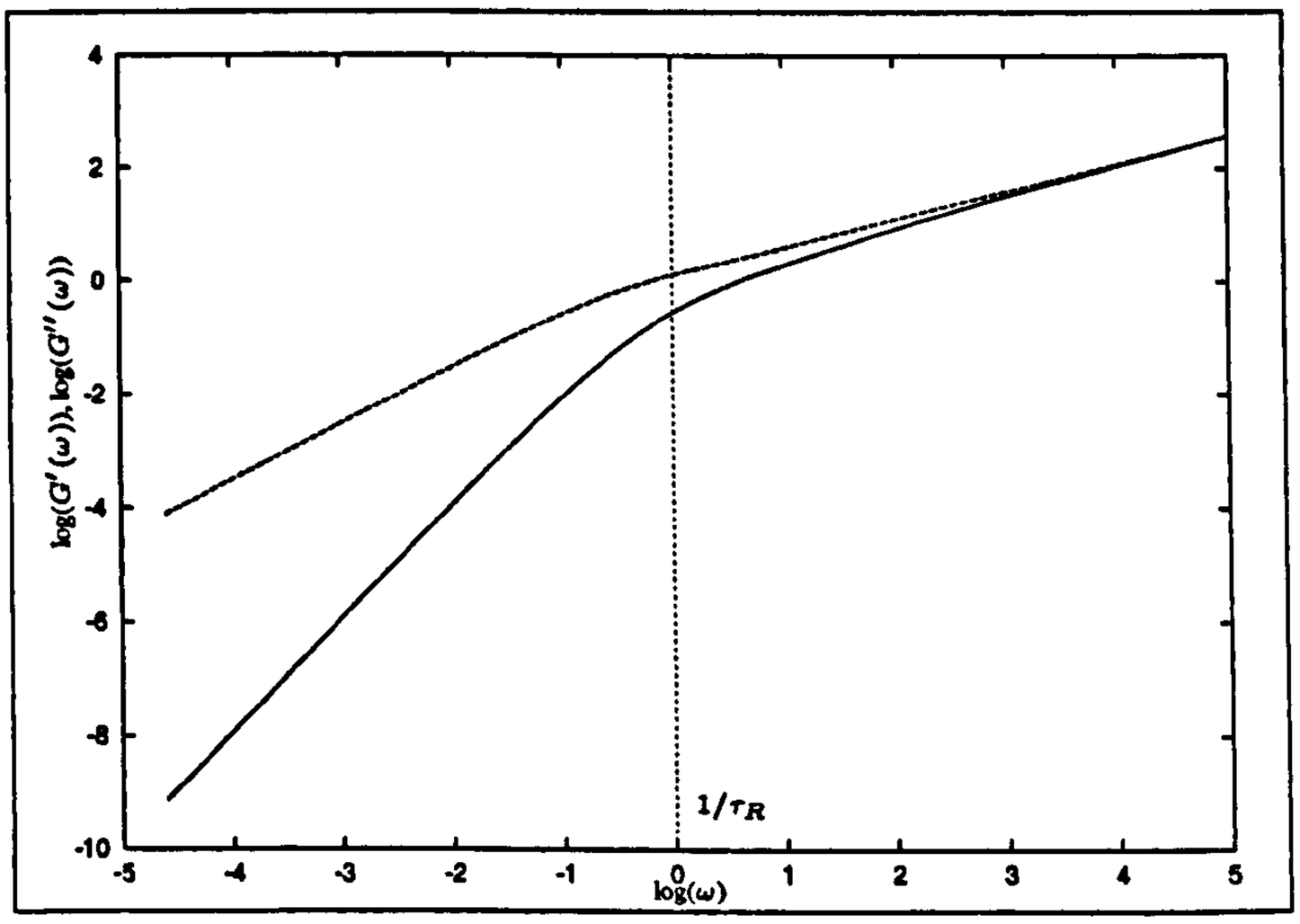


Figure 2.8: Rouse model - Plot showing storage and loss moduli against frequency. Solid line = $\log(G'(\omega))$, dashed line = $\log(G''(\omega))$

### 2.3.3 Pompom Model

The Oldroyd B model is only valid for dilute polymer solutions where intermolecular interactions can be ignored. At higher concentrations the motion of a polymer is highly

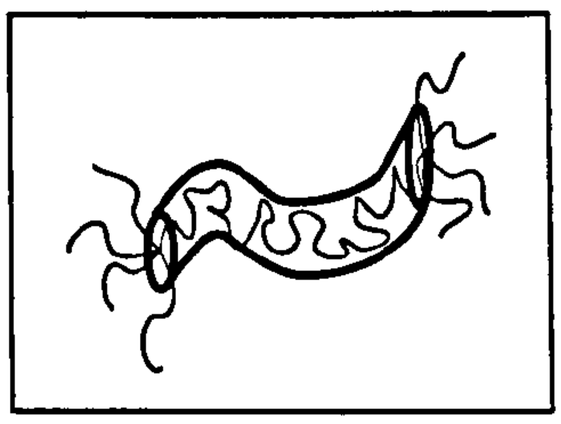

Figure 2.9: Pompom model - chain trapped in a tube with $h$ free arms at each end.

constrained by the presence of other molecules. These constraints are captured in the reptation theory of deGennes and Doi and Edwards [14], [12] for linear polymers where the presence of neighbouring molecules restricts the motion of the polymer to a tube. In the process of reptation the polymers relax their configuration by diffusion along the tube. However, in branched polymers this reptation process is inhibited by the presence of branch points that cannot move freely along the tube. For such entangled branched polymers, McLeish and Larson [30] proposed a simple constitutive equation called the Pompom model to account for the effects of branching. The Pompom model considers the motion of an entangled melt of polymers consisting of a backbone chain connected to $h$ arms at each end (see figure 2.9). The stress is dominated by the backbone section that is modelled by a linear chain connected to the branch points. The presence of the arms restricts the motion of the branch points which is modelled by an effective friction coefficient, $\xi_{bp}$, that depends exponentially on the entanglement length of the arms. As in the previous section

$$\begin{aligned} \boldsymbol{\sigma}^p &= -\nu \int \psi(\mathbf{R})\mathbf{F}\mathbf{R}d^3\mathbf{R} \\ &= \nu \int \psi(\mathbf{u})\kappa L^2 \mathbf{u}\mathbf{u}d^3\mathbf{u} \end{aligned}$$

where $\kappa$ is the entropic spring constant and the end-to-end vector $\mathbf{R} = L\mathbf{u}$ is factorised into its length $L$ and its orientation $\mathbf{u}$. The ratio of the current length of backbone to the equilibrium length of backbone is denoted by $\lambda = L/L_0$ and represents the stretch of the backbone. The maximum stretch of the backbone is $\lambda = h$ since each of the $h$ arms generates an entropic force $f_0$ so that the backbone can maintain a tension of $hf_0$ before

the branch points start to withdraw into the tube. The equation for the stretch, $\lambda$, is obtained by considering a force balance on the molecule. The drag force is proportional to the relative velocity between the branch point and tube:

$$\frac{1}{2}\xi\left(\frac{DL}{Dt} - L\mathbf{u}\cdot\nabla\mathbf{q}\mathbf{u}\right).$$

This term must balance with a Hookean spring term $\kappa(L - L_0)$. Dividing by $L_0$ and replacing $\mathbf{uu}$ by its ensemble average $\mathbf{S} = \int \psi\mathbf{uu}d^3\mathbf{u}$ we obtain the stretch equation

$$\frac{D\lambda}{Dt} = \lambda\nabla\mathbf{q} : \mathbf{S} - \frac{1}{\tau_s}(\lambda - 1) \tag{2.7}$$

where $\tau_s$ is the stretch relaxation time and $\tau_s = \xi/2\kappa$. In the original model $\tau_s$ was constant, however Blackwell *et al.* [8] suggested a modification to account for local branch point withdrawal. Since the branch point friction scales exponentially with arm length even a small change in arm length changes the relaxation time significantly. Blackwell suggested that $\tau_s$ should be replaced [1] with $\tau_s e^{-\frac{2}{h-1}(\lambda-1)}$.

The polymer stress, $\sigma^p$, can be written

$$\sigma^p = 3G\lambda^2\mathbf{S}. \tag{2.8}$$

For the orientation tensor $\mathbf{S}$ we use the differential approximation where

$$\mathbf{S} = \frac{\mathbf{A}}{tr\mathbf{A}}$$

and $\mathbf{A}$ satisfies the Oldroyd B equation

$$\overset{\nabla}{\mathbf{A}} = -\frac{1}{\tau_b}(\mathbf{A} - \mathbf{I}) \tag{2.9}$$

where $\tau_b$ is now the backbone orientation relaxation time. Equations (2.7), (2.8) and (2.9) form the Pompom constitutive equations.

In steady shear flow the evolution equation for $\mathbf{A}$ can be solved to give

$$\mathbf{A} = \begin{pmatrix} 1 + 2\dot{\gamma}^2\tau_b^2 & \dot{\gamma}\tau_b & 0 \\ \dot{\gamma}\tau_b & 1 & 0 \\ 0 & 0 & 1 \end{pmatrix}, \tag{2.10}$$

[1] Here we use the corrected expression $\tau_s e^{-\frac{2}{h-1}(\lambda-1)}$ instead of $\tau_s e^{-\frac{2}{h}(\lambda-1)}$ used in [8].

then equation (2.7) gives

$$0 = \lambda \frac{\dot{\gamma}^2 \tau_b}{3 + 2\dot{\gamma}^2 \tau_b^2} - \frac{1}{\tau_s} e^{\frac{2}{h-1}(\lambda - 1)}(\lambda - 1).$$

Provided that the backbone stretch remains small so that $(\lambda) \ll (h)$, we can make the simplification that the stretch relaxation time remains constant, thus the above equation reduces to

$$0 = \lambda \frac{\dot{\gamma}^2 \tau_b}{3 + 2\dot{\gamma}^2 \tau_b^2} - \frac{1}{\tau_s}(\lambda - 1).$$

This can now be solved to give

$$\lambda = \frac{1}{1 - \frac{\dot{\gamma}^2 \tau_b \tau_s}{3 + 2\dot{\gamma}^2 \tau_b^2}}. \tag{2.11}$$

Thus provided $\tau_s < 2\tau_b$ $\lambda$ will remain close to one for all shear rates, $\dot{\gamma}$. As a consequence the Pompom model is strongly shear thinning. Indeed, it shows a shear-stress maximum. Figure 2.10 shows the shear component of the stress obtained from equation (2.8) in the case where the Pompom molecule has 5 arms. The linear regime, in this case, prevails until around $\dot{\gamma} = 0.5$. When $\dot{\gamma}$ is small $\lambda \approx 1$ so that $\eta_s = \sigma_{xy}/\dot{\gamma} = G\tau_b$. More detail of the Pompom model in shear and extension is given in [25].

## 2.4 Theory of Gelation

In order to describe bubble growth in a reacting polymer we first need a constitutive model for a gelling system. In this section we describe some of the previous work carried out in this area as well as the theory of gelation and key ideas of percolation theory.

### 2.4.1 Gelation

By gelation we mean the formation of a network structure. In chemical gelation permanent covalent bonds are formed between multifunctional molecules while in physical gels a network is formed by some form of ordering. Physical gels may be

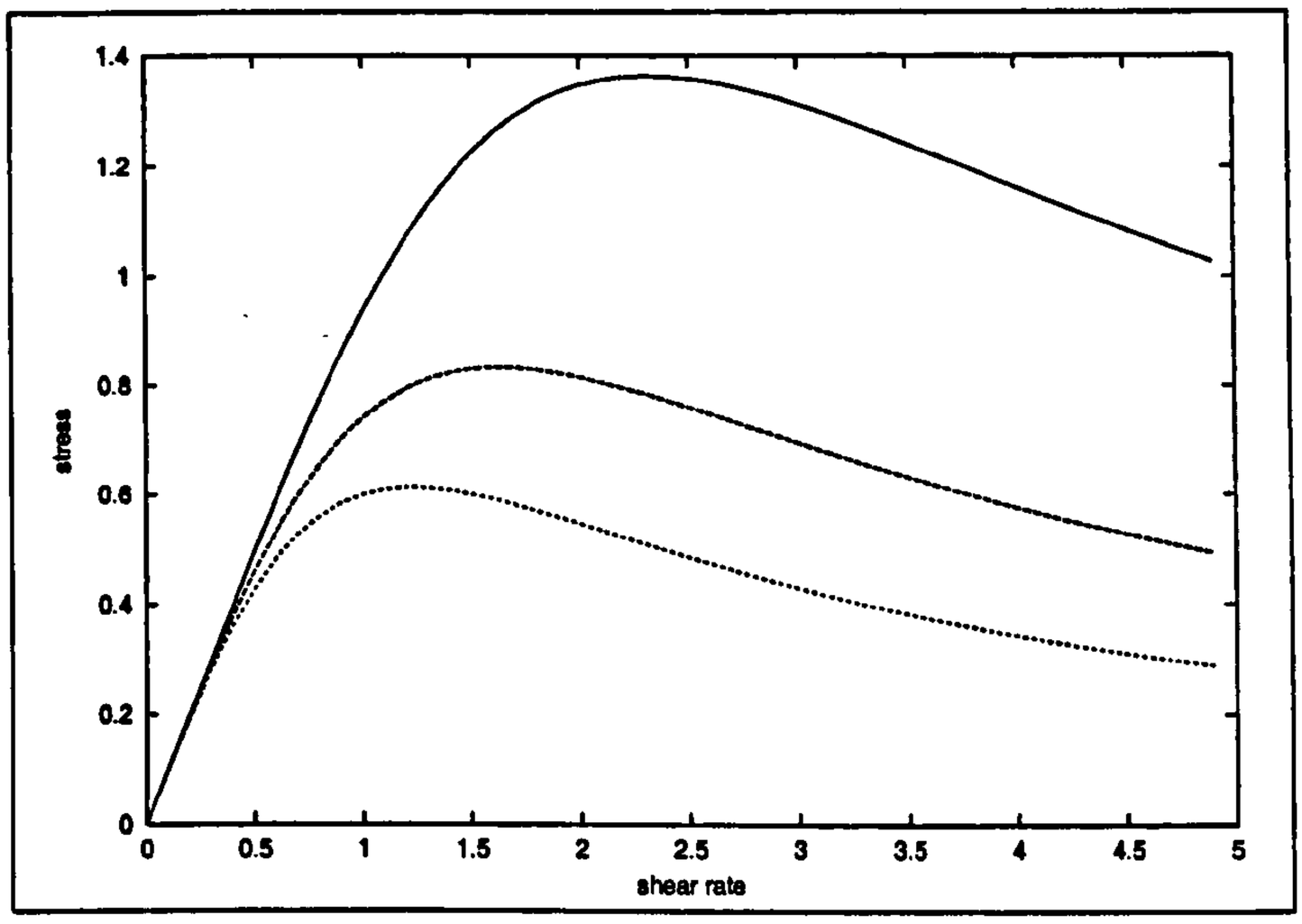


Figure 2.10: Stress against shear-rate for the Pompom model scaled with $1/\tau_b$ for $h = 5$, and (solid line) $\tau_s = 1.0$, (dashed line) $\tau_s = 1/2$, and (dotted line) $\tau_s = 1/3$.

formed by phase separation, crystallisation, the formation of ionic bonds or specific geometric complexes. The main difference between physical and chemical gelation is that physical gelation is reversible and can be reversed by changes to the environment, for example by increasing temperature. We limit ourselves here to the study of chemical gelation.

The process of gelation affects molecular mobility and leads to large rheological changes. These are clearly seen in the shear stress relaxation function, $G(t)$. Figure 2.11 shows a schematic diagram of $G(t)$ derived from data in [59]. For each curve the extent of reaction, $\alpha$, is constant. At early stages of cross-linking ($\alpha < \alpha_c$) stress is able to relax quickly. More chemical bonds are added as the reaction progresses and the longest relaxation time increases until, at the gel point, a power law regime is reached for all $t$. Beyond the gel point, $\alpha > \alpha_c$ the relaxation modulus no longer decays with time but tends to the gel modulus, $G_e$, indicating the presence of the gel. The value of this gel modulus is zero at the gel point and grows with the extent of reaction.

Before the gel point we denote by $\tau_{ch}$ the longest relaxation time of the largest molecules. Near the gel point, $|\alpha_c - \alpha| \ll 1$, $\tau_{ch}$ diverges in a power law. After the gel point we

use $\tau_{ch}$ to represent the longest relaxation time of any molecule not yet fixed in the gel. These components that are able to relax (sol fraction, unattached chain ends and long loops) become part of the gel as the reaction progresses and so $\tau_{ch}$ decreases.

The transient part of the relaxation modulus is the Laplace transform of the relaxation spectrum, $H(\tau)$,

$$G(t) = G_e + \int_0^{\tau_{ch}} H(\tau) e^{-t/\tau} \frac{d\tau}{\tau}.$$

$H(\tau)$ cannot be measured directly, but can be extraced from linear viscoelastic experiments [33]. From the analysis of chemical gelation experiments Chambon and Winter [58, 10] proposed a self-similar relaxation spectrum

$$H(\tau) = \frac{S}{\Gamma(n)} \tau^{-n}$$

where $\Gamma(n)$ is the gamma function and $S$ is the gel stiffness indicated by the slope of $G(t)$ at the gel point. The exponent $n$ is restricted to values between 0 and 1. The case $n = 0$ corresponds to the limit of a Hookean solid with constant relaxation modulus. An upper limit of 1 is required to give a diverging zero shear rate viscosity at the gel point.

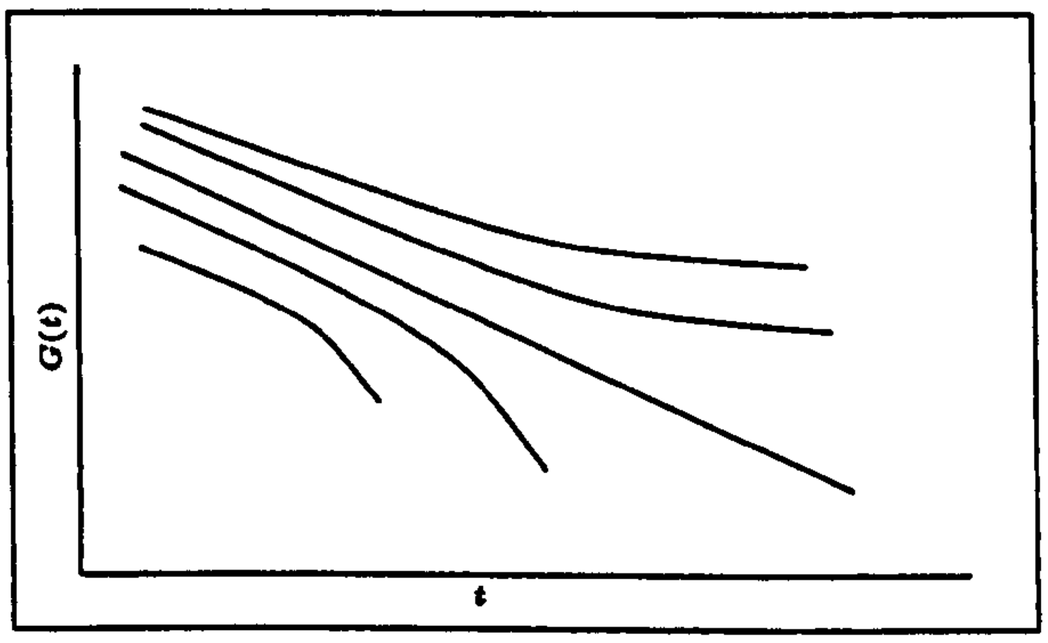


Figure 2.11: Reacting fluid - schematic diagram showing a log-log plot of the relaxation function $G(t)$ at increasing extents of reaction. Lower curves are drawn before the critical point, the straight line represents $G(t)$ at the gel point and the upper curves are drawn after $\alpha_c$.

Near the gel point the zero shear rate viscosity, $\eta_0$ and the gel modulus, $G_e$, are also

observed to grow in power laws [51]:

$$\eta_0 \propto (\alpha_c - \alpha)^{-s} \quad \alpha < \alpha_c,$$

$$G_e \propto (\alpha - \alpha_c)^{z} \quad \alpha > \alpha_c.$$

The viscosity of the sol for $\alpha < \alpha_c$ increases due to the increase in molecule size and diverges at the gel point. Beyond the gel point the gel modulus, $G_e$ increases as an increasing fraction of the molecules attach to the gel and strengthen the spanning network. Figure 2.12 shows a schematic diagram of these features.

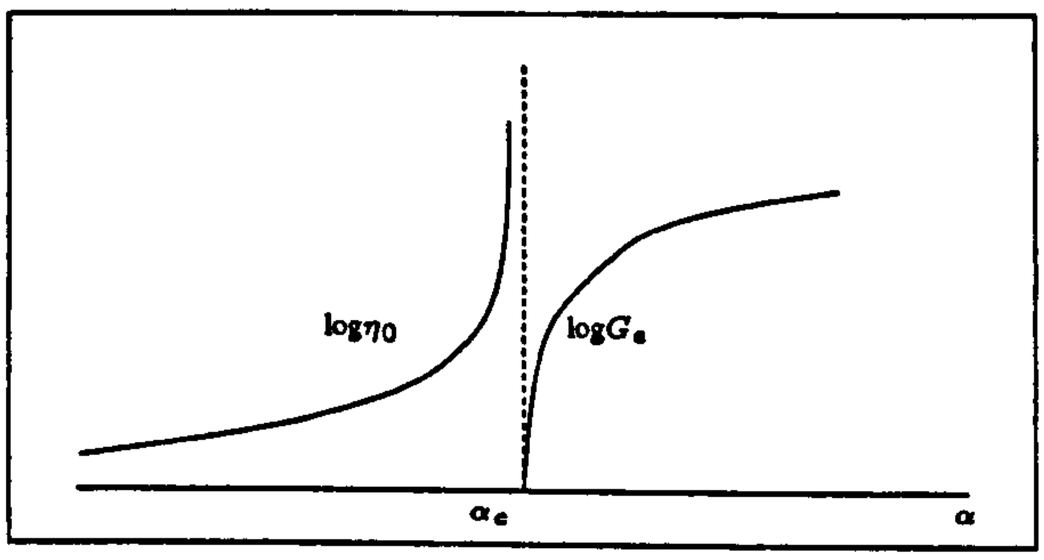


Figure 2.12: Schematic diagram showing the viscosity diverging at the critical point and the increasing gel modulus.

DeGennes [12] in 1979 suggested that the gelation process could be described by the percolation model. The following assumptions regarding the polymerisation process are made:

- the reactivities of all functional groups of the same type are equal and independent of each other
- no intermolecular reactions between functional groups on the same molecule are allowed
- cross-links are randomly formed between any pair of functional groups that can form a bond
- point-like monomers are assumed (no excluded volume effects)

### 2.4.2 Percolation Theory

Percolation theory is a statistical mechanics tool used to model random processes or disordered systems. There are two types of percolation depending on how the lattice is constructed. In **site percolation** sites are either occupied with probability $\alpha$ or unoccupied with probability $1-\alpha$. Clusters of neighbouring occupied sites are formed as shown in figure 2.13. In **bond percolation** the lattice is viewed as a graph consisting of edges and vertices. An edge is either open with probability $\alpha$ or closed with probability $1-\alpha$. A cluster is now defined as a subgraph consisting of open edges (see figure 2.14). In either case a **percolating cluster** is a cluster that spans the lattice from one edge to the other.

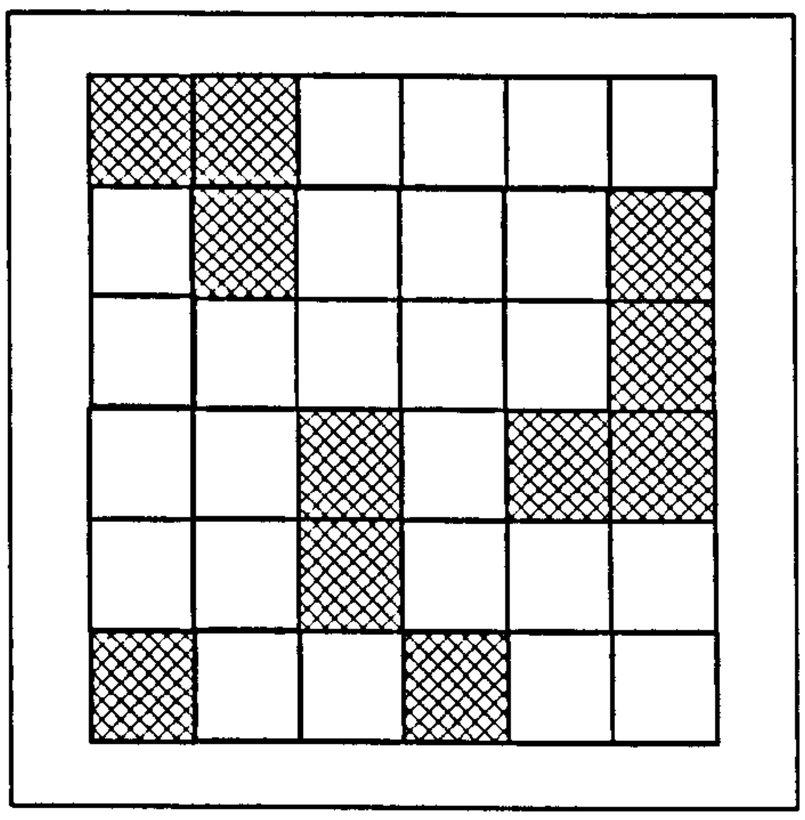

Figure 2.13: Two-dimensional lattice showing site percolation, shaded squares showing occupied sites.

Flory [19] identified the polymerisation process with bond percolation. In this application of bond percolation we think of the vertices on a grid or lattice as being occupied by molecular units with reactive end groups. Neighbouring vertices are joined if the reactive end groups form chemical bonds to form larger polymer molecules consisting of clusters of joined molecular units. A fraction $\alpha$ of all the possible bonds (lines on the lattice) are joined corresponding to the fraction of reacted end groups. Clusters can consist of single isolated molecular units – clusters of size 1 – up to an

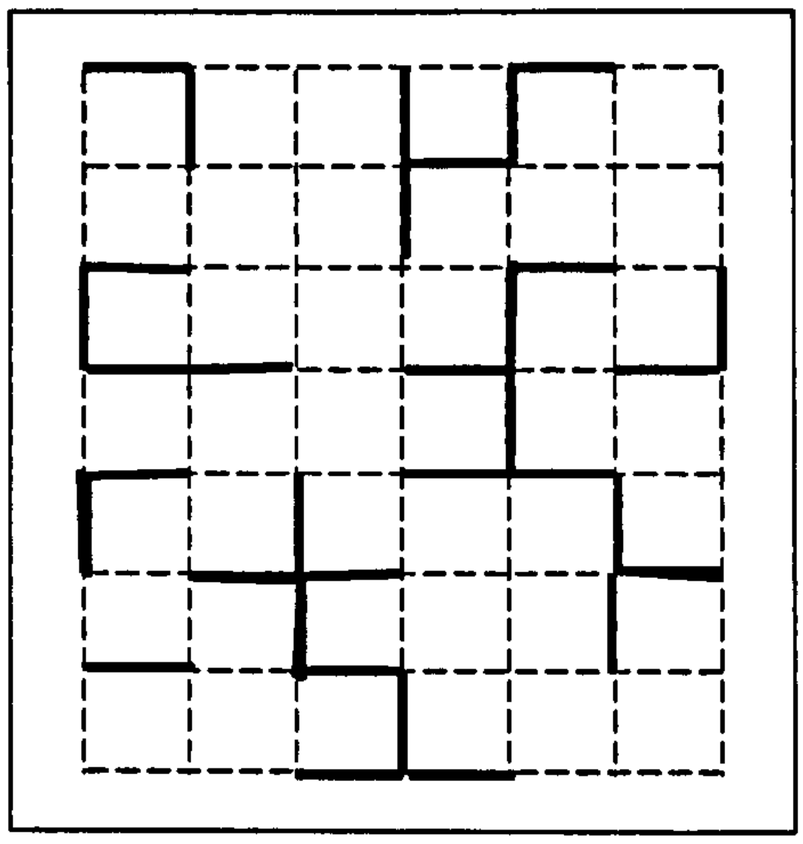

Figure 2.14: Two-dimensional lattice showing bond percolation, dark lines showing open edges.

infinite number. There exists a critical fraction, $\alpha_c$, such that for $\alpha > \alpha_c$ an infinite cluster exists which spans the lattice. This percolating cluster represents the formation of a gel.

In one dimension the lattice is of the form of a line of adjacent molecular units. A cluster of size $m$ is formed if there are $m$ adjacent joined molecular units. If a unit is chosen at random there is a probability $n(m) = \alpha^{m-1}(1-\alpha)^2$ that it is the left hand end of a cluster of size $m$ since the probability that each of the $m-1$ bonds are joined is $\alpha^{m-1}$ and the bonds at each end of the cluster are not joined with probability $(1-\alpha)^2$. The number of such clusters is $L\alpha^{m-1}(1-\alpha)^2$ (neglecting the effects of the ends of the line) where $L$ is the total number of lattice vertices. Thus, the average number of $m$ clusters per vertex - the number density of molecules consisting of $m$ chain segments - is $n(m)$. In one dimension $\alpha_c = 1$ since any bond which is not joined would split the spanning cluster into two clusters.

Flory [19], in 1979, studied bond percolation in a Bethe lattice (also known as a Cayley tree). In a Bethe lattice one starts with a central molecular unit having $z$ reactive end groups (figure 2.15 shows such a lattice with functionality $z = 3$). Each possible bond ends in another unit from which again $z$ possible bonds emanate; one of these is connected with the origin, the other $z-1$ lead to new units. This branching structure

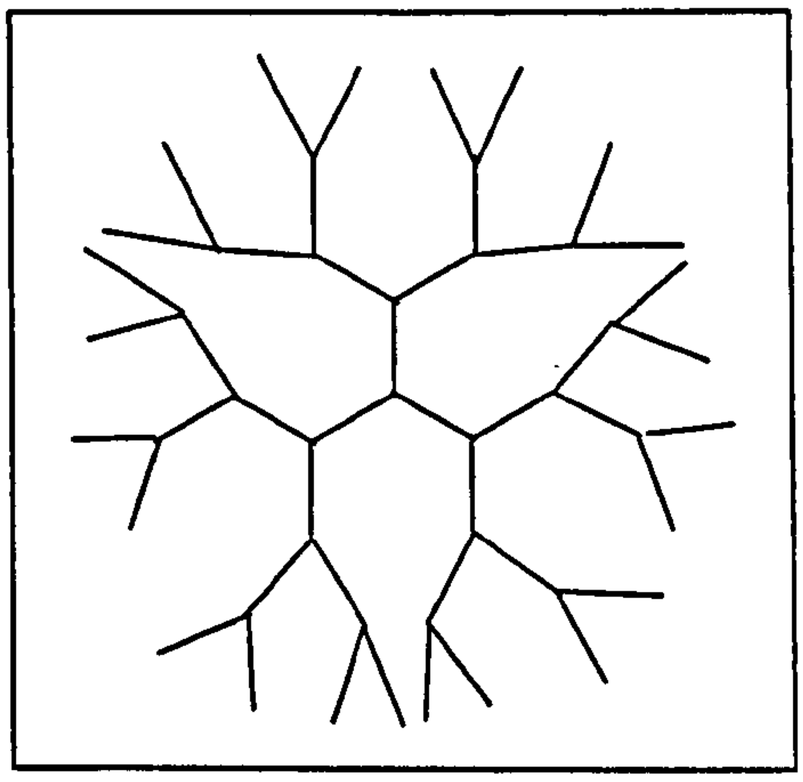

Figure 2.15: Bethe lattice with $z = 3$ bonds.

is continued again and again. There are no closed loops in this structure, which means that we always reach new units if we never go back.

Using a similar argument to the one-dimensional case, the average number of $m$-clusters per vertex is $n(m) = g_m \alpha^{m-1}(1-\alpha)^{2+(z-2)m}$ where $g_m$ depends on the number of different arrangements of the joined molecular units. Considering the ratio $n(m,\alpha)/n(m,\alpha_c)$ we are able to obtain [50]

$$\frac{n(m,\alpha)}{n(m,\alpha_c)} \propto \exp(-cm)$$

where the factor $c$ acts as a cut off for the largest cluster size since only clusters smaller than $c$ contribute significantly to cluster averages. In general this effective largest cluster scales as $c \propto |\alpha - \alpha_c|^{-\frac{1}{\sigma}}$ where $\sigma = 1/2$.

The probability that any chosen vertex is part of an $m$ cluster is $n(m)m$, and so $\sum (n(m)m)\, m$ defines the average cluster size for $\alpha < \alpha_c$. A power law decay is proposed for $n(m)$

$$n(m,\alpha) \propto m^{-\nu}$$

so that the average cluster size can be calculated as

$$S \propto \sum m^{2-\nu} \exp(-cm).$$

For large $m$ this is approximated by

$$\propto \int m^{2-\nu} \exp(-cm) dm.$$

Defining $t = cm$ gives

$$\begin{aligned} &= c^{\nu-3} \int t^{2-\nu} \exp(-t) dt \\ &\propto (\alpha_c - \alpha)^{2\nu-6} \end{aligned}$$

The average cluster size, $S$, can be calculated directly from the Bethe lattice [50] as $S \propto (\alpha_c - \alpha)^{-1}$ for $\alpha < \alpha_c$ giving $\nu = 5/2$.

The 'strength' of the infinite cluster, $P$, is defined as the probability of a chosen molecular unit belonging to the percolating cluster. At $\alpha = \alpha_c$ the probability of a chosen vertex belonging to the infinite cluster is zero so that $\sum n(m, \alpha_c)m = 1$. Therefore,

$$P = \sum n(m, \alpha_c)m - \sum n(m, \alpha)m \propto \sum m^{1-\nu}(1 - \exp(-cm)).$$

For large $m$

$$\begin{aligned} P &\propto \int m^{1-\nu}(1 - \exp(-cm)) dm \\ &\propto c^{\nu-2} \int t^{1-\nu}(1 - \exp(-t)) dt \\ &\propto (\alpha - \alpha_c)^{\frac{\nu-2}{\sigma}} \end{aligned}$$

The scaling laws described for the Bethe lattice are a special case of the more general scaling laws

$$n(m, \alpha) = m^{-\nu} f((\alpha - \alpha_c)m^{\sigma})$$

where the precise form of the scaling function $f$ has to be determined by experiment. The scaling laws for $c$, $P$ and $S$ hold for percolation on any lattice, not just the Bethe lattice. The calculations based on the Bethe lattice are known as the 'classical' or 'mean field' theory. Close to the gel point, as molecules form large three-dimensional networks the polymers are better represented by a three-dimensional lattice rather than a Bethe lattice. Though solutions for three-dimensional lattices are not known analytically the

parameters $\nu$ and $\sigma$ as well as the scaling function $f$ can be determined by Monte-Carlo simulations.

To summarise, the key scaling laws which apply to gelling systems are:

- $n(m,\alpha) \propto m^{-\nu}\exp(-cm)$ where $\nu = 5/2$ for the classical mean field theory on the Bethe lattice and $\nu = 2.2$ for the 3D lattice. $n(m)$ is the average number of $m$ clusters per vertex, analogous to the number density of molecules with molecular weight $m$. Figure 2.16 shows a schematic diagram of this between smallest and largest molecules, $m_x$ and $m_{ch}$. Close to the gel point the precise form of the cut off function at the two ends is of little importance [59] so we use a step function cut off as shown in the diagram. Gimel et al [20] as well as others [59] investigate the precise form of the cut off function and conclude that an exponential decay at the upper end best describes the distribution.

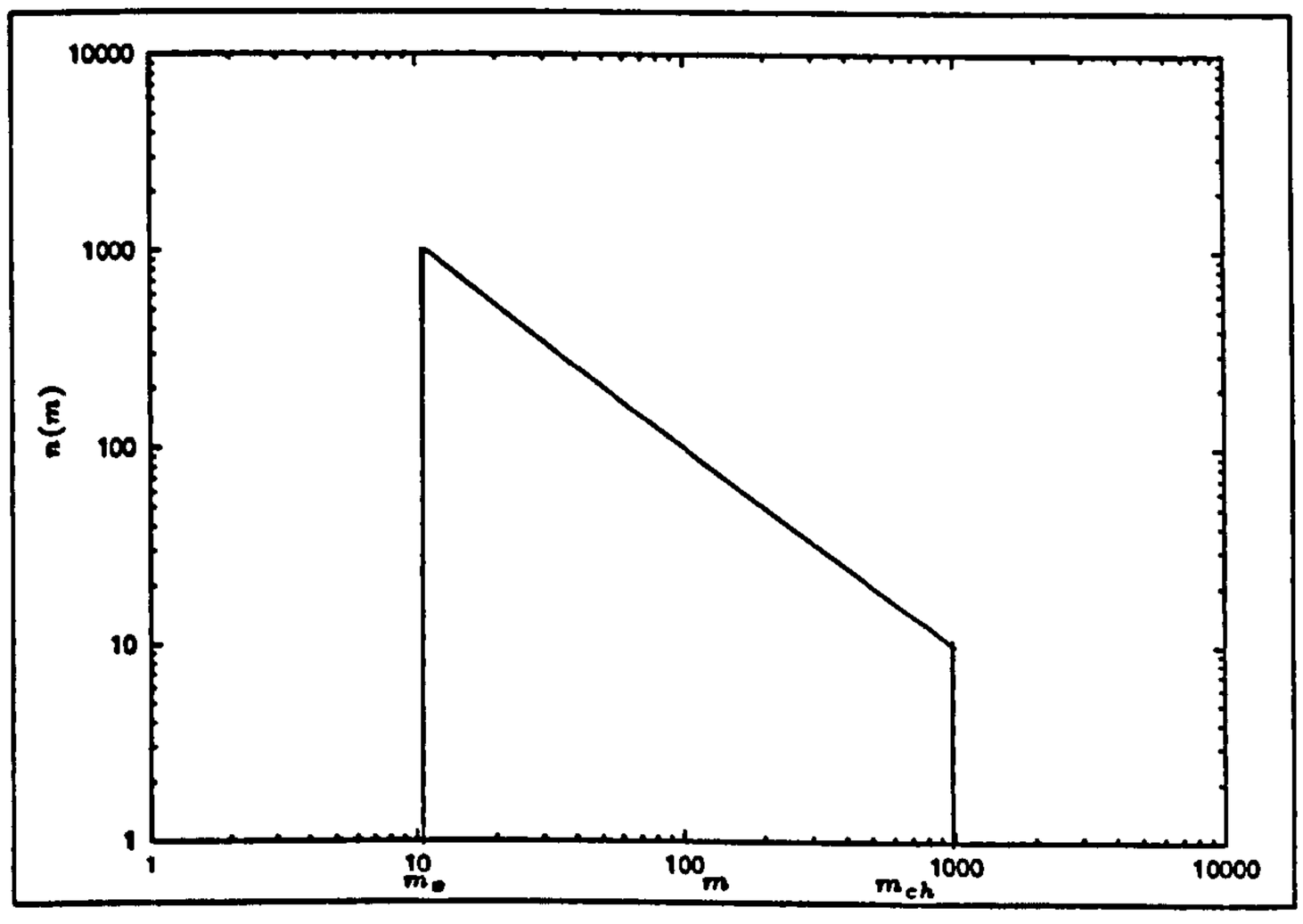


Figure 2.16: Schematic diagram showing the molecular weight distribution near the gel point. $m_x$ is the molecular weight of the smallest self similar molecules, $m_{ch}$ is the molecular weight of the largest molecules.

- The largest cluster size that contributes significantly to $n(m)$ is given by $c \propto |\alpha - \alpha_c|^{-\frac{1}{\sigma}}$ where $\sigma = 1/2$ for the Bethe lattice and $\sigma = 0.45$ for the 3D lattice.

This is equivalent to the largest molecule, $m_{ch}$ in a gelling system.

- Finally, the 'strength' of the infinite cluster, the probability that a chosen vertex belongs to the percolating cluster, is given by $P \propto (\alpha - \alpha_c)^{\frac{\nu-2}{\sigma}}$. This is equivalent to the fraction of chain segments that belong to the gel fraction in a gelling system.

### 2.4.3 Previous Work

The rheology of gelling systems near the gel point has been studied extensively by Mours and Winter [59], [32], [13]. Winter *et al.* [59] provides a detailed review of the subject, including scaling laws for the longest relaxation time, viscosity and elastic modulus of the gel. They also describe a power law molecular weight distribution and scaling of the largest molecular weight near the gel point from which they obtain the linear viscoelastic spectrum. Mours and Winter [32] compare the predictions of these scaling models with oscillatory shear experiments. Gimel *et al.* [20] review experiments reported in the literature to compare percolation parameters with measured data as well as performing their own simulations for the molecular weight distribution. Prochazka, Durand and Nicolai in [37], [38] and [39] have produced experimental work on polyurethane rheology, including comparisons with models for gelling systems. These all confirm that the value of the power law exponent in the molecular weight distribution, $\nu = 2.2$, obtained from Monte Carlo simulations is in good agreement with experiment near the gel point.

Rubinstein, Colby and Gillmor [43] use a combination of percolation theory and Rouse dynamics to predict the relaxation spectrum of polydisperse self-similar molecules. They assume a power-law distribution of molecular weights between smallest and current largest molecular weights with a step function cut off at either end. The smallest molecule has a single relaxation time, with higher modes being absorbed into a solvent viscosity, while the remaining molecules each have a spectrum of relaxation modes. Their scaling argument is presented in section 2.5. Randrianantoandro *et al.* [42] augmented the Rubinstein, Colby and Gillmor model by using Monte-Carlo simulations

to predict the form of the cut off function at the maximum molecular weight. They also included high frequency $\alpha$-relaxation in the linear relaxation spectrum. Comparisons of $G'$ and $G''$ with experiment appear very good below the gel point. Above the gel point there is evidence of slow dynamics not captured by their model that they suggest may be due to dangling arms in the gel.

## 2.5 Constitutive Model For a Gelling Liquid

In reaction injection moulding liquid containing a reactive polymer is injected into a mould where it reacts to produce a fluid with increasing viscosity, and carbon dioxide that causes foaming. The liquid gels and eventually the foam sets. Mora, Artavia and Macosko [31] describe the foaming process in four stages: an initial stage lasting around 30 seconds in which bubbles nucleate and the foam forms a physical gel; a period lasting around two minutes (up to a reaction extent of about 0.6) of liquid foam; a stage where phase separation may occur, cells may open, and the liquid forms a chemical gel at an extent of reaction of about 0.83; and a final stage in which the foam becomes an elastomer. In chapter 3 we will consider the case of a bubble expanding in a reacting liquid where gas is produced as a by-product of the reaction and diffuses into the bubble causing expansion. While we do not model nucleation and the very early stages of foaming, our model examines a single bubble from part way through the first stage of foaming through to the final stages described in [31]. The effects of phase separation are not included in our model. In this section we present a viscoelastic model of a gelling liquid. The linear rheology is the work of Rubinstein, Colby and Gillmor [43] to which we have added a non-linear extension to allow us to examine bubble growth outside the linear regime.

In this model the polymer molecules in the liquid begin as a mono-disperse distribution of self-similar molecules. As the reaction progresses molecules bond to form increasingly large, branched, structures each with a spectrum of relaxation modes. The

largest molecular weight, $m_{ch}$ and the longest relaxation time, $\tau_{ch}$, increase until a gel is formed with a finite elastic modulus but infinite viscosity. Once a gel is formed we use $m_{ch}$ to denote the molecular weight of the largest free molecule. We assume that reactions now occur between the gel and the largest molecules in the sol so that $m_{ch}$ is also the molecular weight of the cross-links in the gel. The longest, finite, relaxation time is denoted by $\tau_{ch}$. The reaction continues until all available end groups have reacted. In this section we give an overview of the calculations required to obtain Rubinstein, Colby and Gillmor's linear rheological results.

We assume that the polymer molecules in the fluid surrounding the bubble begin as self-similar chains with molecular weight $m_x$ and relaxation time $\tau_x$. For polyurethane Randrianantoandro et al [42] quote a figure of 8 polyoxypropylene (POP) triol molecules as being a necessary number of molecules to obtain a self similar chain. We also assume that the polymer solution is semi-dilute so that the polymer molecules are close enough to screen hydrodynamic interactions, but are not entangled.

The molecules start to react and bond to form molecules with a range of molecular weights, each with a Rouse spectrum of relaxation modes [14] approximated as a continuous spectrum $\tau_k$, so that the relaxation modulus $G_m(t)$ for molecules of mass $m$ is given by

$$G_m(t) = \frac{\rho_m \mathcal{R}T}{m} \int_1^{\frac{m}{m_x}} e^{-t/\tau_k} dk.$$

The mode number, $k$, runs from 1 (the slowest mode) to $m/m_x$, the number of segments of molecular weight $m_x$. Here $\rho_m$, $\mathcal{R}$ and $T$ are, respectively, the density of molecules of mass $m$, gas constant and temperature. In Rouse dynamics the friction on a molecular segment is proportional to the number of monomers so that the diffusion coefficient, $D$, is inversely proportional to molecular weight. The longest relaxation time for a molecule of molecular mass $m$ and radius of gyration $r$ will, therefore, scale as $\tau_m \propto mr^2$. The radius of gyration, $r$, increases as $m^{1/d_f}$, where $d_f$ is the fractal dimension of the equilibrium coil size. We use a value for $d_f = 2.5$ obtained from bond percolation on the three dimensional lattice [12, 50]. Mean field theory gives $d_f = 4$ which leads to a physical discrepancy, since any value higher than 3 results in the cluster density

increasing with cluster size [39]. Hence the longest relaxation time, $\tau_m$, satisfies

$$\frac{\tau_m}{\tau_x} = \left(\frac{m}{m_x}\right)^{\left(\frac{2}{d_f}+1\right)}.$$

The $k$th mode corresponds to the relaxation of sections of mass $m/m_x k$, hence from this scaling argument we obtain the relaxation time, $\tau$, for mode $k$ as

$$\tau = \tau_m(k) = \tau_x \left(\frac{m_x}{m}k\right)^{-\left(\frac{2}{d_f}+1\right)}.$$

Changing the variable of integration from $k$ to $\tau$ gives the result of Rubinstein, Colby and Gillmor [43]:

$$G_m(t) = mn(m)\frac{d_r}{2}G_0 \int_{\tau_x}^{\tau_m} \left(\frac{\tau}{\tau_x}\right)^{-\frac{d_r}{2}} e^{-t/\tau}\frac{d\tau}{\tau}. \tag{2.12}$$

Here $2/d_r = 1 + 2/d_f$, $G_0 = \rho\mathcal{R}T/m_x$, and $mn(m) = \rho_m/\rho$ is the number density of molecules of molecular weight $m$. We assume that the number density $n(m)$ follows a power law between the minimum and maximum molecular weights $m_x$ and $m_{ch}$ so that $n(m) \propto m^{-\nu}$. It has been shown (see section 2.4.3) [20], [39] that the value of $\nu$ obtained by Monte-Carlo simulations provides an accurate description near the gel point. For simplicity in our simulations we use this value of $\nu = 2.2$ throughout the reaction though one could use the value of $\nu = 2.5$ from mean field theory [50] to improve accuracy further from the gel point. Following Rubinstein, Colby and Gillmor [43] we impose a step cut-off at the minimum and maximum molecular weights so that prior to the gel point $\alpha_c$

$$n(m) = \frac{(\nu-2)m_x^{\nu-2}}{1-\left(\frac{m_x}{m_{ch}}\right)^{\nu-2}}m^{-\nu} \quad \alpha < \alpha_c; \quad m_x < m < m_{ch}$$

$$n(m) = 0 \qquad\qquad\qquad\qquad \alpha < \alpha_c; \quad m > m_{ch}; m < m_x$$

Randrianantoandro et al [42] use Monte-Carlo simulations to obtain a more accurate exponential cut-off function that is in good agreement with experimental data [20]. However, for the sake of simplicity we retain the step function cut-off.

Integrating (2.12) over all molecular weights from $m_x$ to $m_{ch}$ gives the relaxation

modulus prior to gelation ($\alpha < \alpha_c$) as

$$G(t) = \frac{G_0 \frac{d_r}{2}}{1 - \left(\frac{\tau_{ch}}{\tau_x}\right)^{\frac{-d_r}{2}(\nu-2)}} \int_{\tau_x}^{\tau_{ch}} \left( \left(\frac{\tau}{\tau_x}\right)^{\frac{-d_r}{2}(\nu-1)} - \left(\frac{\tau_{ch}}{\tau_x}\right)^{\frac{-d_r}{2}(\nu-2)} \left(\frac{\tau}{\tau_x}\right)^{\frac{-d_r}{2}} \right) e^{-t/\tau} \frac{d\tau}{\tau}. \tag{2.13}$$

Beyond the gel point the largest molecular weight is infinite and we use $m_{ch}$ to denote the molecular weight of the largest free molecule. Since the only reactions are between the longest molecules in the sol and the gel the number density is now

$$n(m) = (\nu - 2) m_x^{\nu-2} m^{-\nu} \qquad \alpha > \alpha_c; \qquad m_x < m < m_{ch}.$$

The relaxation modulus of the free molecules is still given by equation (2.12) so that integrating over molecular weights from $m_x$ to $m_{ch}$ and changing the order of integration gives

$$G(t)_{sol} = G_0 \frac{d_r}{2} \int_{\tau_x}^{\tau_{ch}} \int_{m_\tau}^{m_{ch}} m n(m) \left(\frac{\tau}{\tau_x}\right)^{-\frac{d_r}{2}} \frac{e^{-t/\tau}}{\tau} dm d\tau.$$

For the remaining $\left(\frac{m_x}{m_{ch}}\right)^{\nu-2}$ making up the gel fraction we assume that molecules of molecular weight $m_{ch}$ are fixed so that modes with relaxation times faster than $\tau_{ch}$ can relax. In addition to these relaxing gel modes there is a gel mode that cannot relax, corresponding to a molecular weight larger than $m_{ch}$, with gel modulus $G_0 \left(\frac{m_x}{m_{ch}}\right)^{\nu-1}$. Thus

$$G(t)_{gel} = G_0 \left(\frac{m_x}{m_{ch}}\right)^{\nu-2} \frac{d_r}{2} \left( \int_{\tau_x}^{\tau_{ch}} \left(\frac{\tau}{\tau_x}\right)^{-\frac{d_r}{2}} e^{-t/\tau} \frac{d\tau}{\tau} \right) + G_0 \left(\frac{m_x}{m_{ch}}\right)^{\nu-1}.$$

In order to combine all the relaxing modes in the solution and the gel, we write

$$\left(\frac{m_x}{m_{ch}}\right)^{(\nu-2)} = \int_{m_{ch}}^{\infty} m n(m) dm,$$

so that

$$\begin{aligned} G(t) = G_0 \frac{d_r}{2} \int_{\tau_x}^{\tau_{ch}} \int_{m_\tau}^{m_{ch}} m n(m) \left(\frac{\tau}{\tau_x}\right)^{-\frac{d_r}{2}} \frac{e^{-t/\tau}}{\tau} dm d\tau & \quad \text{sol modes} \\ + G_0 \frac{d_r}{2} \int_{\tau_x}^{\tau_{ch}} \int_{m_{ch}}^{\infty} m n(m) \left(\frac{\tau}{\tau_x}\right)^{-\frac{d_r}{2}} \frac{e^{-t/\tau}}{\tau} dm d\tau & \quad \text{relaxing gel modes} \\ + G_0 \frac{d_r}{2} \int_{\tau_{ch}}^{\infty} \int_{m_{ch}}^{\infty} m n(m) \left(\frac{\tau}{\tau_x}\right)^{-\frac{d_r}{2}} \frac{1}{\tau} dm d\tau. & \quad \text{non-relaxing gel mode} \end{aligned}$$

Now the relaxing modes from the solution and the gel can be combined and the integration over $m$ performed:

$$G(t) = G_0 \frac{d_r}{2} \left( \int_{\tau_x}^{\tau_{ch}} \left( \frac{\tau}{\tau_x} \right)^{-\frac{d_r}{2}(\nu-1)} e^{-t/\tau} \frac{d\tau}{\tau} + \int_{\tau_{ch}}^{\infty} \left( \frac{\tau_{ch}}{\tau_x} \right)^{-\frac{d_r}{2}(\nu-2)} \left( \frac{\tau}{\tau_x} \right)^{-\frac{d_r}{2}} \frac{d\tau}{\tau} \right) \tag{2.14}$$

We leave the second term here in its integral form for ease of discretization.

In fact there exist faster relaxation times than $\tau_x$ but, since these modes are always able to relax very quickly we include them as a solvent viscosity of $G_0\tau_x$.

To complete our formulation we must relate the characteristic relaxation time, $\tau_{ch}$, to the extent of reaction $\alpha$. Near the gel point, $\alpha_c$, the largest molecular weight $m_{ch} \sim (\alpha - \alpha_c)^{\frac{-1}{\sigma}}$ [43] so that the longest relaxation time $\tau_{ch} \sim (\alpha - \alpha_c)^{\frac{2}{\sigma d_r}}$. The value of $\sigma$ can be obtained from percolation theory [50] or by Monte-Carlo simulations [20] and we use the value of 0.45 obtained by Monte-Carlo simulations. In our model we assume that this scaling applies throughout the reaction. Since the reaction begins with all the molecules having the same molecular weight, $m_x$, before the gel point we have

$$\tau_{ch} = \tau_x \left( \frac{\alpha_c - \alpha}{\alpha_c} \right)^{\frac{-2}{\sigma d_r}} . \tag{2.15}$$

Randrianantoandro et al [42] describe Monte Carlo simulations to determine the prefactors before and after the gel point for their parameter $|(\alpha - \alpha_c)/\alpha_c|$ which scales with $m_z^{-\sigma}$. From the ratio of these prefactors we can determine the scaling for $\tau_{ch}$ with $\alpha$ after the gel point

$$\tau_{ch} = \beta\tau_x \left( \frac{\alpha - \alpha_c}{\alpha_c} \right)^{\frac{-2}{\sigma d_r}} \tag{2.16}$$

where $\beta = 0.0049$. A value of $\beta$ greater than

$$\hat{\beta} = \left( \frac{\alpha_c}{1 - \alpha_c} \right)^{\frac{-2}{\sigma d_r}}$$

allows for the fact that the network may not be an exactly self similar structure and may have 'dangling arm' sections with $\tau > \tau_{ch}$ which are able to relax [42]. In our simulations we choose $\beta = \hat{\beta}$ for the sake of simplicity. Figure 2.17 shows the evolution of the extent of reaction and the longest relaxation time, we see that the longest relaxation time diverges at the gel point.

### 2.5.1 Viscosity and Elastic Modulus

The viscosity of the material before the gel point can be calculated by integrating the relaxation function, $G(t)$, over time.

$$\begin{aligned}\eta &= \int_0^\infty G(T)dT \\ &= G_\alpha\left(\left(\frac{\tau_{ch}}{\tau_x}\right)^{1-\frac{d_r}{2}(\nu-1)}\left(\frac{1}{1-\frac{d_r}{2}(\nu-1)}-\frac{1}{1-\frac{d_r}{2}}\right)-\frac{1}{1-\frac{d_r}{2}(\nu-1)}\right. \\ &+ \left.\left(\frac{\tau_{ch}}{\tau_x}\right)^{-\frac{d_r}{2}(\nu-2)}\left(\frac{1}{1-\frac{d_r}{2}}\right)\right)\end{aligned}$$

where

$$G_\alpha = \frac{G_0\tau_x d_r/2}{\left(1-\left(\frac{\tau_{ch}}{\tau_x}\right)^{-\frac{d_r}{2}(\nu-2)}\right)}$$

Since $\tau_{ch} \sim (\alpha_c - \alpha)^{-2/(\sigma d_r)}$, viscosity scales as

$$\eta \sim (\alpha_c - \alpha)^{\left(\frac{2}{\sigma d_r}-\frac{\nu-1}{\sigma}\right)}.$$

The elastic modulus of the gel, obtained from the second term in equation (2.14) scales as

$$G_e = G_0\left(\frac{\tau_{ch}}{\tau_x}\right)^{-\frac{d_r}{2}(\nu-1)} \sim (\alpha-\alpha_c)^{\frac{\nu-1}{\sigma}}.$$

Figure 2.18 shows the diverging steady viscosity of the sol fraction before the gel point, and the development of the elastic modulus of the gel after the critical point, with reaction extent in agreement with the schematic diagram in figure 2.12. Here viscosity is scaled with the steady viscosity of the polymer at $\alpha = 0$, $G_0\tau_x$, and the elastic modulus is scaled with the elastic modulus of the fully developed gel, $G_0$.

### 2.5.2 Linear Viscoelastic Response

The storage and loss moduli are calculated from the real and imaginary parts of $G^*(\omega) = i\omega \int_0^\infty G(t)e^{-i\omega t}dt$ resulting in

$$G'(\omega) = \frac{G_0 d_r/2}{\left(1-\left(\frac{\tau_{ch}}{\tau_x}\right)^{-\frac{d_r}{2}(\nu-2)}\right)} \int_{\tau_x}^{\tau_{ch}} \frac{\omega^2\tau^2}{1+\omega^2\tau^2} \left(\left(\frac{\tau}{\tau_x}\right)^{-\frac{d_r}{2}(\nu-1)} - \left(\frac{\tau_{ch}}{\tau_x}\right)^{-\frac{d_r}{2}(\nu-2)}\left(\frac{\tau}{\tau_x}\right)^{-\frac{d_r}{2}}\right)\frac{d\tau}{\tau}$$

and

$$G''(\omega) = \frac{G_0 d_r/2}{\left(1-\left(\frac{\tau_{ch}}{\tau_x}\right)^{-\frac{d_r}{2}(\nu-2)}\right)} \int_{\tau_x}^{\tau_{ch}} \frac{\omega\tau}{1+\omega^2\tau^2} \left(\left(\frac{\tau}{\tau_x}\right)^{-\frac{d_r}{2}(\nu-1)} - \left(\frac{\tau_{ch}}{\tau_x}\right)^{-\frac{d_r}{2}(\nu-2)}\left(\frac{\tau}{\tau_x}\right)^{-\frac{d_r}{2}}\right)\frac{d\tau}{\tau}.$$

At the gel point, $\tau_{ch} \to \infty$ and these become

$$G'(\omega) = G_0\frac{d_r}{2}\int_1^\infty \frac{\omega^2\tau^2}{1+\omega^2\tau^2}\left(\frac{\tau}{\tau_x}\right)^{-\frac{d_r}{2}(\nu-1)}\frac{d(\tau/\tau_x)}{\tau/\tau_x}$$

and

$$G''(\omega) = G_0\frac{d_r}{2}\int_1^\infty \frac{\omega\tau}{1+\omega^2\tau^2}\left(\frac{\tau}{\tau_x}\right)^{-\frac{d_r}{2}(\nu-1)}\frac{d(\tau/\tau_x)}{\tau/\tau_x}.$$

By defining a change of variables $u = \omega\tau$ we can express the storage and loss moduli as

$$G'(\omega) = G_0\frac{d_r}{2}(\omega\tau_x)^{\frac{d_r}{2}(\nu-1)}\int_{\omega\tau_x}^\infty \frac{u^2}{1+u^2}u^{-\frac{d_r}{2}(\nu-1)-1}du$$

and

$$G''(\omega) = G_0\frac{d_r}{2}(\omega\tau_x)^{\frac{d_r}{2}(\nu-1)}\int_{\omega\tau_x}^\infty \frac{u}{1+u^2}u^{-\frac{d_r}{2}(\nu-1)-1}du.$$

Before the gel point, for frequencies $\omega \ll 1/\tau_{ch}$ $G' \propto \omega^2$ and $G'' \propto \omega$ . In figures 2.19 and 2.20 we see a change of gradient from 2 at low frequencies to $\frac{d_r}{2}(\nu-1) = 2/3$ for intermediate frequencies ($1/\tau_{ch} \ll \omega \ll 1/\tau_x$) in the storage modulus and from unity at low frequencies to $\frac{d_r}{2}(\nu-1)$ at intermediate frequencies in the loss modulus. At the

gel point, as $1/\tau_{ch} \rightarrow 0$, the slope of 2/3 in both $G'$ and $G''$ extends to all frequencies $\omega \ll 1/\tau_x$. The storage modulus shows the elastic modulus of the material at high frequencies before and after the gel point. However, after the gel point we also see the solid like behaviour of the material at low frequencies due to the increasing presence of the gel fraction. The value of the maximum in $G''(w)$ increases with $\alpha$ up to the gel point as the molecular weight increases. Beyond the gel point it decreases again as higher molecular weight material becomes part of the gel.

Our model gives qualitatively similar results to those of Randrianantoandro et al [42]. At high frequencies their model shows a further change in gradient due to the $\alpha$-relaxation in the low molecular weight segments which we incorporate into an effective solvent viscosity. Their model also predicts an undershoot in $G'$ after the gel point, caused by the difference in the form of the high molecular weight cut off function. Mours and Winter [32] investigate relaxation patterns of nearly critical gels. They present the results of oscillatory shear experiments near the gel point and plot the frequency dependence of $G'$ and $G''$. Their results show the same changes of slope as the model we use, further justifying our model up to frequencies corresponding to the low molecular weight cut off. Beyond this their results show the steeper gradient of the $\alpha$-relaxation process described by Randrianantoandro.

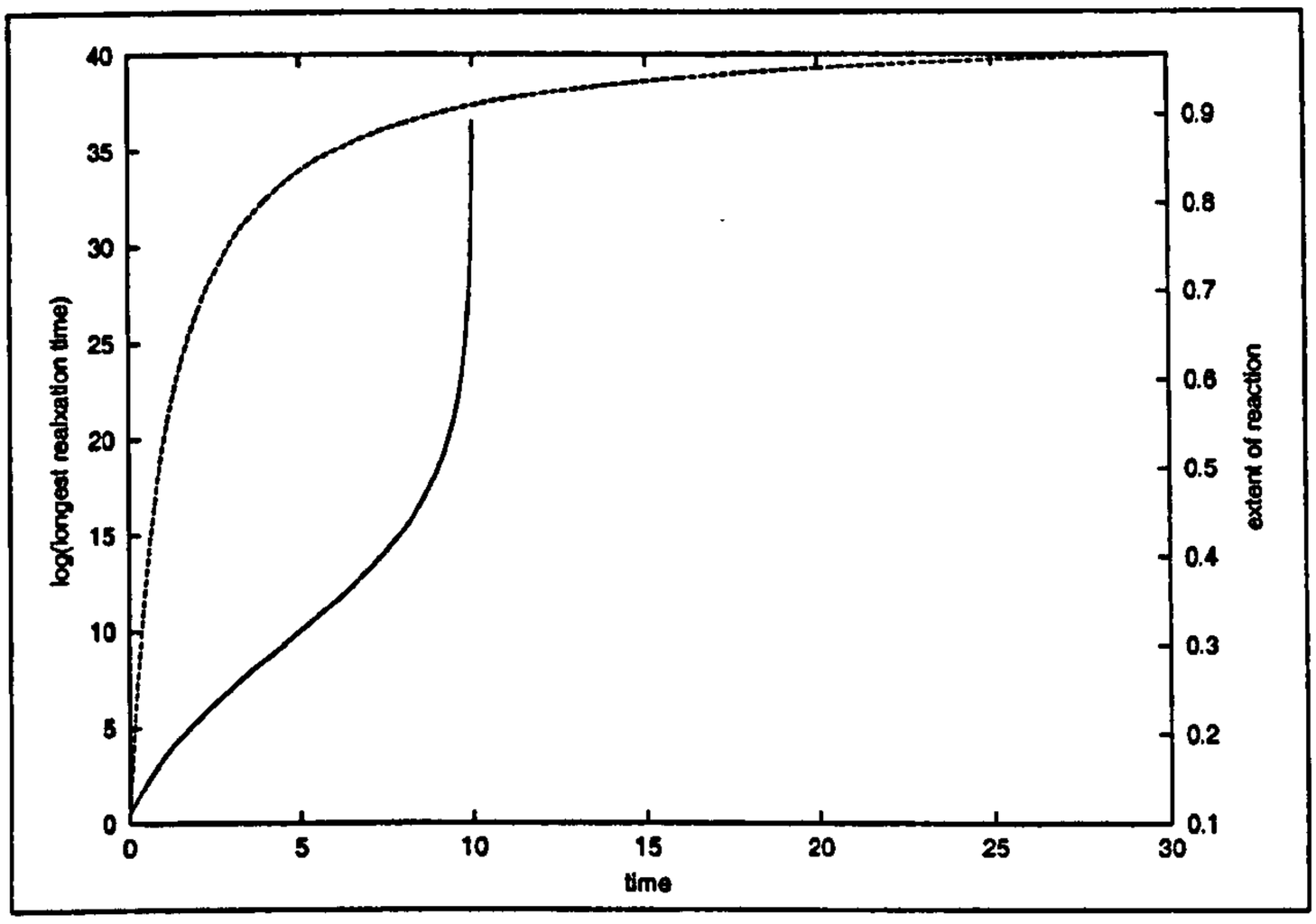


Figure 2.17: The evolution of the longest relaxation time (solid line) and the extent of reaction (broken line).

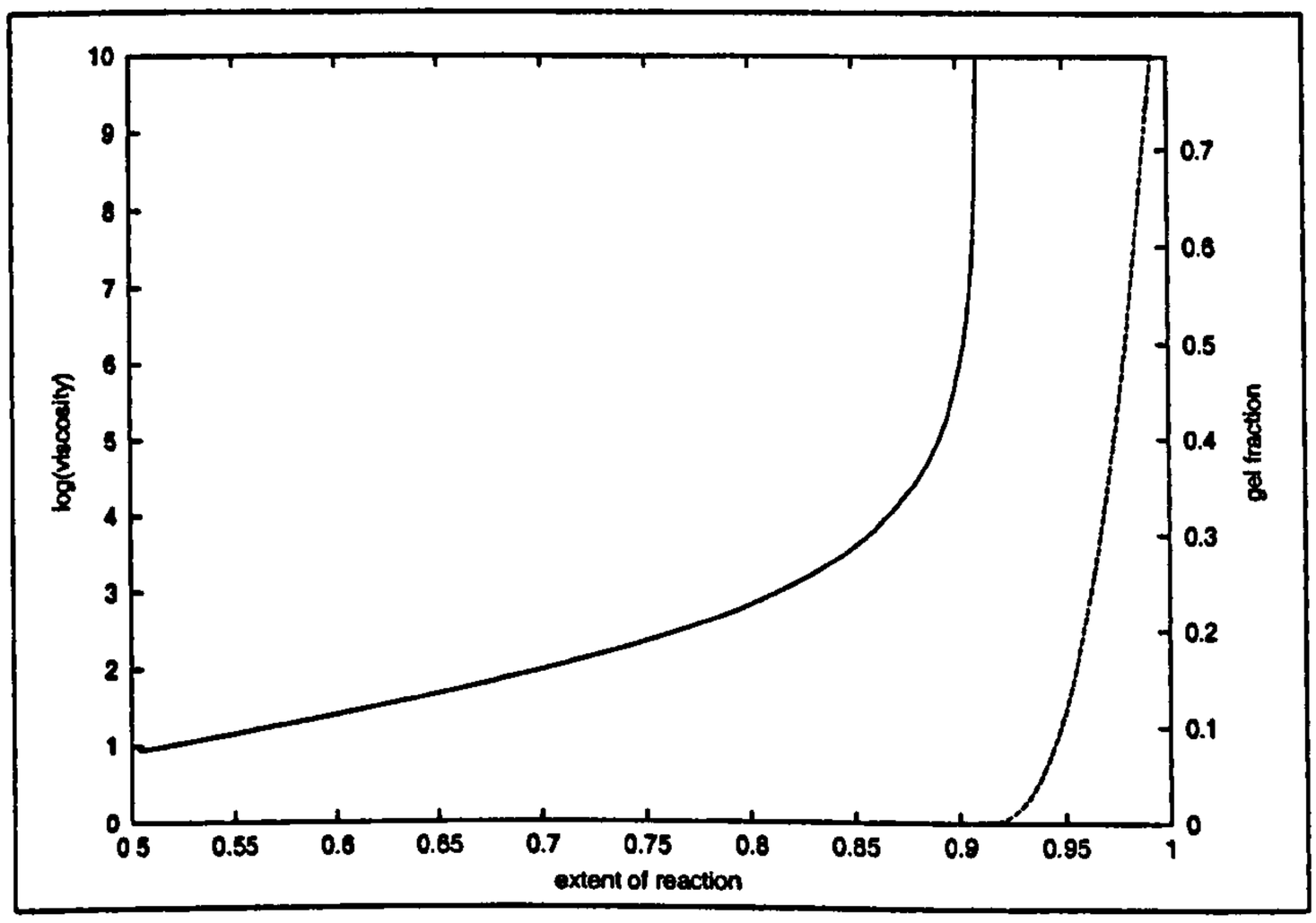


Figure 2.18: Viscosity relative to the viscosity at $\alpha = 0$ in the sol phase (solid line) and elastic modulus relative to the elastic modulus of the fully developed gel in the gel phase (broken line).

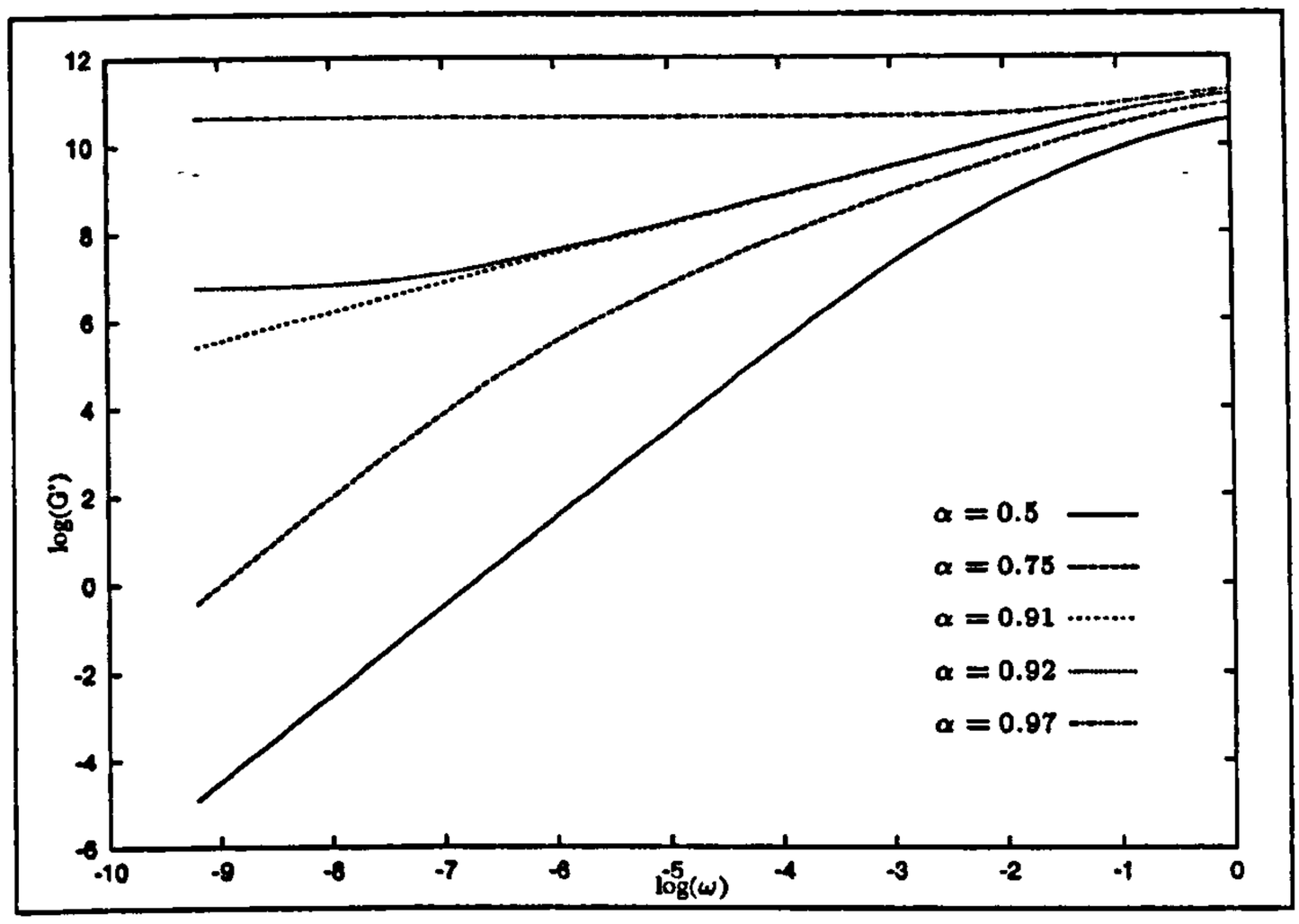


Figure 2.19: Storage modulus, $G'(\omega)$, at various extents of reaction.

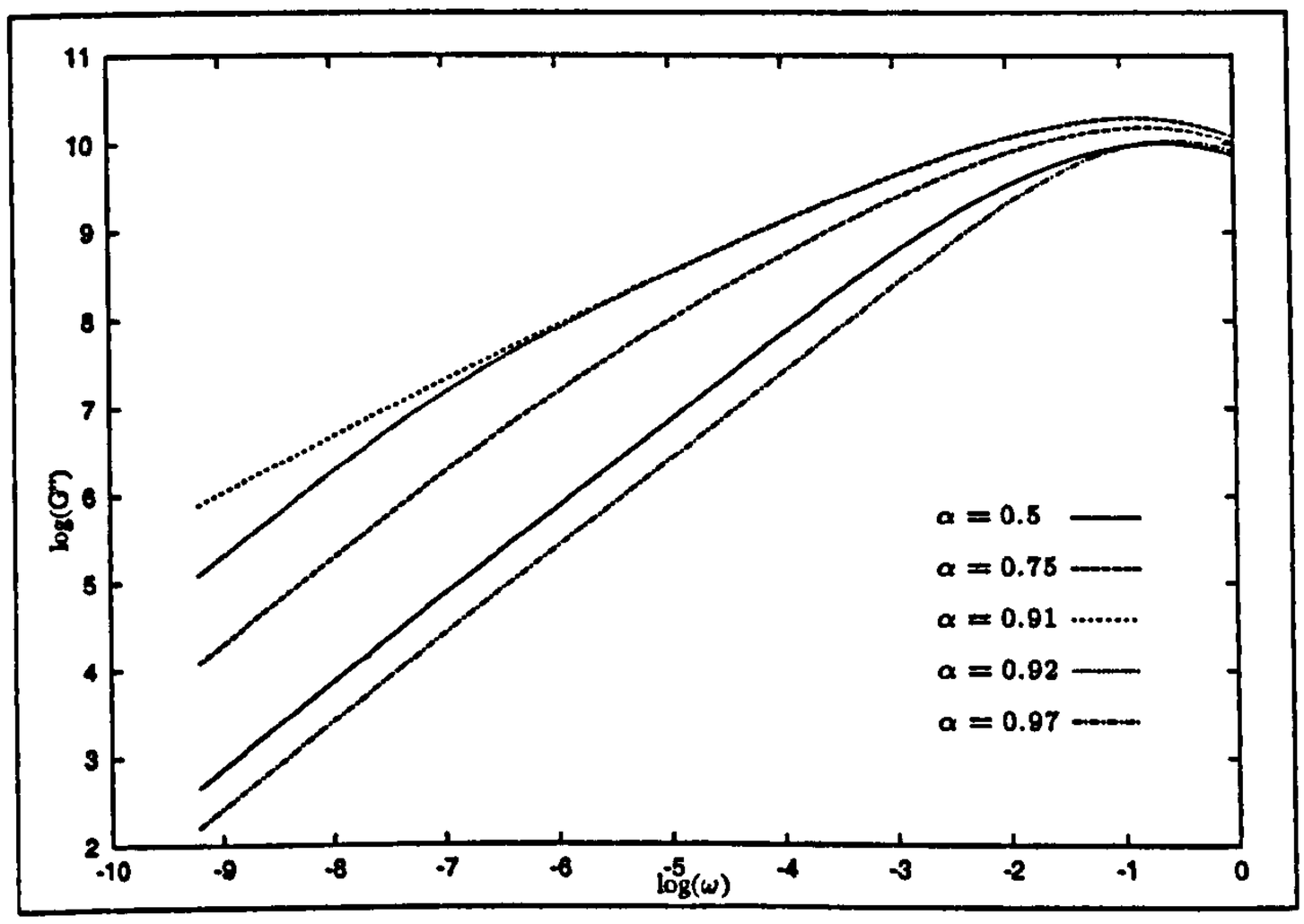


Figure 2.20: Loss modulus, $G''(\omega)$, at various extents of reaction.

# Chapter 3

# Expansion of Individual Bubbles

When the bubble volume fraction is small bubbles are surrounded by enough fluid so that there are no interactions between neighbouring bubbles. Thus, in this chapter we present models of spherical bubbles surrounded by spherical envelopes of liquid. In order to model the thermoplastic and thermoset injection moulding processes we consider first, the case when the liquid rheology remains constant and, second, the case of a changing fluid rheology. Initially we formulate the spherical bubble problem in terms of non-reacting fluid models, using the Oldroyd B and Pompom models for the liquid phase. Here bubble growth is driven by the diffusion of gas from a limited supply dissolved in the liquid. We go on to discuss two limiting cases: no gas diffusion where bubble expansion is due to a fixed mass of gas present initially; and diffusion limited growth where the gas pressure in the bubble remains at the ambient pressure. In the second section we use the model for polymer gelation discussed in section 2.5. We assume that gas production is proportional to the extent of reaction and that evolution of the extent of reaction follows second order kinetics. In this way we model bubble growth, driven by gas diffusion, in a fluid with evolving rheology.

The results presented in section 3.1.3 and 3.2.3 are also presented in reference [16].

## 3.1 Non-Reacting Fluid Models

Thermoplastic foam products are produced by injecting polymer that has been pressurised to enable it to absorb a blowing agent, and heated to a temperature above the glass transition temperature. Foaming results from a sudden reduction in pressure. We model the foam as a system of identical spherical bubbles of gas, each surrounded by a layer of viscoelastic fluid. The volume of this layer could be estimated by dividing the initial volume of liquid by the observed number of bubbles in the cured foam.

We consider a spherical bubble of gas with an initial volume $\frac{4}{3}\pi u_0$, and gas pressure $p_{g0}$, expanding in a uniform spherical envelope of incompressible viscoelastic fluid which contains a limited supply of a dissolved ideal gas. Since we are not attempting to model the initial rapid phase of bubble expansion immediately following nucleation, the initial bubble volume is not the volume at nucleation but a larger volume when the gas pressure is $p_{g0}$. Growth is driven by the pressure difference between the gas pressure inside the bubble, $p_g$, and a background pressure outside the envelope, $p_a$. We assume that the expansion rate is sufficiently small that fluid inertia may be neglected (see section 3.1.3), bubble growth is isothermal, and the bubble-fluid interface remains in thermodynamic equilibrium.

### 3.1.1 Governing Equations

In this section we begin by deriving the equations that govern bubble growth in a general fluid, specifying later to the Oldroyd B constitutive equation.

Fluid incompressibility gives $\nabla \cdot \mathbf{q} = 0$, where $\mathbf{q}$ is the velocity field. This defines the radial velocity,

$$q_r = \frac{q(t)}{r^2} = \frac{R^2\dot{R}}{r^2},$$

where $R$ is the bubble radius and $r$ is the general radial position. The velocity field for the expanding bubble in spherical polar coordinates gives

$$\nabla \mathbf{q} + \nabla \mathbf{q}^{\mathbf{T}} = 2 \begin{pmatrix} \frac{\partial q_r}{\partial r} & 0 & 0 \\ 0 & \frac{q_r}{r} & 0 \\ 0 & 0 & \frac{q_r}{r} \end{pmatrix} = 2\frac{R^2\dot{R}}{r^3} \begin{pmatrix} -2 & 0 & 0 \\ 0 & 1 & 0 \\ 0 & 0 & 1 \end{pmatrix}.$$

We can write the stress in the liquid (following (2.1)) as $\boldsymbol{\sigma} = -p\mathbf{I} + \mathbf{S}$ and, due to the spherical symmetry, $S_{\theta\theta} = S_{\phi\phi}$, and $p$, $S_{rr}$ and $S_{\theta\theta}$ are assumed to depend on $r$ and $t$ only. Neglecting inertia, the radial momentum equation, $\nabla \cdot \boldsymbol{\sigma} = 0$, gives

$$0 = -\frac{\partial p}{\partial r} + \left( \frac{1}{r^2}\frac{\partial}{\partial r}\left(r^2 S_{rr}\right) - \frac{2S_{\theta\theta}}{r} \right)$$

Evaluating the derivative of $r^2 S_{rr}$ and rearranging allows us to write

$$\frac{\partial p}{\partial r} = \frac{2\left(S_{rr} - S_{\theta\theta}\right)}{r} + \frac{\partial S_{rr}}{\partial r}. \tag{3.1}$$

Since the fluid volume is conserved it is useful to transform from a radial coordinate $r$ to a Lagrangian volume coordinate $x$ such that $r^3 = u + x$. Here, $\frac{4}{3}\pi u$ is the bubble volume and $\frac{4}{3}\pi x$ is the general fluid volume so that $x = X$ is the Lagrangian position of the outer edge of the envelope. At the boundaries $x = 0$ and $x = X$

$$-p(x=0) + S_{rr}(x=0) = -p_g + \frac{2K}{u^{\frac{1}{3}}} \quad \text{(inner surface boundary condition)}$$
$$-p(x=X) + S_{rr}(x=X) = -p_a \quad \text{(outer surface boundary condition)}$$

where $K$ is the surface tension at the bubble surface. Integrating (3.1) across the fluid layer and using these boundary conditions gives:

$$0 = p_g - p_a + \frac{2}{3}\int_0^X \frac{S_{rr} - S_{\theta\theta}}{x+u}dx - \frac{2K}{u^{1/3}}. \tag{3.2}$$

The initial concentration of gas in the fluid is $c_0$, and $p_{g0} = Hc_0$ where $H$ is Henry's constant. As the bubble expands the pressure drops and a concentration gradient

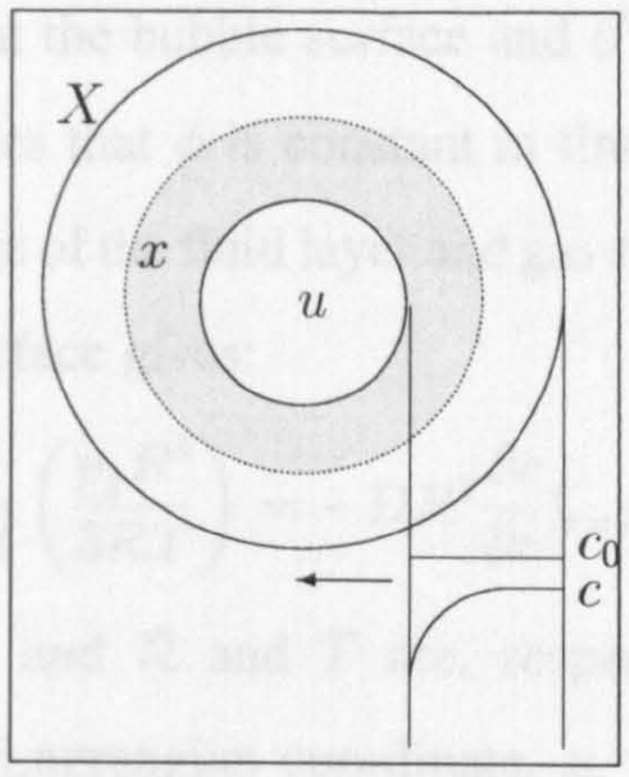


Figure 3.1: Diagram showing the bubble surrounded by fluid, initial gas concentration profile $c_0$ and general concentration profile $c$.

propagates through the fluid (see figure 3.1.1) causing gas to diffuse into the bubble. The concentration at the bubble surface is given by Henry's law as

$$c(0,t) - c_0 = H(p_g - p_{g0}).$$

The concentration, $c(x,t)$, is the number of moles of gas per unit volume of fluid. Henry's law is valid for dilute solutions where gas concentrations are of the order of 1%; we justify its use in section 3.1.3. The diffusion of gas through the liquid is determined by the change in gas concentration

$$\frac{Dc}{Dt} = \nabla \cdot \mathbf{j},$$

where $\mathbf{j}$ is the flux of gas into the bubble. In spherical polar coordinates $\mathbf{j} = D\partial c/\partial r\hat{\mathbf{r}}$ and the change in gas concentration becomes

$$\frac{Dc}{Dt} = \frac{D}{r^2}\frac{\partial}{\partial r}\left(r^2\frac{\partial c}{\partial r}\right). \tag{3.3}$$

Substituting $r^3 = x + u$ gives the gas diffusion equation

$$\frac{\partial c}{\partial t} = 9D\frac{\partial}{\partial x}\left((x+u)^{\frac{4}{3}}\frac{\partial c}{\partial x}\right).$$

We introduce a concentration potential $\phi(x,t)$ so that $\frac{\partial \phi}{\partial x} = c - c_0$ to aid in the numerical solution [1, 3]. The diffusion equation then becomes

$$\frac{\partial \phi}{\partial t} = 9D(x+u)^{\frac{4}{3}}\frac{\partial^2 \phi}{\partial x^2}, \tag{3.4}$$

with $\partial\phi/\partial x = H(p_g - p_{g0})$ at the bubble surface and $\partial^2\phi/\partial x^2 = 0$ at the outer edge of the fluid layer which implies that $\phi$ is constant in time there. Thus there is no gas transport through the outer edge of the fluid layer and gas supply is limited. Conservation of mass across the bubble interface gives:

$$\frac{d}{dt}\left(\frac{p_g R^3}{3\mathcal{R}T}\right) = -DR^2\frac{\partial c}{\partial r}|_{r=R}. \tag{3.5}$$

Here $R$ is the bubble radius and $\mathcal{R}$ and $T$ are, respectively, the gas constant and temperature. In terms of the Lagrangian coordinate, $x$, and concentration potential $\phi$ this becomes

$$\frac{d}{dt}\left(\frac{p_g u}{\mathcal{R}T}\right) = 9Du^{\frac{4}{3}}\frac{\partial^2\phi}{\partial x^2}|_{x=0}.$$

Substituting from (3.4) and integrating with respect to time gives

$$p_g u = p_{g0}u_0 + \mathcal{R}T\phi(0,t) \tag{3.6}$$

since we can arbitrarily set $\phi(0,0) = 0$.

For the Oldroyd B fluid model

$$S_{rr} - S_{\theta\theta} = -2\mu\frac{\dot{u}}{x+u} + G(A_{rr} - A_{\theta\theta}),$$

so that the momentum equation can be written as

$$\frac{4}{3}\mu\dot{u}\left[\frac{1}{u} - \frac{1}{X+u}\right] = p_g - p_a + \frac{2}{3}G\int_0^X \frac{A_{rr} - A_{\theta\theta}}{x+u}dx - \frac{2K}{u^{\frac{1}{3}}}. \tag{3.7}$$

Equation (2.5) gives expressions for $A_{rr}$ and $A_{\theta\theta}$ which can then be subtracted to give an equation for the first normal stretch difference. Due to the coordinate transformation the stretch at any position in the fluid can be followed in the Lagrangian frame giving

$$\frac{\partial A_{rr}}{\partial t} = -\frac{4\dot{u}}{3(x+u)}A_{rr} - \frac{1}{\tau}(A_{rr} - 1) \tag{3.8}$$

$$\frac{\partial(A_{rr} - A_{\theta\theta})}{\partial t} = \frac{2\dot{u}}{3(x+u)}[(A_{rr} - A_{\theta\theta}) - 3A_{rr}] - \frac{1}{\tau}(A_{rr} - A_{\theta\theta}) \tag{3.9}$$

Initially $A_{rr} = 1$ and $A_{rr} - A_{\theta\theta} = 0$ everywhere.

The five equations (3.4) and (3.6) – (3.9) together with initial conditions $A_{rr} = 1$ and $A_{rr} - A_{\theta\theta} = 0$, $u = u_0$ and $p_g = p_{g0}$ govern bubble growth.

### 3.1.2 Non-dimensional Equations

We scale all lengths with $u_0^{\frac{1}{3}}$ and scale times with the polymer relaxation time $\tau$. Pressure is scaled so that the dimensionless gas pressure is the ratio of the current pressure difference to the initial pressure difference: $P_g = (p_g - p_a)/(p_{g0} - p_a)$. The number of moles of gas which have diffused out of the liquid, $\phi$, is scaled with the initial number of moles of gas in the bubble, $p_{g0}u_0/\mathcal{R}T$ giving the following dimensionless equations where all variables are dimensionless:

$$\frac{4}{3}\dot{u}\left[\frac{1}{u} - \frac{1}{X+u}\right] = P_g De + \frac{2}{3}\gamma\int_0^X \frac{A_{rr} - A_{\theta\theta}}{x+u}dx - \frac{1}{\Gamma u^{\frac{1}{3}}}, \tag{3.10}$$

$$\frac{\partial A_{rr}}{\partial t} = -\frac{4\dot{u}}{3(x+u)}A_{rr} - (A_{rr} - 1), \tag{3.11}$$

$$\frac{\partial(A_{rr} - A_{\theta\theta})}{\partial t} = \frac{2\dot{u}}{3(x+u)}[(A_{rr} - A_{\theta\theta}) - 3A_{rr}] - (A_{rr} - A_{\theta\theta}), \tag{3.12}$$

$$\left(\frac{p_a + (p_{g0} - p_a)P_g}{p_{g0}}\right)u = 1 + \phi(0,t), \tag{3.13}$$

$$\frac{\partial\phi}{\partial t} = N(x+u)^{\frac{4}{3}}\frac{\partial^2\phi}{\partial x^2}, \tag{3.14}$$

together with boundary conditions:

$$\begin{aligned} \tfrac{\partial\phi}{\partial x} &= \Phi\tfrac{p_{g0}-p_a}{p_{g0}}(P_g - 1), \quad \text{(at the bubble surface)} \\ \tfrac{\partial^2\phi}{\partial x^2} &= 0, \qquad\qquad\qquad\quad \text{(at } x = X\text{)} \end{aligned} \tag{3.15}$$

and initial conditions $A_{rr} = 1$ and $A_{rr} - A_{\theta\theta} = 0$, $u = 1$ and $P_g = 1$. There are five non-dimensional groups summarised in table 3.1.

### 3.1.3 Results and Discussion

The full system of equations (3.10) – (3.14) are solved using an Euler method with an adaptive time step for (3.10), (3.11) and (3.12) and a Crank-Nicolson method for the diffusion equation. Parameters used to generate the figures are outlined in table 3.2 though these are typical of values found in the literature. Values of the dimensionless

| | | |
|---|---|---|
| Deborah number | $De = \frac{(p_{g0}-p_a)\tau}{\mu}$ | ratio of the rate of bubble growth in the solvent to the relaxation rate of the polymer |
| viscosity ratio | $\gamma = \frac{G\tau}{\mu}$ | ratio of polymer to solvent contributions to the steady shear viscosity |
| capillary number | $\Gamma = \frac{u_0^{\frac{1}{3}}\mu}{2K\tau}$ | ratio of viscous force to surface tension |
| time scale ratio | $N = \frac{9D\tau}{u_0^{\frac{2}{3}}} = \frac{\tau}{T_d}$ | ratio of the polymer relaxation time, $\tau$, to gas diffusion time, $T_d$ |
| | $\Phi = \mathcal{R}TH$ | |
| | $X$ | dimensionless volume of fluid in the liquid layer |

Table 3.1: Dimensionless groups arising in the non-dimensional formulation of the equations governing bubble growth.

| parameter | | value | units |
|---|---|---|---|
| pressure outside the fluid layer | $p_a$ | 1 | $10^5$N m$^{-2}$ |
| initial bubble gas pressure | $p_{g0}$ | 10 | $10^5$N m$^{-2}$ |
| elastic modulus | $G$ | 1–10 | $10^5$N m$^{-2}$ |
| solvent viscosity | $\mu$ | 1, 6 | $10^5$Ns m$^{-2}$ |
| polymer relaxation time | $\tau$ | 1 | s |
| initial bubble volume | $u_0$ | 1 | $10^{-18}$m$^3$ |
| surface tension | $K$ | 0–5 | $10^{-1}$N m$^{-1}$ |
| gas constant | $R$ | 8.3 | $J$mol$^{-1}$K$^{-1}$ |
| temperature | $T$ | 370 | K |
| Henry's law constant | $H$ | 10.5 | $10^{-5}$mol N$^{-1}$m$^{-1}$ |
| Diffusivity | $D$ | 0.1–$\infty$ | $10^{-12}$m$^2$s$^{-1}$ |
| Fluid density | $\rho$ | 1200 | kg m$^{-3}$ |

Table 3.2: Parameters values used in calculations of bubble expansion for figures 3.2– 3.16.

| dimensionless groups | value |
|---|---|
| $De$ | 9 |
| $\gamma$ | 5 |
| $\Gamma$ | $\infty$ |
| $X$ | 53.6 |
| $N$ | 0.9 |
| $\Phi$ | 0.32 |

Table 3.3: Dimensionless numbers used in calculations of bubble expansion for figures 3.2–3.16 unless otherwise stated in the captions.

groups are given in table 3.3. The Henry's law constant, $H$, controls the concentration of gas in the liquid for a given bubble gas pressure. The values of $H$ and $p_{g0}$ given in table 3.2 lead to an initial gas concentration of $105\text{molm}^{-3}$. For a liquid density of $1200\text{kgm}^{-3}$ and molar mass of $0.044\text{kgmol}^{-1}$ for carbon dioxide this is 0.385% initial gas concentration. Since Henry's law is valid for dilute solutions where gas concentrations are of the order of 1% use of Henry's law is justified in this parameter regime.

In order to neglect inertia from this model, the Reynolds number for the bubble expansion must be small. Balancing the inertia term with the viscosity term in the momentum equation gives a Reynolds number

$$\frac{\rho U L}{\mu} = \frac{\rho u_o{}^{\frac{2}{3}}(p_{g0} - p_a)}{\mu^2}$$

(using $\frac{De}{\tau}$ as the time scale for the bubble expansion). Thus, inertia is negligible as long as the ratio of the pressure difference, $p_{g0} - p_a$, to viscosity squared is small. For the parameter values given in table 3.2 the Reynolds number for the expansion is $1.97 \times 10^{-10}$.

In this problem there are three distinct timescales controlling the expansion of the bubble. These are: the diffusion time for gas transport into the bubble from the surrounding fluid; the viscous growth time for a bubble in a viscous fluid of the solvent viscosity; and the relaxation time of the polymer, $\tau$.

From equation (3.14) the time scale for gas to diffuse across the fluid layer is of the order $(u_0 X)^{\frac{2}{3}}/9D = X^{\frac{2}{3}}\tau/N$, whereas solvent viscosity imposes a maximum bubble expansion rate of order $(p_{g0} - p_a)/\mu = De/\tau$. Depending upon the relative values of these, bubble growth may be controlled by any one of the three timescales.

**Instantaneous Diffusion**

We can examine the effects of viscoelasticity on growth rate by considering the limit $N \gg DeX^{\frac{2}{3}}$ when diffusion is, essentially, instantaneous so that the bubble growth is

limited by the rheology of the surrounding fluid. In this case the concentration profile of gas in the liquid is independent of fluid volume and is dictated by the gas pressure in the bubble through Henry's law. Now boundary condition (3.15) at the bubble surface applies throughout the fluid layer and the conservation of mass equation (3.13) becomes

$$\left(\frac{p_a + (p_{g0} - p_a)P_g}{p_{g0}}\right) u = 1 + \Phi \frac{p_{g0} - p_a}{p_{g0}}(1 - P_g)X. \tag{3.16}$$

This enables the bubble growth equations to be solved independently of the diffusion equation. In the case when $\Phi X$ is large so that there is a large reservoir of gas available within the layer, the gas pressure $P_g$ remains approximately constant until $u \simeq \Phi X$ after which the pressure difference decays to zero in absence of surface tension. In the opposite limit when $\Phi X \ll 1$ and $p_{g0} \gg p_a$ so that most of the gas is already within the bubble at $t = 0$, the pressure decreases as $1/u$.

In figure 3.2 we compare the growth rate of bubbles at different Deborah numbers for the same value of $\gamma$. At large Deborah numbers we see two distinct phases of bubble growth: an initial rapid expansion in which the bubble volume increases rapidly, and a slower second phase of expansion. As the polymers are initially unstretched they do not provide any resistance during the initial phase of expansion, so that the resistance comes only from the solvent viscosity. The rapid expansion during this phase causes the polymer to stretch so that $A_{\theta\theta} - A_{rr}$ increases (see figure 3.3). This phase of expansion stops once the normal stress difference $\gamma(A_{\theta\theta} - A_{rr})/De$ at the surface of the bubble becomes comparable to the pressure difference. During the second phase the pressure difference is balanced by the elastic normal stress difference within the fluid. The growth of the bubble is therefore controlled by the relaxation of the elastic stress, which relaxes on a timescale of order $\tau$, the unit of time in our non-dimensionalisation.

We can attempt to estimate the timescales for the first phase in the two limits described above of large and small $\Phi X$. If $\Gamma$ and $X$ are both large and polymer does not contribute to the stress then equation (3.10) may be approximated as

$$\frac{\dot{u}}{u} = \frac{3}{4} P_g De.$$

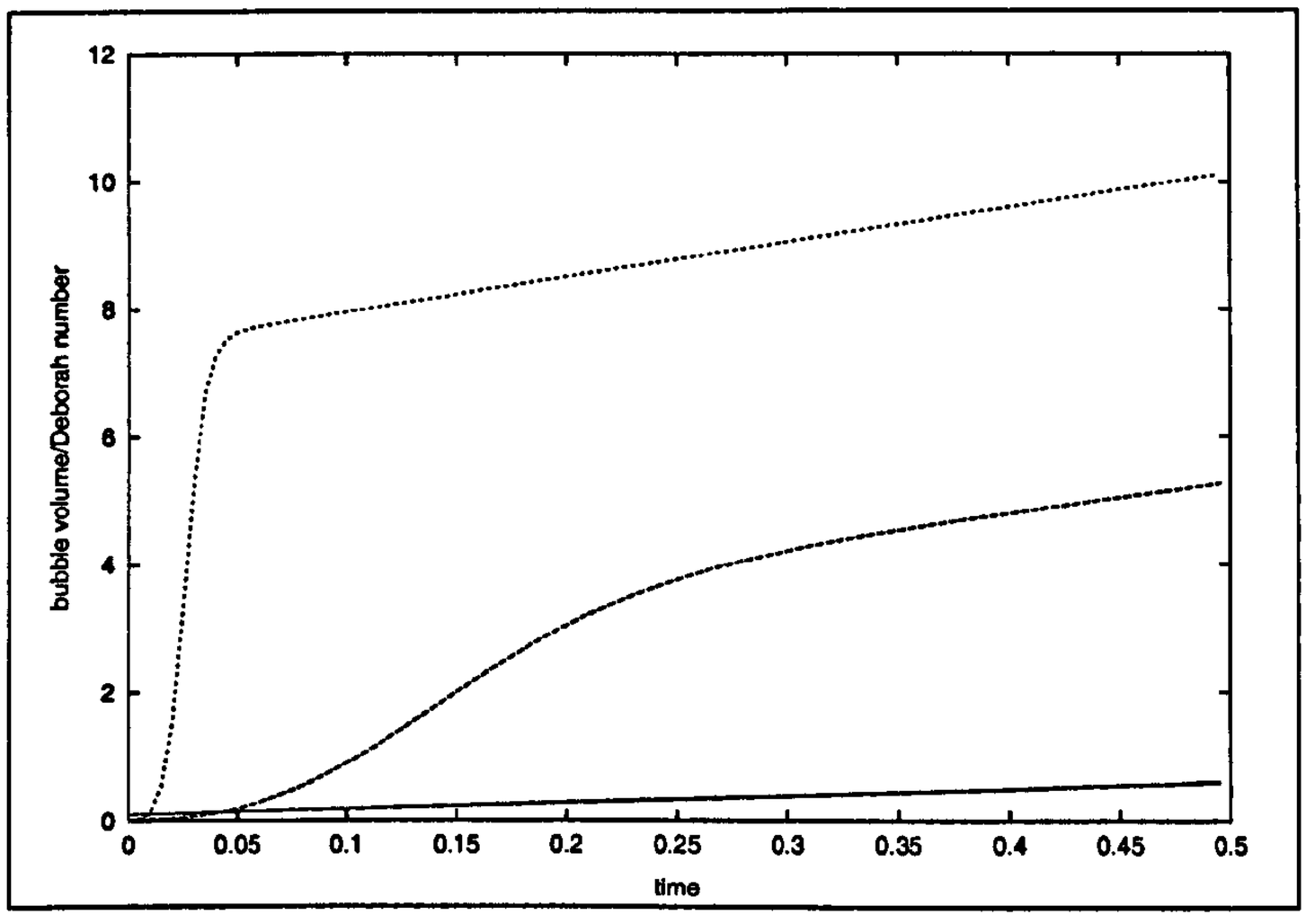


Figure 3.2: Effect of viscoelasticity on bubble volume when $\gamma = 5$. Solid line: $De = 9$; long dashed line: $De = 99$; short dashed line: $De = 999$.

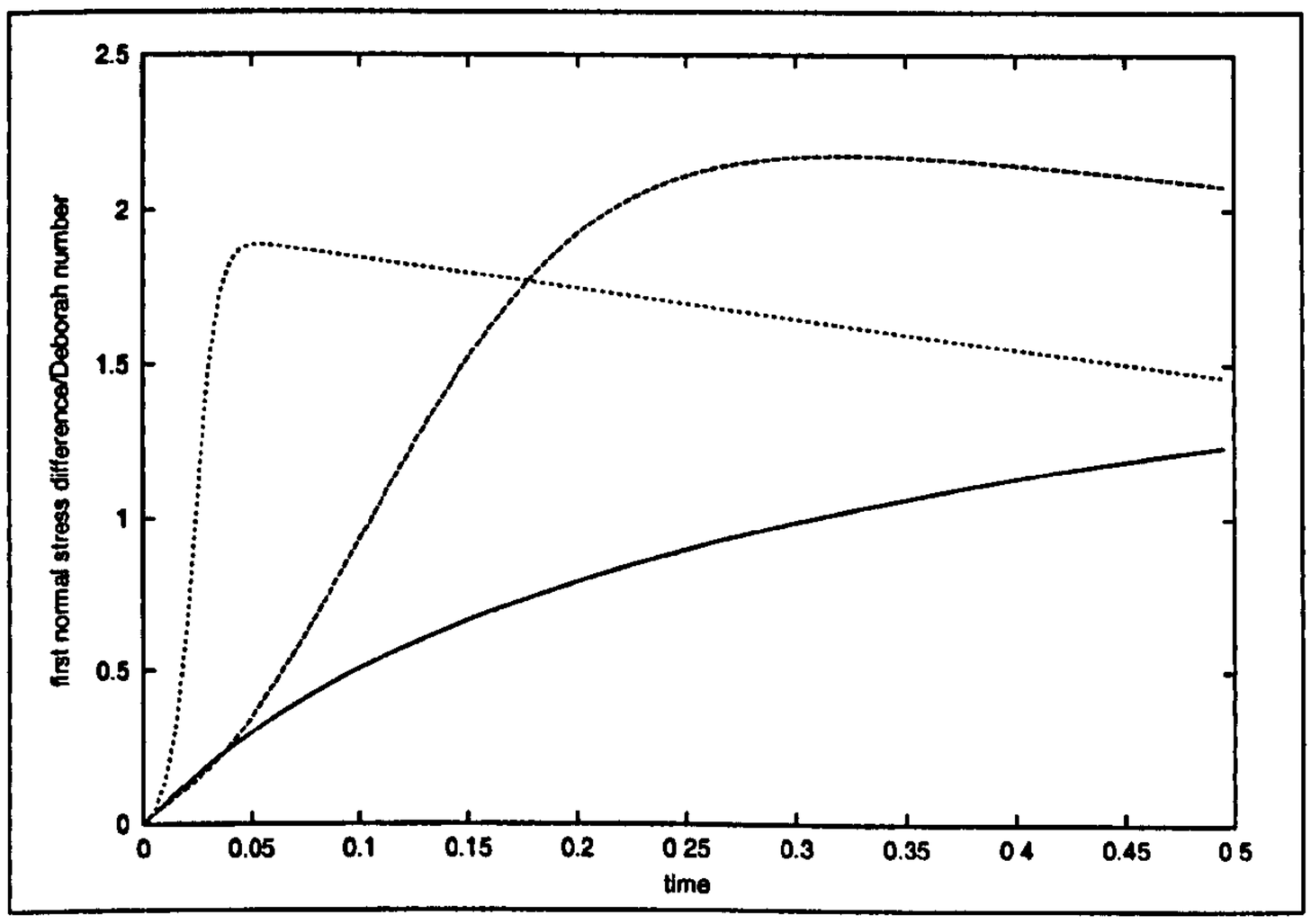


Figure 3.3: Effect of viscoelasticity on the first normal stress difference at the bubble surface when $\gamma = 5$. Solid line: $De = 9$; long dashed line: $De = 99$; short dashed line: $De = 999$.

As the bubble grows $A_{\theta\theta}$ increases while $A_{rr}$ decreases so that, neglecting $A_{rr}$ in equation (3.12), the polymer stretch difference on the bubble surface evolves approximately as

$$\frac{\partial(A_{\theta\theta} - A_{rr})}{\partial t} = \left(\frac{2\dot{u}}{3u} - 1\right)(A_{\theta\theta} - A_{rr}).$$

Using these approximate equations we find, for $\Phi X$ large, that the bubble volume increases exponentially as approximately $\exp(3Det/4)$ and $A_{\theta\theta} - A_{rr} \simeq \exp(\frac{1}{2}De - 1)t$. Thus the elastic stress will balance the pressure difference after a time of order $\frac{2}{De-2}\log\frac{De}{\gamma}$. This scaling can be seen approximately in figure 3.3 where the maximum pressure difference occurs at 0.04 for $De = 999$ and at time 0.3 for $De = 99$.

**Diffusion Limited Case**

When $N \ll DeX^{\frac{2}{3}}$ bubble growth is limited by diffusion. In fact, since $De$ is an overestimate of the bubble growth rate, this limit is reached for values of $N \approx DeX^{\frac{2}{3}}$. Growth is slow initially as the bubble has a small surface area over which the gas can diffuse (see figure 3.4). The expansion rate increases as the bubble gets larger but subsequently decreases once the gas pressure approaches the pressure outside the fluid layer and the concentration of gas in the liquid reaches a uniform profile. In the initial phase of expansion the pressure drops rapidly inside the bubble as it expands. The polymer stress builds to a maximum and then decays as the expansion rate decreases. However the stress is prevented from relaxing completely by gas diffusing into the bubble. Between $t = 5$ and 15 we see a plateau in the first normal stress difference and a decrease in the rate of pressure drop (see figures 3.5 and 3.6, $N = 0.9$ curve) corresponding to an increase in gas transport into the bubble. The stress is finally allowed to relax once the gas concentration in the bulk falls. In the limit of diffusion controlled growth the bubble gas pressure remains at the ambient background pressure, $p_g = p_a$, Thus bubble growth is controlled by equations (3.13) and (3.14). These can be solved analytically in the case of infinite fluid volume and zero initial radius as follows.

In terms of the radial coordinate, $r$, conservation of mass across the bubble interface

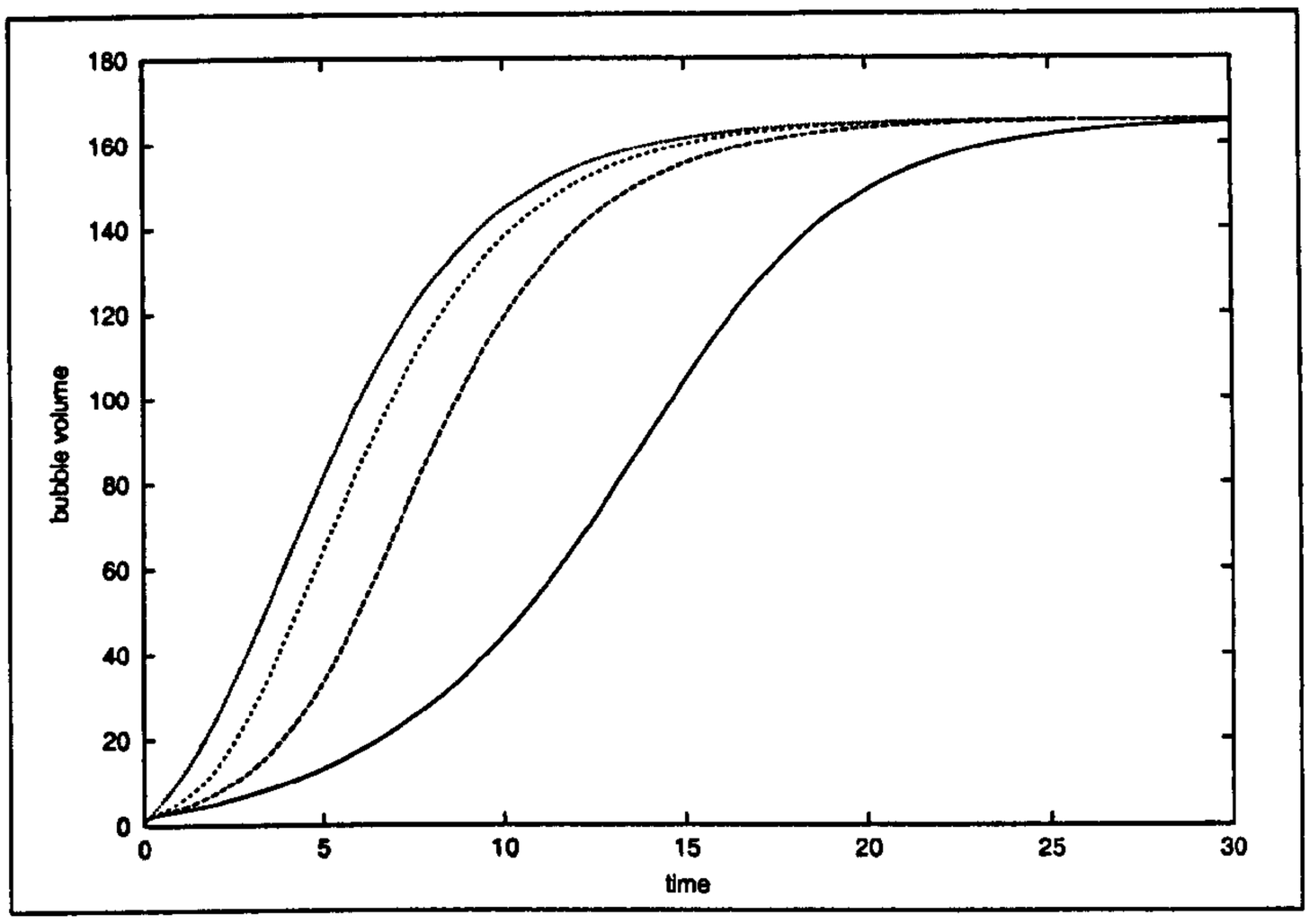


Figure 3.4: Effect of diffusivity on bubble growth rate when $\gamma = 5$. Solid line: $N = 0.9$; long dashed line: $N = 4.5$; short dashed line: $N = 18$; dotted line is the limit $N \to \infty$.

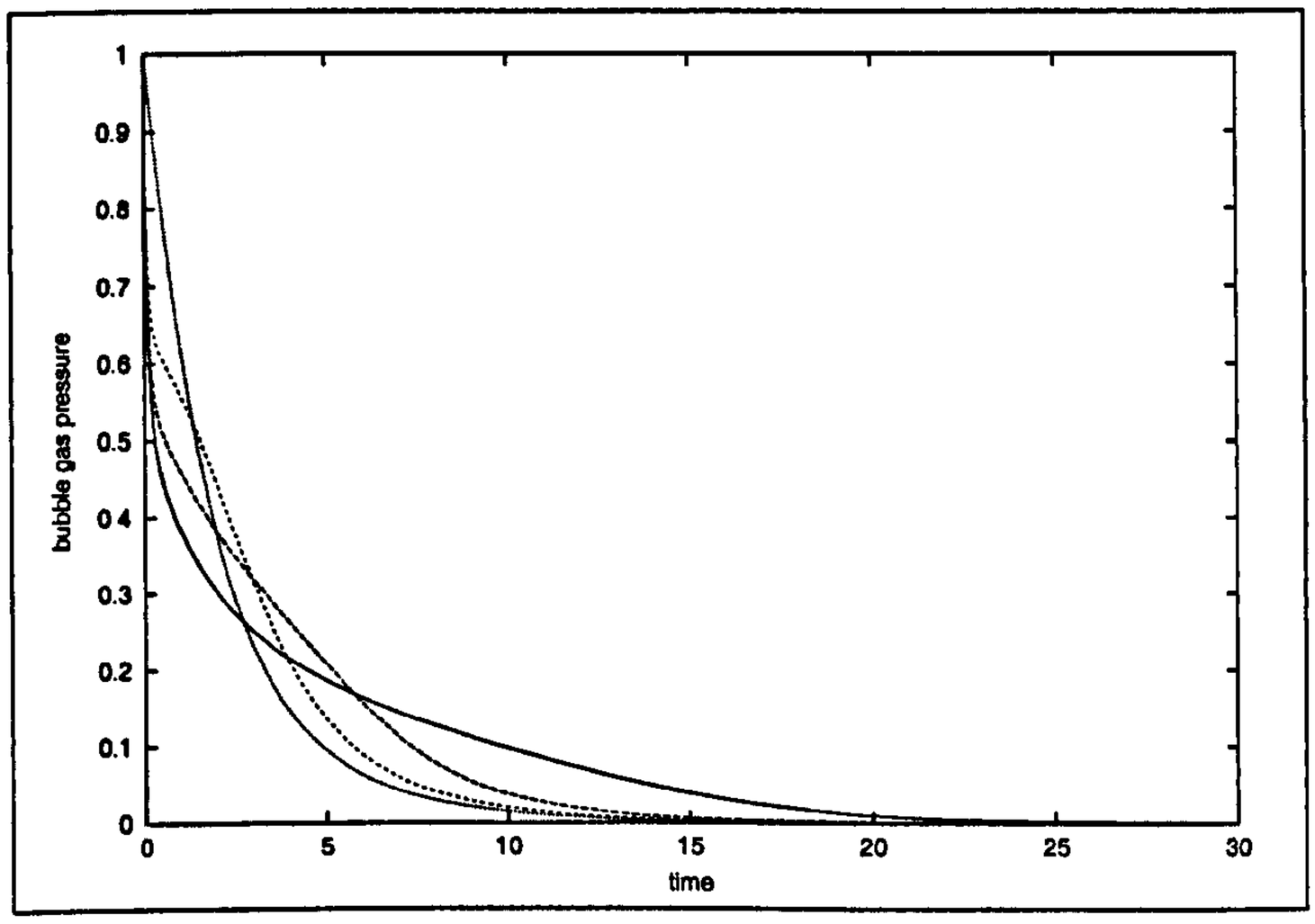


Figure 3.5: Effect of diffusivity on dimensionless gas pressure (ratio of the pressure difference to the initial pressure difference) when $\gamma = 5$. Solid line: $N = 0.9$; long dashed line: $N = 4.5$; short dashed line: $N = 18$; dotted line is the limit $N \to \infty$.

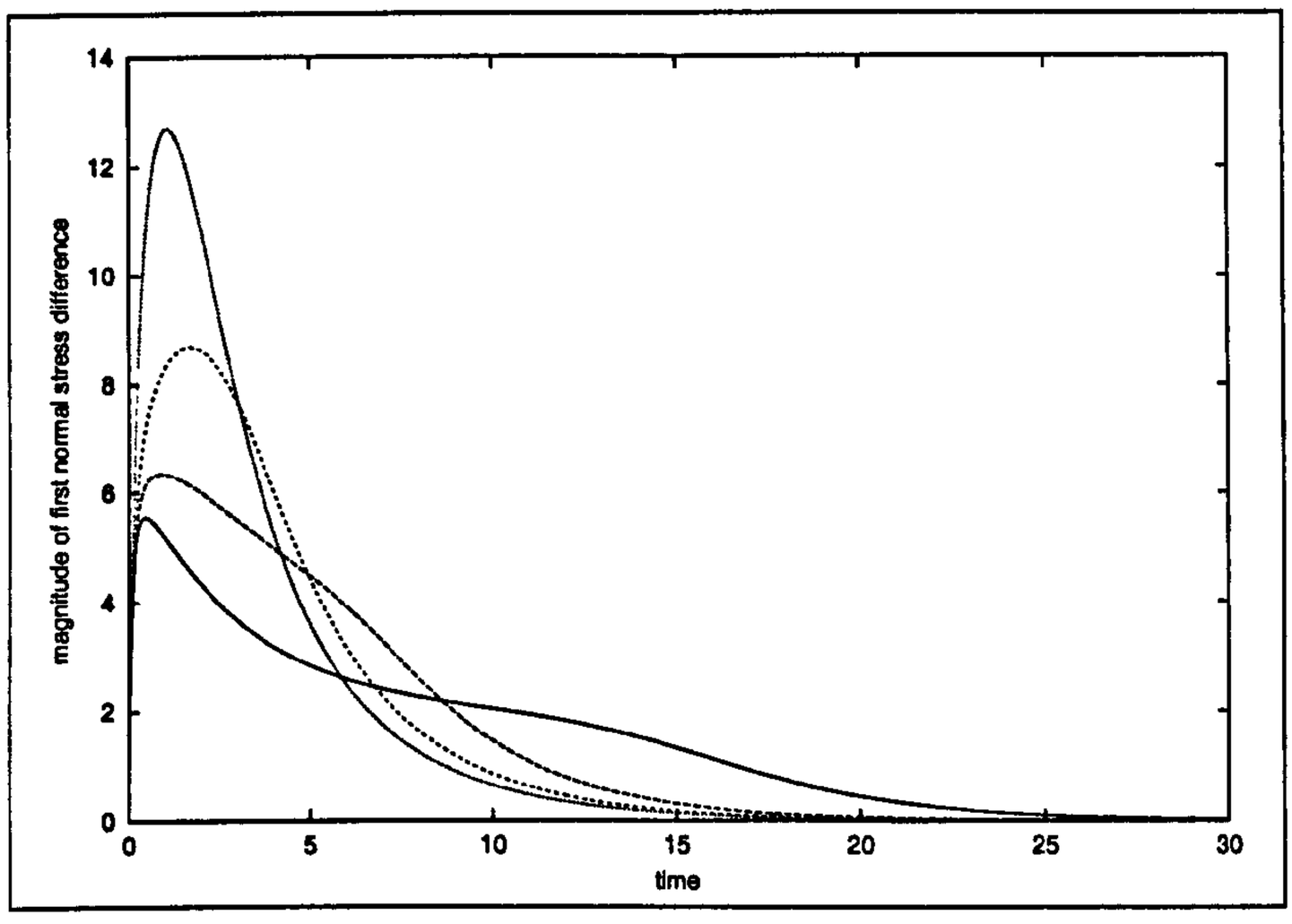


Figure 3.6: Effect of diffusivity on the magnitude of the first normal stress difference, $\gamma|A_{rr} - A_{\theta\theta}|$, at the bubble surface when $\gamma = 5$. Solid line: $N = 0.9$; long dashed line: $N = 4.5$; short dashed line: $N = 18$; dotted line is the limit $N \to \infty$.

gives:

$$\frac{d}{dt}\left(\frac{p_g R^3}{3\mathcal{R}T}\right) = -DR^2 \frac{\partial c}{\partial r}\bigg|_{r=R}.$$

where $R$ is the bubble radius. This reduces to the non-dimensional equation

$$\frac{dR}{dt} = -\frac{N}{9}\frac{p_{g0}}{p_a}\frac{\partial c}{\partial r}\bigg|_{r=R}. \tag{3.17}$$

Gas diffusion in terms of $r$ gives

$$\frac{\partial c}{\partial t} = \frac{N}{9r^2}\frac{\partial}{\partial r}\left(r^2\frac{\partial c}{\partial r}\right). \tag{3.18}$$

When the fluid layer is of infinite depth the concentration far from the bubble surface remains at an initial level $c(\infty, t) = c_0$. For zero initial bubble radius $R(0) = 0$ there is a similarity solution available for equations (3.17) and (3.18).

Substituting the similarity variable $\eta = \frac{r^2}{t}$ in equation (3.18) gives the following equation for $c(\eta)$

$$-\frac{9}{4N}\left(\frac{6N}{9\eta} + 1\right)\frac{dc}{d\eta} = \frac{d^2c}{d\eta^2}.$$

This can be solved for $\frac{dc}{d\eta}$ to give

$$\frac{dc}{d\eta} = A\eta^{-3/2}e^{-9\eta/(4N)}. \tag{3.19}$$

Changing the variable to $\zeta = \eta^{-1/2}$ allows us to write an expression for $c(\zeta)$

$$c = -2A\int_0^{\zeta} e^{-9/(4N\nu^2)}d\nu. \tag{3.20}$$

Since the gas concentration in the liquid, $c$, depends only on the combination $\frac{r^2}{t}$ the region having a particular concentration will have moved a distance $r \propto t^{1/2}$ in time $t$. In particular, since $c(R,t)$ is constant (because $p_g = p_a$ throughout the expansion in this case), and $R(0) = 0$, $R = \alpha t^{1/2}$. Thus, $A$ and $\alpha$ satisfy

$$\mathcal{R}TH = -2A\int_0^{1/\alpha} e^{-9/(4N\nu^2)}d\nu. \tag{3.21}$$

Using the expression for $\frac{dc}{d\eta}$ from equation (3.19) at $r = R$ in (3.17) gives

$$\frac{dR}{dt} = -\frac{2NA}{9}\frac{p_{g0}}{p_a}e^{-9\alpha^2/(4N)}\frac{t^{1/2}}{R^2}$$

which can be solved to give

$$R = -\left(\frac{4}{9}NA\frac{p_{g0}}{p_a}e^{-9\alpha^2/(4N)}\right)^{1/3}t^{1/2}.$$

Thus $\alpha$ satisfies

$$\alpha^3 e^{9\alpha^2/(4N)} = \frac{4}{9}\frac{p_{g0}}{p_a}NA. \tag{3.22}$$

Since the gas pressure always drops to the ambient pressure eventually during the expansion we see a region of bubble growth where $R \propto \sqrt{t}$. If the fluid domain is finite this proportionality is lost towards the end of the expansion since the amount of gas available is limited by the volume of the fluid. This can be seen in figure 3.7 for the case of bubble growth in a Newtonian liquid. A similar figure is obtained for a viscoelastic liquid ($\gamma > 0$) though the beginning of the $\sqrt{t}$ section is delayed as viscoelasticity inhibits the bubble growth rate and prevents pressure from dropping as rapidly.

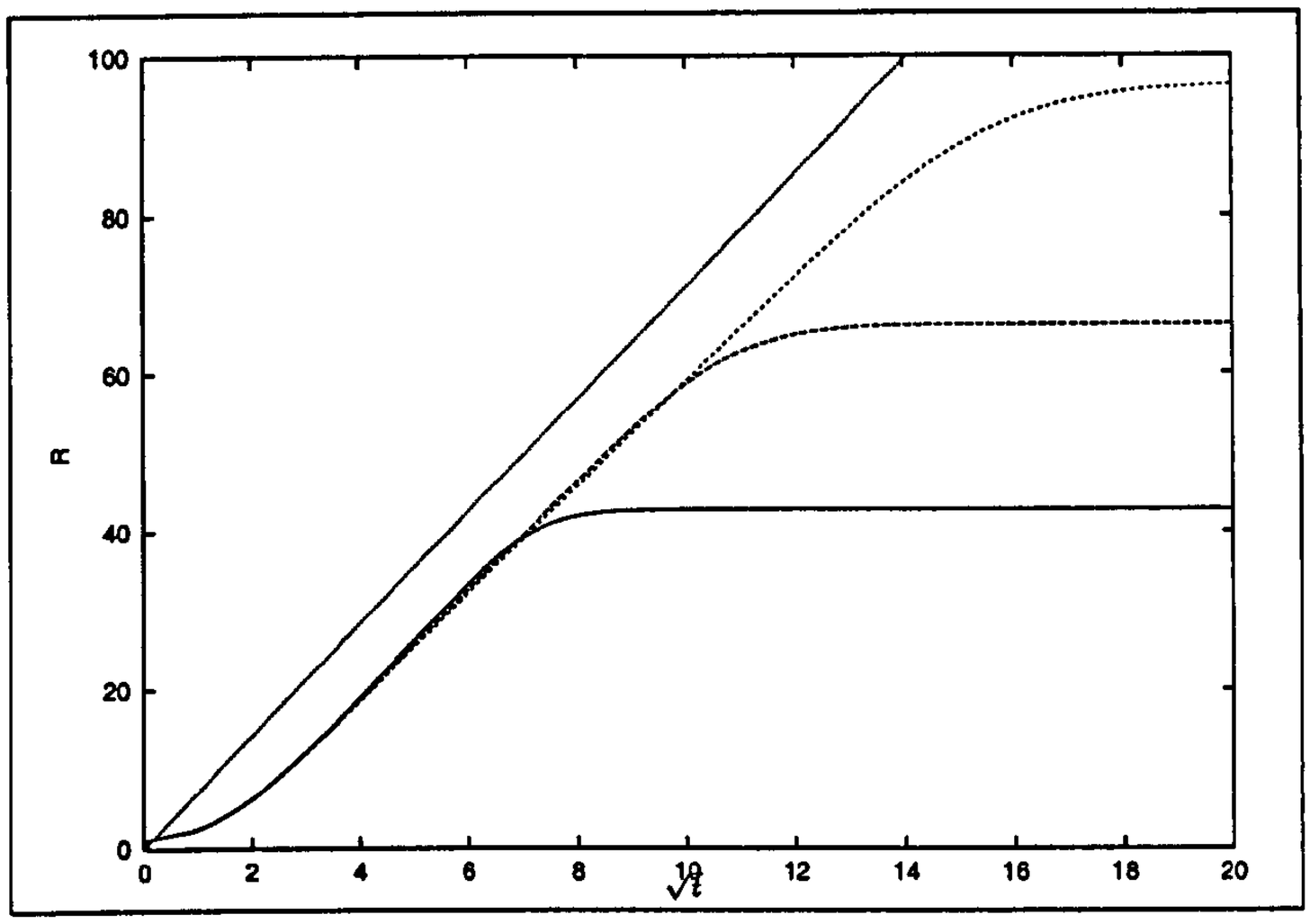


Figure 3.7: Diagram showing the growth of bubbles in a Newtonian liquid against $\sqrt{t}$. Solid line: initial fluid depth $29R_0$ ($X = 27000$); dashed line: initial fluid depth $45R_0$ ($X = 100000$); dotted line: initial fluid depth $66.7R_0$ ($X = 310000$). Straight line shows diffusion controlled growth when $p_g = p_a$, $R \propto \sqrt{t}$.

**Limit of Zero Gas Diffusion**

In the limit of $\Phi X \ll 1$ equation 3.13 reduces to

$$p_a + (p_{g0} - p_a)P_g = \frac{p_{g0}}{u}$$

In this limit we assume that the expansion is isothermal so that the gas pressure is related to the bubble volume by

$$1 + (u_\infty - 1)P_g = \frac{u_\infty}{u} \tag{3.23}$$

Here $\phi(0,t) = 0$ and there is no mass transfer from the fluid. Thus the problem is reduced to three equations, (3.10), (3.11) and (3.12), which are solved using a forward Euler method with adaptive time stepping. An initial gas pressure of 165.55 is used so that the volume of gas is equivalent to that in the previous sections.

For a viscoelastic fluid ($\gamma > 0$) the growth of the bubble can be roughly divided into two phases. During the initial phase the elastic stress is small and $X \gg u$, so equation 3.10

reduces to

$$\frac{4}{3}\frac{\dot{u}}{u} = P_g De.$$

For $p_{g0} \gg p_a$ the gas pressure $P_g \sim 1/u$ and the bubble volume grows linearly as approximately $1 + 3Det/4$. Figure 3.8 compares the early growth phase with the linear prediction. Provided that $De$ is greater than unity the expansion stretches the polymers causing the elastic stress to increase. At the bubble surface $A_{\theta\theta} - A_{rr}$ increases approximately as $u^{2/3}\exp(-t)$. This initial phase ends when the normal stress difference $\gamma(A_{rr} - A_{\theta\theta})/De$ at the bubble surface balances the pressure difference, when $\left(1 + \frac{3}{4}Det\right)\exp(-3t/5) = (De/\gamma)^{3/5}$. For large $De$ this will be at a time of order $De^{-2/5}\gamma^{-3/5}$. Subsequent expansion is controlled by the relaxation of polymer stress at rate $1/\tau$.

Nucleation and the early stages of bubble growth involve a period of surface tension dominated growth or collapse. In this work we assume that the initial bubble volume is large enough that $\Gamma > 1/De$. In this case the bubble is able to grow and surface tension again dominates the growth rate towards the end of the expansion as $P_g De - 1/\Gamma u^{\frac{1}{3}} \to 0$. Decreasing the capillary number reduces the final bubble volume. Figure 3.9 shows the equilibrium bubble volume against capillary number and compares these data with those obtained by performing a perturbation analysis. As $t \to \infty$, $\dot{u} \to 0$, $(A_{rr} - A_{\theta\theta}) \to 0$ and, therefore, from equation 3.10, $P_g De \to \frac{1}{\Gamma u^{(1/3)}}$ so that equation (3.23) yields a first order approximation for $u$:

$$u = u_\infty \left(1 - \frac{3}{2\left(\frac{3p_a}{2(p_{g0}-p_a)}u_\infty^{1/3} De\Gamma + 1\right)}\right).$$

**Moderate Diffusivities**

As diffusivity is increased the pattern of bubble growth remains qualitatively similar, but with an increase in the bubble growth rate. Increased diffusion reduces the extent of the initial rapid pressure drop until, in the limit of infinite diffusion, this initial phase is lost

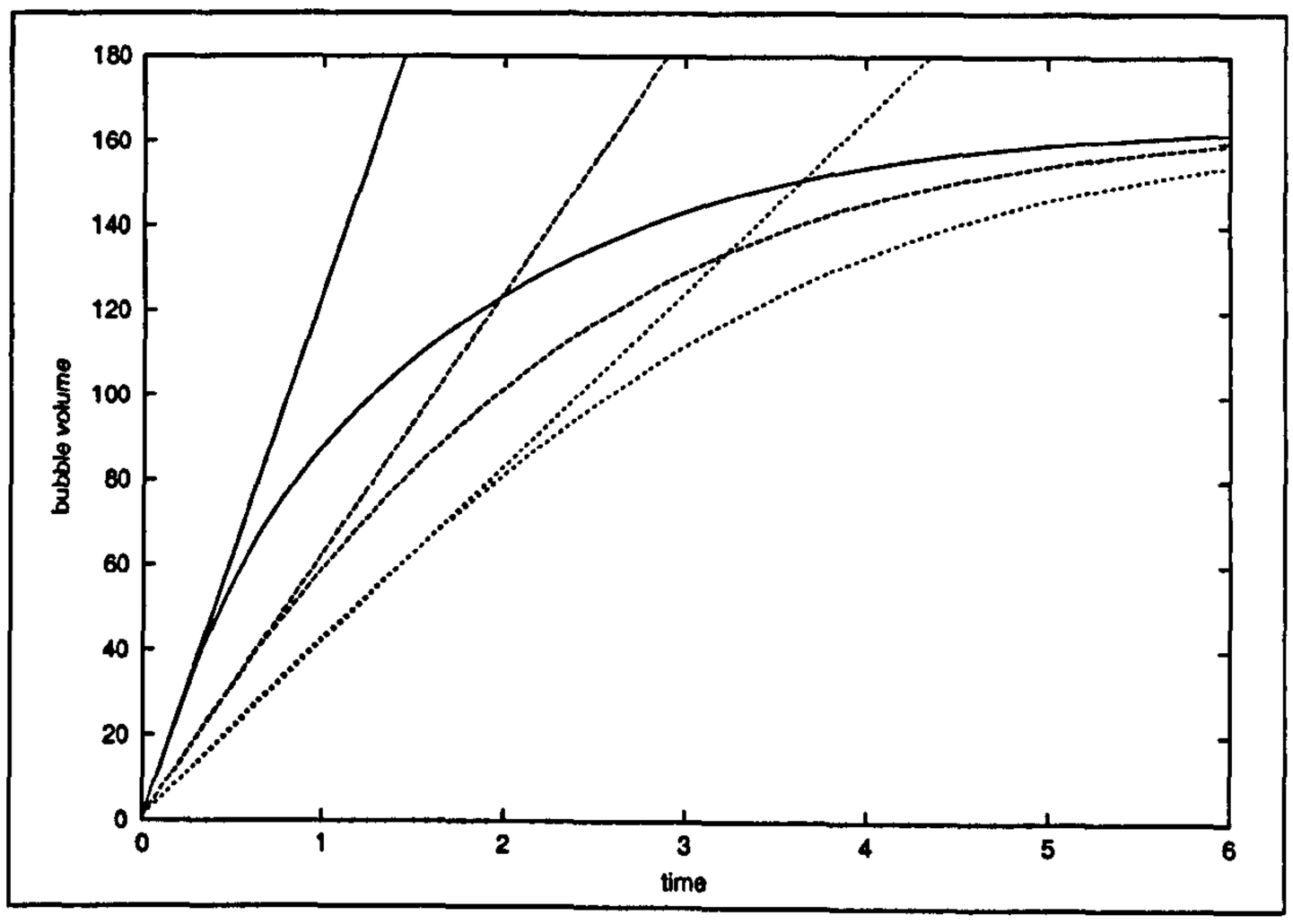


Figure 3.8: Comparison of early bubble growth phase with the linear prediction. Solid curve: $\gamma = 1, De = 164.55$; dashed curve: $\gamma = 1/2, De = 82.28$; dotted curve: $\gamma = 1/3, De = 54.85$. Lines show $1 + 3Det/4$ in each case.

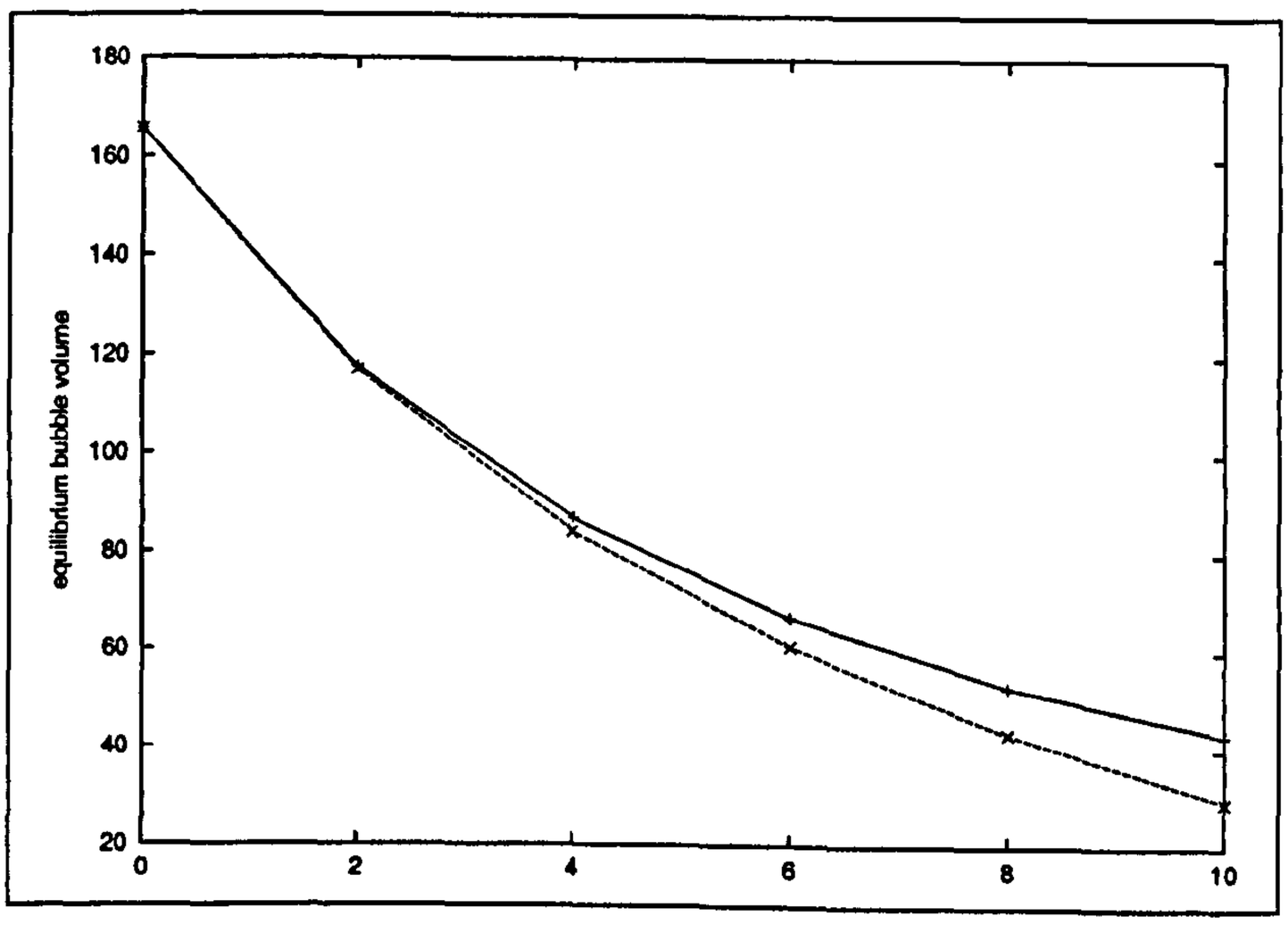


Figure 3.9: Effect of surface tension on the equilibrium bubble volume. + obtained from model predictions, × obtained from the perturbation analysis.

altogether (see figure 3.5). Increasing diffusion also causes the final stress relaxation to occur sooner and the more rapid bubble growth increases the magnitude of the first normal stress difference at its peak. These two regions eventually become indistinct (figure 3.6).

The parameter $\gamma$ is the ratio of the polymer to solvent contributions to the zero shear-rate viscosity with $\gamma = 0$ corresponding to a Newtonian fluid and $\gamma = \infty$ to an upper convected Maxwell fluid. Initially the polymers are unstretched and so the first stage of bubble growth is resisted only by the solvent stress. Consequently bubbles grow more rapidly in a viscoelastic liquid than in a Newtonian fluid of the same zero shear-rate viscosity. This is shown in figure 3.10, where we compare the growth in bubble volume between a fluid with $\gamma = 5$ and a Newtonian fluid at $N = 0.9$ and in the limit of infinite diffusivity. The difference in growth rate is most marked at high diffusivity where the initial growth rate is controlled by the fluid viscosity. At low diffusivity viscoelastic effects are less significant due to slower growth rate.

The potential, $\phi$, is the relative number of moles of gas diffused from the liquid at time $t$. In the absence of surface tension, as $t \to \infty$, the dimensionless gas pressure $P_g \to 0$ and $\phi \to \Phi(p_{g0} - p_a)X/p_{g0}$. This leads to an equilibrium bubble volume given by

$$u_\infty = \frac{p_{g0} + \Phi(p_{g0} - p_a)X}{p_a}. \tag{3.24}$$

Again, the effect of including surface tension at the bubble surface ($\Gamma < \infty$) is to increase the equilibrium gas pressure and reduce the equilibrium bubble volume, see figure 3.11. Figure 3.12 has been included to provide a comparison with Arafmanesh and Advani's results [2]. They did not include a solvent term and so were forced to use an iterative technique to obtain solutions. By taking a small solvent viscosity in our model we have a very good agreement with their results. Figure 3.12 shows the effect of diffusivity in a deep fluid layer, the largest rate of diffusion producing the largest bubble growth rate.

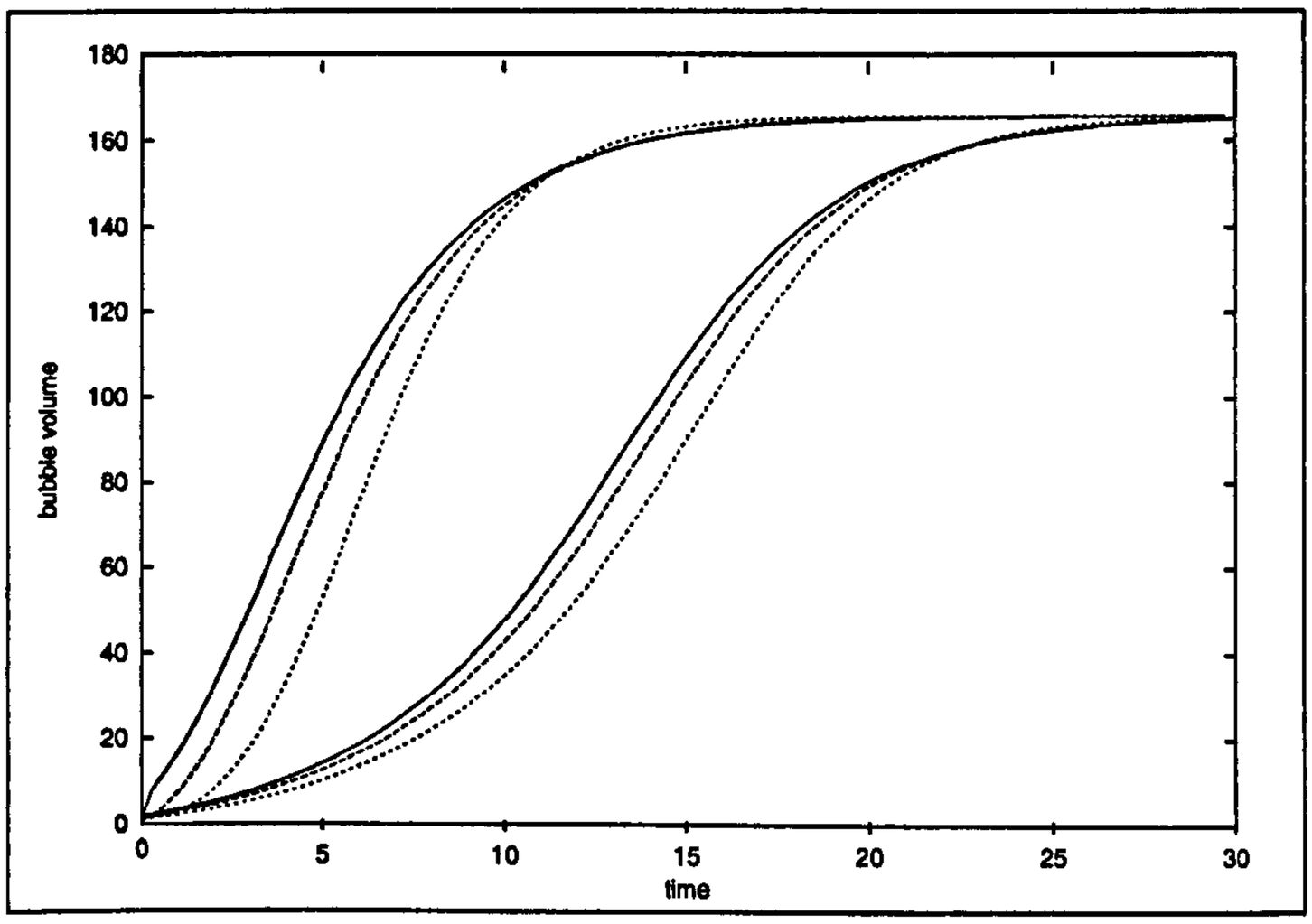


Figure 3.10: Comparison of bubble growth in a viscoelastic liquid and a Newtonian liquid of the same zero shear rate viscosity. The solid lines represent a viscoelastic liquid with $\gamma = \infty$ and $De = 9$, the long dashed lines represent a viscoelastic liquid with $\gamma = 4$ and $\mu = 2$, and the short dashed line represents a Newtonian liquid with $\gamma = 0$. The lower curves show bubble growth rate when $N = 0.9$ and the upper curves show bubble growth rate in the limit of infinite diffusion.

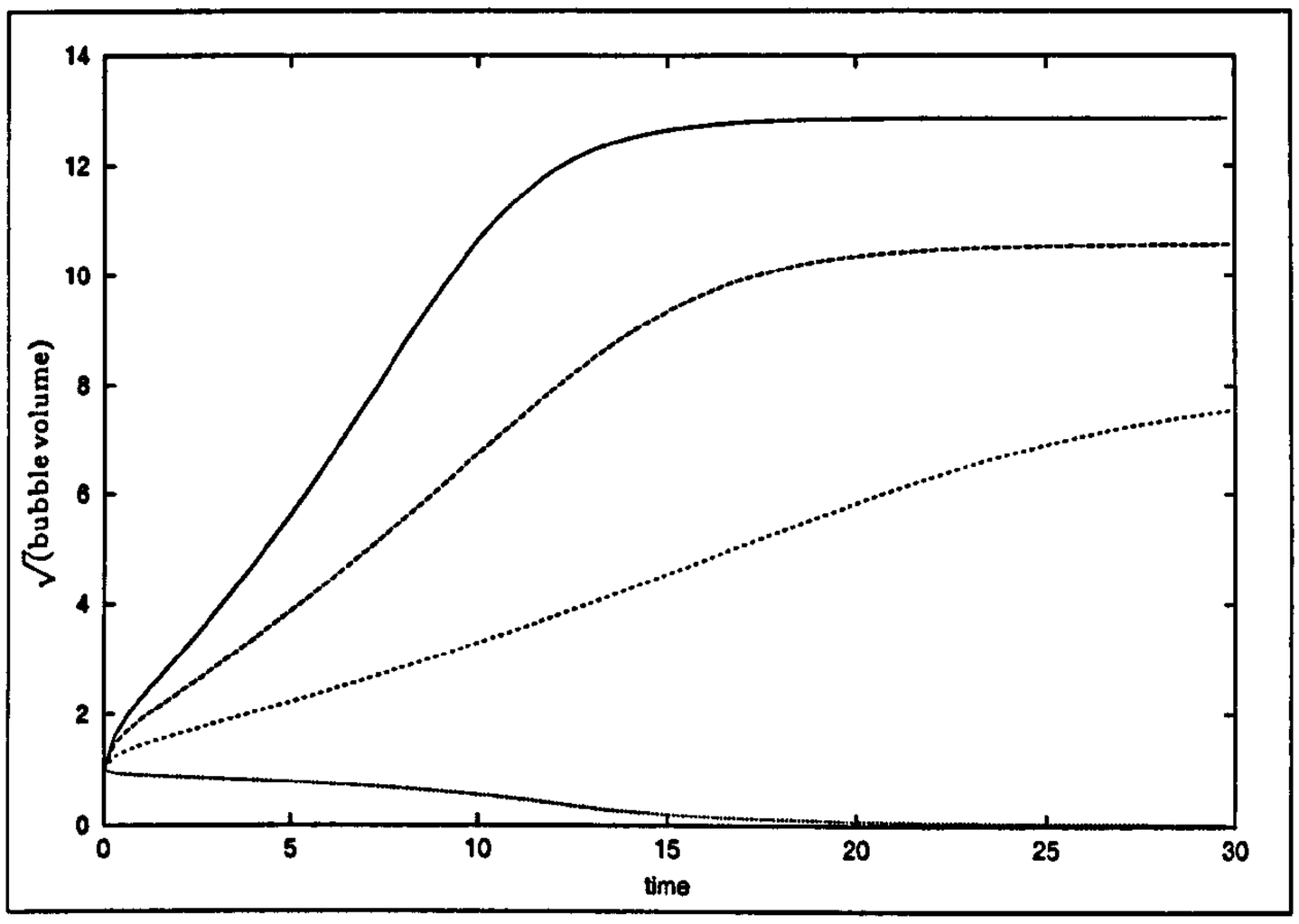


Figure 3.11: Effect of surface tension ($\Gamma < \infty$) on bubble growth rate, $N = 0.9$, $De = 9$ and $\gamma = 5$. The solid line shows $\Gamma = \infty$; the two lines with positive bubble growth rate ($\Gamma > 1/De$) show successively smaller equilibrium bubble volumes with $\Gamma = 0.5$ and $\Gamma = 0.2$ respectively. The line with negative bubble growth rate shows $\Gamma = 0.1 < 1/De$.

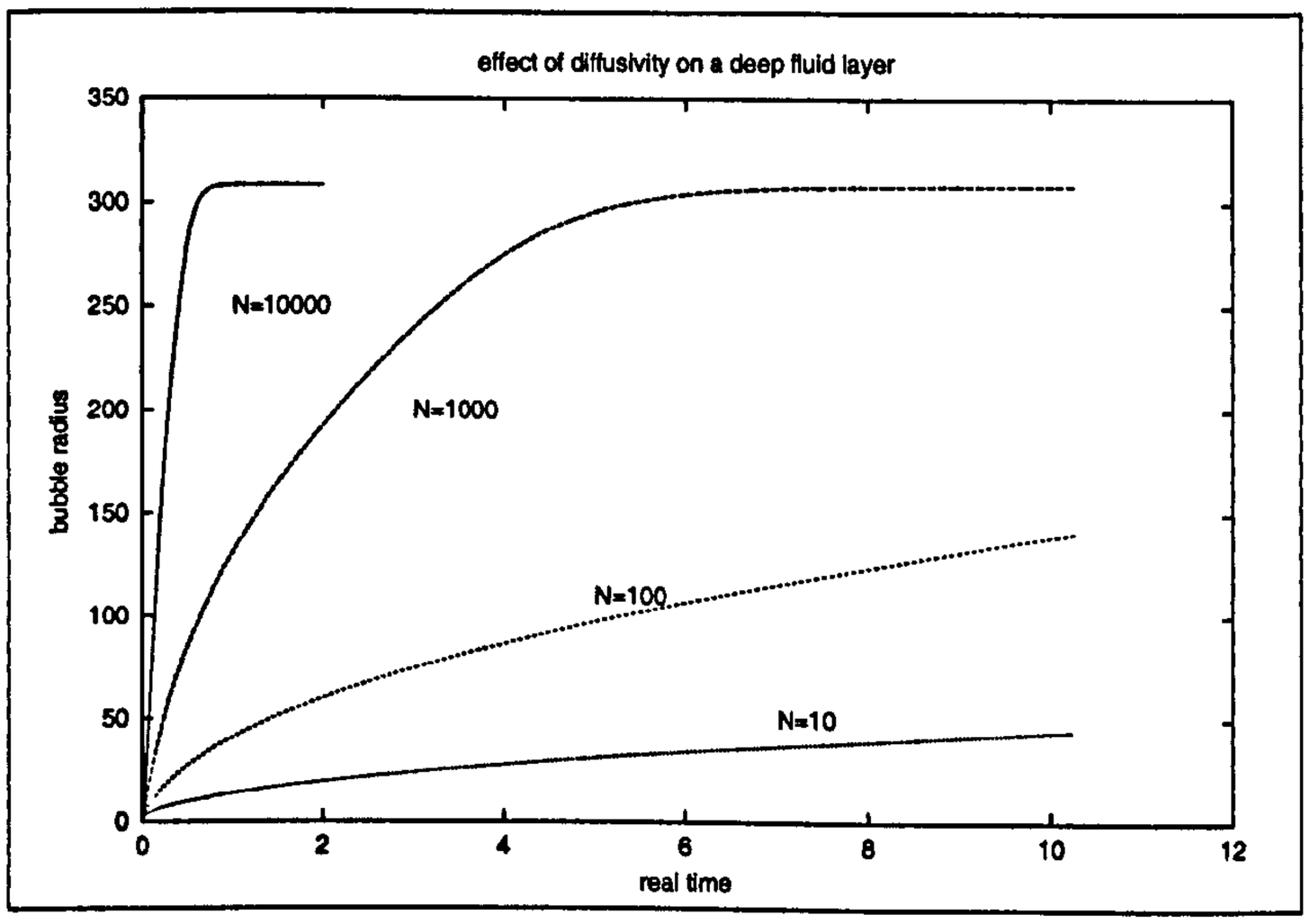


Figure 3.12: Effect of changes in diffusivity, here time is not scaled. $\mu = 0.01, \gamma = 0.1$

### 3.1.4 Bubble Expansion in a Liquid modelled by the Pompom Fluid Model

In this section we outline the modifications required to model expansion of a bubble in a liquid where molecules can be represented by the pompom model described in section 2.3.3. In addition to parameterising the viscous drag and elasticity of the polymer molecules, as in the Oldroyd B model, the pompom model allows the structure of the molecule to be changed via the parameter $h$ which controls the number of arms. We investigate the effects of changing the number of arms and the separation of stretch, $\lambda$, and orientation of the backbone, $\mathbf{A}$, on bubble growth.

Expansion of a bubble surrounded by a pompom liquid requires one extra equation to evolve the stretch of the backbone and orientation of the backbone separately. Now the first normal stress difference $S_{rr} - S_{\theta\theta}$ is given by

$$S_{rr} - S_{\theta\theta} = -2\mu\frac{\dot{u}}{x+u} + \frac{3G\lambda^2}{tr(\mathbf{A})}(A_{rr} - A_{\theta\theta}).$$

and, in the spherical geometry of the expanding bubble, the equation for the evolution of the stretch of the backbone, $\lambda$, is given by

$$\dot{\lambda} = -\frac{4}{3}\frac{\dot{u}}{(x+u)}\lambda\frac{(A_{rr} - A_{\theta\theta})}{(A_{rr} + 2A_{\theta\theta})} - \frac{\tau_b}{\tau_s}e^{2\frac{\lambda-1}{h-1}}(\lambda - 1). \tag{3.25}$$

As in the Oldroyd B model, the evolution equations for $\mathbf{A}$ are given by

$$\begin{aligned}\frac{\partial A_{rr}}{\partial t} &= -\frac{4\dot{u}}{3(x+u)}A_{rr} - (A_{rr} - 1), \qquad (3.26)\\ \frac{\partial(A_{rr} - A_{\theta\theta})}{\partial t} &= \frac{2\dot{u}}{3(x+u)}[(A_{rr} - A_{\theta\theta}) - 3A_{rr}] - (A_{rr} - A_{\theta\theta}).\end{aligned}$$

Since the expression for the stress is modified to include the stretch and orientation separately, the radial component of the momentum equation 3.2 becomes

$$\frac{4}{3}\dot{u}\left[\frac{1}{u} - \frac{1}{X+u}\right] = P_g De + 2\gamma\int_0^X \frac{\lambda^2(A_{rr} - A_{\theta\theta})}{(A_{rr} + 2A_{\theta\theta})(x+u)}dx - \frac{1}{\Gamma u^{\frac{1}{3}}}. \tag{3.27}$$

In equations (3.25) to (3.27) above, time is scaled with the backbone relaxation time, $\tau_b$, while other variables are scaled as in section 3.1.2.

In the limit $N \gg DeX^{2/3}$ gas diffusion is effectively instantaneous and the expansion is controlled by the fluid rheology. The structure of the pompom molecule can be modified by changing the parameter $h$ which controls the number of arms. Increasing the number of arms leads to a slower growth rate which is most apparent at high Deborah numbers. Thus we use a Deborah number of 50 for the figures in this section. Times are scaled with the backbone relaxation time, $\tau_b$, and the stretch relaxation time $\tau_s/\tau_b = 1/3$, other dimensionless numbers and parameter values are given in table 3.2. In figure 3.13 we show the bubble growth rate with $h = 2$, 5 and 10 arms. Early bubble growth for $h = 2$ is similar to that for the Oldroyd B model, as the number of arms is increased and the pompom molecules become less rod-like even this early similarity is lost. The stretch relaxation time, given by $\tau_s e^{-2(\lambda-1)/(h-1)}$, is increased by increasing $h$ since the viscous drag on the molecule ends is increased. Thus the maximum stretch increases (figure 3.14) though the magnitude of the orientation $|A_{rr} - A_{\theta\theta}|/tr(\mathbf{A})$ remains almost unchanged (figure 3.15) as $h$ increases. In figure 3.14 we can see that the molecule is stretched to its finite limit dictated by $\lambda = h$ when $h = 2$.

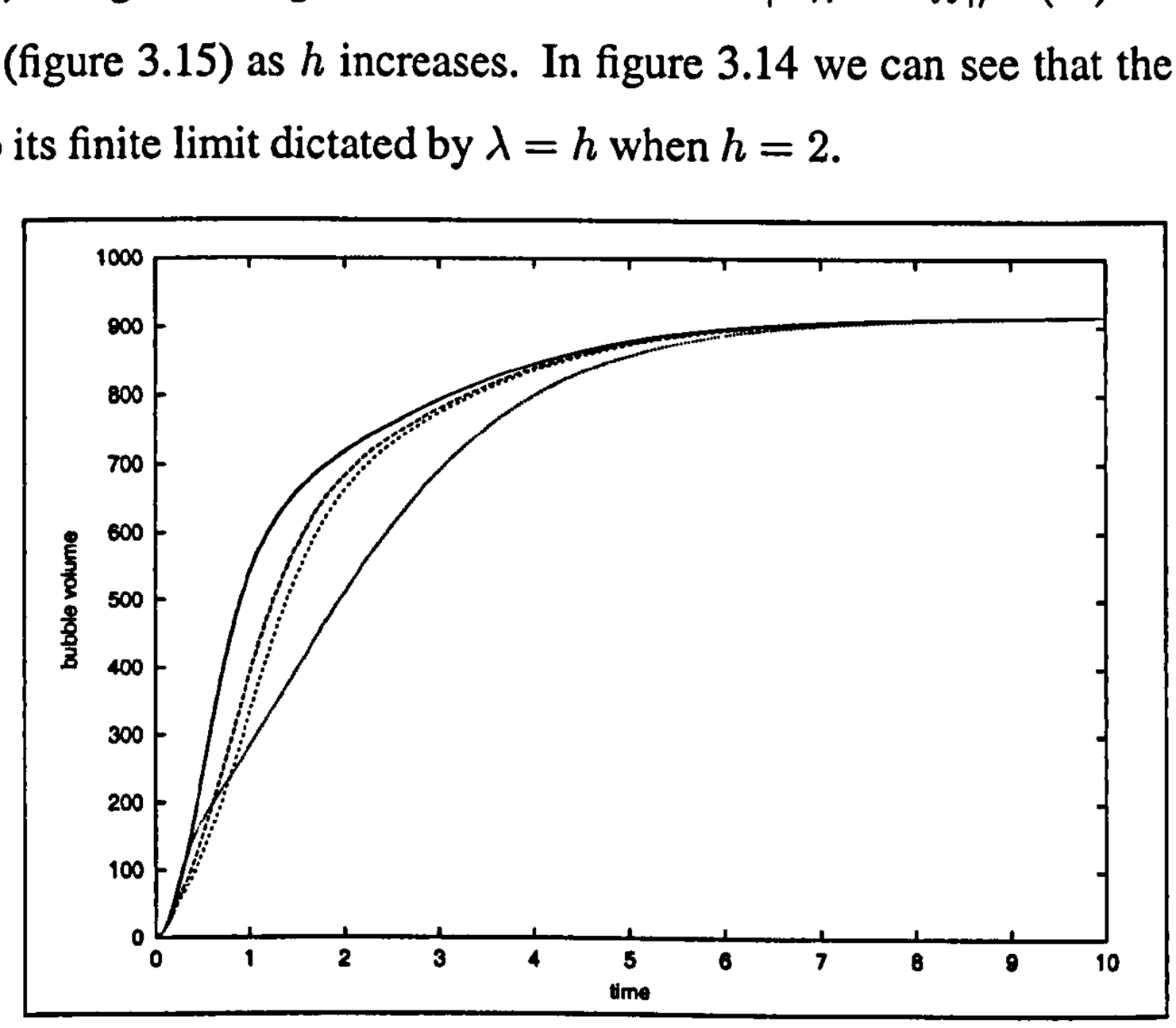


Figure 3.13: Effect of changes in the number of arms on bubble growth rate. Solid line: $h = 2$; long dashed line: $h = 5$; short dashed line: $h = 10$; dotted line: Oldroyd B model. $De = 50$; $\gamma = 5$.

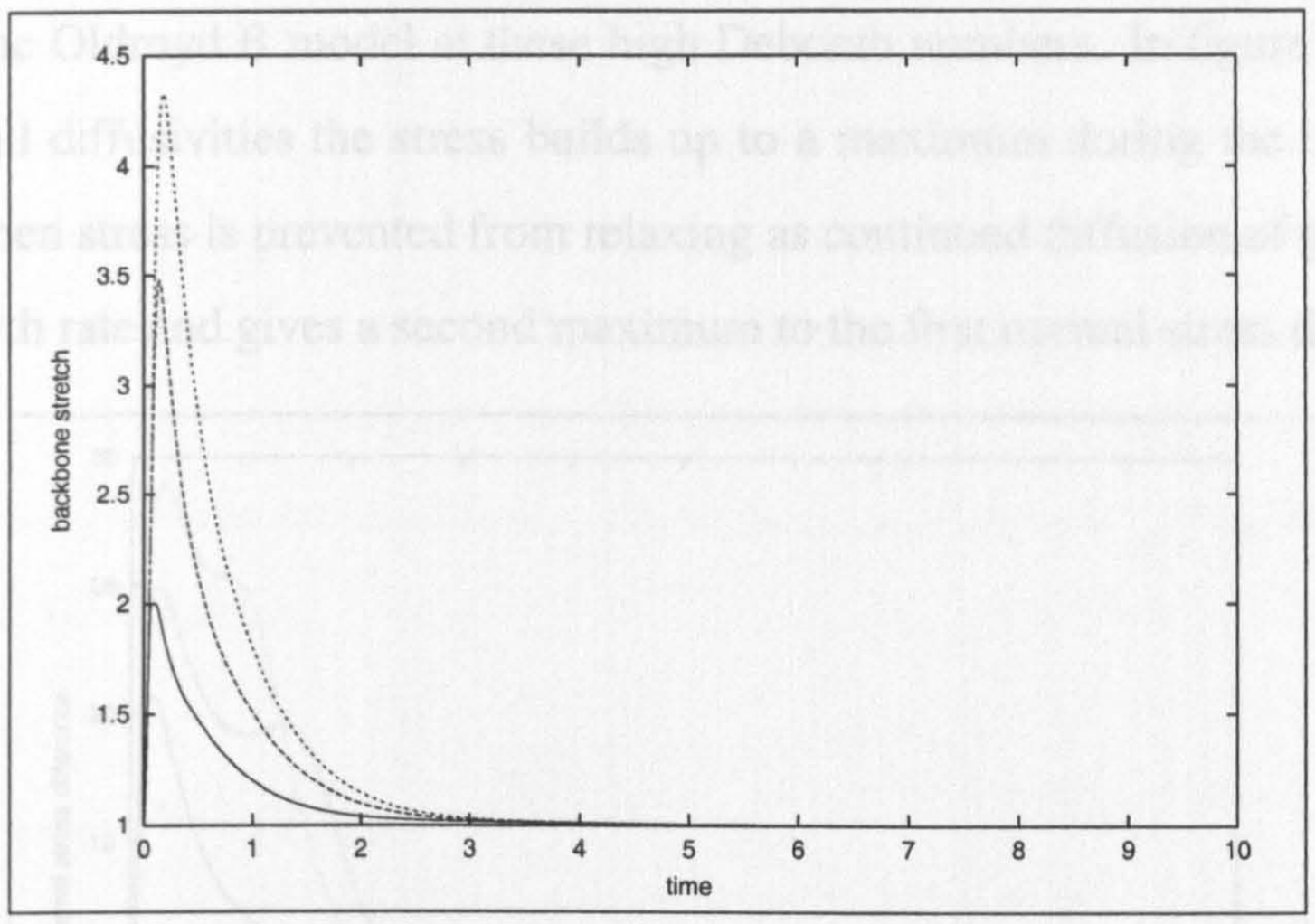


Figure 3.14: Effect of changes in the number of Pompom arms on the stretch, $\lambda$, of the backbone. Solid line: $h = 2$; dashed line: $h = 5$; dotted line: $h = 10$. $De = 50$; $\gamma = 5$.

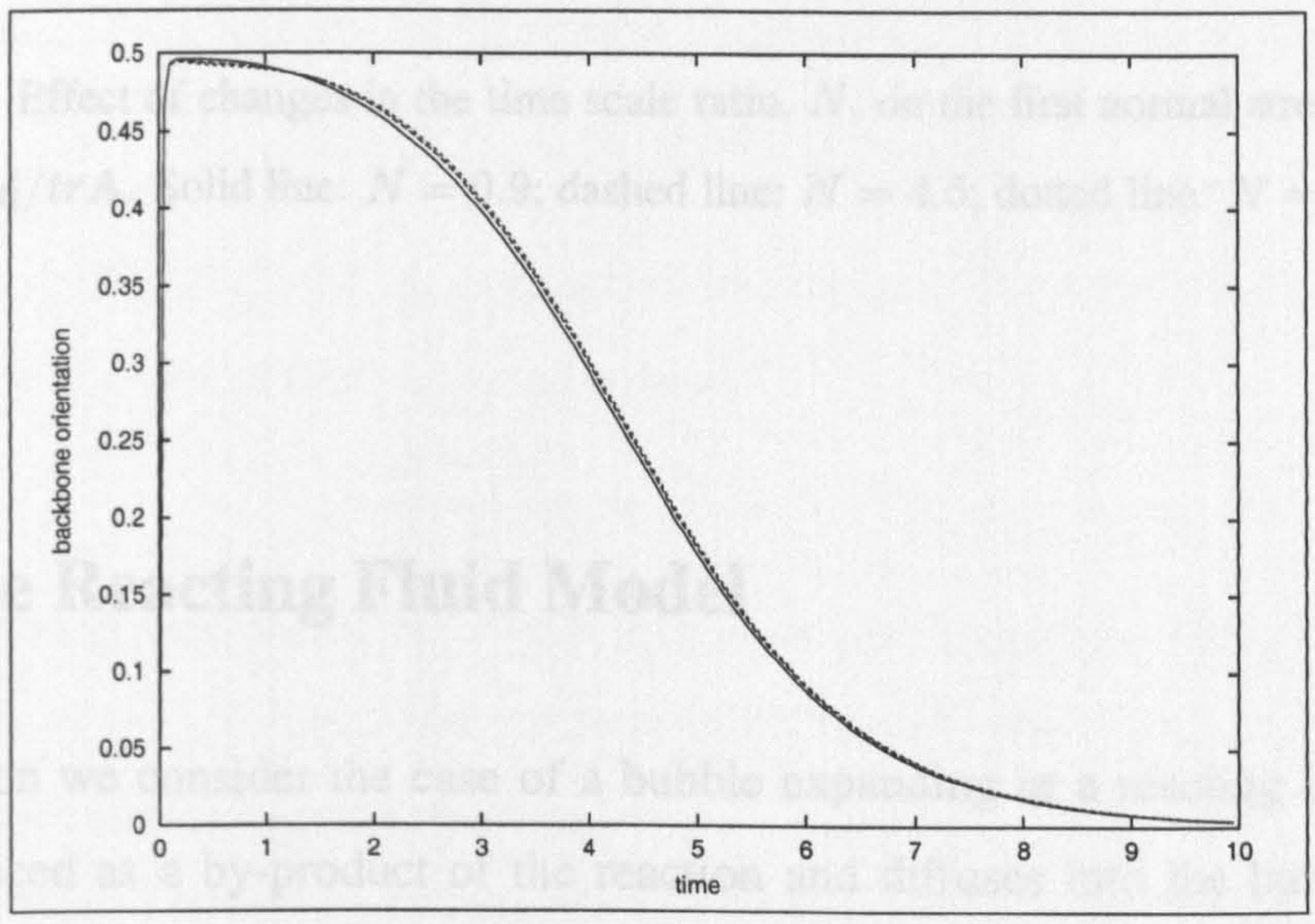


Figure 3.15: Effect of changes in the number of Pompom arms on the orientation, $|A_{rr} - A_{\theta\theta}|/tr(\mathbf{A})$, of the backbone. Solid line: $h = 2$; dashed line: $h = 5$; dotted line: $h = 10$. $De = 50$; $\gamma = 5$.

Finally we note that the effect of diffusivity on the first normal stress difference is similar to that for the Oldroyd B model at these high Deborah numbers. In figure 3.16 we see that for small diffusivities the stress builds up to a maximum during the initial period of growth, then stress is prevented from relaxing as continued diffusion of gas increases bubble growth rate and gives a second maximum to the first normal stress difference.

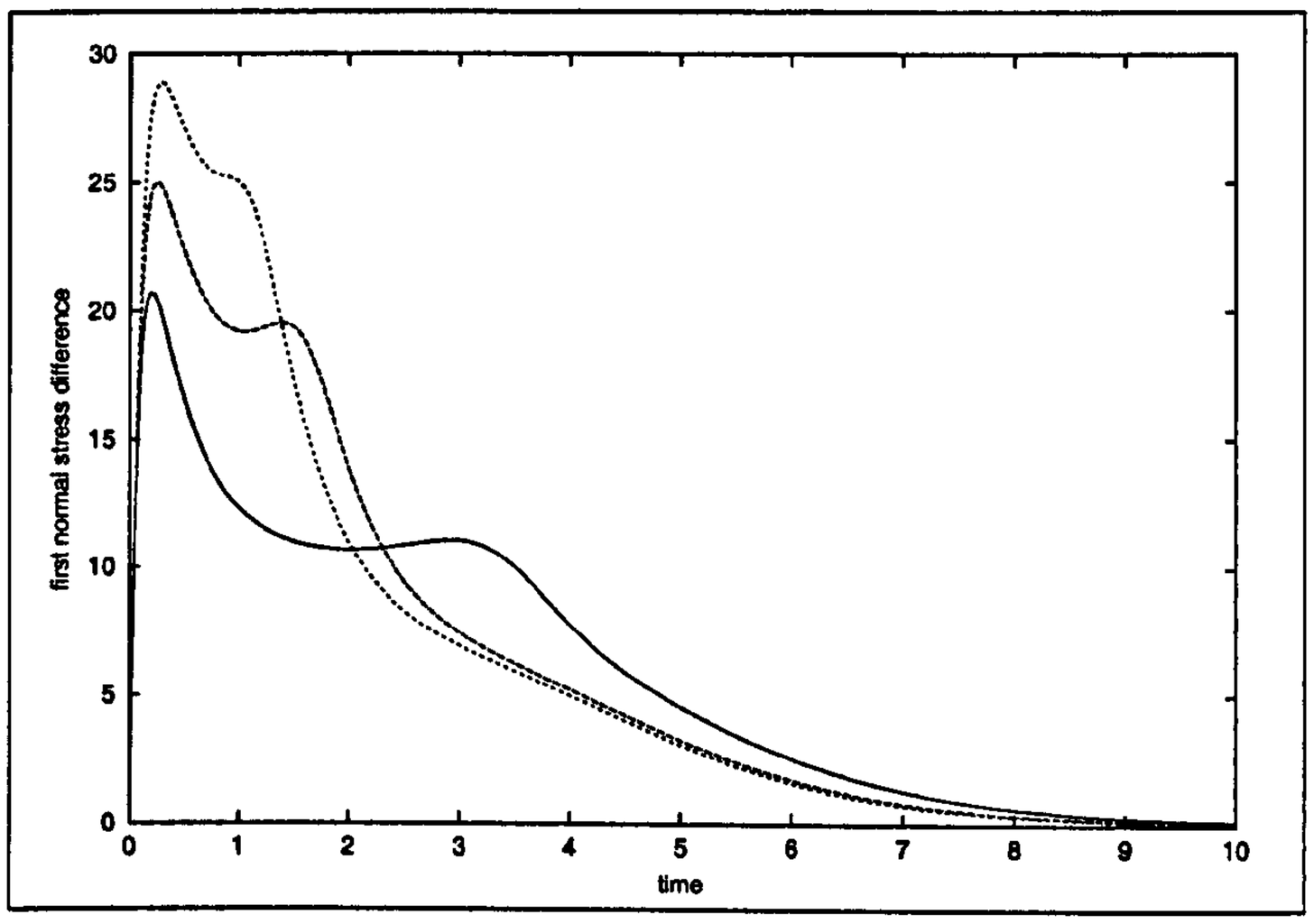


Figure 3.16: Effect of changes in the time scale ratio, $N$, on the first normal stress difference, $3\gamma|A_{rr} - A_{\theta\theta}|/trA$. Solid line: $N = 0.9$; dashed line: $N = 4.5$; dotted line: $N = 9$. $De = 50$; $\gamma = 5$.

## 3.2 The Reacting Fluid Model

In this section we consider the case of a bubble expanding in a reacting liquid where gas is produced as a by-product of the reaction and diffuses into the bubble causing expansion. We detail modifications to the equations of the previous sections and present the method of solution and a summary of results. All equations are given in dimensionless form with the scaling described in section 3.1.2 with the exception of time, which is now scaled with the reaction rate, and the concentration potential, $\phi$ which

is scaled with the amount of gas generated by the reaction. These modifications will be fully described in section 3.2.1. As discussed in section 2.5, the polymer molecules in the liquid begin as a mono-disperse distribution of self-similar molecules. As the reaction progresses molecules bond to form increasingly large, branched, structures each with a spectrum of relaxation modes. The longest relaxation time increases until a gel is formed with a finite elastic modulus but infinite viscosity. The reaction continues until all available end groups have reacted. Throughout this process gas is produced as a by-product of the reaction.

### 3.2.1 Generation of Gas

In this section we describe the additional equation which governs the reaction rate and detail changes to the diffusion equation (3.14) and the conservation of mass equation (3.13) to allow for gas production.

Polymerisation is governed by the following equation, from reference [29], for catalyst, $[C]$, isocyanate, $[NCO]$ and active hydrogen compound, $[OH]$, concentrations:

$$\frac{d[NCO]}{dt} = -k[C]^a[NCO]^b[OH]^c.$$

Here $k = \exp(-E_a/RT)$ and $E_a$ is an activation energy. When the stoichiometric ratio is unity, in the absence of catalyst, this becomes

$$\frac{d[NCO]}{dt} = -k[NCO]^{b+c}$$

where $b + c$ is the order of the reaction which is usually equal to 2. Defining the extent of reaction, $\alpha = 1 - [NCO]$, as the fraction of reacted isocyanate end groups we obtain a second order kinetics equation for $\alpha$ as

$$\frac{d\alpha}{dt} = c_\alpha(1-\alpha)^2.$$

$1/c_\alpha$ is the timescale for the reaction. Scaling time with this timescale, the evolution of the extent of reaction follows the dimensionless equation

$$\frac{d\alpha}{dt} = (1-\alpha)^2. \tag{3.28}$$

We assume that gas is generated at a rate proportional to $\frac{d\alpha}{dt}$, where $\alpha$ is the fraction of reacted end groups at time $t$. The concentration of gas generated is $\varsigma H p_a(\alpha - \alpha_0)$ where $\alpha_0$ is the initial extent of reaction and $\varsigma$ is a dimensionless parameter that dictates the maximum number of moles of dissolved gas per unit volume that could be generated by the reaction. In order to satisfy Henry's law at the bubble surface the initial gas pressure is given by $p_{g0} = p_a(1+\varsigma\alpha_0)$. Scaling the concentration potential, $\phi$, with the number of moles of gas generated by the reaction at completion, $\varsigma H p_a X u_0$, the diffusion equation (3.14) becomes

$$\frac{\partial \phi}{\partial t} = N(x+u)^{\frac{4}{3}}\frac{\partial^2 \phi}{\partial x^2} - \frac{1}{X}\frac{d\alpha}{dt}(X - x). \tag{3.29}$$

The boundary condition (3.15) is

$$\frac{\partial \phi}{\partial x} = \frac{1}{\varsigma X}\frac{p_{g0} - p_a}{p_a}(P_g - 1) \tag{3.30}$$

at the bubble surface and $\partial^2\phi/\partial x^2 = 0$ at $x = X$. The dimensionless group $N = 9D/u_0^{\frac{2}{3}}c_\alpha$ is now the ratio of the gas diffusion rate to the reaction rate. The conservation of mass equation, (3.13), becomes

$$\left(\frac{p_a + (p_{g0} - p_a)P_g}{p_{g0}}\right)u = 1 + \varsigma\Phi\frac{p_a}{p_{g0}}X\left(\phi(0,t) + (\alpha - \alpha_0)\right). \tag{3.31}$$

### 3.2.2 Nonlinear Rheology

In this section we describe how we utilise the results of section (2.5) in the momentum equation (3.10) and stress evolution equations (3.11) and (3.12).

The linear spectrum is discretized into a set of discrete modes given by

$$G(t) = \sum G_k e^{-t/\tau_k}.$$

In order to extend this to nonlinear flows, each mode is treated as a mode in a multimode Oldroyd B fluid so that the first normal stress difference becomes

$$S_{rr} - S_{\theta\theta} = -2\mu\frac{\dot{u}}{x+u} + \sum_k G_k(A_{rr} - A_{\theta\theta})_k.$$

This simple nonlinear extension does not introduce any additional parameters and will be valid provided that molecular strains remain modest so that molecular segments do not extend beyond their maximum length.

For $\alpha < \alpha_c$ we use equation (2.13) to obtain $G_k$. $A_{rr}$ and $A_{rr} - A_{\theta\theta}$ for each mode satisfy

$$\frac{\partial A_{rr}}{\partial t} = -\frac{4\dot{u}}{3(x+u)}A_{rr} - \frac{1}{\tau c_\alpha}(A_{rr} - 1) \tag{3.32}$$

and

$$\frac{\partial (A_{rr} - A_{\theta\theta})}{\partial t} = \frac{2\dot{u}}{3(x+u)}[(A_{rr} - A_{\theta\theta}) - 3A_{rr}] - \frac{1}{\tau c_\alpha}(A_{rr} - A_{\theta\theta}). \tag{3.33}$$

The values of the elastic moduli change during the reaction due to the loss of translational modes and the subsequent gain of internal modes. In addition new modes are 'switched on' as larger molecules are produced. This means that in order to conserve stress we must adjust A for each mode so that when $G$ changes by an amount $\Delta G$,

$$(G + \Delta G)\mathbf{A}_{new} = G\mathbf{A} + \Delta G\mathbf{I}. \tag{3.34}$$

Finally, we sum the modes in the momentum equation (3.10):

$$\frac{4}{3}\dot{u}\left[\frac{1}{u} - \frac{1}{X+u}\right] = P_g M + \frac{2}{3}\gamma \sum_1^{\tau_{ch}/\tau_x} G_k \int_0^X \frac{(A_{rr} - A_{\theta\theta})_k}{x+u} dx\, d(ln\tau) - \frac{1}{\Gamma u^{\frac{1}{3}}}. \tag{3.35}$$

Here $M = (p_{g0} - p_a)/\mu c_\alpha$ is the ratio of the bubble growth rate in the solvent to the reaction rate, $\gamma = G_0/\mu c_\alpha$ and $\Gamma = u_0^{1/3}\mu c_\alpha/2S$.

For $\alpha > \alpha_c$ we consider separately the relaxing modes with $\tau < \tau_{ch}$ and the single gel mode which corresponds to an elastic solid. For $\tau < \tau_{ch}$ we obtain expressions for $G$ for each mode from the first term on the right hand side of (2.14), since these modes can relax $A_{rr}$ and $A_{rr} - A_{\theta\theta}$ for each mode satisfy (3.32) and (3.33). The gel mode is equivalent to the non-relaxing modes with $\tau > \tau_{ch}$ in equation (2.14) so we use the second term of equation (2.14) to obtain the $G_k$. These modes do not relax and so $A_{rr}$ and $A_{rr} - A_{\theta\theta}$ for each mode satisfy equations (3.32) and (3.33) with $\tau = \infty$. The increase in modulus of this mode with extent of reaction can be attributed to three sources: first from the translational modes of molecules attaching to the gel; second from modes near

$\tau_{ch}$ in these molecules, which are frozen as they attach to the gel; and third from modes already in the gel which become frozen as $\tau_{ch}$ changes. Hence, as $\alpha$ increases and $\tau_{ch}$ decreases past the gel point, all modes with $\tau > \tau_{ch}$ are switched from the sol to the gel fraction. Both their modulus, $\Delta G_{off}$, and their stress, $\Delta G_{off} A_{off}$, are added to the gel mode accounting for contributions two and three above. The contribution from the translational modes corresponds to an additional stress contribution $\Delta G_{gel}\mathbf{I}$. Thus, for the gel mode,

$$(G_{gel} + \Delta G_{gel} + \Delta G_{off})\mathbf{A}_{new} = G_{gel}\mathbf{A} + \Delta G_{gel}\mathbf{I} + \Delta G_{off}\mathbf{A}_{off}. \tag{3.36}$$

The sum in the momentum equation now includes a gel term with $\tau = \infty$ in addition to the terms from $\tau_x < \tau < \tau_{ch}$.

Equations (3.28) for the reaction rate; (3.29) for gas diffusion; (3.31) for bubble gas pressure; (3.32), (3.33) and (3.34) for the elastic stresses; (3.35) for the bubble growth rate; and (2.15) and (2.16) for the evolution of the shortest relaxation rate provide a dimensionless equation set governing bubble growth in a gelling system. Here time is scaled with the reaction time, $\phi$ with the total number of moles of gas produced by the reaction at completion and bubble gas pressure and lengths are scaled as in section 3.1.2. The method of solution is that described in section 3.1.3. Numerically, we find that twenty modes per decade give a sufficiently accurate description of the viscoelastic spectrum.

### 3.2.3 Effects on Bubble Growth

In this section we describe the effects of the competing timescales on bubble growth. Tables 3.4 and 3.5 outline the parameters used to generate the figures in addition to those in the previous section and the dimensionless groups arising in the formulation of the reacting model. The definitions differ from those in table 3.1 since time here is scaled with the reaction time $1/c_\alpha$.

We now consider the growth rate of a bubble in a reacting polymer in which gas is

| parameter | | value | units |
|---|---|---|---|
| molar mass of initial polymers | $m_x$ | 0.5 | kg mol$^{-1}$ |
| relaxation rate of initial polymers | $\tau_x$ | 0.00133 | s |
| liquid density | $\rho$ | 1200 | kg m$^{-3}$ |
| rate of reaction | $c_\alpha$ | 1, 10 | s$^{-1}$ |
| $\frac{\text{max. gas concentration produced by reaction}}{\text{background gas concentration}}$ | $\varsigma$ | 10 | - |
| extent of reaction at the gel point | $\alpha_c$ | 0.91 | - |
| extent of reaction at nucleation | $\alpha_0$ | 0.1 | - |
| molecular weight distribution, $n(m)$, exponent | $\nu$ | 2.2 | - |
| largest molecular weight scaling exponent | $\sigma$ | 0.45 | - |
| fractal dimension of the equilibrium coil size of a molecule | $d_f$ | 2.5 | - |
| solvent viscosity | $\mu$ | 0.1 | $10^5$Ns m$^{-2}$ |

Table 3.4: Additional parameters used for bubble expansion in a reacting polymer for figures 3.17–3.23.

| | | |
|---|---|---|
| $M = \frac{(p_{g0}-p_a)}{\mu c_a}$ | 10, 1 | ratio of the rate of bubble growth in the solvent to the reaction rate |
| $\gamma = \frac{G_0}{\mu c_a}$ | 738, 73.8 | |
| $\Gamma = \frac{u_0^{\frac{1}{3}} \mu c_a}{2S}$ | $\infty$ | ratio of viscous force to surface tension |
| $N = \frac{9D}{u_0^{\frac{4}{3}} c_a}$ | $0.9 \rightarrow \infty$ | ratio of the rate of gas diffusion to the reaction rate |
| $\Phi = RTH$ | 0.32 | |
| $X$ | 53.6 | dimensionless fluid volume |

Table 3.5: Dimensionless groups arising in the non-dimensional formulation of the equations governing bubble growth in a gelling system together with the values for figures 3.17–3.23.

produced as a reaction by-product.

As in the non-reacting model the rate of diffusion of gas is of order

$$\frac{9D}{(u_0 X)^{\frac{2}{3}}}$$

while the initial bubble expansion rate is of order

$$\frac{\varsigma p_a \alpha_0}{\mu}.$$

There is now a third timescale, the reaction rate $c_\alpha$, which determines both the production of gas and the evolution of the fluid rheology. Here we describe how the balance of these timescales controls bubble growth dynamics. For simplicity we have assumed that the gas diffusion constant, $D$, is independent of the extent of reaction. Although there will be a change in diffusivity between the initial and final states of the material, most of the gas is produced in the early stages of the reaction and in most cases diffusion takes place well before the gel point.

The initial phase of bubble growth is controlled by supply of gas into the bubble. There are now two distinct sources of gas available to drive bubble growth. First, some gas

is present in the liquid initially and will immediately begin to diffuse into the bubble. Second, gas will be produced within the liquid as the reaction progresses and, if the production rate exceeds the rate of transport into the bubble, the gas concentration in the liquid will increase with time. If gas diffusion is slow compared to the initial bubble expansion rate there is an initial drop in the gas pressure inside the bubble as it expands. However, as the excess gas produced by the reaction diffuses into the bubble we see an increase in gas pressure (see figure 3.17). The bubble gas pressure only begins to fall once the reaction rate decreases and the gas concentration in the fluid decays. A distinct change in bubble growth rate can be seen around $t = 2.5$ for $N = 9$ and $t = 1$ for $N = 90$ in figure 3.18 as excess gas has diffused into the bubble and the expansion changes from being controlled by gas diffusion to gas production. Increasing the diffusivity increases the rate at which gas is transported into the bubble. This produces an increase in the bubble gas pressure at early times and a consequent increase in the rate of bubble growth (figures 3.17 and 3.18).

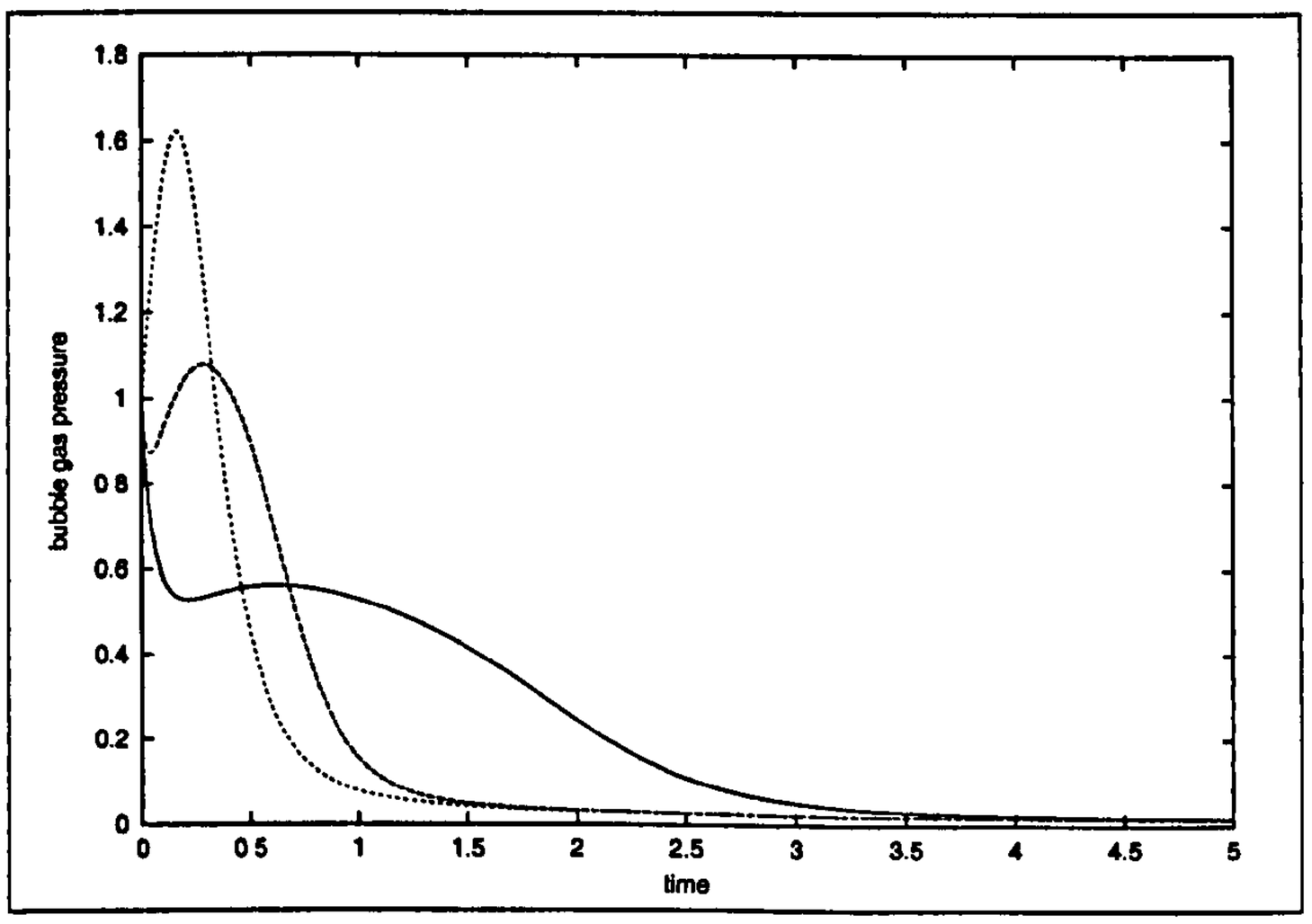


Figure 3.17: Effect of diffusivity on dimensionless bubble gas pressure when $M = 10$. Solid line: $N = 9$; dashed line: $N = 90$; dotted line shows the limit of infinite diffusion.

Comparing figures 3.6 and 3.19 we see the effect of the polymerisation on the elastic stress. For a non-reacting system, figure 3.6, reducing the diffusivity (and hence the

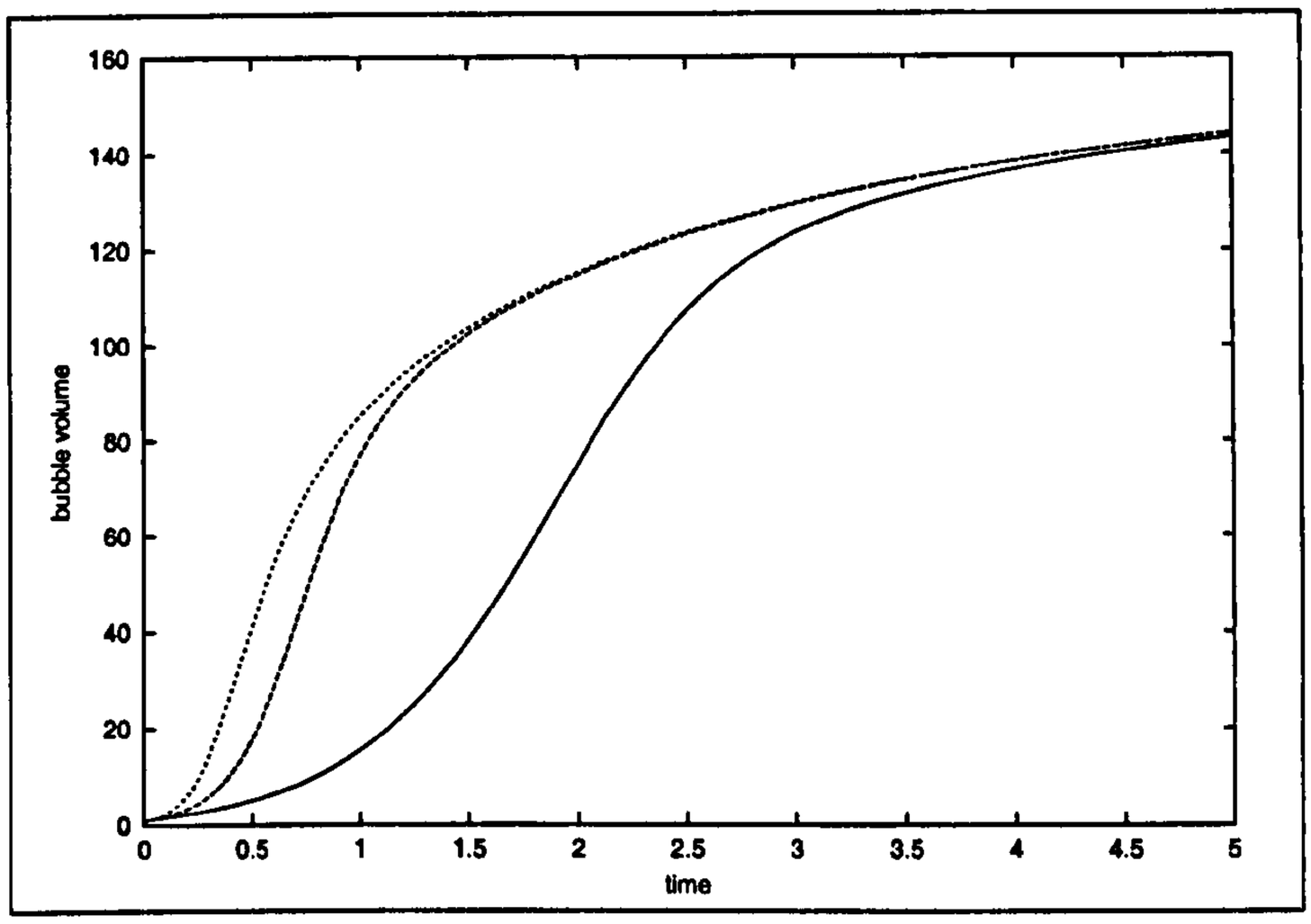


Figure 3.18: Effect of diffusivity on bubble growth when $M = 10$. Solid line: $N = 9$; dashed line: $N = 90$; dotted line shows the limit of infinite diffusion.

bubble growth rate) produced a much lower first normal stress difference. However, in figure 3.19 we see that the main effect of diffusivity is to delay the point of maximum first normal stress difference with relatively little change in the magnitude. Although a lower diffusivity reduces the bubble expansion rate at early times, it delays the maximum rate of expansion to times when the molecular weight is larger and so the fluid is more viscoelastic.

In the three cases shown in figures 3.17, 3.18 and 3.19 the final bubble volume is independent of diffusivity. In these cases the rate of the reaction is sufficiently slow for the gas pressure to reach equilibrium before the gel point is reached. At faster reaction rates the gas bubble will not have reached its equilibrium size before gelation and so the equilibrium bubble volume will depend on the values of $N$ and $M$ (see figure 3.21). The asymptotes given by the limit of infinite diffusivity in figure 3.20 show that the ratio of the bubble expansion rate to reaction rate, $M$, dictates a maximum equilibrium volume. The ratio of the rate of gas diffusion to reaction rate, $N$, dictates the proportion of that volume achieved. Figures 3.22 and 3.23 show the increase in gas pressure and first normal stress difference caused by continued gas diffusion after the gel point when

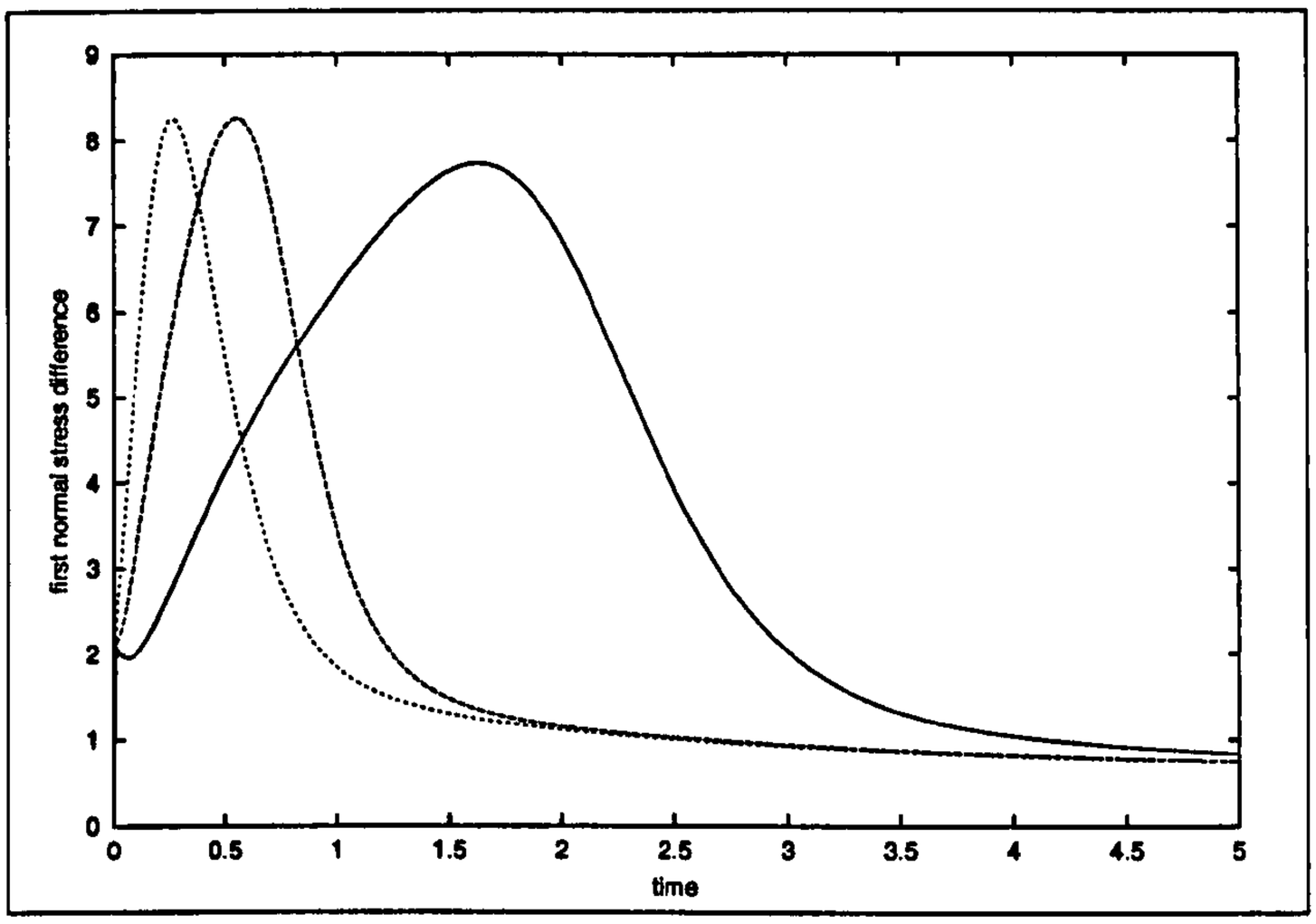


Figure 3.19: Effect of diffusivity on the magnitude of the first normal stress difference, $|\gamma \sum G(k)(A_{rr}(k) - A_{\theta\theta}(k))|$, when $M = 10$. Solid line: $N = 9$; dashed line: $N = 90$; dotted line shows the limit of infinite diffusion.

the diverging fluid rheology prevents further bubble growth. The slower the rate of gas diffusion the greater the increase in gas pressure and first normal stress difference since a smaller amount of gas had diffused into the bubble prior to gelation.

Increasing $\gamma$ increases the viscosity of the liquid throughout the reaction and so decreases the equilibrium bubble volume while increasing the magnitude of the first normal stress difference and the equilibrium gas pressure. This effect is much more pronounced at high reaction rates. Increasing $\alpha_0$, the extent of reaction when the bubble nucleates, increases the initial gas pressure in the bubble and so the equilibrium bubble volume at completion of the reaction is increased.

## 3.3 Justification of the Full Reacting Model

In this section we justify the complexity of our reacting model by comparing the results for bubble expansion using this model with results generated by using two simplified models. In our reacting model we add new relaxation modes as the longest relaxation

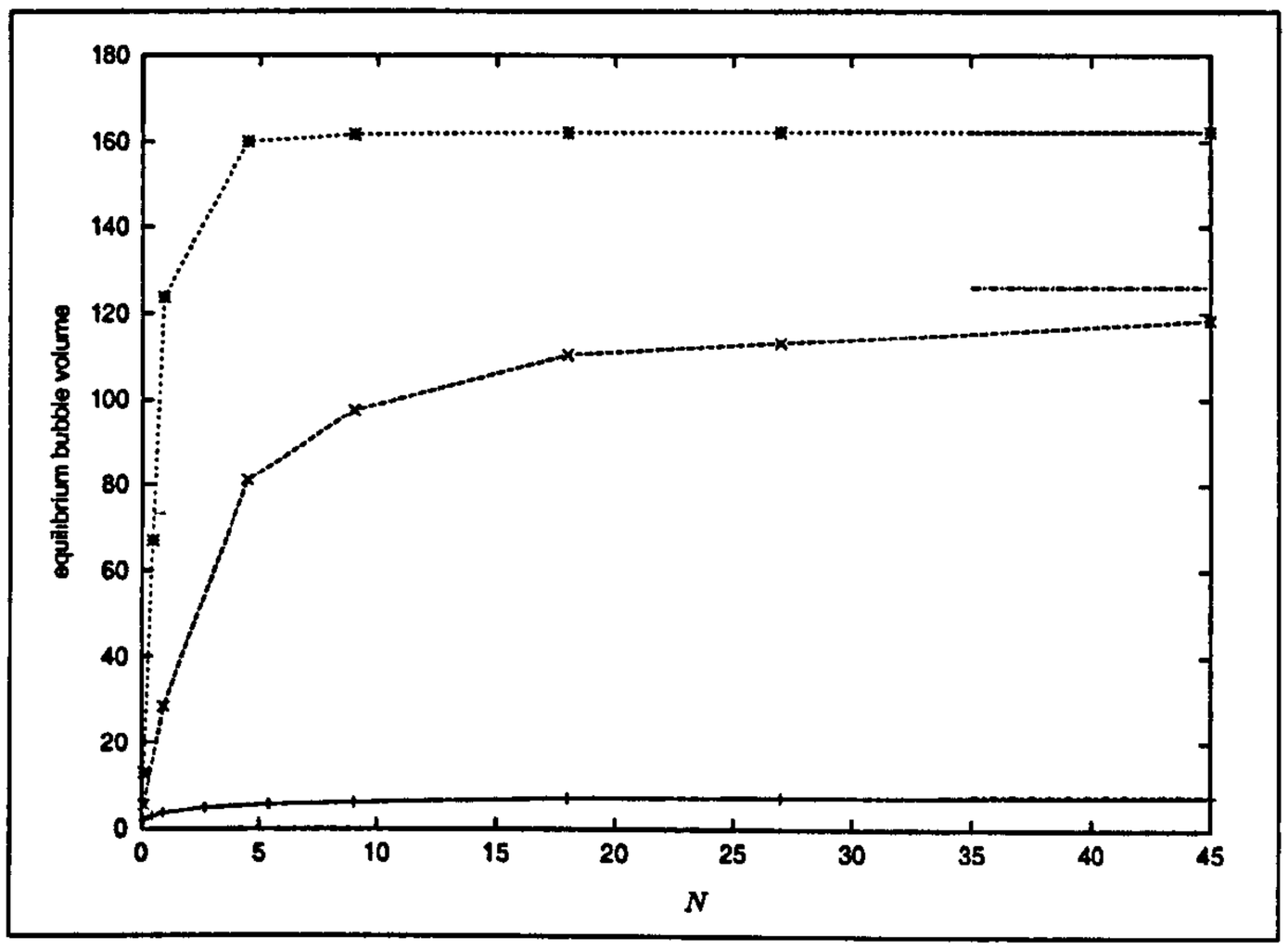


Figure 3.20: Effect of varying the values of the ratio of the rate of diffusion to the reaction rate, $N$, and the ratio of the bubble growth rate to the reaction rate, $M$, on the equilibrium bubble volume. Solid line: $M = 0.1$; dashed line: $M = 1$; and dotted line $M = 5$.

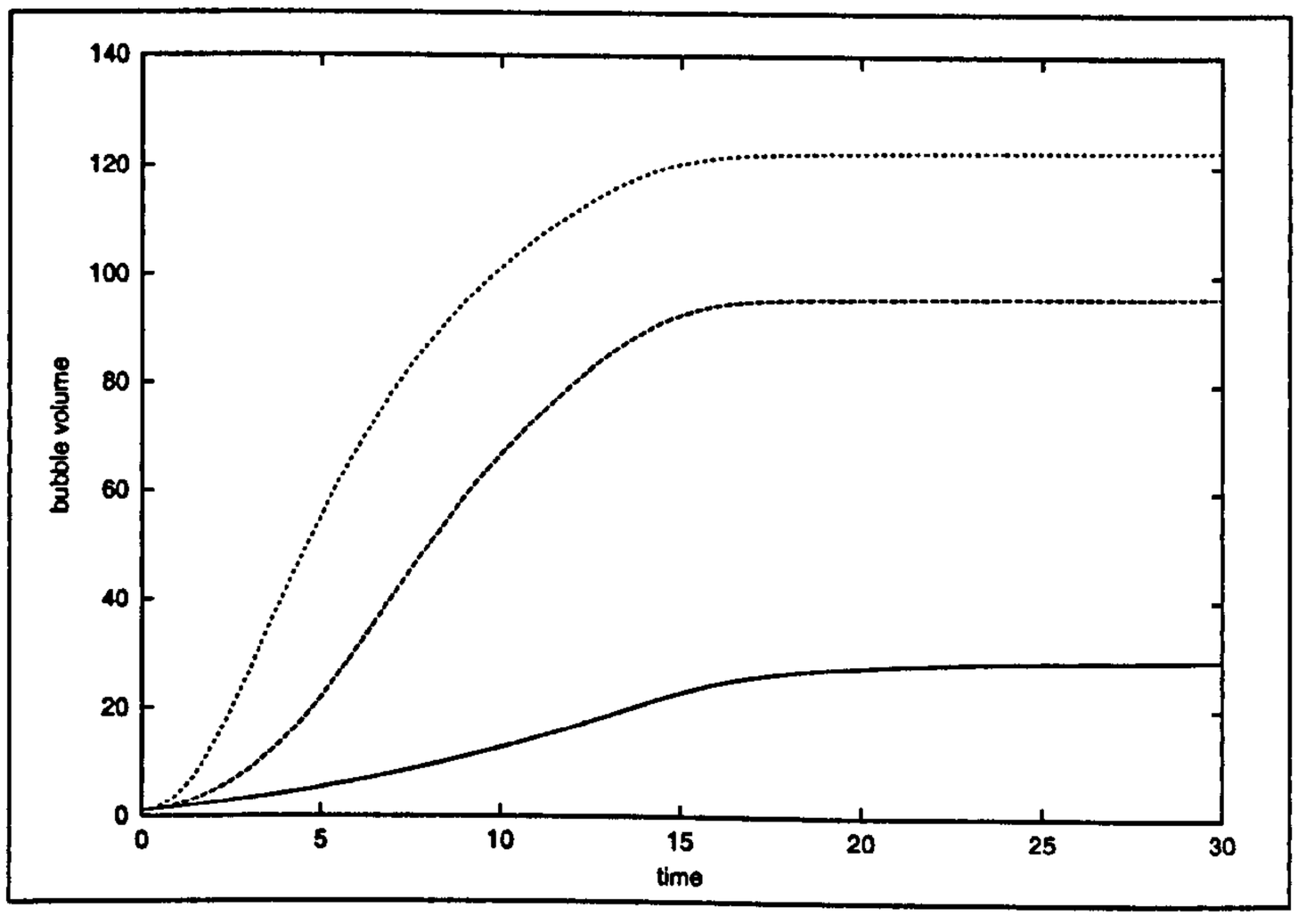


Figure 3.21: Effect of diffusivity on bubble growth when $M = 1$ and $\gamma = 73.8$. Solid line: $N = 0.9$; dashed line: $N = 9$; dotted line shows the limit of infinite diffusion.

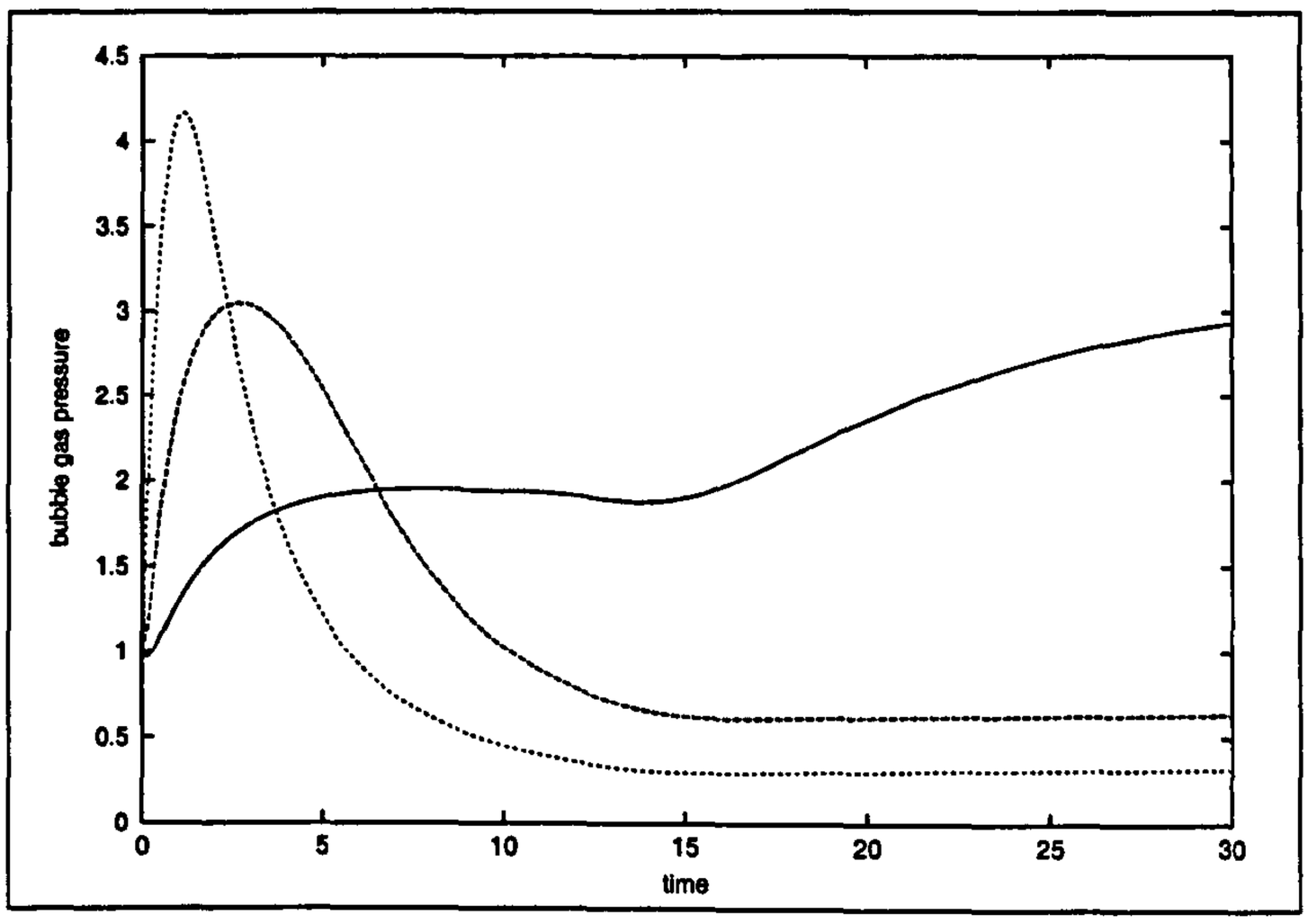


Figure 3.22: Effect of diffusivity on dimensionless bubble gas pressure when $M = 1$. Solid line: $N = 0.9$; dashed line: $N = 9$; dotted line shows the limit of infinite diffusion.

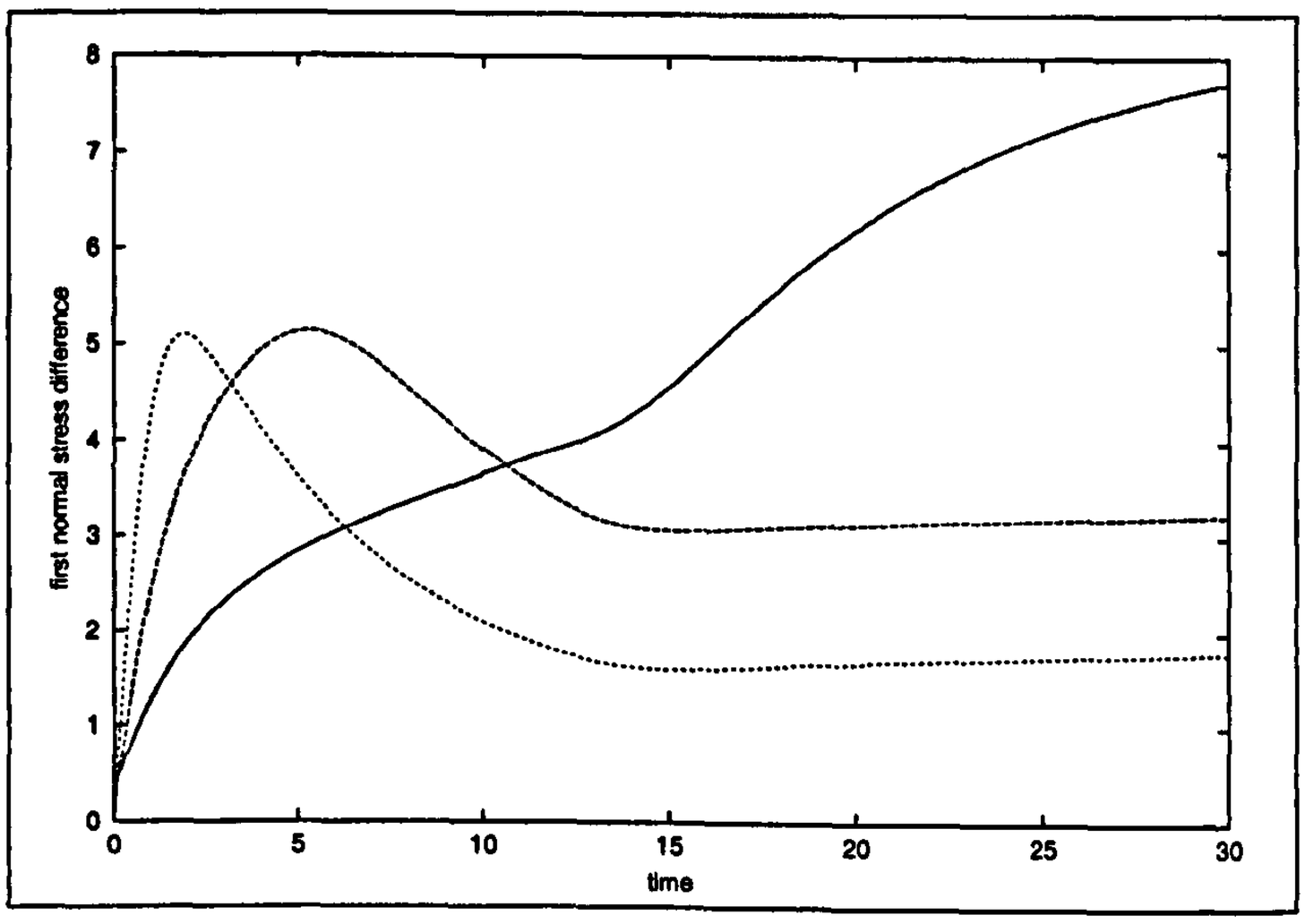


Figure 3.23: Effect of diffusivity on the magnitude of the first normal stress difference, $|\gamma \sum G(k)(A_{rr}(k) - A_{\theta\theta}(k))|$, when $M = 1$. Solid line: $N = 0.9$; dashed line: $N = 9$; dotted line shows the limit of infinite diffusion.

time increases. In the diagrams presented in the previous section we discretize the relaxation spectrum by $\tau_k = \tau_x e^{-k\times\delta k}$ where $k$ is an integer. Thus, $\delta k = 0.1$ gives approximately 20 modes per decade and up to 400 relaxation modes in total. When this is applied across a number of discrete fluid shells in the case of the spherical bubble, or elements as described in figure 4.2 as in the case of the hexagonal bubble geometry, there is a significant time penalty compared to the single mode calculations of section 3.1. In figure 3.24 we compare the bubble expansion, as far as the gel point, at a reaction rate of 10 ($M = 1$), with differing numbers of modes per decade. It can be seen that 1 mode per 5 decades gives a very poor degree of accuracy. The plateau regions correspond to the addition of new modes.

Though using 1 mode per decade reduces the computational time without a significant loss of accuracy, it would be beneficial to provide a simple one or two mode model that could predict bubble expansion to a reasonable degree of accuracy. The simplest model for a reacting fluid might be that of a generalized Newtonian fluid with viscosity that increases with the extent of reaction. We use a viscosity equivalent to the total viscosity of the full reacting model outlined in section 2.5.2. As the reaction approaches the critical extent of reaction the longest relaxation time and, hence, the viscosity, diverge to infinity. The elasticity of the material allows the bubble to continue expanding beyond this point. However if the fluid was Newtonian with increasing viscosity, the diverging viscosity would halt bubble expansion at the gel point. At low reaction rates most of the bubble expansion takes place before the gel point while the molecules are small and stress relaxes quickly. When the reaction rate, $c_\alpha = 1$, the Newtonian model gives a reasonable approximation, particularly at early times as can be seen in figure 3.25. At high reaction rates the molecules increase in size quickly and so the elasticity of the material becomes significant. In figure 3.26 the reaction rate, $c_\alpha = 10$, and we see that the Newtonian model gives a poor description of bubble expansion except at very early times.

In order to improve the prediction without making the model very much more complex we devised a model that incorporates the early time accuracy of the generalized

Newtonian model with the late time necessity of an elastic model. At early times we use an increasing Newtonian viscosity, as above, with no elastic contribution. At later times the Newtonian viscosity remains constant and we introduce a single Oldroyd B mode with increasing relaxation time equal to $\tau_{ch}$ and elastic modulus, $G$ fixed to give the correct viscosity as section 2.5.2. After the gel point the gel mode is added by a second mode with infinite relaxation time. As the longest relaxation time drops we revert to a decreasing Newtonian viscosity and no elastic contribution. Figure 3.25 shows that at low reaction rates the point at which the elastic mode contributes can be adjusted to give a very close fit. However, at high reaction rates figure 3.26 shows that the predictions are still poor. The generalized Newtonian model gives a very poor fit due to the rapid increase in viscosity. Expansion starts up again after the gel point as the viscosity of the sol fraction decreases as an increasing fraction of the material becomes gel. The single Oldroyd B mode model gives a slightly better fit until well after the gel point.

The above models justify use of the full reacting model at high reaction rates while providing a fast approximate prediction of bubble expansion at low reaction rates.

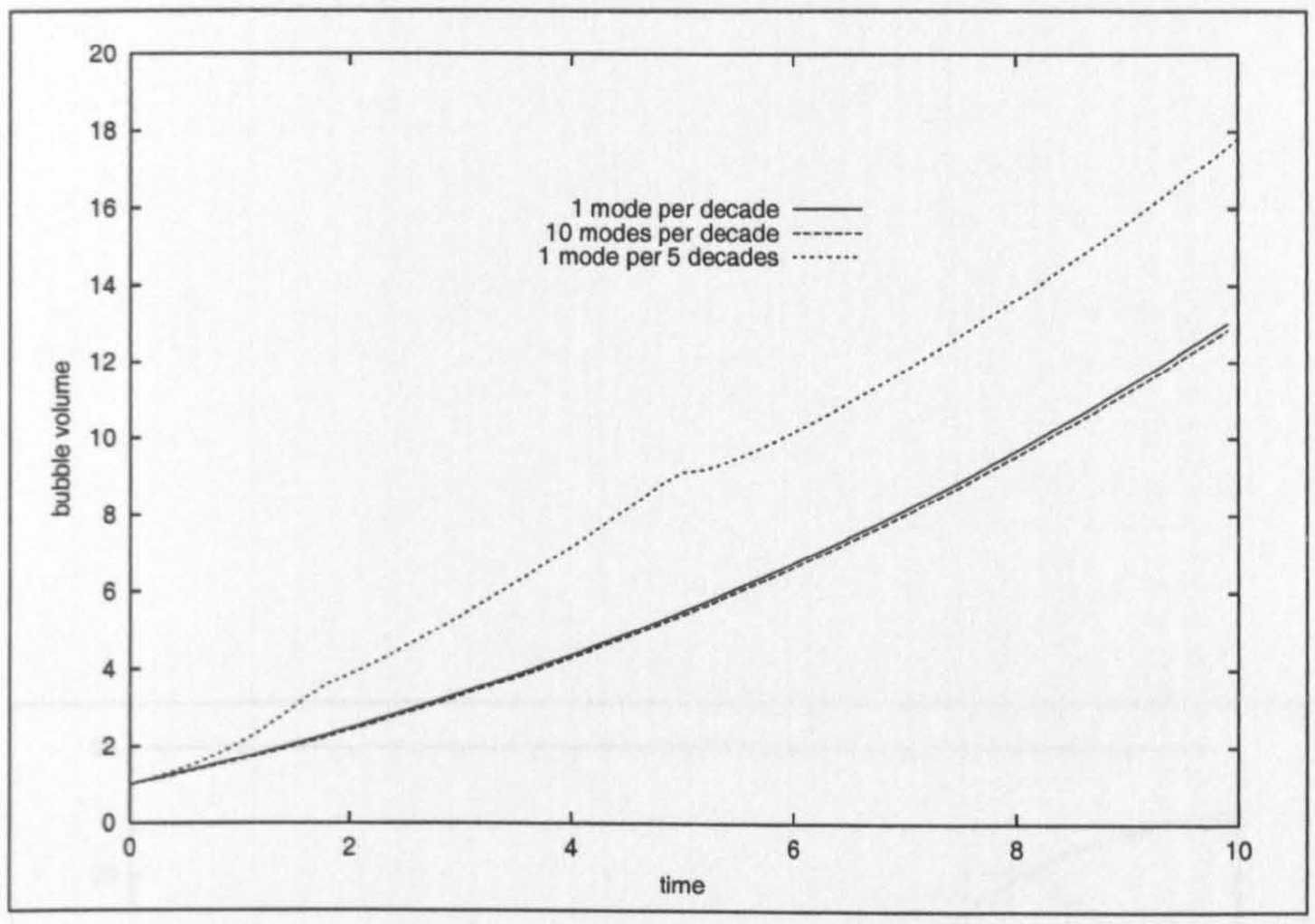


Figure 3.24: Comparison of different mode densities on bubble expansion using the full reacting model.

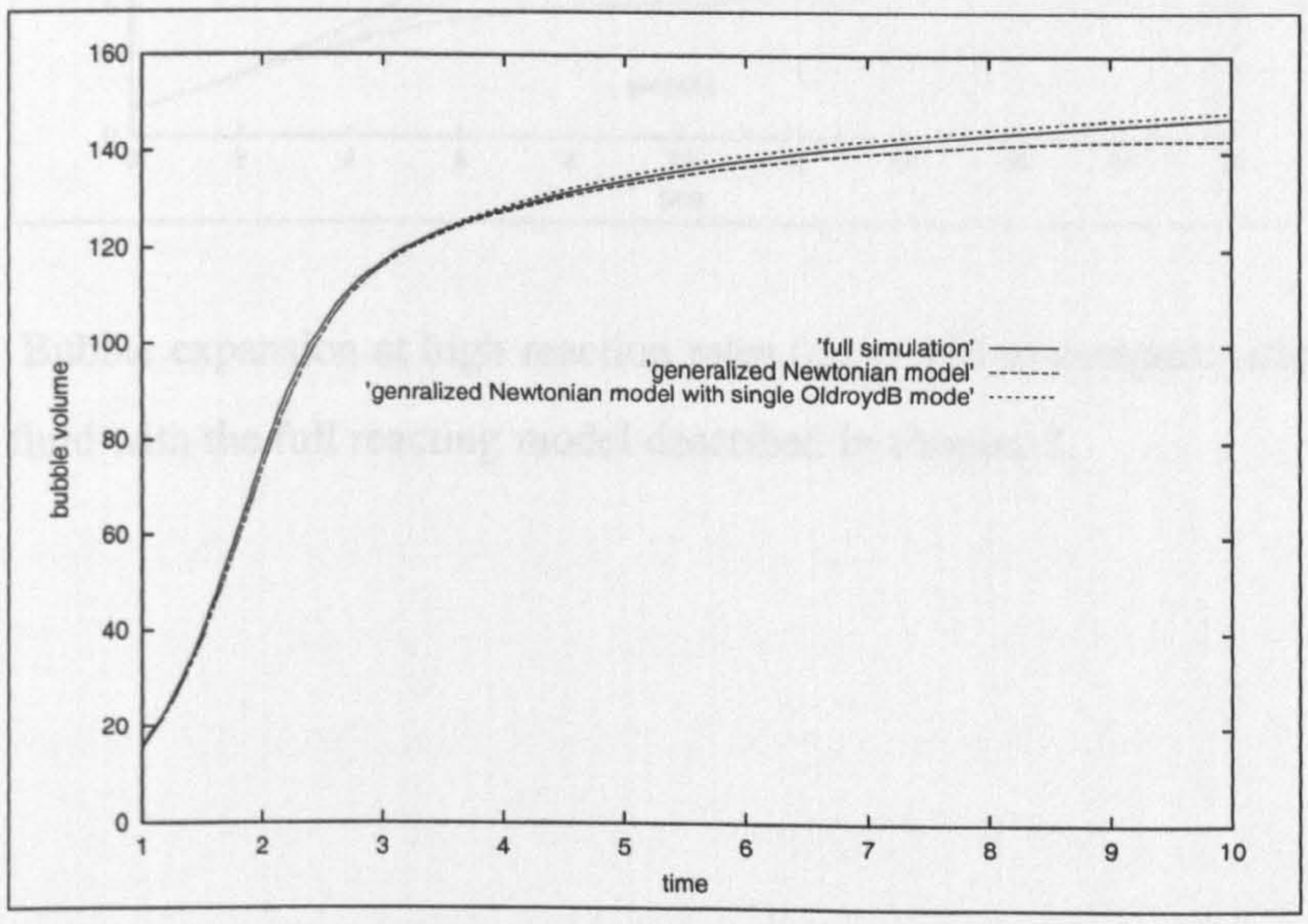


Figure 3.25: Bubble expansion at low reaction rates ($c_\alpha = 1$) to compare simplified models for a reacting fluid with the full reacting model described in chapter 2.

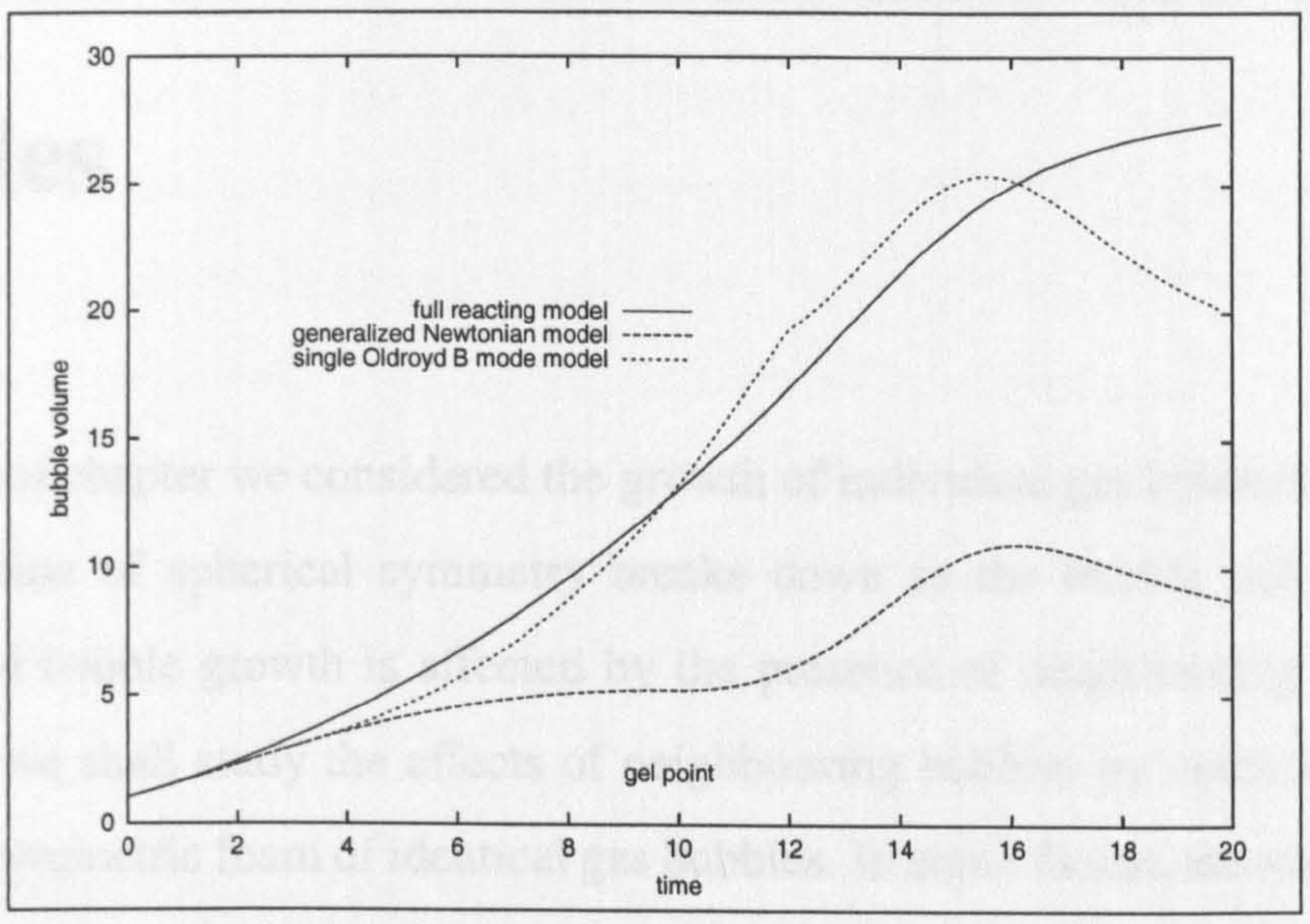


Figure 3.26: Bubble expansion at high reaction rates ($c_\alpha = 10$) to compare simplified models for a reacting fluid with the full reacting model described in chapter 2.

# Chapter 4

# Analysis of the Window Between Two Bubbles

In the previous chapter we considered the growth of individual gas bubbles in isolation. The assumption of spherical symmetry breaks down as the bubble volume fraction increases and bubble growth is affected by the presence of neighbouring bubbles. In this chapter we shall study the effects of neighbouring bubbles by considering bubble growth in a symmetric foam of identical gas bubbles. In static foams, the surface tension forces acting on the films separating neighbouring bubbles must be in equilibrium at the Plateau borders where films meet. Thus, in a two dimensional foam three films joined at a common line must meet at 120°. Consequently we can construct a symmetric two-dimensional foam from a hexagonal array of cells. In section 4.1 we shall compare the solution of the full two-dimensional equations governing bubble growth using a finite element method with two approximations. The first approximation is that of circular symmetry — section 4.1.2. The second is the opposite extreme: a one-dimensional approximation of a two-dimensional hexagonal array of bubbles separated by thin liquid windows — section 4.1.3. We compare the solutions obtained from the three methods and provide estimates of when each of the two approximations are useful.

In three dimensions four films meet at angles of 109.47°. Unlike the two-dimensional

case, it is not possible to construct a symmetric three-dimensional foam with planar faces. Kelvin showed that space can be partitioned into identical cells with equal volume and minimal surface area. The resulting cell is a tetrakaidecahedron which has six planar quadrilateral faces and eight nonplanar hexagonal faces. However, in practice pentagonal faces are dominant [27]. Although we will not solve the full three-dimensional flow problem, in view of the geometric differences between two and three dimensional bubble growth, in section 4.3 we study two axisymmetric models that model the stretching of a strut in an open cell foam and the expansion of a circular window between bubbles in a closed cell foam.

Throughout this chapter we shall assume that the expansion rate is sufficiently small that fluid inertia may be neglected, bubble growth is isothermal, and the bubble-fluid interface remains in thermodynamic equilibrium. We shall use two different constitutive models for the liquid phase. First we use the Oldroyd B model to determine the effect of viscoelasticity on bubble growth in a non-reacting polymer foam. Second, we model a reacting foam where the rheology changes as the reaction progresses using the model for a gelling liquid from chapter 2.

## 4.1 Bubble Growth in a Two Dimensional Hexagonal Lattice

We consider a symmetrical two-dimensional arrangement of bubbles in a hexagonal lattice. Due to the symmetry of this system we only need to perform calculations on a triangular region that makes up 1/12 of the hexagonal cell, shown in figure 4.1. Bubble expansion is, again, driven by a difference in pressures between the gas pressure inside the bubble, $p_g(t)$ and ambient pressure outside the system, $p_a$.

Neglecting inertia the momentum equation gives

$$\nabla \cdot \boldsymbol{\sigma} = 0, \tag{4.1}$$

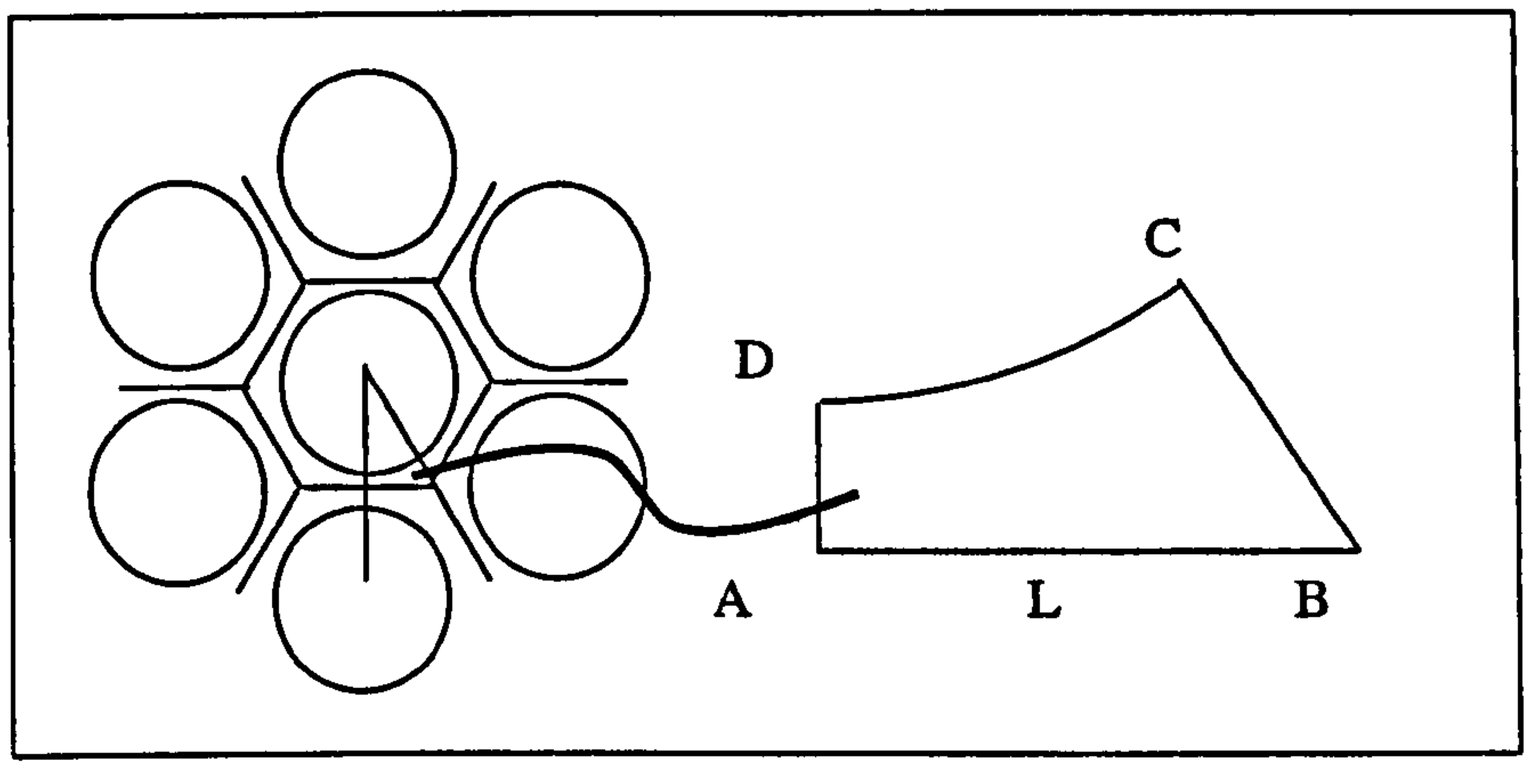


Figure 4.1: Diagram showing the two dimensional arrangement of circular bubbles.

together with conservation of mass

$$\nabla \cdot \mathbf{u} = 0. \tag{4.2}$$

By symmetry there are no tangential tractions and no flow through the boundary of the element and so by specifying the rate of increase of the cell length, $\dot{L}$, these equations can be solved for the velocity and pressure within the fluid. In order to find $\dot{L}$ we consider the work done by the fluid stress, bubble gas pressure, ambient pressure and surface tension ($K$) in changing the bubble area an infinitesimal amount. Balancing the work done in the liquid with the work done in expanding the bubble gives the equation

$$\int_{A_f} \boldsymbol{\sigma} : \mathbf{E}\, dA_f = (p_g - p_a)\frac{dA_b}{dt} - K\frac{dC}{dt}. \tag{4.3}$$

Here $A_f$ is the fluid area, $A_b$ is the bubble area, and $C$ is the length of the liquid-bubble interface CD. The concentration of gas in the liquid, $c(\mathbf{x}, t)$ is governed by the diffusion equation

$$\frac{Dc}{Dt} = D\nabla^2 c, \tag{4.4}$$

with boundary conditions satisfying Henry's law along the bubble-liquid interface (CD in figure 4.1) and a zero flux condition on the three remaining boundaries (AB, AD and BC) by symmetry.

Mass conservation across the fluid-bubble interface relates the current gas pressure in the bubble to the amount of gas which has been transferred from the fluid.

$$\frac{d}{dt}\left(\frac{p_g A_b}{\mathcal{R}T}\right) = D\int_C \nabla c \cdot \hat{\mathbf{n}} dC \tag{4.5}$$

**Non-Dimensional Equations**

We scale lengths with the initial bubble radius, $R_0$, times with the polymer relaxation time, $\tau$, and the pressure difference, $p_g - p_a$, with the initial pressure difference, $p_{g0} - p_a$ in order to obtain a dimensionless conservation of energy equation from (4.3):

$$\int_{A_f} \boldsymbol{\sigma} : \mathbf{E}\, dA_f = P_g De \frac{dA_b}{dt} - \frac{1}{\Gamma}\frac{dC}{dt}. \tag{4.6}$$

Here $P_g = \frac{p_g - p_a}{p_{g0} - p_a}$ is the dimensionless gas pressure difference and $\boldsymbol{\sigma}$, $\mathbf{E}$, $A_f$, $A_b$ and $C$ are also dimensionless. Scaling the gas concentration with $\mathcal{R}T/p_{g0}$ we obtain the dimensionless gas diffusion equation

$$\frac{Dc}{Dt} = N\nabla^2 c \tag{4.7}$$

where $N = D\tau/R_0^2$, together with boundary conditions

$$\begin{aligned} c &= \frac{\Phi(p_a + (p_{g0} - p_a)P_g)}{p_{g0}} && \text{at the bubble-liquid interface (CD)} \\ \hat{\mathbf{n}} \cdot \nabla c &= 0 && \text{on the boundary on AB, AD and BC.} \end{aligned} \tag{4.8}$$

Integrating the mass conservation equation (4.5) over time gives a non-dimensional mass conservation equation

$$(p_a + (p_{g0} - p_a)P_g)A_b = p_{g0}\left(A_{b0} + N\int_t\int_C \nabla c \cdot \hat{\mathbf{n}}\, dC\, dt\right). \tag{4.9}$$

By applying the divergence theorem to the surface integral term, substituting the expression for $\nabla^2 c$ from the diffusion equation (4.7) and integrating with respect to time we could obtain a similar expression to (3.6) in chapter 3. However, here we leave

the expression with the flux across the bubble-liquid interface so that we can apply it to bubbles of differing size in chapter 5.

The dimensionless groups arising are summarised in table 4.1. Equations (4.6) – (4.9) together with dimensionless forms of (4.1) and (4.2) and constitutive equations for the evolution of the polymer stress, **S**, provide the dimensionless equation set governing bubble growth.

| | | |
|---|---|---|
| Deborah number | $De = \frac{(p_{g0}-p_a)\tau}{\mu}$ | ratio of the rate of bubble growth in the solvent to the relaxation rate of the polymer |
| viscosity ratio | $\gamma = \frac{G\tau}{\mu}$ | ratio of polymer to solvent contributions to the steady shear viscosity |
| capillary number | $\Gamma = \frac{R_0\mu}{K\tau}$ | ratio of viscous force to surface tension |
| | $\Phi = \mathcal{R}TH$ | |
| time scale ratio | $N = \frac{9D\tau}{R_0^2} = \frac{\tau}{T_d}$ | ratio of the polymer relaxation time, $\tau$, to gas diffusion time, $T_d$ |

Table 4.1: Dimensionless groups arising in the non-dimensional formulation of the equations governing bubble growth.

### 4.1.1 Finite Element Solution

In this section we first describe an existing two-dimensional simulation developed by Harlen, [22], in which a bubble expands at a rate dictated by the limit of infinite diffusion as in (3.16) in an Oldroyd B fluid. We go on to outline the adaptations required to extend this simulation to include the effects of gas diffusion.

**Eulerian-Lagrangian Finite Element Method**

A finite element scheme is employed to discretize the fluid region. The fluid model used is the Oldroyd B model of section 2.3.1 in which the polymer contribution to the fluid stress is $G\mathbf{A}$ with elastic modulus $G$ and configuration tensor $\mathbf{A}$ satisfying

$$\overset{\nabla}{\mathbf{A}} = -(\mathbf{A} - \mathbf{I}), \tag{4.10}$$

and extra stress under our non-dimensionalisation

$$\mathbf{S} = 2\mathbf{E} + \gamma(\mathbf{A} - \mathbf{I}). \tag{4.11}$$

The presence of the free surface, and the absence of flow through the boundaries, makes the flow calculations well suited to Lagrangian computational methods. Consequently we shall use the split Eulerian-Lagrangian finite element method developed by Harlen *et al.* [22]. The equations are solved on triangular finite elements that move and deform with the fluid.

Following the approach taken in [22] the polymeric stress is split into a 'viscous' part equivalent to the stress exerted by the dumbbell in order to retain its current length and an 'elastic' part caused by changes in the length of the dumbbell. Using equation (4.10) we may write the polymer contribution to the stress

$$\mathbf{A} - \mathbf{I} = \mathbf{A} \cdot \mathbf{E} + \mathbf{E} \cdot \mathbf{A} - \overset{\circ}{\mathbf{A}},$$

where $\overset{\circ}{\mathbf{A}} = \partial\mathbf{A}/\partial t + \mathbf{q} \cdot \nabla\mathbf{A} - \mathbf{A} \cdot \mathbf{\Omega} + \mathbf{\Omega} \cdot \mathbf{A}$ is the corotational derivative and $\mathbf{\Omega} = \frac{1}{2}(\nabla\mathbf{q} - \nabla\mathbf{q}^T)$ is the vorticity tensor. Thus the extra stress can be written in the form

$$S_{ij} = \mu_{ijkl}E_{kl} - \gamma\overset{\circ}{A}_{ij}.$$

where $\mu_{ijkl} = (\delta_{ik} + \gamma A_{ik})\delta_{jl} + \delta_{ik}(\delta_{jl} + \gamma A_{jl})$ is an effective viscosity. We approximate the velocity field, $\mathbf{q}$, by a sum over the finite element nodes $\mathbf{q}(\mathbf{x}) = \sum_m \mathbf{q}^m\phi^m$ where $\mathbf{q}^m$ is the velocity of the grid node at position $\mathbf{x}_m$ and $\phi^m$ are linear interpolating functions with $\phi^m(\mathbf{x}_m) = 1$, $\phi^m(\mathbf{x}_n) = 0$ for $n \neq m$. The pressure field is interpolated using

the same interpolating functions while $\mathbf{A}$ and $\mathring{\mathbf{A}}$ are interpolated as piecewise constants. The extra stress, $S_{ij}$ is therefore approximated as

$$\begin{aligned} S_{ij} &= \sum_m \left\{ \left( q_i^m \frac{\partial \phi^m}{\partial x_j} + q_j^m \frac{\partial \phi^m}{\partial x_i} \right) \right. \\ &+ \frac{\gamma}{2} \left[ A_{ik} \left( q_k^m \frac{\partial \phi^m}{\partial x_j} + q_j^m \frac{\partial \phi^m}{\partial x_k} \right) + \left( q_i^m \frac{\partial \phi^m}{\partial x_k} + q_k^m \frac{\partial \phi^m}{\partial x_i} \right) A_{kj} \right] \\ &- \left. \gamma \mathring{A}_{ij} \right\} \end{aligned} \tag{4.12}$$

In order to minimise the residual obtained when the above approximations are made the standard Galerkin method of weighted residuals is applied to the conservation of momentum equation so that, when multiplied by the interpolating function $\phi^n$, and integrated over the fluid domain, we obtain

$$\int_{A_f} \left( -\nabla p + \nabla \cdot \mathbf{S} \right) \phi^n dA_f = 0.$$

Integrating by parts leads to

$$\int_C \left( -p\phi^n n_i + S_{ij} n_j \phi^n \right) dC - \int_{A_f} \left( -p \frac{\partial \phi^n}{\partial x_i} + S_{ij} \frac{\partial \phi^n}{\partial x_j} \right) dA_f = 0.$$

On the bubble-liquid interface, CD, $-p\mathbf{n} + \mathbf{S} \cdot \mathbf{n} = -p_g \mathbf{n} + S\kappa \mathbf{n}$. On AB, AD and BC the normal componant of the velocity field, $\mathbf{q} \cdot \mathbf{n}$, is known so only the tangential component is required. Since $\mathbf{n} \times \mathbf{S} \cdot \mathbf{n} = 0$ on these boundaries there is no contribution to the line integral coming from these sections of the boundary, so that the only contribution comes from the bubble-liquid interface, CD. The liquid phase pressure, $p$, is approximated by $p = \sum_m p^m \phi^m$ so that the volume integral can be written

$$\begin{aligned} \sum_m \int_{A_f} & \left\{ -p^m \phi^m \frac{\partial \phi^n}{\partial x_i} + \left( q_i^m \frac{\partial \phi^m}{\partial x_j} \frac{\partial \phi^n}{\partial x_j} + q_j^m \frac{\partial \phi^m}{\partial x_i} \frac{\partial \phi^n}{\partial x_j} \right) \right. \\ &+ \frac{\gamma}{2} \left[ A_{ik} \left( q_k^m \frac{\partial \phi^m}{\partial x_j} \frac{\partial \phi^n}{\partial x_j} + q_j^m \frac{\partial \phi^m}{\partial x_k} \frac{\partial \phi^n}{\partial x_j} \right) \right. \\ &+ \left. \left. \left( q_i^m \frac{\partial \phi^m}{\partial x_k} \frac{\partial \phi^n}{\partial x_j} + q_k^m \frac{\partial \phi^m}{\partial x_i} \frac{\partial \phi^n}{\partial x_j} \right) A_{kj} \right] - \gamma \mathring{A}_{ij} \frac{\partial \phi^n}{\partial x_j} \right\} dA_f. \end{aligned} \tag{4.13}$$

The $p$ terms here simplify to

$$\sum_m -p^m \int_{A_f} \phi^m \frac{\partial \phi^n}{\partial x_i} dA_f;$$

while the velocity terms are

$$\sum_m \quad \left\{ q_i^m \int_{A_f} \left( \frac{\partial \phi^m}{\partial x}\frac{\partial \phi^n}{\partial x} + \frac{\partial \phi^m}{\partial y}\frac{\partial \phi^n}{\partial y} \right) dA_f + q_x \int_{A_f} \frac{\partial \phi^m}{\partial x_i}\frac{\partial \phi^n}{\partial x} dA_f \right.$$

$$+ \quad q_y \int_{A_f} \frac{\partial \phi^m}{\partial x_i}\frac{\partial \phi^n}{\partial y} dA_f + \frac{\gamma}{2} \left[ A_{ix} q_x^m \int_{A_f} \left( \frac{\partial \phi^m}{\partial x}\frac{\partial \phi^n}{\partial x} + \frac{\partial \phi^m}{\partial y}\frac{\partial \phi^n}{\partial y} \right) dA_f \right.$$

$$+ \quad A_{iy} q_y^m \int_{A_f} \left( \frac{\partial \phi^m}{\partial x}\frac{\partial \phi^n}{\partial x} + \frac{\partial \phi^m}{\partial y}\frac{\partial \phi^n}{\partial y} \right) dA_f + A_{ix} q_x^m \int_{A_f} \frac{\partial \phi^m}{\partial x}\frac{\partial \phi^n}{\partial x} dA_f$$

$$+ \quad A_{ix} q_y^m \int_{A_f} \frac{\partial \phi^m}{\partial x}\frac{\partial \phi^n}{\partial y} dA_f + A_{iy} q_x^m \int_{A_f} \frac{\partial \phi^m}{\partial y}\frac{\partial \phi^n}{\partial x} dA_f$$

$$+ \quad A_{iy} q_y^m \int_{A_f} \frac{\partial \phi^m}{\partial y}\frac{\partial \phi^n}{\partial y} dA_f + A_{xx} q_i^m \int_{A_f} \frac{\partial \phi^m}{\partial x}\frac{\partial \phi^n}{\partial x} dA_f$$

$$+ \quad A_{xy} q_i^m \int_{A_f} \frac{\partial \phi^m}{\partial x}\frac{\partial \phi^n}{\partial y} dA_f + A_{yx} q_i^m \int_{A_f} \frac{\partial \phi^m}{\partial y}\frac{\partial \phi^n}{\partial x} dA_f$$

$$+ \quad A_{yy} q_i^m \int_{A_f} \frac{\partial \phi^m}{\partial y}\frac{\partial \phi^n}{\partial y} dA_f + A_{xx} q_x^m \int_{A_f} \frac{\partial \phi^m}{\partial x_i}\frac{\partial \phi^n}{\partial x} dA_f$$

$$+ \quad A_{xy} q_x^m \int_{A_f} \frac{\partial \phi^m}{\partial x_i}\frac{\partial \phi^n}{\partial y} dA_f + A_{yx} q_y^m \int_{A_f} \frac{\partial \phi^m}{\partial x_i}\frac{\partial \phi^n}{\partial x} dA_f$$

$$\left. + \quad A_{yy} q_y^m \int_{A_f} \frac{\partial \phi^m}{\partial x_i}\frac{\partial \phi^n}{\partial y} dA_f \right] \right\};$$

and $\mathring{\mathrm{A}}$ terms to

$$-\gamma \sum_m \left( \mathring{A}_{ix} \int_{A_f} \frac{\partial \phi^n}{\partial x} dA_f + \mathring{A}_{iy} \int_{A_f} \frac{\partial \phi^n}{\partial y} dA_f \right).$$

This can be written as a matrix equation of the form

$$\begin{pmatrix} UU & UV & pU \\ VU & VV & pV \end{pmatrix} \begin{pmatrix} q_x^m \\ q_y^m \\ p^m \end{pmatrix} = \begin{pmatrix} fU \\ fV \end{pmatrix}. \tag{4.14}$$

Contributions to the coefficients from the element consisting of nodes $l$, $m$ and $n$ are as follows:

$$\begin{aligned}
UU &= \frac{1}{4a}\{2(1+\gamma A_{xx})dx^m dx^n + \gamma A_{xy}(dx^m dy^n + dx^n dy^m) \\
&+ \left(1+\frac{\gamma}{2}(A_{xx}+A_{yy})\right) dy^m dy^n\Big\} \\
UV &= \frac{1}{4a}\left\{\gamma A_{xy}(dx^m dx^n + dy^m dy^n) + \left(1+\frac{\gamma}{2}(A_{xx}+A_{yy})\right) dx^m dy^n\right\} \\
VU &= \frac{1}{4a}\left\{\gamma A_{xy}(dx^m dx^n + dy^m dy^n) + \left(1+\frac{\gamma}{2}(A_{xx}+A_{yy})\right) dx^n dy^m\right\} \\
VV &= \frac{1}{4a}\left\{\left(1+\frac{\gamma}{2}(A_{xx}+A_{yy})\right) dx^m dx^n + \gamma A_{xy}(dx^m dy^n + dx^n dy^m)\right. \\
&+ \left. 2(1+\gamma A_{yy})dy^m dy^n\right\} \\
pU &= -\frac{dy^m}{6} \\
pV &= -\frac{dx^m}{6} \\
fU &= \frac{\gamma}{2}\left(\mathring{A}_{xx}dx^n + \mathring{A}_{xy}dy^n\right) + \int_C (-pn_x + S_{xx}n_x + S_{xy}n_y)\,\phi^n dC
\end{aligned}$$

and

$$fV = \frac{\gamma}{2}\left(\mathring{A}_{xy}dx^n + \mathring{A}_{yy}dy^n\right) + \int_C (-pn_y + S_{yx}n_x + S_{yy}n_y)\,\phi^n dC, \qquad (4.15)$$

where $dx^m = x^n - x^l$ (similarly for $dx^n$, $dy^m$ and $dy^n$) and $a$ is the area of the triangle. In order to stabilise the liquid pressure across the fluid domain a small pressure term is added to the continuity equation. The modified continuity equation is

$$\nabla \cdot \mathbf{q} + h^2 \epsilon \nabla^2 p = 0,$$

where $\epsilon$ is a small parameter and $h^2$ is twice the area of the element [57]. Applying Galerkin's standard formulation and integrating the $\nabla^2$ term by parts leads to

$$\int_{A_f} \frac{\partial q_i}{\partial x_i}\phi^n dA_f + h^2\epsilon\left(\int_C \frac{\partial p}{\partial x_i}\phi^n n_i dC - \int_{A_f} \frac{\partial p}{\partial x_i}\frac{\partial \phi^n}{\partial x_i} dA_f\right) = 0$$

Since there are no pressure gradients normal to the boundary of the fluid region by thermodynamic equilibrium and symmetry considerations, the boundary integral is equal to zero. Applying the finite element approximation for $\mathbf{q}$ and $p$, we obtain

$$\sum_m \left(q_i^m \int_{A_f} \frac{\partial \phi^m}{\partial x_i}\phi^n dA_f - h^2\epsilon p^m \int_{A_f} \frac{\partial \phi^m}{\partial x_i}\frac{\partial \phi^n}{\partial x_i} dA_f\right) = 0,$$

which simplifies to

$$\sum_m \left( q_x^m \frac{dy^m}{6} + q_y^m \frac{dx^m}{6} - \frac{h^2\epsilon}{4a} p^m (dx^m dx^n + dy^m dy^n) \right) = 0. \tag{4.16}$$

The mass and momentum equations are solved simultaneously by solving

$$\begin{pmatrix} A & B \\ B^T & C \end{pmatrix} \begin{pmatrix} \mathbf{q}^m \\ p^m \end{pmatrix} = \begin{pmatrix} \mathbf{f} \\ 0 \end{pmatrix} \tag{4.17}$$

where

$$A = \begin{pmatrix} UU & UV \\ VU & VV \end{pmatrix}, \quad B = \left(\tfrac{dy^m}{6}, \tfrac{dx^m}{6}\right), \quad \text{and } C = \frac{h^2\epsilon}{4a} \left(dx^m dx^n + dy^m dy^n\right).$$

At each time step, equation (4.17) is solved for current values of $\mathbf{A}$ and $\mathring{\mathbf{A}}$ and an estimate for the expansion rate $\dot{L}$. By separating the terms in equation (4.6) into those that are linear and quadratic in the velocity we can obtain a new estimate for $\dot{L}$. The velocity is then recalculated and the value of $L$ is further refined by linear interpolation. In practice at most three iterations are required to find the correct value of $\dot{L}$.

Once the velocity field has been found, the positions of the nodes of the finite elements are updated. The configuration tensor $\mathbf{A}$ is then found by integrating equation (4.10) in the frame of the deforming element, where the upper convected derivative becomes $\frac{d\mathbf{A}}{dt}$. The solution for $\mathbf{A}$ is thereby reduced to a first-order ordinary differential equation.

**Finite Element Solution for Gas Diffusion**

The gas diffusion equation (4.7) is solved using the same finite elements used to solve the momentum equation and makes use of the Lagrangian nature of the grid to remove the advection term. For stability we use a backward Euler scheme to discretize time and the Laplacian is discretized using the standard Galerkin method and the resulting linear system is solved by a preconditioned conjugate gradient method, details are given in chapter 1. Thus, when discretized in time, the gas diffusion equation (4.7) becomes

$$\frac{c^{n+1} - c^n}{\Delta t} - N\nabla^2 c^{n+1} = 0. \tag{4.18}$$

Here superscripts denote discretization in time and subscripts denote discretization in space. The gas concentration is approximated by a sum over computational space elements $c(\mathbf{x}) = \sum_m \phi_m c_m$ where $c_m$ are the values of the concentration, $c(x_m)$, at the grid nodes $x_m$ and $\phi_m$ are the linear interpolating functions discussed above. When applying this approximation to equation (4.18) we obtain

$$\sum_m c_m^{n+1}\phi_m - \sum_m c_m^n \phi_m - N\Delta t \sum_m c_m^{n+1}\nabla^2\phi_m = R_{res}$$

where $R_{res}$ is the residual - the difference between the true solution of equation 4.18 and the solution obtained by applying the approximation.

Now we apply Galerkin's method of weighted residuals as for the momentum equation:

$$\int_{A_f} \sum_m c_m^{n+1}\phi_m\phi_k dA_f - \int_{A_f} \sum_m c_m^n \phi_m\phi_k dA_f - N\Delta t \int_{A_f} \sum_m c_m^{n+1}\phi_k\nabla^2\phi_m dA_f = 0.$$

Integrating the $\nabla^2$ term by parts and rearranging leads us to

$$\begin{aligned}\sum_m c_m^{n+1} \int_{A_f} (\phi_m\phi_k + N\Delta t\nabla\phi_m\nabla\phi_k)\, dA_f &= N\Delta t \int_C \hat{\mathbf{n}}\cdot\nabla c^{n+1}\phi_k dC \\ &+ \sum_m c_m^n \int_{A_f} \phi_m\phi_k dA_f \qquad (4.19)\end{aligned}$$

where $C$ is the boundary of the liquid domain. The line integral on the right hand side is obtained from boundary conditions and, in this case, equals zero on all four fluid boundaries since $\mathbf{n}\cdot\nabla c$ is zero on AB, AD and BC while on CD the gas concentration is known so that $\phi_k = 0$ for all the unknown elements of $c$.

The value of the bubble gas pressure from equation (4.9) is calculated from the flux of gas across the bubble-liquid interface given by the line integral

$$\hat{\mathbf{n}}\cdot N\Delta t \int_C^D \nabla c^{n+1}\, dC.$$

**Convergence**

The calculations were performed using grids with approximately 1000 elements and a timestep of $10^{-3}L/\dot{L}$. Spatial accuracy was checked by comparing calculated values for

A, u $\dot{L}$ and bubble area for one set of parameter values with those obtained using a finer grid with approximately 4000 elements and were found to be within a relative error of 0.5%. A seperate check of temporal accuracy using a timestep of $5 \times 10^{-4} L/\dot{L}$ found relative errors in A of at most 1% and smaller errors in other quantities.

### 4.1.2 Circular Bubbles

When the bubble area fraction is small we might expect bubbles to remain circular during the expansion, thus we can consider a simplified model where circular bubbles are surrounded by a circular liquid layer. The formulation here is very similar to that for spherical bubbles in chapter 3.

In cylindrical polar coordinates liquid pressure, $p$, and stresses, $S_{rr}$ and $S_{\theta\theta}$, are assumed to depend on $r$ and time $t$ only. Neglecting inertia, the radial component of the momentum equation, $\nabla \cdot \boldsymbol{\sigma} = 0$, gives

$$\frac{\partial p}{\partial r} = \frac{(S_{rr} - S_{\theta\theta})}{r} + \frac{\partial S_{rr}}{\partial r}. \tag{4.20}$$

Since the fluid area is conserved we transform from a radial coordinate $r$ to a Lagrangian area coordinate $x$ such that $r^2 = u + x$. Here, $\pi u$ is the bubble area and $\pi x$ is the general fluid area so that $x = X$ is the Lagrangian position of the outer edge of the envelope. At the boundaries $x = 0$ and $x = X$

$$-p(u) + S_{rr}(u) = -p_g + \frac{S}{u^{\frac{1}{2}}}, \qquad \text{(inner surface boundary condition)}$$

$$-p(X+u) + S_{rr}(X+u) = -p_a, \qquad \text{(outer surface boundary condition)}$$

where $S$ is the surface tension at the bubble interface. Integrating (4.20) across the fluid layer and using these boundary conditions gives:

$$0 = P_g De + \frac{1}{2}\gamma \int_0^X \frac{S_{rr} - S_{\theta\theta}}{x+u} dx - \frac{1}{\Gamma}\frac{1}{u^{\frac{1}{2}}}.$$

For the Oldroyd B model $S_{rr} - S_{\theta\theta} = -2\dot{u}/(x+u) + \gamma(A_{rr} - A_{\theta\theta})$ so that

$$\dot{u}\left[\frac{1}{u} - \frac{1}{X+u}\right] = P_g De + \frac{1}{2}\gamma \int_0^X \frac{A_{rr} - A_{\theta\theta}}{x+u} dx - \frac{1}{\Gamma}\frac{1}{u^{\frac{1}{2}}}. \tag{4.21}$$

Due to the coordinate transformation, the evolution of $A_{rr}$ and $A_{\theta\theta}$, given by equation (2.5), can be followed in the Lagrangian frame:

$$\frac{\partial A_{rr}}{\partial t} = -\frac{\dot{u}}{(x+u)}A_{rr} - (A_{rr} - 1), \tag{4.22}$$

and

$$\frac{\partial (A_{rr} - A_{\theta\theta})}{\partial t} = \frac{\dot{u}}{(x+u)}[(A_{rr} - A_{\theta\theta}) - 2A_{rr}] - (A_{rr} - A_{\theta\theta}). \tag{4.23}$$

Initially $A_{rr} = 1$ and $A_{rr} - A_{\theta\theta} = 0$ everywhere. We introduce a concentration potential $\phi(x,t)$,where $\partial\phi/\partial x = c - c_0$ to aid in the numerical solution [1, 3] of the gas diffusion equation (4.4) as in chapter 3. The diffusion equation then becomes

$$\frac{\partial \phi}{\partial t} = 4N(x+u)\frac{\partial^2 \phi}{\partial x^2}, \tag{4.24}$$

with $\partial\phi/\partial x = \Phi(p_{g0} - p_a)(P_g - 1)/p_{g0}$ at the bubble surface satisfying Henry's law and $\partial^2\phi/\partial x^2 = 0$ at the outer edge of the fluid layer so that there is no mass transport there. Substituting equation (4.24) for the left hand side of equation (4.5) and integrating with respect to time gives

$$(p_a + (p_{g0} - p_a)P_g)u = p_{g0}(1 + \phi(0,t)), \tag{4.25}$$

since we can arbitrarily set $\phi(0,0) = 0$.

The five equations (4.21) – (4.25) govern bubble growth for isolated bubbles which remain circular during the expansion.

### 4.1.3 Thin Film Approximation

In the opposite limit where bubbles are separated by thin films, we can obtain a second one-dimensional approximation. Since there is no traction along either the bubble surface or the $x$-axis the flow in the liquid region is approximately an extensional flow in the $x$-direction. Thus, when the fluid layer is thin, the velocity gradient and, hence, the polymer stress will be approximately uniform over the thickness of the fluid layer. We can, therefore, construct a one dimensional thin film model analogous to those used

to model spin lines [18, 28].

We divide the fluid region into $n$ trapezoidal elements and a triangle as shown in figure 4.2. $\Delta x_i$ and $\Delta y_i$ are the width and height of element $i$.

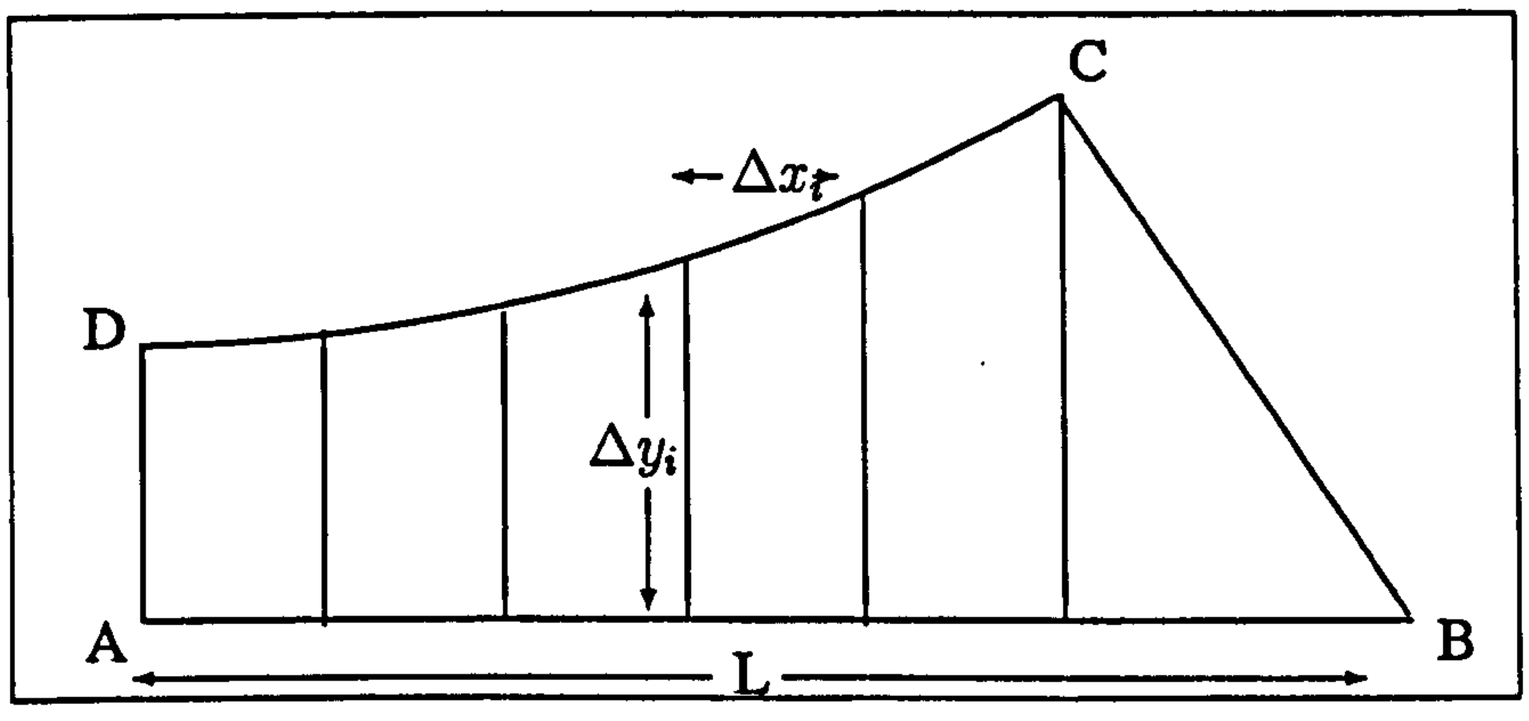


Figure 4.2: Diagram enlarging the computational region.

In Cartesian coordinates the velocity field **q** in planar extension is given by

$$\nabla \mathbf{q} = \begin{pmatrix} \frac{\partial q_x}{\partial x} & 0 & 0 \\ 0 & \frac{\partial q_y}{\partial y} & 0 \\ 0 & 0 & 0 \end{pmatrix}$$

and so in each element

$$\nabla \mathbf{q} = \begin{pmatrix} -\frac{\dot{\Delta} y}{\Delta y} & 0 & 0 \\ 0 & \frac{\dot{\Delta} y}{\Delta y} & 0 \\ 0 & 0 & 0 \end{pmatrix} = \begin{pmatrix} \frac{\dot{\Delta} x}{\Delta x} & 0 & 0 \\ 0 & -\frac{\dot{\Delta} x}{\Delta x} & 0 \\ 0 & 0 & 0 \end{pmatrix}.$$

Integrating the momentum equation over element $i$ and applying the divergence theorem we obtain

$$\int_{A_i} \nabla \cdot \boldsymbol{\sigma} \, dA_i = 0 \Rightarrow \int_{C_i} \boldsymbol{\sigma} \cdot \mathbf{n} \, dC_i = 0$$

where $A_i$ is the interior and $C_i$ is the boundary of element $i$. To obtain the contributions to the integral from the left and right hand sides we assume that, since the fluid layer is thin, fluid pressure, $p$, and stress components, $S_{xx}$ and $S_{yy}$, are independent of $y$. Thus the integrals along the vertical boundaries are

$$-(-p + \sigma_{xx})_i \Delta y_i \, \mathbf{x} \qquad \text{and} \qquad (-p + \sigma_{xx})_{i+1} \Delta y_{i+1} \, \mathbf{x}.$$

The contribution from the gas-liquid interface is obtained by using the boundary condition

$$\boldsymbol{\sigma} \cdot \mathbf{n} = (-p_g + K\kappa)\mathbf{n}$$

where $\kappa$ is the curvature, $K$ is the surface tension on the bubble surface and $\mathbf{n}dC = \mathbf{x}dy - \mathbf{y}dx$. The expression for the curvature is obtained from the rate of change along the free surface of the tangent to the free surface

$$\kappa = \left| \frac{d^2\mathbf{h}}{dC^2} \right|,$$

where $\mathbf{h} = x\,\mathbf{x} + \Delta y\,\mathbf{y}$, $dC = \sqrt{1 + \Delta y'^2}\,dx$ and $'$ indicates a derivative with respect to $x$. This gives

$$\kappa = \frac{\Delta y''}{(1 + \Delta y'^2)^{3/2}} = -\frac{1}{\Delta y'}\frac{d}{dx}\left(\frac{1}{(1 + \Delta y'^2)^{1/2}}\right).$$

Thus the contribution from the gas-liquid interface gives

$$-\left(-p_g(\Delta y_{i+1} - \Delta y_i) - \frac{S}{(1 + \Delta y_{i+1}'^2)^{1/2}} + \frac{S}{(1 + \Delta y_i'^2)^{1/2}}\right)\mathbf{x} + \int (-p_g + S\kappa)\,dx\mathbf{y}.$$

Finally the contribution from the symmetry line along the bottom of element $i$ is

$$\int (-p + S_{yy})\mathbf{y}\,dx.$$

Contributions from each of the four integrals are then combined. Balancing the y components give an expression for the pressure in the fluid,

$$S_{yy} = -(p_g - p) + S\kappa. \tag{4.26}$$

The x components relate the stress and fluid pressure at the left hand end of each element to that of the right hand end of each element, using equation (4.26) to eliminate the fluid pressure we obtain the non-dimensional equation for the force balance on each element

$$\begin{aligned}(S_{xx} - S_{yy})_{i+1}\,\Delta y_{i+1} &= (S_{xx} - S_{yy})_i\,\Delta y_i \\ &- \frac{1}{\Gamma}\left(\kappa_{i+1}\Delta y_{i+1} - \kappa_i \Delta y_i + \frac{1}{(1 + \Delta y_{i+1}'^2)^{1/2}} - \frac{1}{(1 + \Delta y_i'^2)^{1/2}}\right).\end{aligned} \tag{4.27}$$

To obtain an expression for the expansion rate, $\dot{L}$, we, again, consider the work done in expanding the bubble an infinitesimal amount as in equation 4.6. For our discrete system, we obtain

$$\sum_i \sigma : \mathbf{E} a_i = P_g De \frac{dA_b}{dt} - \frac{1}{\Gamma} \sum_i \frac{dC_i}{dt}$$

where $a_i = \frac{1}{2}(\Delta y_{i+1} + \Delta y_i)\Delta x_i$ is the area of element $i$ and $C_i$ is the length of the bubble-liquid interface for element $i$. Thus

$$\frac{1}{2} \sum_i (\Psi_{i+1} + \Psi_i)\dot{\Delta x_i} = \sqrt{3} P_g De L \frac{dL}{dt} - \frac{1}{\Gamma} \sum_i \frac{\partial C_i}{\partial t} \tag{4.28}$$

where we define $\Psi = (S_{xx} - S_{yy})\Delta y$.

For the Oldroyd B fluid model

$$\Psi = \left( -4 \frac{\dot{\Delta y}}{\Delta y} + \gamma (A_{xx} - A_{yy}) \right) \Delta y \tag{4.29}$$

while from equation (4.10) the evolution of elastic stresses are given by

$$\begin{aligned} \dot{A_{xx}} &= -2 \frac{\dot{\Delta y}}{\Delta y} A_{xx} - (A_{xx} - 1) \\ \dot{A_{yy}} &= 2 \frac{\dot{\Delta y}}{\Delta y} A_{yy} - (A_{yy} - 1). \end{aligned} \tag{4.30}$$

Since this approximation holds when the window is thin we shall assume that gas diffusion is effectively instantaneous so that gas concentration is uniform throughout the fluid. By Henry's law the amount of gas that has diffused into the bubble is

$$\Phi \frac{(p_{g0} - p_a)}{P_{g0}} (1 - P_g) A_f$$

and so from conservation of mass equation (4.9)

$$(p_{g0} - p_a) P_g = p_{g0} \left( \frac{\frac{\sqrt{3}}{2} {L_0}^2 - A_f + \Phi A_f}{\frac{\sqrt{3}}{2} L^2 - A_f + \Phi A_f} \right) - p_a. \tag{4.31}$$

Finally we have an equation for conservation of fluid area:

$$(\Delta y_{i+1} + \Delta y_i)\dot{\Delta x_i} = -(\dot{\Delta y_{i+1}} + \dot{\Delta y_i})\Delta x_i. \tag{4.32}$$

Equations (4.27) – (4.32) govern the deformation of the region under consideration. As with the calculation of the full finite element problem, we separate the solution of the

force balance and conservation of mass equations from the evolution of the constitutive equation. Using an initial estimate for the expansion rate at the midpoint of the window we calculate values of $\Delta y_i$ from equation (4.27) using the Crank-Nicolson method to evaluate the curvature terms, we then adjust the expansion rate via a secant method to satisfy equation (4.28) using values of $\Delta x$ obtained from equation (4.32). In order to conserve the area of the whole of the fluid region, the change in area of the triangle is calculated and distributed equally between the trapezia allowing their lengths to be adjusted. Once the $\Delta y$ and $\Delta x$ have been updated the bubble gas pressure is calculated by equation (4.31) and the stresses are updated by evolving equations (4.30).

### 4.1.4 Reacting Fluid Model

Here we implement the reacting fluid model described in chapter 3 in the one-dimensional approximation.

In the reacting fluid model the total amount of gas produced by the reaction at time $t$ is $\varsigma\Phi\frac{p_a}{p_{g0}}A_f\alpha(t)$. The gas concentration is uniform throughout the fluid so that by Henry's law it is $\varsigma\Phi\frac{p_a}{p_{g0}}\alpha_0 P_g$ and the amount of gas transported into the bubble is

$$\frac{\varsigma\Phi p_a}{p_{g0}}A_f(\alpha - \alpha_0 P_g).$$

Since $p_{g0} - p_a = \varsigma\alpha_0 p_a$, gas pressure can be determined from

$$\begin{aligned}(p_{g0} - p_a)\left(\frac{\sqrt{3}}{2}L^2 - A_f + \Phi A_f\right)P_g &= p_{g0}\left(\frac{\sqrt{3}}{2}L_0^2 - A_f\right) - p_a\left(\frac{\sqrt{3}}{2}L^2 - A_f\right) \\ &+ \varsigma\Phi p_a\alpha A_f. \end{aligned} \tag{4.33}$$

As in chapter 3, the extent of reaction is governed by the second order kinetics equation (3.28).

The force balance equation, equation (4.27), and virtual work arguments of section 4.1.3, now include contributions to the stress from each of the $k$ modes so that

$$S_{xx} - S_{yy} = -4\frac{\dot{\Delta y}}{\Delta y} + \gamma\sum_k G_k(A_{xx} - A_{yy})_k.$$

The elastic moduli for the different modes, $G_k$, are calculated, as described in sections 2.5 and 3.2.2, from equation (2.13) for $\alpha < \alpha_c$ and from equation (2.14) for $\alpha > \alpha_c$.

Before the gel point, $\alpha_c$, the stretch in each of the modes is governed by

$$\begin{aligned} \dot{A_{xxk}} &= -2\frac{\dot{\Delta y}}{\Delta y}A_{xxk} - \frac{1}{c_\alpha \tau_k}(A_{xxk} - 1) \\ \dot{A_{yyk}} &= 2\frac{\dot{\Delta y}}{\Delta y}A_{yyk} - \frac{1}{c_\alpha \tau_k}(A_{yyk} - 1) \end{aligned} \tag{4.34}$$

where $c_\alpha$ is the reaction rate and time is scaled with the reaction time, $1/c_\alpha$.

After the gel point the relaxing modes in both the sol and gel with $\tau_k < \tau_{ch}$ are governed by equations (4.34) and the non-relaxing gel mode follows these equations with an infinite relaxation time. Calculation of **A** allowing for the rearrangement of modes and scaling of the longest relaxation time are described in section 3.2.2.

Parameter values used in addition to those for the non-reacting Oldroyd B fluid are the same as in the spherically symmetric case given in table 3.4. The dimensionless groups are summarised in table 4.2; the definitions differ from those in table 4.1 since time here is scaled with the reaction time $1/c_\alpha$.

| | | |
|---|---|---|
| $M = \frac{(p_{g0}-p_a)}{\mu c_\alpha}$ | $\frac{10}{c_\alpha}$ | ratio of the rate of bubble growth in the solvent to the reaction rate. |
| $\gamma = \frac{G_0}{\mu c_\alpha}$ | $\frac{738}{c_\alpha}$ | |
| $\Gamma = \frac{R_0 \mu c_\alpha}{K}$ | $10000 c_\alpha$ | ratio of viscous force to surface tension |
| $\Phi = RTH$ | 0.32 | |
| $X$ | 0.0655 | dimensionless fluid area obtained by using initial gas area fraction of 0.8 |

Table 4.2: Dimensionless groups arising in the non-dimensional formulation of the equations governing bubble growth.

## 4.2 Results and Discussion

We assume that the bubbles will be sufficiently far from each other initially so that the bubbles are circular and the polymers are unstretched. As in chapter 3 we do not attempt to model nucleation and the very early stages of bubble growth so the value of the initial bubble radius, $R_0$, is not the value at nucleation but that defined by the gas pressure being at $p_{g0}$. The values of the parameters used are equivalent to those used in chapter 3 and are summarised in table 3.2.

### 4.2.1 Full Two-Dimensional Simulations

For an isolated spherical bubble we saw in chapter 3 that the only effect of surface tension is to modify the pressure difference between the gas and the fluid and, hence, the final bubble size. Consequently the expansion of an isolated bubble is governed by three timescales: a polymer relaxation time, $\tau$; a viscous growth time, $De/\tau$; and a gas diffusion time, $N/\tau$. However, bubbles expanding in a hexagonal lattice do not necessarily remain circular so that there is an additional timescale controlling the expansion: the time for surface tension to restore circular bubbles. At high capillary number the surface tension timescale is much longer than the bubble expansion timescale and so the bubbles expand to some quasi-equilibrium shape before relaxing to either a circular shape or, if the gas area fraction is greater than $\pi/(2\sqrt{3}) = 0.907$, to circular arcs connected to thin, 'black', films.

We first consider the case when the rate of gas diffusion is faster than the viscous expansion rate ($N \gg DeX$). In this regime we would expect to see the effects of viscoelasticity as the expansion rate is controlled by the fluid rheology. When the expansion is rapid compared to the polymer relaxation time (high Deborah number) it can be divided into two regions. Initially we see a period of rapid thinning as the resistance to expansion is from the solvent alone. This can be seen in figure 4.3 which compares an expansion in a viscoelastic liquid and Newtonian liquid of the same

zero shear rate viscosity. The solvent contribution to the zero shear-rate viscosity is smaller in the viscoelastic liquid so the early expansion is more rapid. The first normal stress difference increases during this phase until it balances the gas pressure difference. Beyond this time further expansion occurs, as polymer stress relaxes, at the polymer relaxation rate. This two-phase expansion behaviour was seen in our earlier calculations for spherical bubbles at high Deborah number, see section 3.1.3 and figure 3.2.

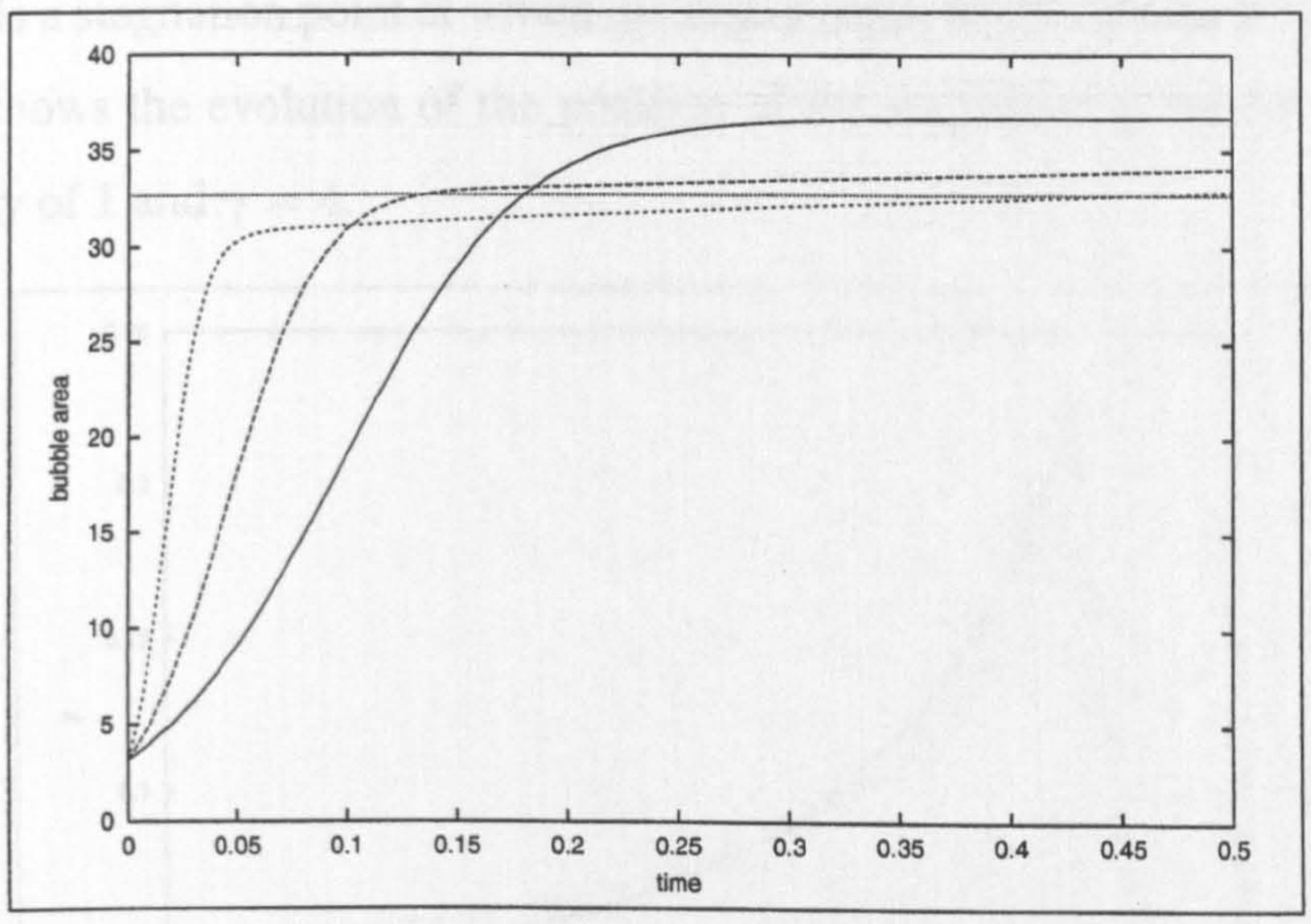


Figure 4.3: The effect of $\gamma$ on the bubble area when the zero shear rate viscosity is constant ($\mu + G\tau = 1$). Solid line: $\gamma = 0$; dashed line: $\gamma = 1$; dotted line: $\gamma = 4$.

In figure 4.4 we compare the shape of the liquid-bubble interface for a bubble volume of 27.7 (indicated by the horizontal line in figure 4.3). It can be seen that the viscoelastic liquid has bubbles with flatter fluid windows that are thicker in the middle. Initially the extension rates are highest in the middle of the window, producing higher polymer extensions that resist further extension of this region. Indeed, for high Deborah number expansions we see an elastic recoil in which fluid is pulled back towards the middle region so that the window thickens there even though the bubble is still expanding. This elastic recoil can be seen in figure 4.5 where we show the evolution of the thickness of the narrow end of the liquid region. As the ratio of polymer to solvent contributions to the zero shear rate viscosity, $\gamma$, is increased (keeping the zero shear rate viscosity fixed)

the magnitude of the 'bounce' increases and the maximum thickness attained occurs earlier. Figure 4.7 shows snapshots of the polymer stress distribution in the liquid during the expansion, plotted as the difference in eigenvalues of $\mathbf{A}$. Initially, (a), there is no polymer stress while at time $t = 0.05$ (just before the turning point in the minimum fluid depth) (b) shows the middle of the window becoming stretched. Pictures (c) and (d) show the stress during the relaxation phase where recoil is seen. During the recoil phase there is a stagnation point at which the liquid depth neither increase nor decreases. Figure 4.6 shows the evolution of the position of the stagnation point for a zero shear rate viscosity of 1 and $\gamma = 4$.

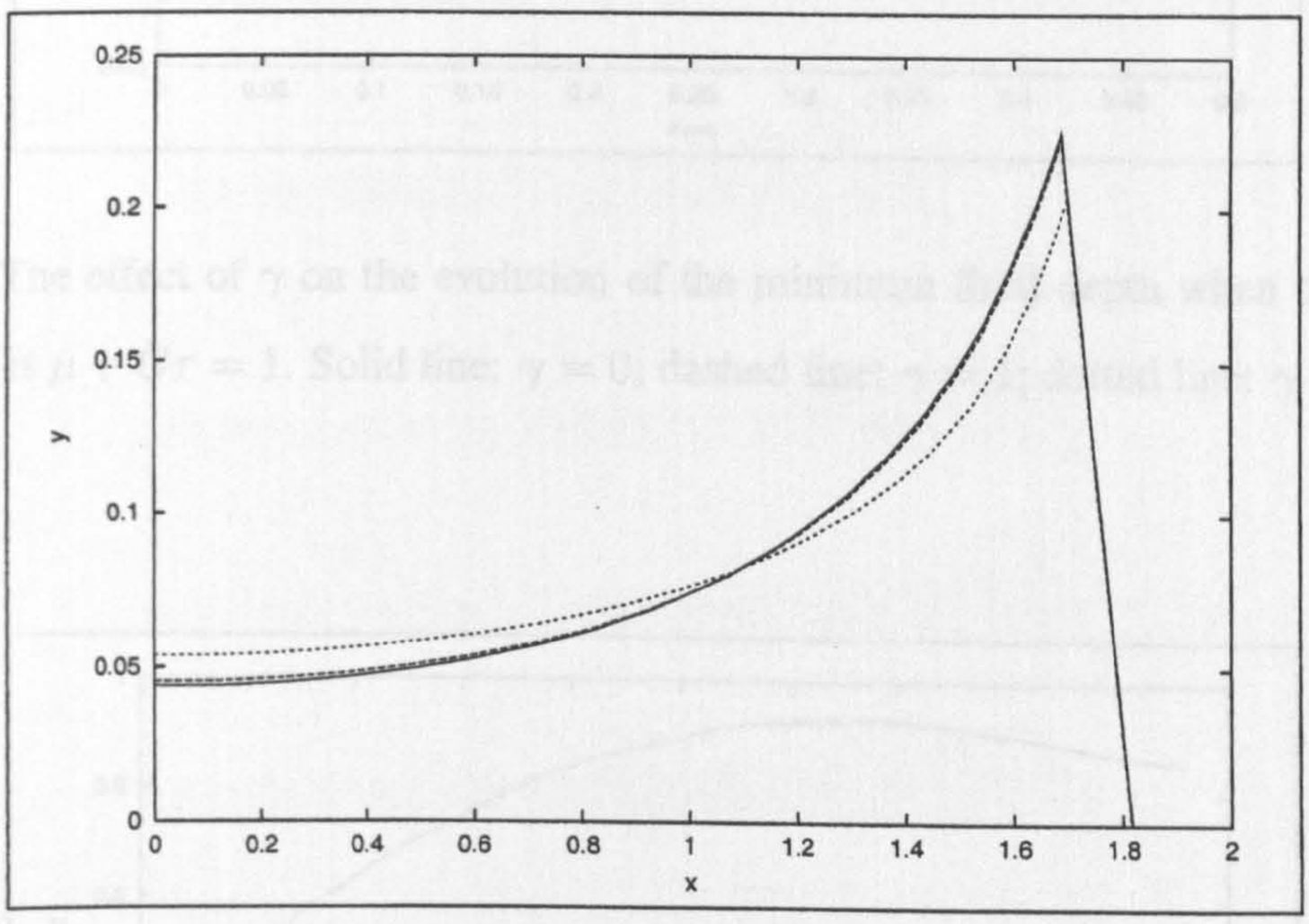


Figure 4.4: The effect of $\gamma$ on the liquid-bubble interface when the bubble volume is 27.7 and the zero shear rate viscosity is $\mu + G\tau = 1$. Solid line: $\gamma = 0$; dashed line: $\gamma = 1$; dotted line: $\gamma = 4$.

At small capillary numbers surface tension affects the bubble growth in two ways: it relaxes the shape towards a circular bubble; and it reduces the final bubble size by maintaining a higher bubble gas pressure. We do not attempt to model window breakage here. In the absence of intermolecular forces windows will not break in finite time but tend to circular arcs connected by very thin, 'black', films. The rupture of thin films due to Van Der Waals forces is considered by Vaynblat, Lister and Witelski [56] and Zhang

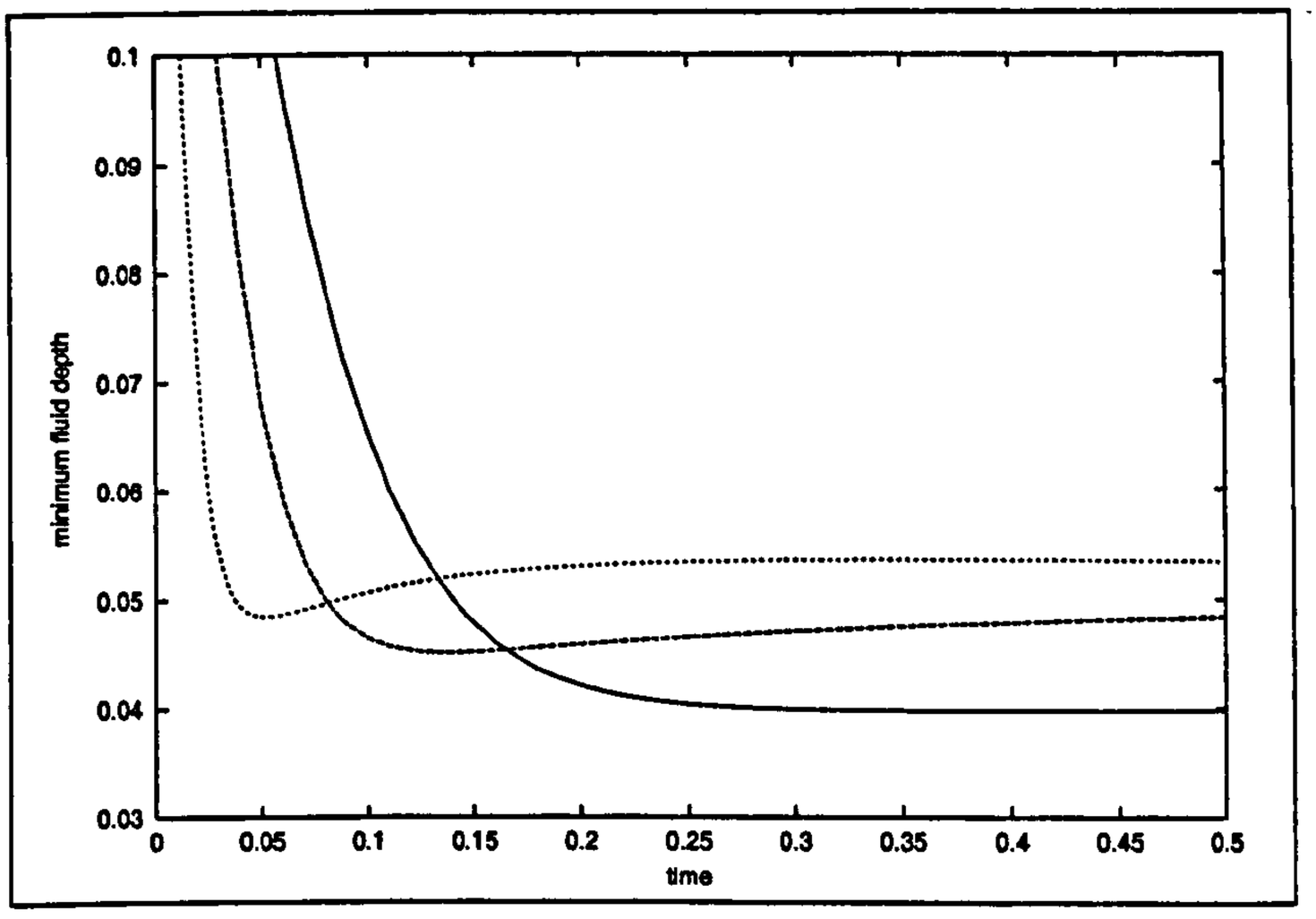


Figure 4.5: The effect of $\gamma$ on the evolution of the minimum fluid depth when the zero shear rate viscosity is $\mu + G\tau = 1$. Solid line: $\gamma = 0$; dashed line: $\gamma = 1$; dotted line: $\gamma = 4$.

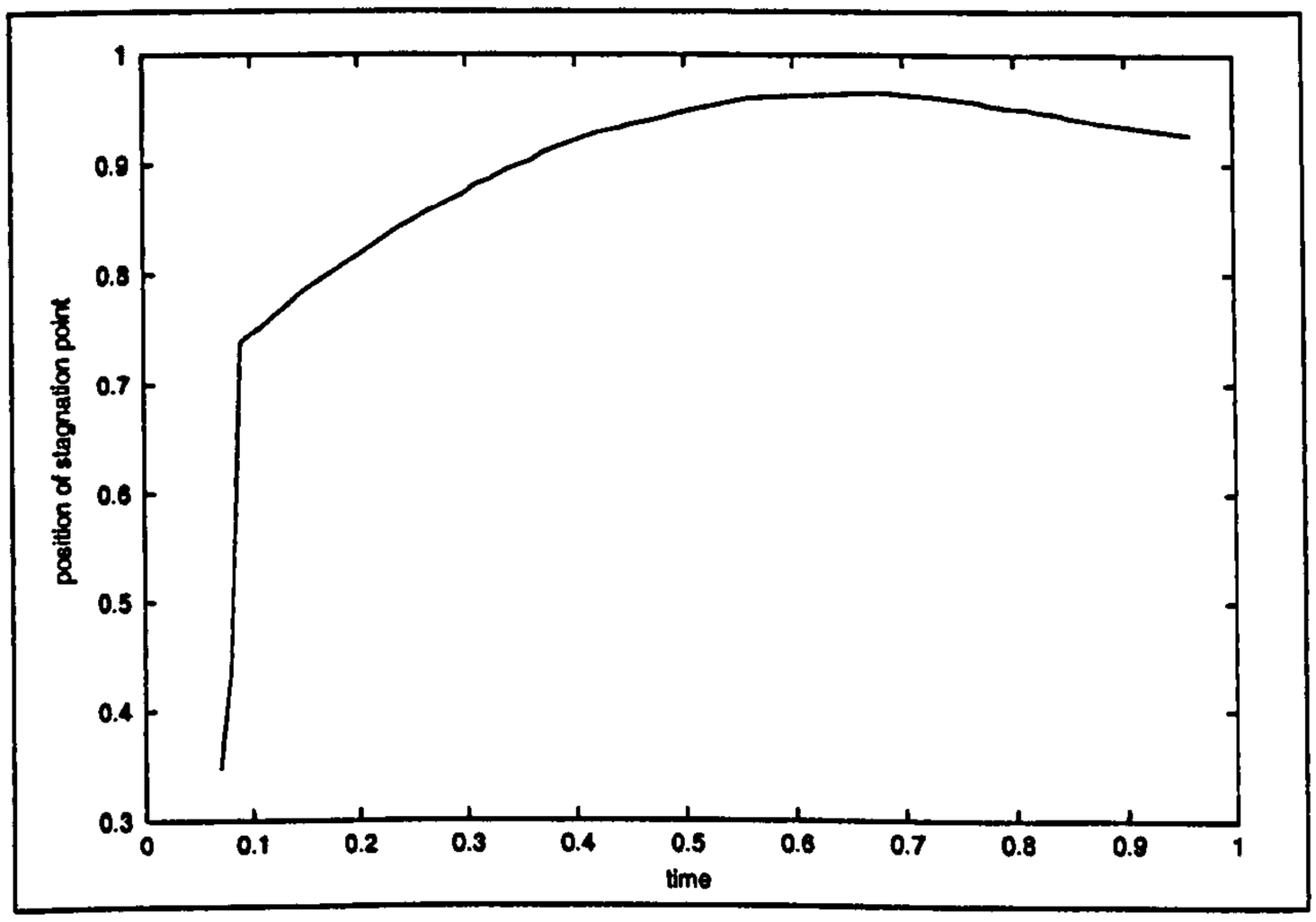


Figure 4.6: The evolution of the position of the stagnation point predicted by the thin film approximation when the zero shear rate viscosity is $\mu + G\tau = 1$ and $\gamma = 4$.

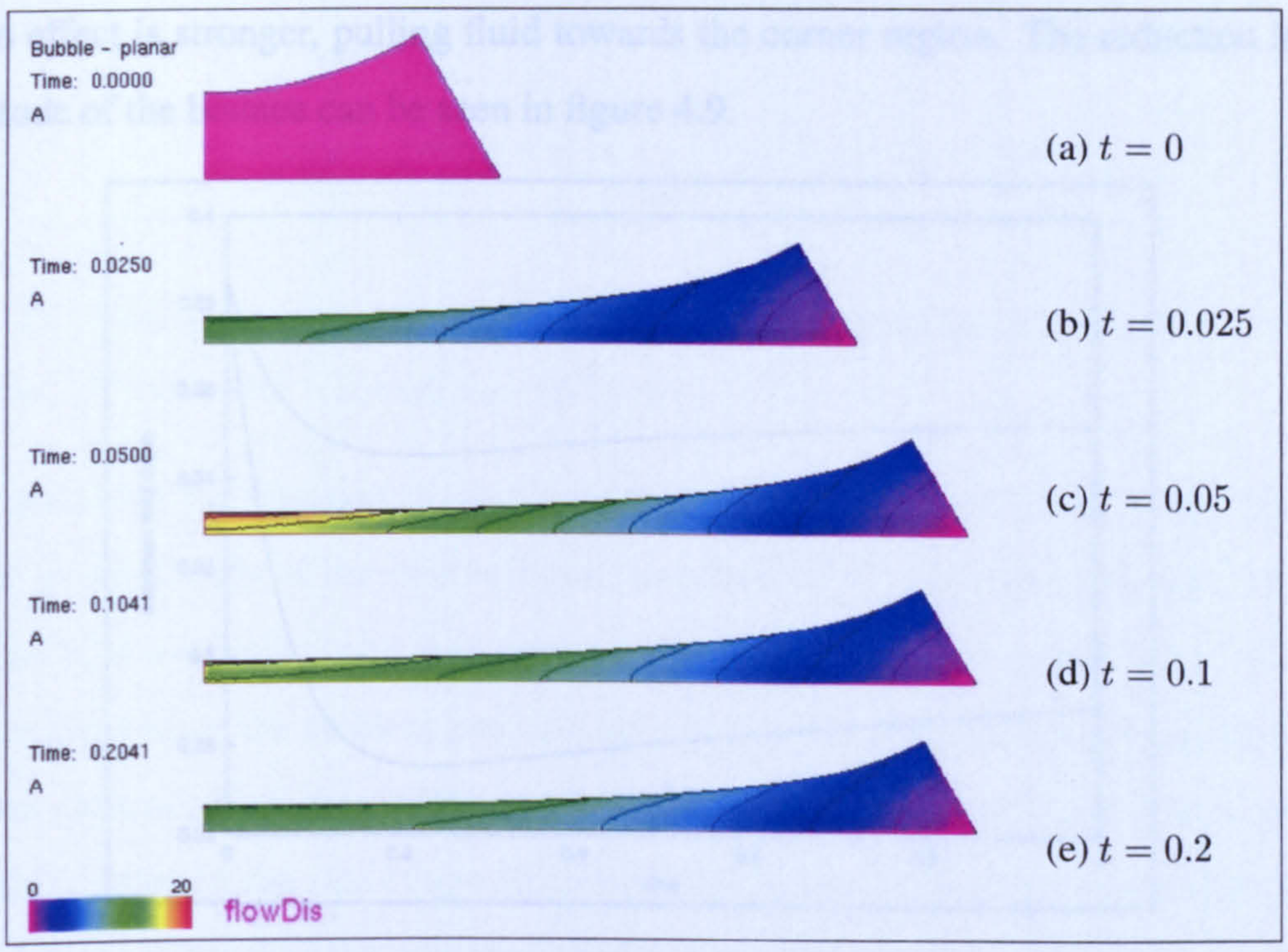


Figure 4.7: Polymer stress plotted as the difference in eigenvalues of **A** at: (a) $t = 0$; (b) $t = 0.025$; (c) $t = 0.05$; (d) $t = 0.1$; and (e) $t = 0.2$ with contour interval of 2.

and Lister [60] who include depth dependent, inter-molecular, forces.

In figure 4.8 we show the evolution of the fluid depth in the corner region in a Newtonian liquid. The bubble achieves its equilibrium area at $t = 0.3$, after which time surface tension acts to restore circular arcs by drawing fluid towards the corner region. In the viscoelastic case the initial expansion phase ends when the elastic stress balances the pressure difference, after which time there is competition between viscoelasticity and surface tension. For small capillary numbers the elastic recoil is lost as the surface tension effect is stronger, pulling fluid towards the corner region. The reduction in the magnitude of the bounce can be seen in figure 4.9.

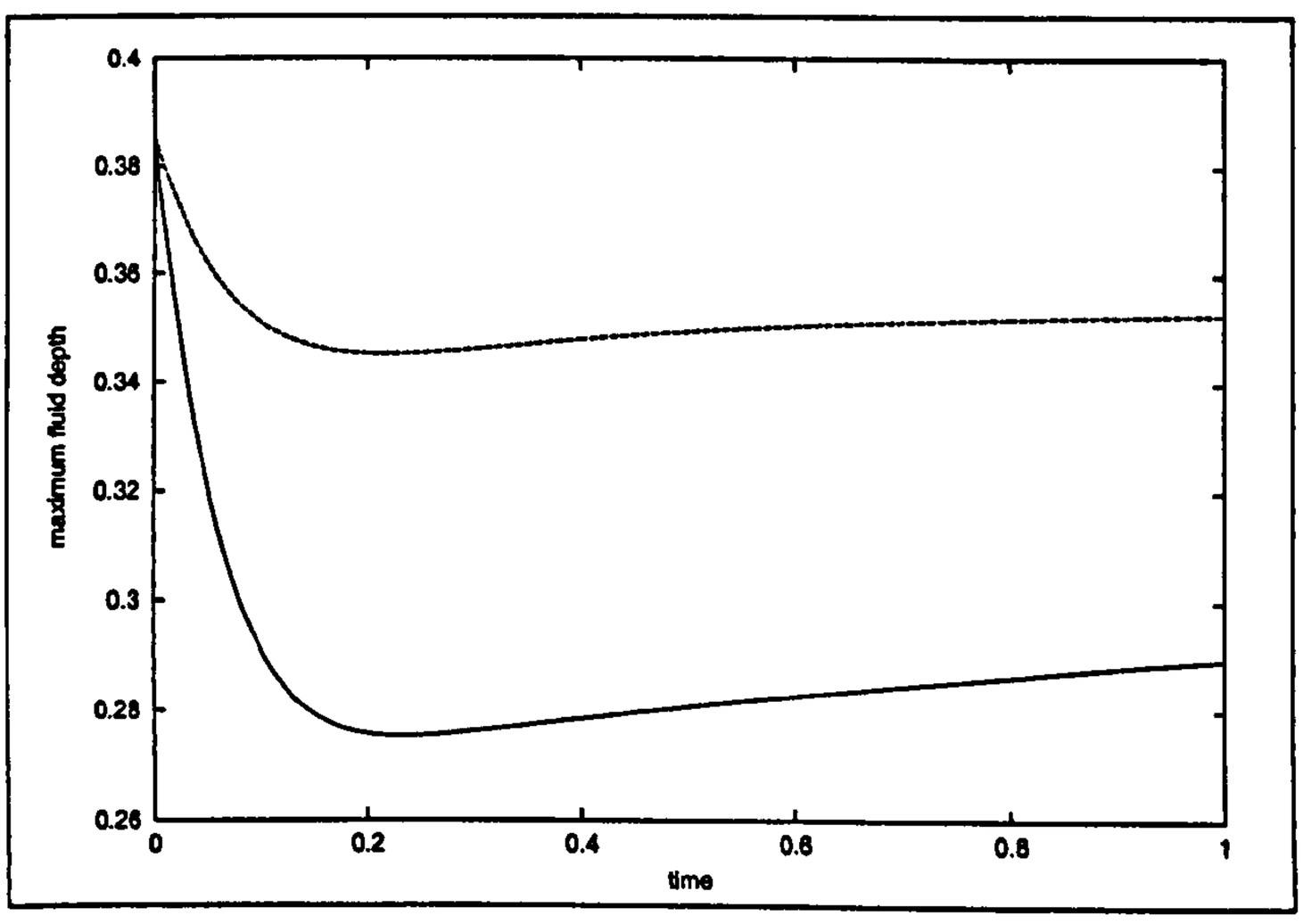


Figure 4.8: Diagram showing the effect of surface tension on the evolution of the maximum fluid depth in a Newtonian liquid. Solid line: $1/\Gamma = 1$; dashed line: $1/\Gamma = 6$

When the rate of gas diffusion across the fluid layer is slower than the viscous expansion time ($N \ll DeX$) the expansion is controlled by gas diffusion. In this limit viscoelastic effects are unimportant as the expansion is too slow to stretch the polymers. Consequently the results for a viscoelastic liquid are the same as for a Newtonian fluid. Figure 4.10 shows the effect of diffusivity on the bubble expansion rate. Here we increase the gas solubility by increasing the constant of proportionality in Henry's law, $H$, and reduce the initial gas pressure, $p_{g0}$, so that the expansion is

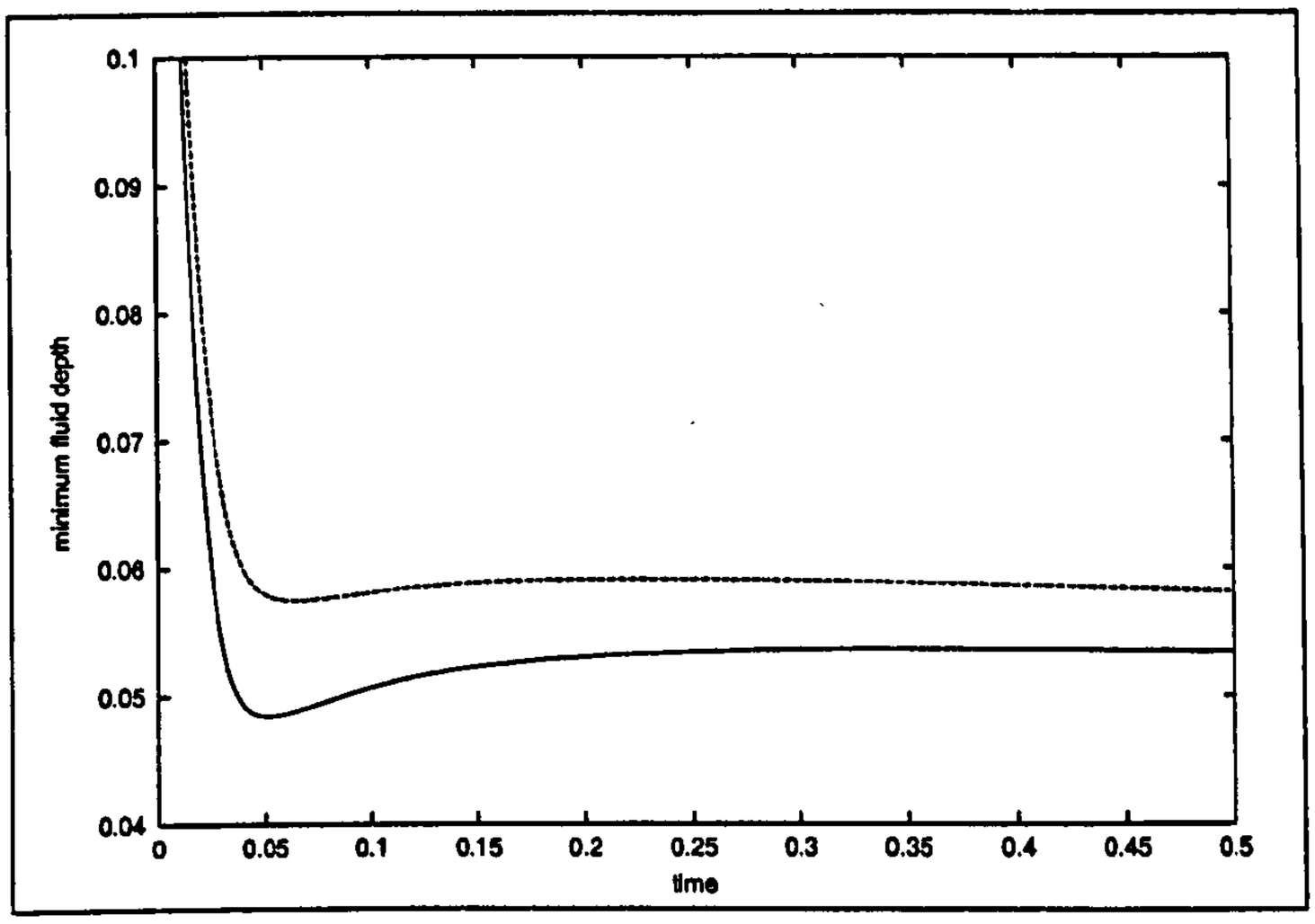


Figure 4.9: Evolution of the minimum fluid depth in a viscoelastic liquid: $\mu + G\tau = 1; \gamma = 4$. Solid line: $1/\Gamma = 5 \times 10^{-4}$; dashed line: $1/\Gamma = 5$.

driven mainly by the transport of gas from the liquid. The bubble expansion rate is small initially as the length of the bubble-liquid interface over which gas diffuses is small, increases to a maximum, and decreases towards the end of the expansion as the gas pressure approaches the ambient pressure and the gas concentration profile in the liquid becomes uniform. The $N = 0.001$ curve shows an initial expansion rate that is greater than that dictated by the rate of gas diffusion. This is caused by the over pressure in the bubble being greater than the rate of gas diffusion.

**Comparison of one-dimensional and circular approximations with the full two-dimensional simulations**

Each of the full two-dimensional simulations takes approximately 3 hours of CPU time on a 633MHz Pentium processor. We now consider whether accurate results may be obtained by using either the circular model presented in section 4.1.2 or the one-dimensional approximation presented in section 4.1.3.

We begin by checking the accuracy of all three models with an analytic solution. In

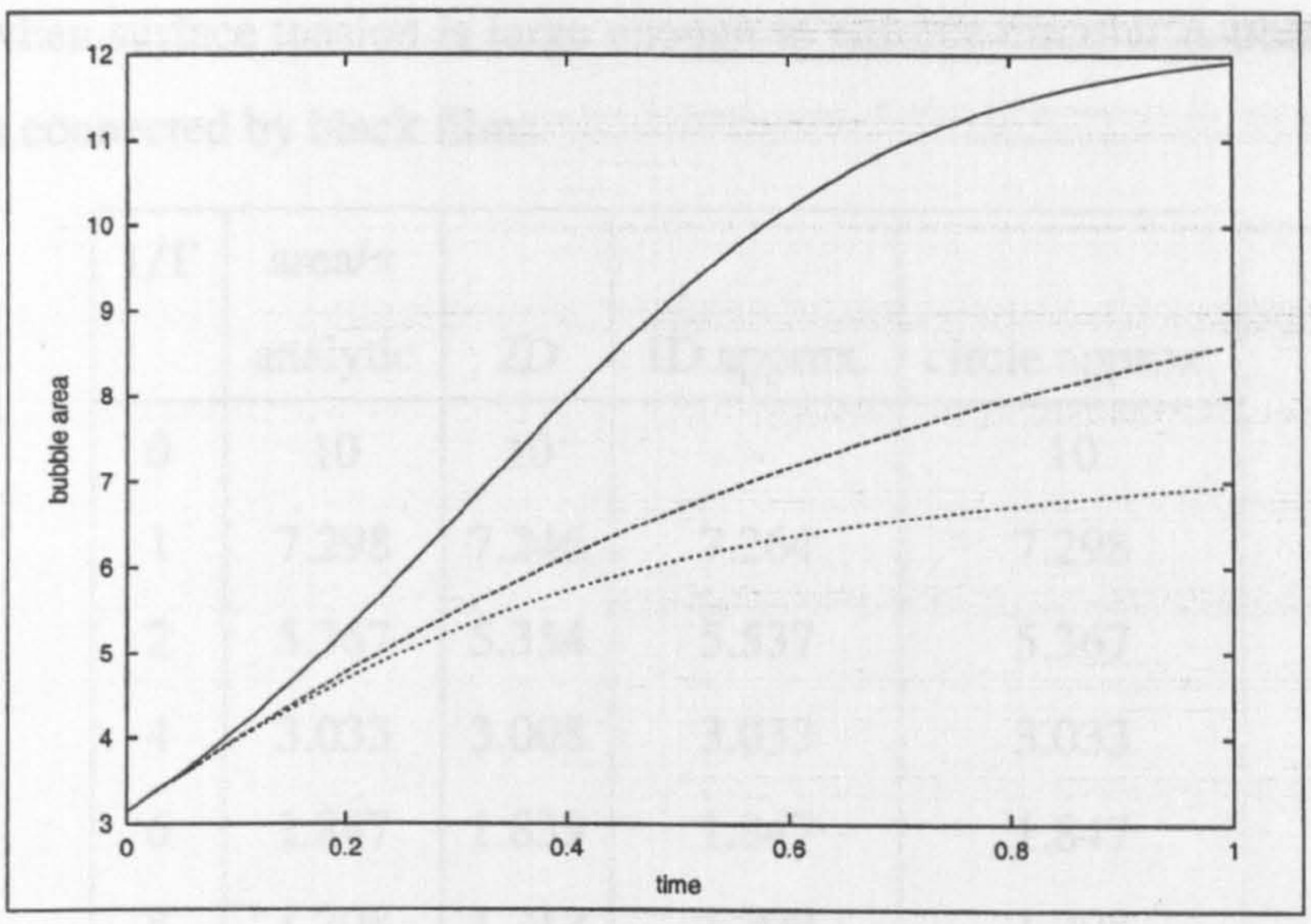


Figure 4.10: Effect of diffusivity on bubble area in a Newtonian liquid. Solid line: limit of infinite diffusion; dashed line: $N = 0.01$; dotted line: $N = 0.001$.

the absence of the $\Phi$ term the final bubble radius, $r$, can be predicted analytically. Since surface tension enforces a circular shape, as time tends to infinity surface tension balances the final gas pressure difference so that

$$P_g De - \frac{1}{\Gamma r} = 0$$

at the end of the expansion. Since diffusivity does not affect the final bubble area we substitute this into the conservation of mass equation (4.31) where $\frac{\sqrt{3}}{2}L^2 - A_f = \frac{\pi}{12}r^2$ to obtain an equation for the final bubble radius. In the case when $\Phi = 0$ this is

$$p_a r^2 + \frac{(p_{g0} - p_a)}{De\Gamma} r - p_{g0} = 0$$

Table 4.3 shows a comparison between analytic values and the equilibrium bubble area as predicted by the full two-dimensional model and the one-dimensional and circular approximations. The circular approximation predicts the final bubble area exactly though it cannot capture the shape of the bubble-liquid interface or the dynamics of the bubble area at intermediate times. The full two-dimensional simulation slightly under predicts the final area while the one-dimensional approximation predicts the final area

accurately when surface tension is large enough to enforce circular bubbles rather than circular arcs connected by black films.

| $1/\Gamma$ | area/$\pi$ analytic | 2D | 1D approx. | circle approx. |
|---|---|---|---|---|
| 0 | 10 | 10 | - | 10 |
| 1 | 7.298 | 7.246 | 7.264 | 7.298 |
| 2 | 5.367 | 5.354 | 5.537 | 5.367 |
| 4 | 3.033 | 3.008 | 3.033 | 3.033 |
| 6 | 1.847 | 1.839 | 1.847 | 1.847 |
| 8 | 1.208 | 1.212 | 1.209 | 1.208 |

Table 4.3: Effect of surface tension on the bubble area - comparison between analytic values and predictions from the two-dimensional simulations and one-dimensional and circular approximations. $\Phi = 0$, all other parameters as in table 4.1. Here the one-dimensional approximation has 50 computational elements and the circular approximation has 5. The two-dimensional simulation has 258 elements.

In figure 4.11 we compare the evolution of the bubble area for initial gas area fractions in the range $\beta = 0.1 - 0.75$ in the limit of infinite diffusion. The circular geometry provides an adequate description as long as the fluid layer is not too thin ($\beta < 0.75$) while the one-dimensional approximation is good provided that the liquid layer is not too deep ($\beta > 0.23$) and gas diffusion is effectively instantaneous ($N > DeX$).

In figure 4.12 we compare the shape of the bubble between the full simulation and the one-dimensional approximation in the limit of infinite diffusivity. The one-dimensional model reproduces qualitatively the behaviour seen with the full calculations including the elastic recoil behaviour. However, for small values of $\beta < 0.63$ it underestimates the difference in thickness between the thinnest and thickest parts of the film. Unlike the full two-dimensional calculations, the one-dimensional theory does not impose the $\pi/3$

tangent to the bubble surface at the point C where the free surface meets the edge of the next image. Consequently it appears easier to draw fluid out of the strut than is true in practice.

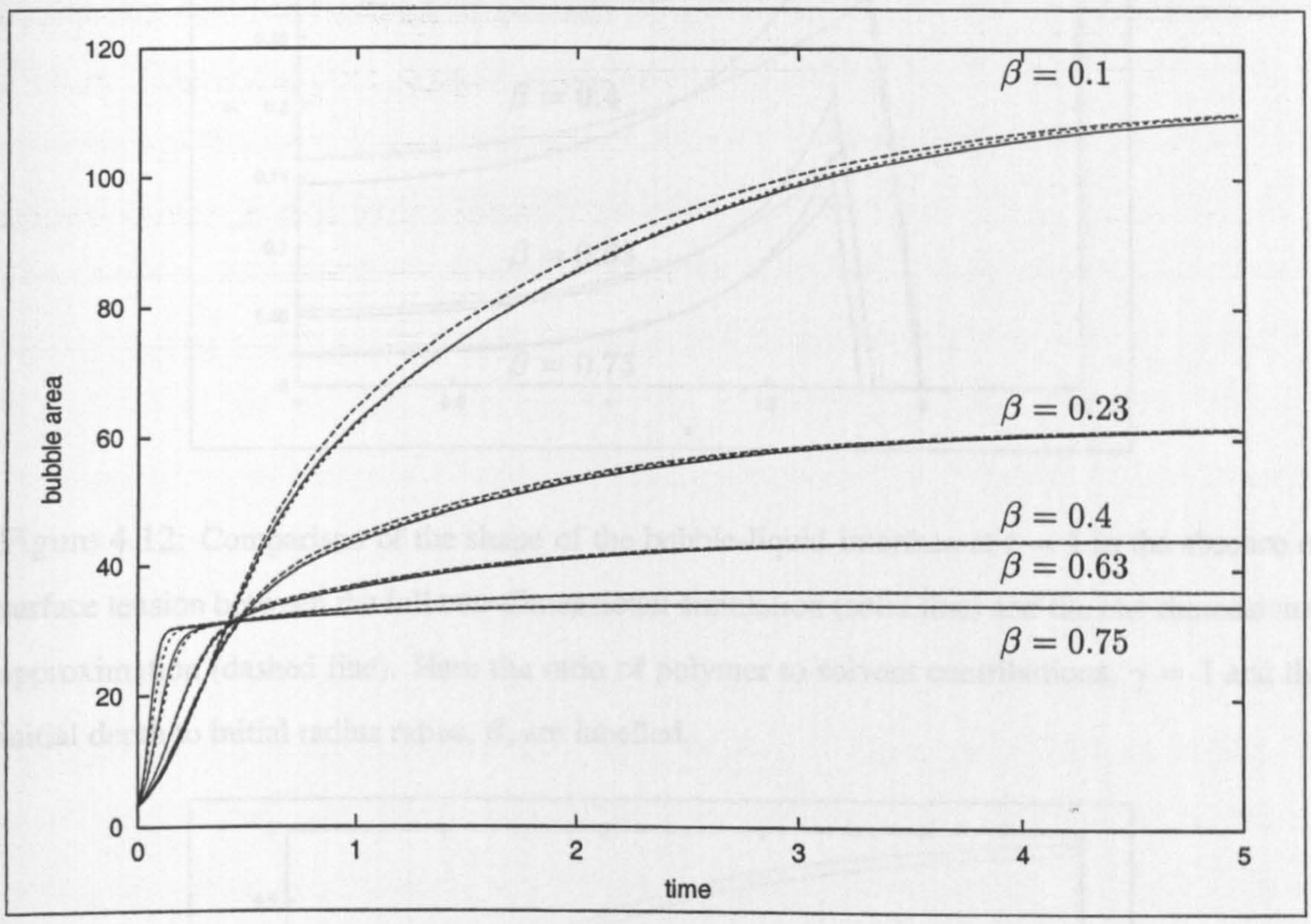


Figure 4.11: Evolution of the bubble area in the absence of surface tension comparing results obtained from the full two-dimensional simulation (solid line) with the one-dimensional approximation (dashed line) and circular approximation (dotted line). Here the ratio of polymer to solvent contributions, $\gamma = 1$ and the initial gas area fractions, $\beta$, are labelled.

If $\beta$ is small enough the presence of other bubbles will not affect the shape of the interface and bubbles will remain circular throughout the expansion. Figure 4.13 shows the evolution of the distance of the bubble centre to the edge of the interface in the middle and the corner of the liquid window (for circular bubbles the two are equal). We see that, with a surface tension of $1/\Gamma = 2$ and a ratio of $\beta \approx 0.1$ the expansion is closely predicted by the circular geometry until $t = 1$.

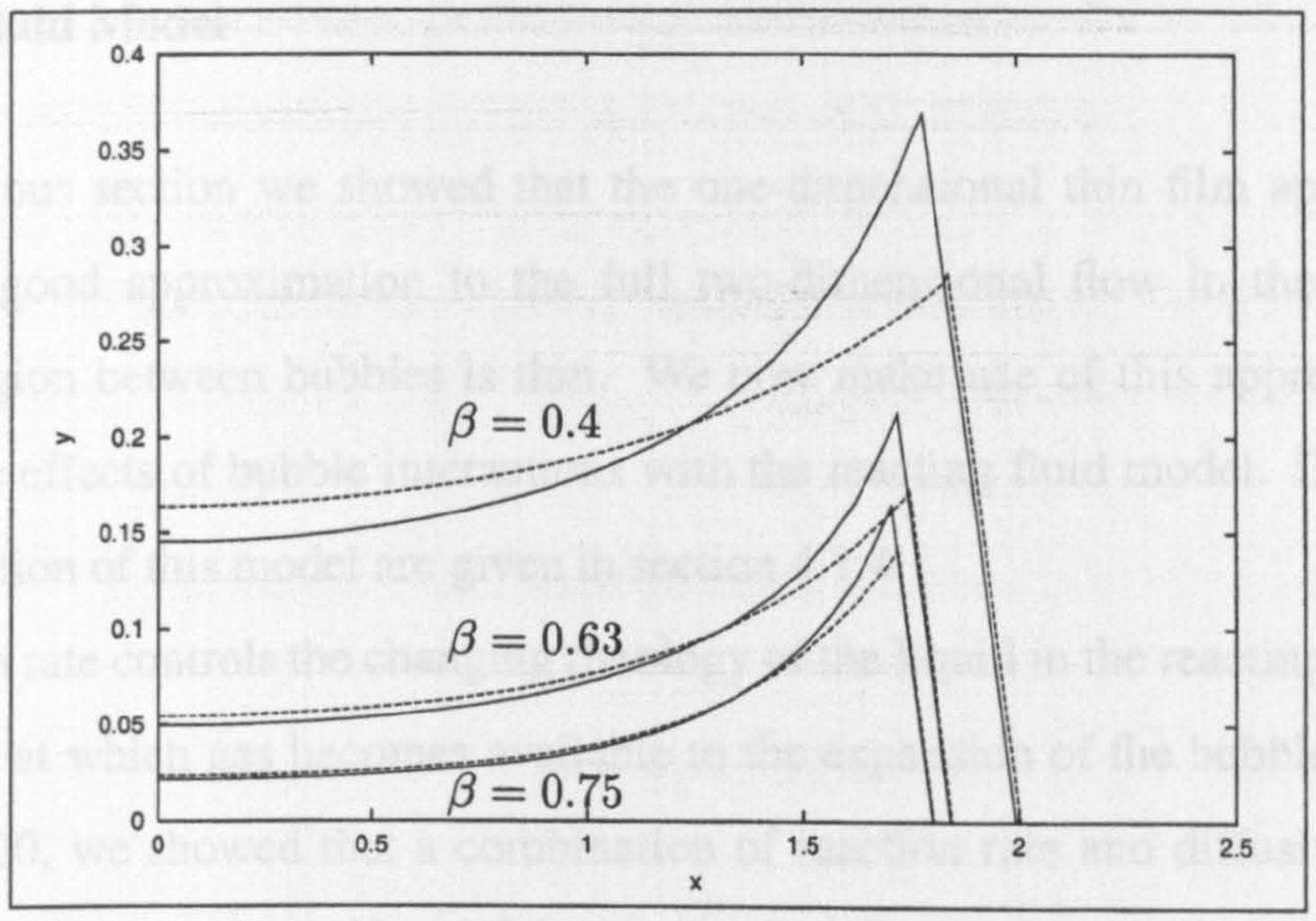


Figure 4.12: Comparison of the shape of the bubble-liquid interface at $t = 1$ in the absence of surface tension between the full two-dimensional simulation (solid line) and the one-dimensional approximation (dashed line). Here the ratio of polymer to solvent contributions, $\gamma = 1$ and the initial depth to initial radius ratios, $\beta$, are labelled.

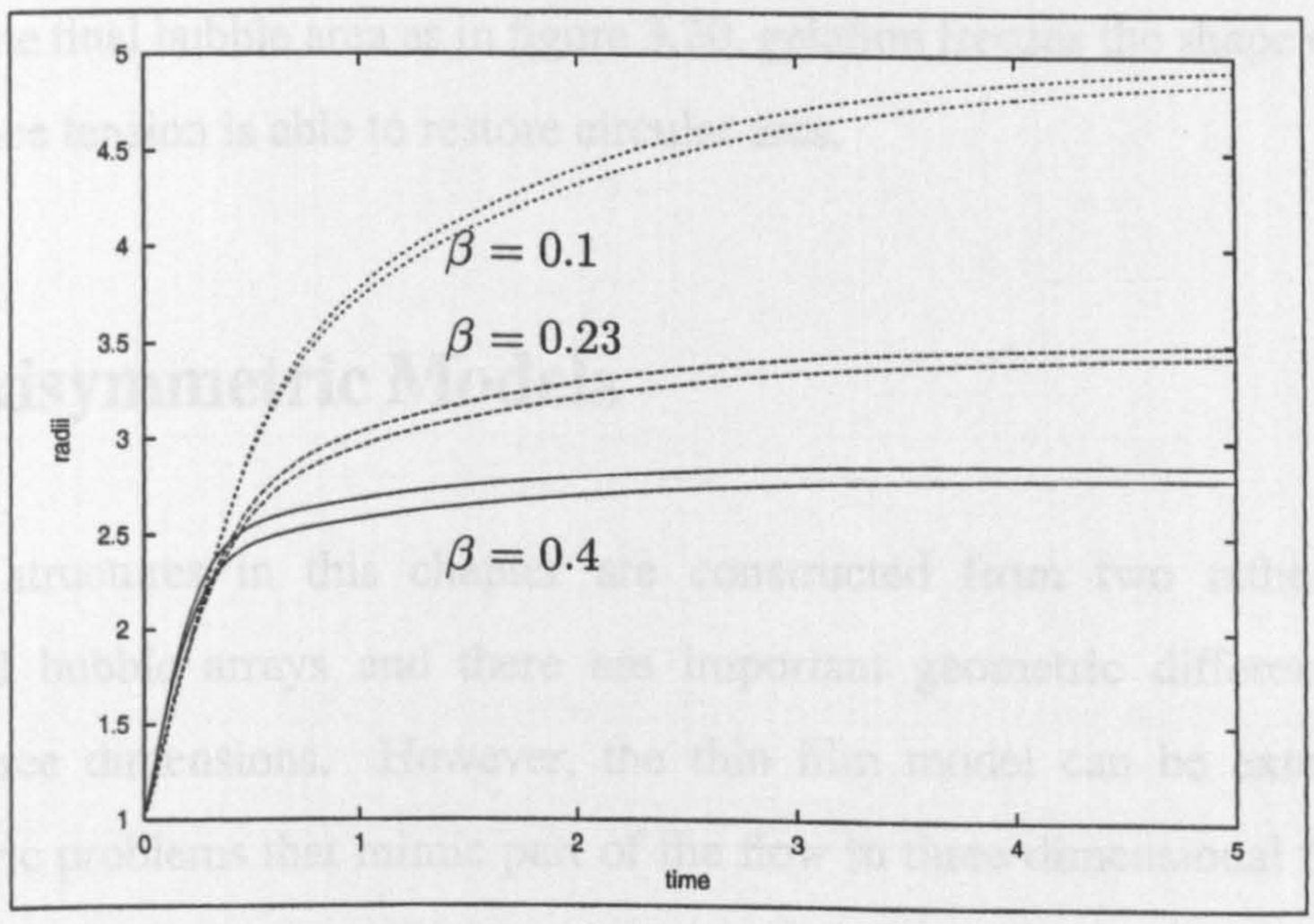


Figure 4.13: Evolution of the distance of the bubble centre to the middle and corner edges of the interface for the full two-dimensional simulation (solid line) and the one-dimensional approximation (dashed line). Here the ratio of polymer to solvent contributions, $\gamma = 1$ and the initial gas area fractions, $\beta$, are labelled.

### Reacting Fluid Model

In the previous section we showed that the one-dimensional thin film approximation provides a good approximation to the full two-dimensional flow in the limit when the fluid region between bubbles is thin. We now make use of this approximation to consider the effects of bubble interactions with the reacting fluid model. Details of the implementation of this model are given in section 4.1.4.

The reaction rate controls the changing rheology of the liquid in the reacting fluid model and the rate at which gas becomes available to the expansion of the bubble. In chapter 3, figure 3.20, we showed that a combination of reaction rate and diffusivity, through the dimensionless numbers $N$ and $M$ , dictate the volume the bubble is able to attain before gelation stops growth. Here we consider the limit of infinte diffusion, shown by the asymptotes in figure 3.20. Figure 4.14 shows the evolution of the distance from the bubble centre to the edges of the bubble-liquid interface in the middle of the liquid window and in the corner region for a value $M = 0.1$. Here we see that, in addition to restricting the final bubble area as in figure 3.20, gelation freezes the shape of the bubble before surface tension is able to restore circular arcs.

## 4.3 Axisymmetric Models

The foam structures in this chapter are constructed from two rather than three dimensional bubble arrays and there are important geometric differences between two and three dimensions. However, the thin film model can be extended to two axisymmetric problems that mimic part of the flow in three dimensional foams. In the first, the axis of symmetry is AB giving a geometry that represents a strut in an open cell foam (figure 4.15). In the second, the axis of symmetry is AC giving a geometry that represents a circularly symmetric section of the window between two bubbles (figure 4.16).

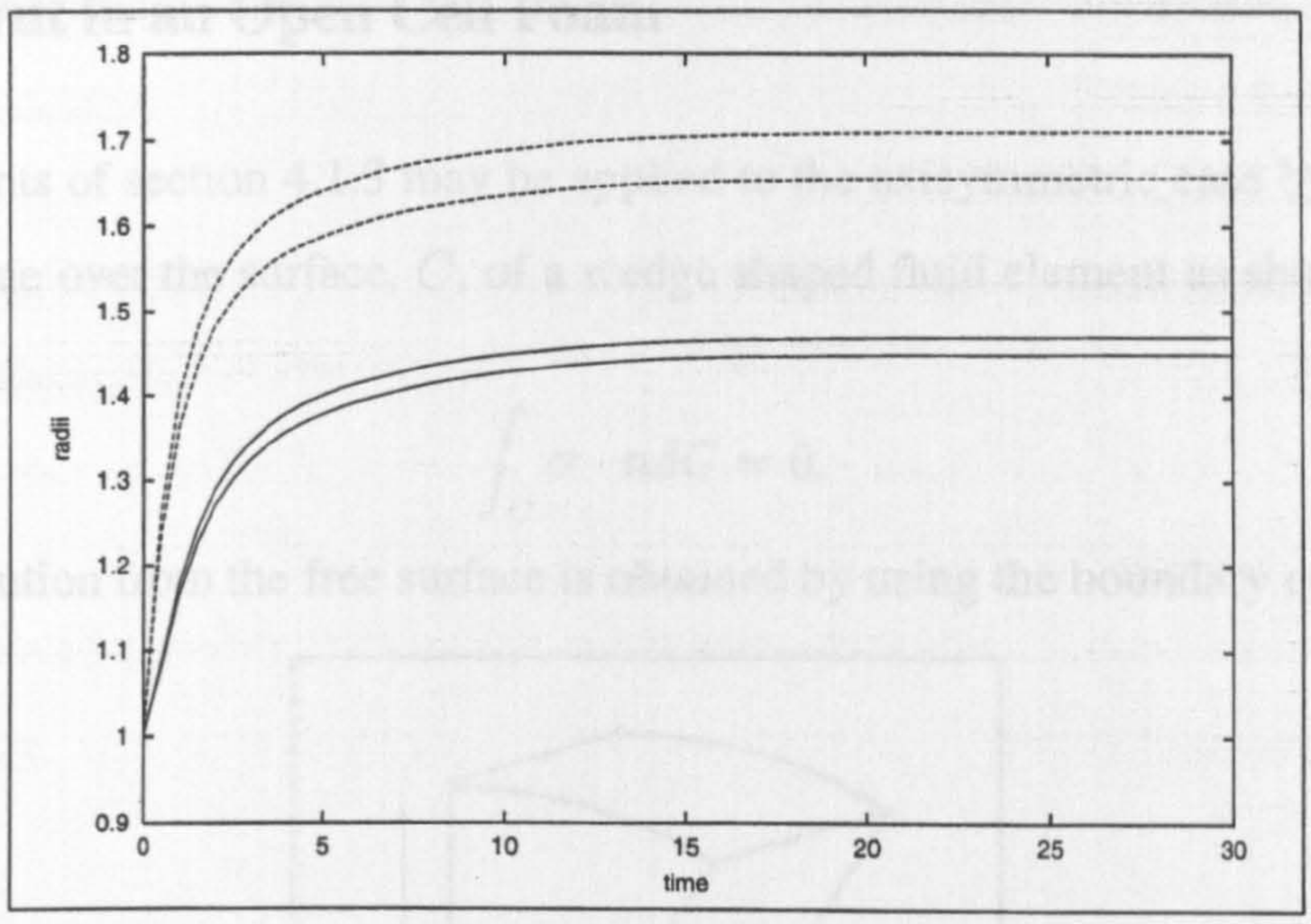


Figure 4.14: Diagram showing the evolution of the distance from the bubble centre to the edge of the bubble-liquid interface in the middle of the liquid window and in the corner region for a value $M = 0.1$. Solid lines: $1/\Gamma = 10$; dashed lines: $1/\Gamma = 5$.

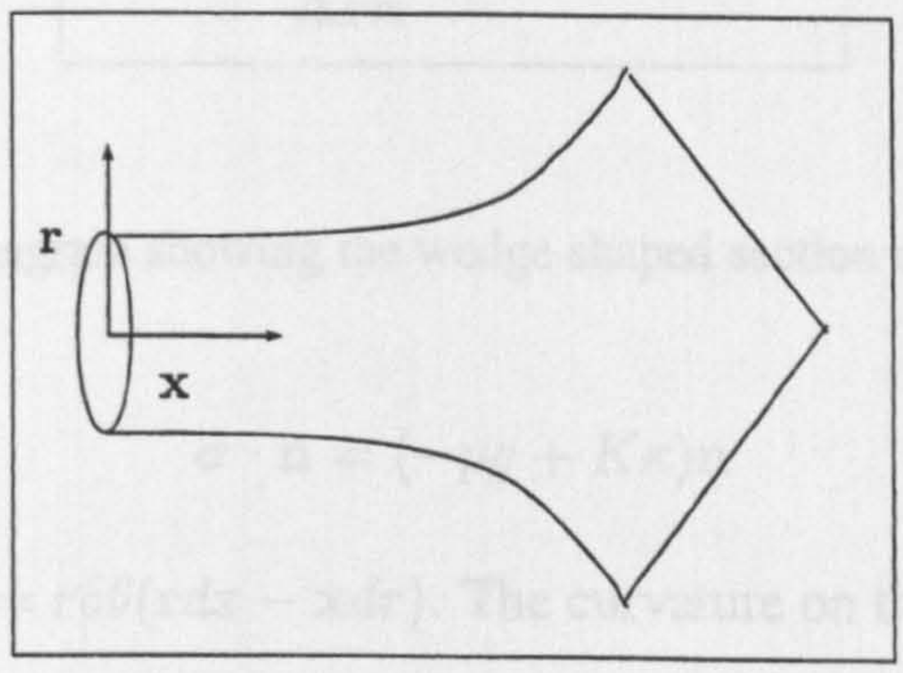


Figure 4.15: Diagram showing the axisymmetric model for a strut in an open cell foam.

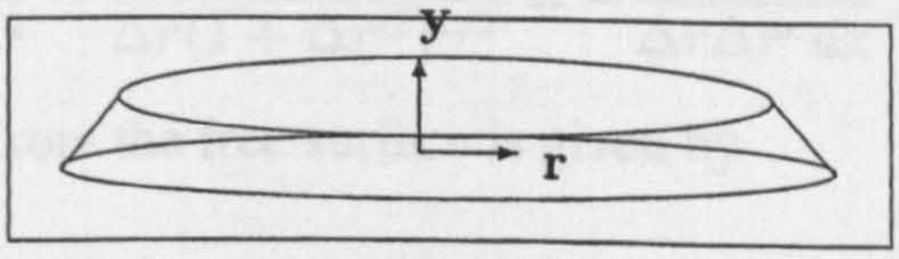


Figure 4.16: Diagram showing the axisymmetric model for a circularly symmetric section of window between two neighbouring bubbles.

### 4.3.1 Strut in an Open Cell Foam

The arguments of section 4.1.3 may be applied to the axisymmetric case by integrating the axial force over the surface, $C$, of a wedge shaped fluid element as shown in figure 4.17 so that

$$\int_C \boldsymbol{\sigma} \cdot \mathbf{n} dC = 0.$$

The contribution from the free surface is obtained by using the boundary condition

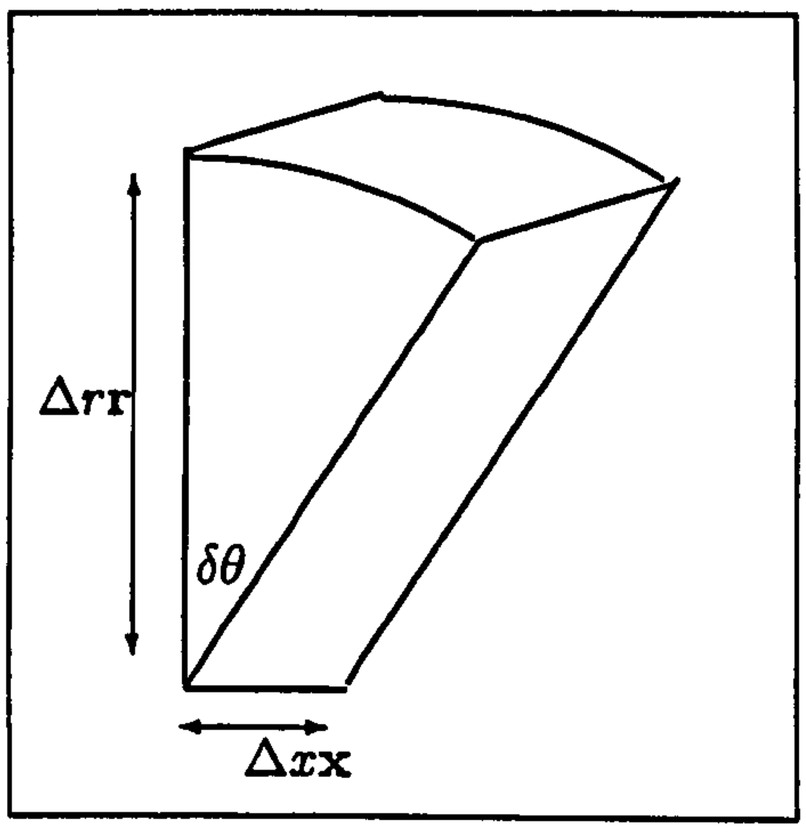


Figure 4.17: Diagram showing the wedge shaped section of a fluid element.

$$\boldsymbol{\sigma} \cdot \mathbf{n} = (-pg + K\kappa)\mathbf{n}$$

where the normal $\mathbf{n}dC = r\delta\theta(\mathbf{r}dx - \mathbf{x}dr)$. The curvature on the liquid-gas surface now has two terms. In addition to the longitudinal curvature there is a second term from the azimuthal curvature not found in the planar case. Thus

$$\kappa = \frac{\Delta r''}{(1+\Delta r'^2)^{3/2}} - \frac{1}{\Delta r(1+\Delta r'^2)^{1/2}} = -\frac{1}{\Delta r \Delta r'}\frac{d}{dx}\left(\frac{\Delta r}{(1+\Delta r'^2)^{1/2}}\right).$$

Hence the contribution from the free surface is given by

$$\begin{aligned}\delta\theta \quad & \left\{\int(-p_g + K\kappa)r dx\mathbf{r}\right. \\ - \quad & \left.\left(-\frac{1}{2}p_g(\Delta r_{i+1}^2 - \Delta r_i^2) - K\left(\frac{\Delta r_{i+1}}{(1+\Delta r_{i+1}'^2)^{1/2}} - \frac{\Delta r_i}{(1+\Delta r_i'^2)^{1/2}}\right)\right)\mathbf{x}\right\}.\end{aligned} \tag{4.35}$$

The contributions from the two edge faces with normal $\theta$ combine to give

$$-\delta\theta \int \sigma_{\theta\theta} r \, dx\mathbf{r}.$$

In this uniaxial extension flow $\sigma_{\theta\theta} = \sigma_{rr}$ and balancing the $\mathbf{r}$ componants from the free surface and the edge faces gives

$$\sigma_{\theta\theta} = \sigma_{rr} = -p_g + K\kappa. \tag{4.36}$$

The circular sectional face with normal $\mathbf{x}$ contributes a term

$$\int \sigma_{xx} r dr d\theta \mathbf{x},$$

which can be written

$$\delta\theta \left\{ \int_0^{\Delta r_{i+1}} (S_{xx} - S_{rr})\, r dr + \int_0^{\Delta r_{i+1}} \sigma_{rr} r dr \right\}.$$

Substituting $\sigma_{rr}$ from equation 4.36 and evaluating the integral gives

$$\frac{\delta\theta}{2} \left( (S_{xx} - S_{rr})_{i+1} \Delta r_{i+1}^2 + (-p_g + K\kappa_{i+1}) \Delta r_{i+1}^2 \right),$$

with a similar expression for the term arising from the other circular sectional face.

Combining the $\mathbf{x}$ components gives the following non-dimensional force balance on each fluid element

$$\Psi_{i+1} = \Psi_i - \frac{1}{\Gamma} \left( \frac{\Delta r_{i+1}}{(1 + \Delta r_{i+1}'^2)^{1/2}} + \frac{\Delta r_{i+1}'' \Delta r_{i+1}^2}{(1 + \Delta r_{i+1}'^2)^{3/2}} - \frac{\Delta r_i}{(1 + \Delta r_i'^2)^{1/2}} - \frac{\Delta r_i'' \Delta r_i^2}{(1 + \Delta r_i'^2)^{3/2}} \right) \tag{4.37}$$

where $\Psi = (S_{xx} - S_{rr}) \Delta r^2$.

Though this geometry represents a strut in an open cell foam we assume that there is a 'skin' round the outside of the foam so that gas pressure is prevented from leaking away allowing it to drive the expansion. We can, again, link the pressure difference, $P_g$, to the stress in the liquid:

$$\sum_i \frac{1}{6} \left( (S_{xx} - S_{rr})_{i+1} + (S_{xx} - S_{rr})_i \right) \dot{\Delta x}_i (\Delta r_{i+1}^2 + \Delta r_{i+1} \Delta r_i + \Delta r_i^2) =$$

$$3 P_g De L^2 \frac{dL}{dt} - \frac{1}{\Gamma} \sum_i \frac{dC_i}{dt}. \tag{4.38}$$

Conservation of fluid area gives

$$\frac{\dot{\Delta x}}{\Delta x} = -\frac{2\Delta r_{i+1}\dot{\Delta r}_{i+1} + \Delta r_{i+1}\dot{\Delta r}_i + \dot{\Delta r}_{i+1}\Delta r_i + 2\Delta r_i\dot{\Delta r}_i}{\Delta r_{i+1}^2 + \Delta r_{i+1}\Delta r_i + 2\Delta r_i^2} \tag{4.39}$$

and gas pressure is now given by

$$(p_{g0} - p_a)P_g = p_{g0}\left(\frac{\pi {L_0}^3 - X + \Phi X}{\pi L^3 - X + \Phi X}\right) - p_a. \tag{4.40}$$

The Oldroyd B model gives an expression for $S_{xx} - S_{rr}$:

$$S_{xx} - S_{rr} = -3\frac{\dot{\Delta r}}{\Delta r} + \gamma(A_{xx} - A_{rr}),$$

where the evolution of **A** is governed by

$$\begin{aligned} \dot{A_{rr}} &= 2\frac{\dot{\Delta r}}{\Delta r}A_{rr} - (A_{rr} - 1) \\ (\dot{A_{rr}} - \dot{A_{xx}}) &= -4\frac{\dot{\Delta r}}{\Delta r}((A_{rr} - A_{xx}) + 3A_{rr}) - (A_{rr} - A_{xx}). \end{aligned} \tag{4.41}$$

### 4.3.2 Circularly Symmetric Section of the Window Between Two Bubbles

For the second axisymmetric case we integrate the momentum equation, using the divergence theorem, round the section of fluid element of surface $C$ shown in figure 4.18 so that

$$\int_C \boldsymbol{\sigma} \cdot \mathbf{n} dC = 0.$$

Contributions from the outer and inner curved surfaces are given by

$$(\delta\theta\sigma_{rr,i+1}r_{i+1}\Delta y_{i+1} - \delta\theta\sigma_{rr,i}r_i\Delta y_i)\,\mathbf{r} \tag{4.42}$$

The contribution from the free surface is obtained using the boundary condition $\boldsymbol{\sigma}.\mathbf{n} = (-p_g + K\kappa)\mathbf{n}$ where $\mathbf{n} = r\delta\theta(\mathbf{y}dr - \mathbf{r}dy)$.

There are, again, two curvature terms contributing to the surface tension, giving

$$\kappa = \frac{\Delta y''}{(1 + \Delta y'^2)^{3/2}} + \frac{\Delta y'}{r(1 + \Delta y'^2)^{1/2}}.$$

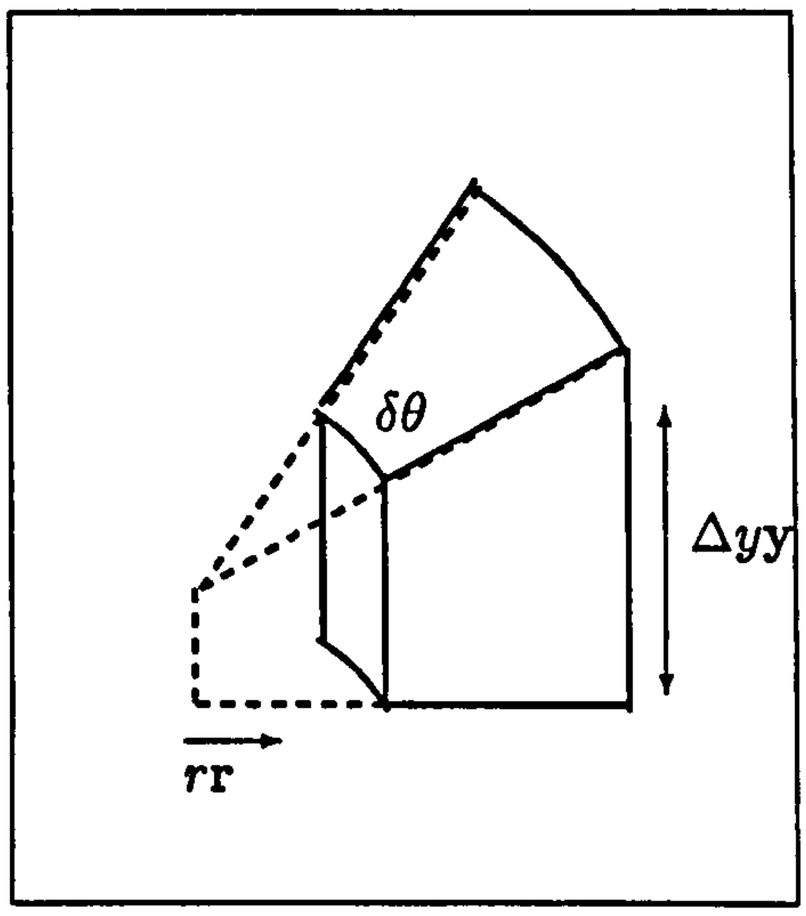


Figure 4.18: Diagram showing the section of fluid element used to obtain a force balance.

From the bottom surface we obtain

$$-\delta\theta \int \sigma_{yy} r \, dry.$$

and the two edge faces combine to contribute

$$-\delta\theta \int \sigma_{\theta\theta} \Delta y \, drr.$$

The force balance in the y direction gives

$$-p_g + K\kappa - \sigma_{yy} = 0.$$

Substituting this into the r force balance to eliminate the fluid pressure, and using the symmetry condition $\sigma_{\theta\theta} = \sigma_{rr}$, gives the following force balance

$$\Psi_{i+1}(r_{i+1} + r_i) = \Psi_i(r_{i+1} + r_i) - \frac{1}{\Gamma}(\kappa_{i+1} - \kappa_i)(r_i \Delta y_{i+1} + r_{i+1} \Delta y_i) \qquad (4.43)$$

where $\Psi = (S_{rr} - S_{yy})\Delta y$. From the work done we obtain

$$\sum_i (\Upsilon_{i+1} + \Upsilon_i) \left( r_{i+1}^2 \Delta y_{i+1} - r_i^2 \Delta y_i - \frac{1}{3}(r_{i+1}^2 + r_{i+1} r_i + r_i^2)(\Delta y_{i+1} - \Delta y_i) \right) = \sqrt{3} P_g De L^2 \frac{dL}{dt} - \frac{1}{\Gamma} \sum_i \frac{dC_i}{dt}. \qquad (4.44)$$

where $\Upsilon = (S_{rr} - S_{yy})\dot{r}/r$. The gas pressure is obtained from mass conservation as:

$$(p_{g0} - p_a)P_g = p_{g0}\left(\frac{\frac{\sqrt{3\pi}}{3}L_0{}^3 - X + \Phi X}{\frac{\sqrt{3\pi}}{3}L^3 - X + \Phi X}\right) - p_a. \tag{4.45}$$

In this geometry conservation of fluid volume is given by

$$\begin{aligned}
&\dot{r}_{i+1}\left(2r_{i+1}\Delta y_{i+1} - \frac{1}{3}(2r_{i+1} + r_i)(\Delta y_{i+1} - \Delta y_i)\right) + \frac{1}{3}\dot{\Delta y}_{i+1}\left(2r_{i+1}^2 - r_{i+1}r_i - r_i^2\right) \\
&\quad = \dot{r}_i\left(2r_i\Delta y_i + \frac{1}{3}(r_{i+1} + 2r_i)(\Delta y_{i+1} - \Delta y_i)\right) + \frac{1}{3}\dot{\Delta y}_i\left(-r_{i+1}^2 - r_{i+1}r_i + 2r_i^2\right).
\end{aligned} \tag{4.46}$$

For the Oldroyd B model the stress difference in the liquid is given by

$$S_{rr} - S_{yy} = -3\frac{\dot{\Delta y}}{\Delta y} + \gamma(A_{rr} - A_{yy}),$$

with $A_{rr}$ and $A_{yy}$ satisfying

$$\begin{aligned}
\dot{A_{yy}} &= 2\frac{\Delta y}{\Delta y}A_{yy} - (A_{yy} - 1) \\
(\dot{A_{rr}} - \dot{A_{yy}}) &= -\frac{\dot{\Delta y}}{\Delta y}((A_{rr} - A_{yy}) + 3A_{yy}) - (A_{rr} - A_{yy}).
\end{aligned} \tag{4.47}$$

### 4.3.3 Results and Discussion

The method of solution is as described in section 4.1.3 for the one-dimensional model of planar flow.

In the planar case the surface tension arising from the curvature of the bubble-liquid interface acts to restore circular bubbles and to limit the size of the bubble by modifying the bubble gas pressure. In the axisymmetric geometries the presence of the extra curvature adds a second surface tension term. In the case of the liquid strut it acts in the opposite direction, providing an additional driving force proportional to $1/\Delta r$. In a Newtonian fluid, expansion is divided into two phases as the two surface tension terms compete against each other. This can be seen in figure 4.19. During the first phase the longitudinal surface tension is dominant and so the strut extends at a rate controlled by

a modified gas pressure difference. At the end of this phase the longitudinal surface tension balances the gas pressure difference and the azimuthal term becomes dominant. As the strut becomes thinner this term increases in magnitude and eventually the strut breaks. In figure 4.20 we show the evolution of the minimum and maximum fluid depths in the case when $1/\Gamma = 2$. In the planar case this bubble would shrink due to surface tension. Here, however, the azimuthal surface tension causes the narrow end of the strut to thin while the interface surface tension causes the wide end of the strut to increase in depth.

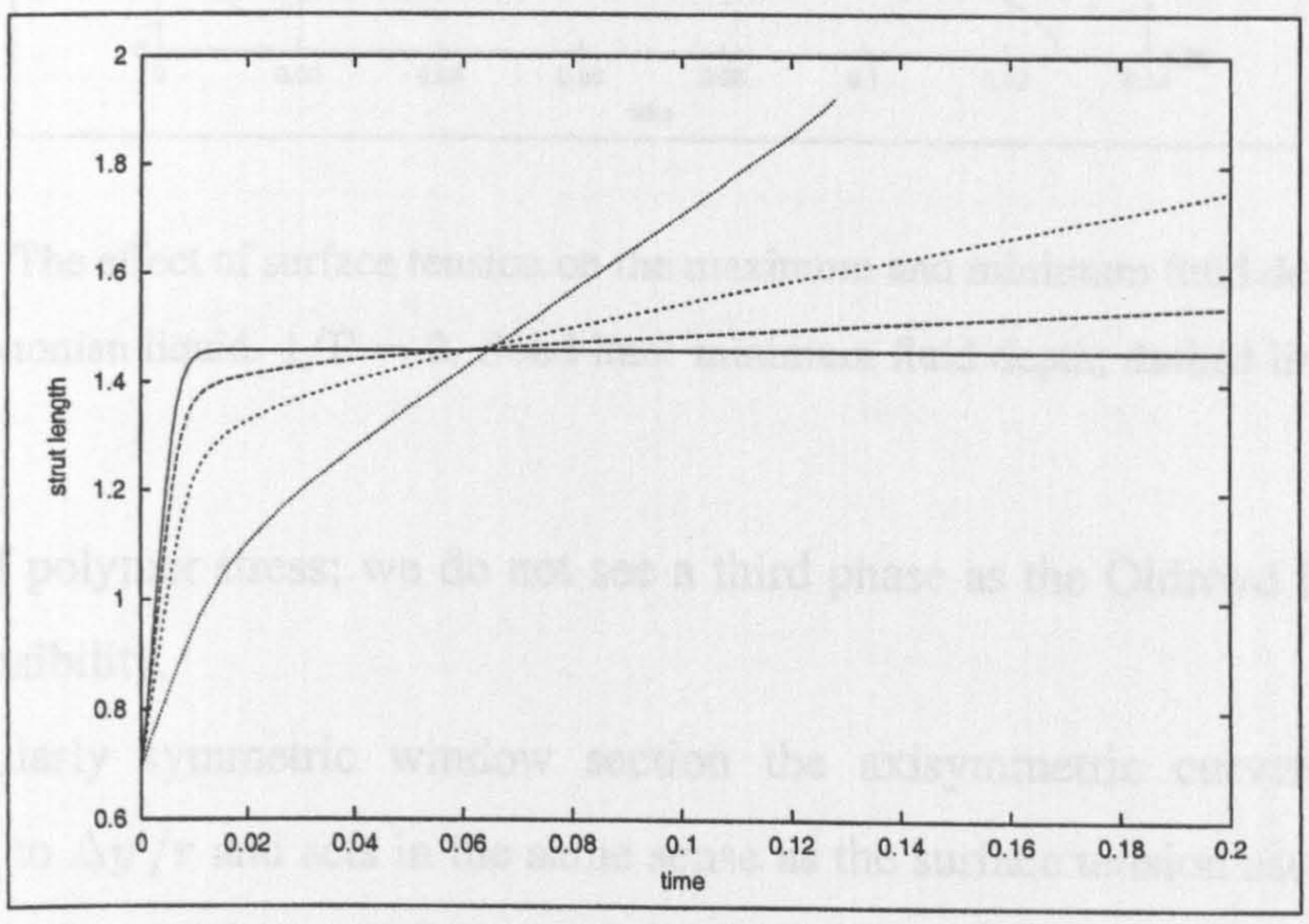


Figure 4.19: The effect of surface tension on the length of a fluid strut in a Newtonian liquid. Solid line: $1/\Gamma = 0.0001$; long dashed line: $1/\Gamma = 0.4$; short dashed line: $1/\Gamma = 1$; dotted line: $1/\Gamma = 2$.

Entov and Hinch [15] investigate the special case of a cylindrical filament of a FENE fluid stretching due to the capillary pressure alone. They found that the filament evolution could be divided into three phases. In the first phase the stretching is resisted by the solvent viscosity. In the second phase the resistance is provided by the polymer stress. In the final phase the finite extensibility of the polymers leads to filament break-up. The lengthening of our strut shows very similar behaviour through the first two phases (figure 4.21): a rapid viscous phase followed by a slower phase controlled by the

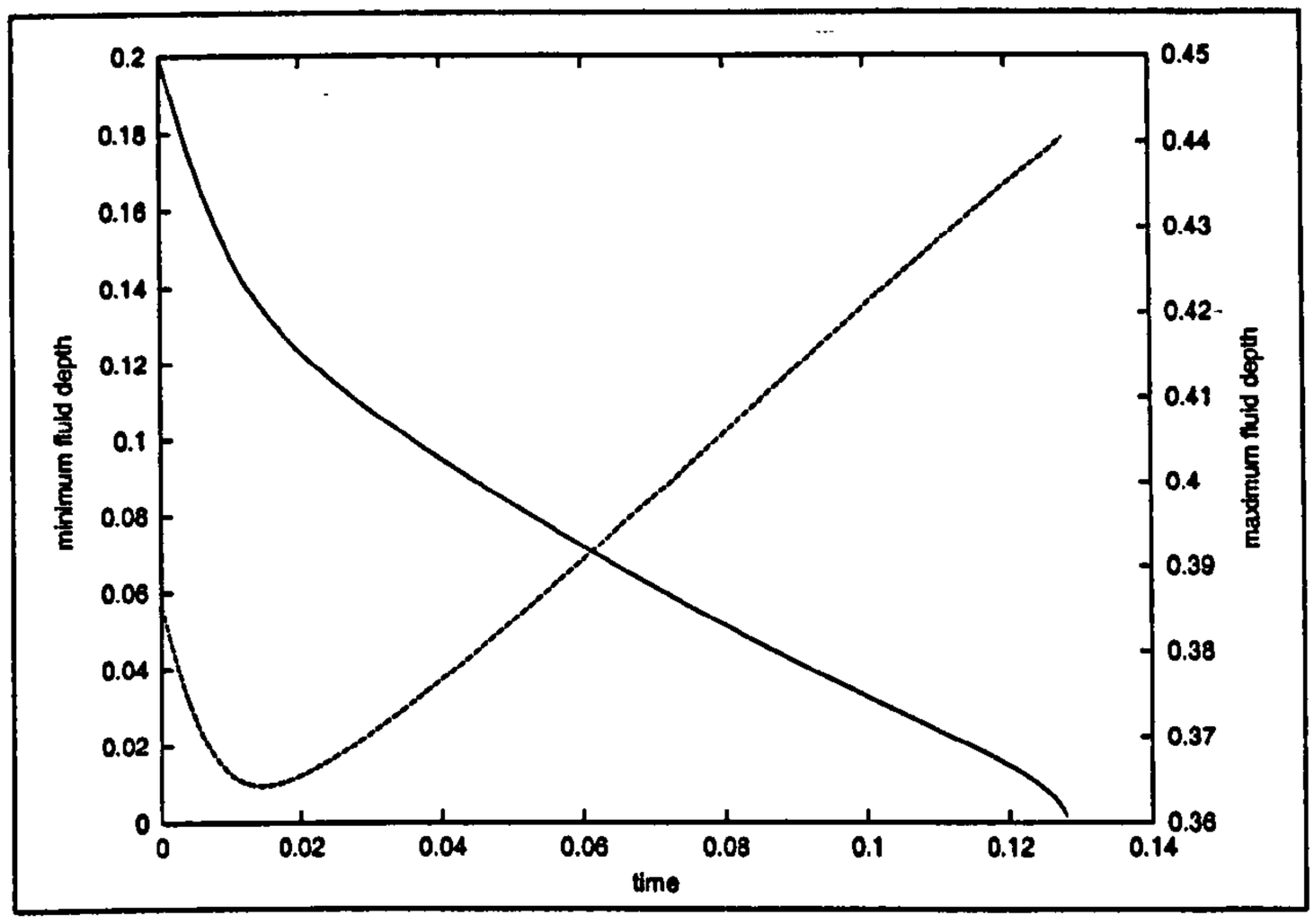


Figure 4.20: The effect of surface tension on the maximum and minimum fluid depths in a fluid strut in a Newtonian liquid. $1/\Gamma = 2$. Solid line: minimum fluid depth; dashed line: maximum fluid depth.

relaxation of polymer stress; we do not see a third phase as the Oldroyd B model has infinite extensibility.

In the circularly symmetric window section the axisymmetric curvature term is proportional to $\Delta y'/r$ and acts in the same sense as the surface tension associated with the interface, thus inhibiting bubble growth. Surface tension in the planar case has little effect on the initial expansion rate. However, the axisymmetric surface tension pulls liquid back towards the centre of the window, reducing the bubble growth rate throughout the expansion. Figure 4.22 shows how the additional surface tension term exaggerates the inhibiting effect causing the bubble to shrink, instead of expand, at much larger values of the capillary number. In the planar geometry, for the parameter values chosen, bubble expansion occurs provided that $1/\Gamma < 9$; in this circularly symmetric window geometry, expansion only occurs, with the parameters of table 3.2, for $1/\Gamma < 3$. Viscoelasticity affects the expansion in the same way as in the planar case, dividing it into an initial viscous phase and a second phase controlled by the polymer relaxation rate.

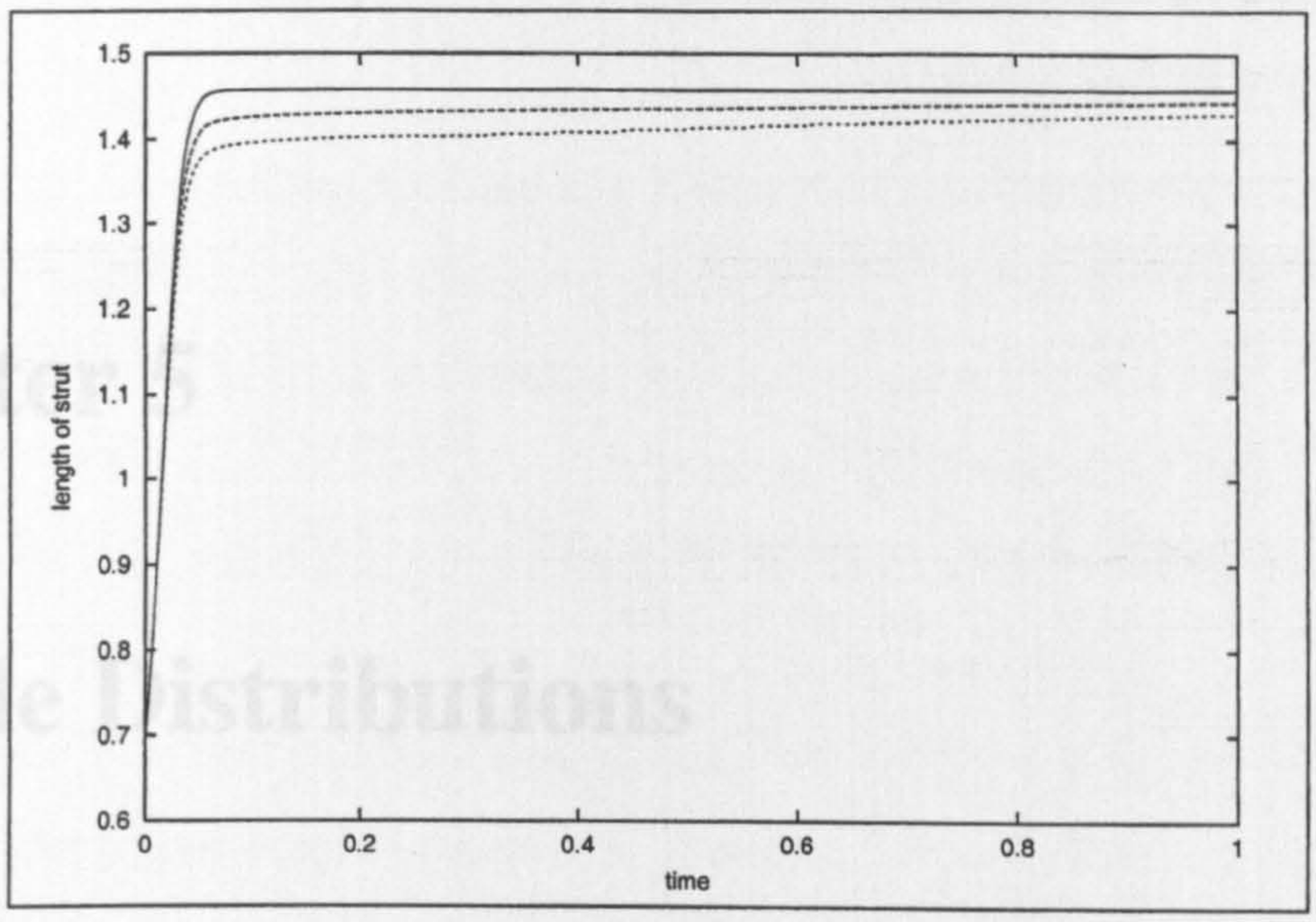


Figure 4.21: The effect of viscoelasticity on the evolution of the length of a fluid strut in the limit of large capillary number. Solid line: $\gamma = 0$; dashed line: $\gamma = 10$; dotted line: $\gamma = 20$.

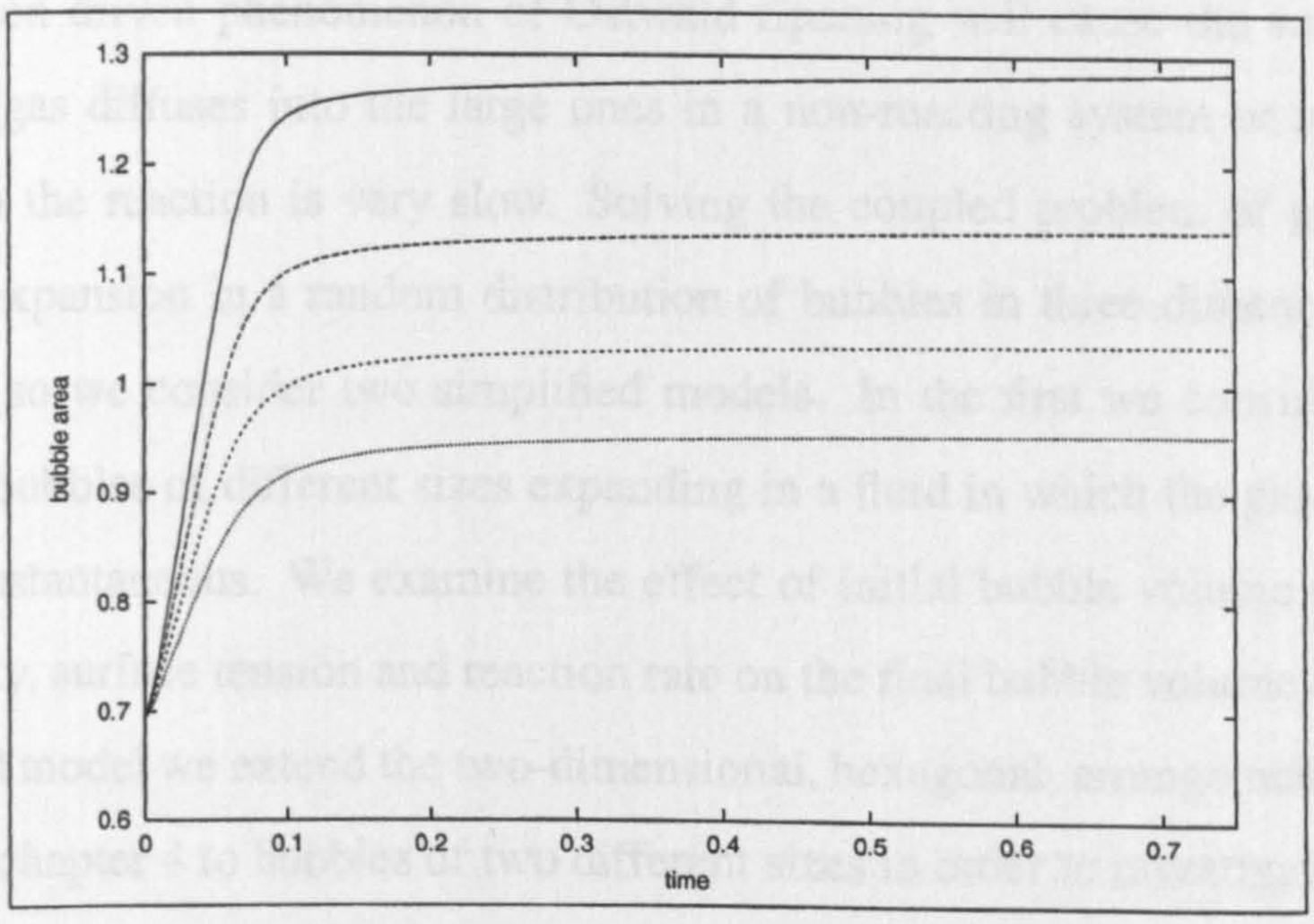


Figure 4.22: The evolution of the length of the circularly symmetric section of the bubble window against time (second axisymmetric model) for a viscoelastic liquid with $\gamma = 4$. Solid line: $1/\Gamma = 0.0001$; long-dashed line: $1/\Gamma = 0.5$; short-dashed line: $1/\Gamma = 1$; dotted line: $1/\Gamma = 1.5$.

# Chapter 5

# Bubble Distributions

So far in this thesis we have examined the expansion of foams consisting of identical gas bubbles. In this chapter we consider foams consisting of bubbles of unequal size to analyse the competition for the available gas in the liquid. It is expected that the surface tension driven phenomenon of Ostwald ripening will cause the small bubbles to shrink as gas diffuses into the large ones in a non-reacting system or in a reacting system when the reaction is very slow. Solving the coupled problem of gas diffusion and bubble expansion in a random distribution of bubbles in three dimensions is very difficult and so we consider two simplified models. In the first we consider a system of spherical bubbles of different sizes expanding in a fluid in which the gas diffusion is effectively instantaneous. We examine the effect of initial bubble volume distribution, viscoelasticity, surface tension and reaction rate on the final bubble volume distribution. In the second model we extend the two-dimensional, hexagonal, arrangement of bubbles described in chapter 4 to bubbles of two different sizes in order to investigate the effects of viscoelasticity and gas diffusion when bubbles are in close proximity to one another.

## 5.1 Foam Consisting of Spherical Bubbles

In a foaming process bubbles nucleate at different times producing bubbles of different sizes. Nucleation is a highly complex process and has been the subject of much investigation [23, 44, 48]. In our model we shall consider bubbles of differing sizes to represent bubbles that nucleate at different times. The number of bubbles and initial bubble volumes are treated as input parameters. We assume that bubbles are sufficiently far apart that conservation of momentum and the equations for evolution of stretch can be applied locally in the neighbourhood of each bubble. Each bubble works against an infinite fluid domain so that the momentum equation 3.2 non-dimensionalised with the largest initial bubble volume is given by

$$0 = P_g De + \frac{2}{3}\int_0^\infty \frac{S_{rr} - S_{\theta\theta}}{x+u}dx - \frac{1}{\Gamma u^{\frac{1}{3}}}.$$

For an Oldroyd B fluid, $S_{rr} - S_{\theta\theta} = -2\frac{\dot{u}}{x+u} + \gamma(A_{rr} - A_{\theta\theta})$ so that the momentum equation is given by

$$\frac{4}{3}\frac{\dot{u}}{u} = P_g De + \frac{2}{3}\gamma\int_0^\infty \frac{A_{rr} - A_{\theta\theta}}{x+u}dx - \frac{1}{\Gamma u^{\frac{1}{3}}}. \tag{5.1}$$

The configuration tensor A satisfies equations (3.11) and (3.12).

In the case of the reacting fluid model $S_{rr} - S_{\theta\theta}$ includes contributions from all the $k$ relaxation modes so that

$$S_{rr} - S_{\theta\theta} = -2\frac{\dot{u}}{x+u} + \gamma\sum_k G_k(A_{rr} - A_{\theta\theta})_k.$$

The momentum equation then simplifies to

$$\frac{4}{3}\frac{\dot{u}}{u} = P_g De + \gamma\sum_k\left(\frac{2}{3}G_k\int_0^\infty \frac{(A_{rr} - A_{\theta\theta})_k}{x+u}dx\right) - \frac{1}{\Gamma u^{\frac{1}{3}}}$$

and the elastic moduli for each mode are obtained from equations (2.13) before the gel point and (2.14) after the gel point. The coefficients of the configuration tensor for each of the $k$ relaxing modes satisfy Oldroyd B type equations of the form (3.11) and (3.12) with relaxation times $\tau_k$ and for the non-relaxing gel mode satisfies Oldroyd B equations

with infinite relaxation time. Allowance must be made for the rescaling of the elastic moduli as the number density of modes evolve so that the total stress is consistent as described in the discussion leading to equations (3.34) and (3.36).

**Instantaneous Gas Diffusion**

In the limit of instantaneous diffusion the concentration profile throughout the liquid is uniform. Therefore, for bubbles of differing radii to coexist the gas pressures must all be equal. In the non-reacting system there is no production of gas and the total flux of gas into all the bubbles is given by Henry's law as

$$\sum_i \phi_i = \frac{\Phi(p_{g0} - p_a)}{p_{g0}}(1 - P_g)X.$$

Here $X$ is an effective liquid volume that acts to limit the supply of gas even though the bubbles are considered to expand in an infinite fluid domain. In the non-reacting system the equation of gas conservation therefore becomes

$$(p_a + (p_{g0} - p_a)P_g)\sum_i u_i = p_{g0}\sum_i u_{0i} + \Phi(p_{g0} - p_a)(1 - P_g)X \qquad (5.2)$$

In the reacting system the amount of gas produced by the reaction is $\varsigma\Phi p_a\alpha X$ so that the total gas flux into the bubbles is the difference between the amount of gas produced and that remaining in the liquid so that

$$(p_a + (p_{g0} - p_a)P_g)\sum_i u_i = p_{g0}\sum_i u_{0i} + \Phi\left(\varsigma p_a\alpha - (p_{g0} - p_a)P_g\right)X.$$

### 5.1.1 Results and Discussion

We begin by considering the competition between two bubbles of different sizes in a non-reacting fluid. The non-dimensional parameter $X$ limiting the supply of gas is chosen to be 10 with other parameters given in table 3.2 unless otherwise stated.

In the limit of large capillary number in a Newtonian liquid ($\gamma = 0$) the expansion rate, $\dot{u}/u$, from equation 5.1 simplifies to

$$\frac{4}{3}\frac{\dot{u}}{u} = P_g De.$$

This expansion rate is independent of the size of the bubble, thus the bubble volume ratios remain constant in time. Figure 5.1 shows the expansion of two bubbles in a Newtonian fluid in this limit for differing initial bubble volume ratios.

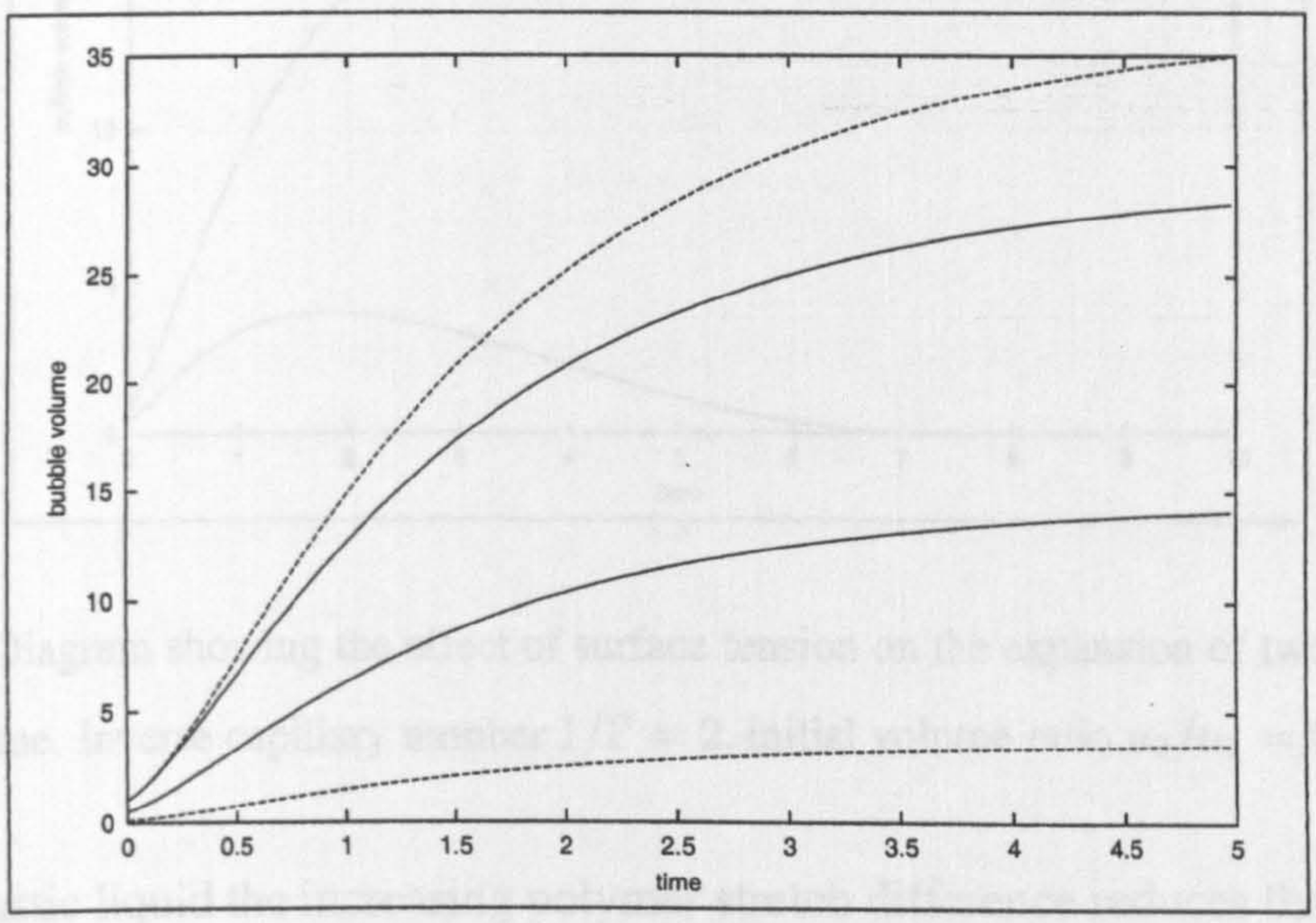


Figure 5.1: Diagram showing the effect of the initial volume ratio on the expansion of two bubbles in a Newtonian liquid in the limit of large capillary number. Solid lines show the evolution of the bubble volumes for two bubbles with initial volumes 1 and 0.5, and dashed lines show the evolution of the bubble volumes for two bubbles with initial volumes 1 and 0.1.

Surface tension causes a phenomenon known as Ostwald ripening. In a Newtonian liquid ($\gamma = 0$) equation 5.1 shows that a bubble will shrink when

$$P_g De - \frac{1}{\Gamma u^{1/3}} < 0.$$

Surface tension has a greater effect on small bubbles due to their higher curvature. Consequently the larger bubble will expand faster than the small bubble. Since the gas pressures in all the bubbles are equal, this lowers the gas pressure in both bubbles until a

point when, for the smaller bubble, $P_g De < 1/\Gamma u^{1/3}$. Figure 5.2 shows this competition for gas between two bubbles with an inverse capillary number of $1/\Gamma = 2$ and initial bubble volume ratio 0.5.

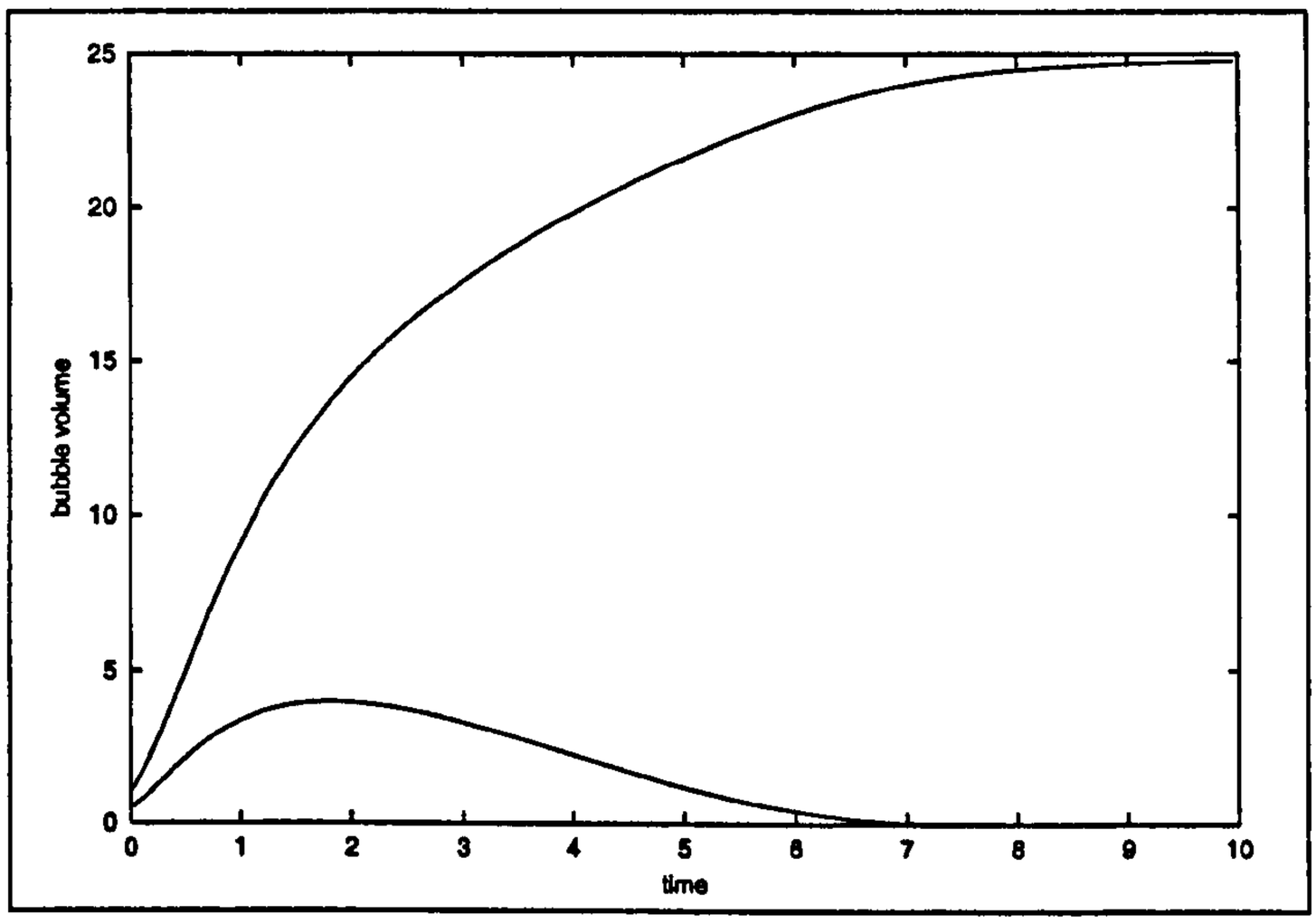


Figure 5.2: Diagram showing the effect of surface tension on the expansion of two bubbles as a function of time. Inverse capillary number $1/\Gamma = 2$, initial volume ratio $u_2/u_1 = 0.5$.

In a viscoelastic liquid the increasing polymer stretch difference reduces the growth rate from that of a Newtonian fluid of equal solvent viscosity. However, the smaller bubble is affected to a larger extent than large bubbles due to the $1/(x+u)$ term in the elastic stress in equation (5.1), resulting in a wider distribution of final bubble volumes. Again this is a conseqence of the higher surface curvature of the small bubble. In figure 5.3 we plot the final bubble ratio, $u_2/u_1$ as a function of initial volume ratio for two bubbles in a viscoelastic liquid for the case of infinite capillary number. Provided the system is quenched before surface tension can act to eliminate the smaller bubble, viscoelasticity widens the distribution of bubble sizes compared to a Newtonian liquid.

We now turn our attention to the case of a reacting fluid. When the reaction rate is small the results are very similar to those for the non-reacting system. However, at high reaction rates the onset of gelation occurs before the bubbles have attained their final volumes. Gas pressure and stress can become frozen into the system so that the final

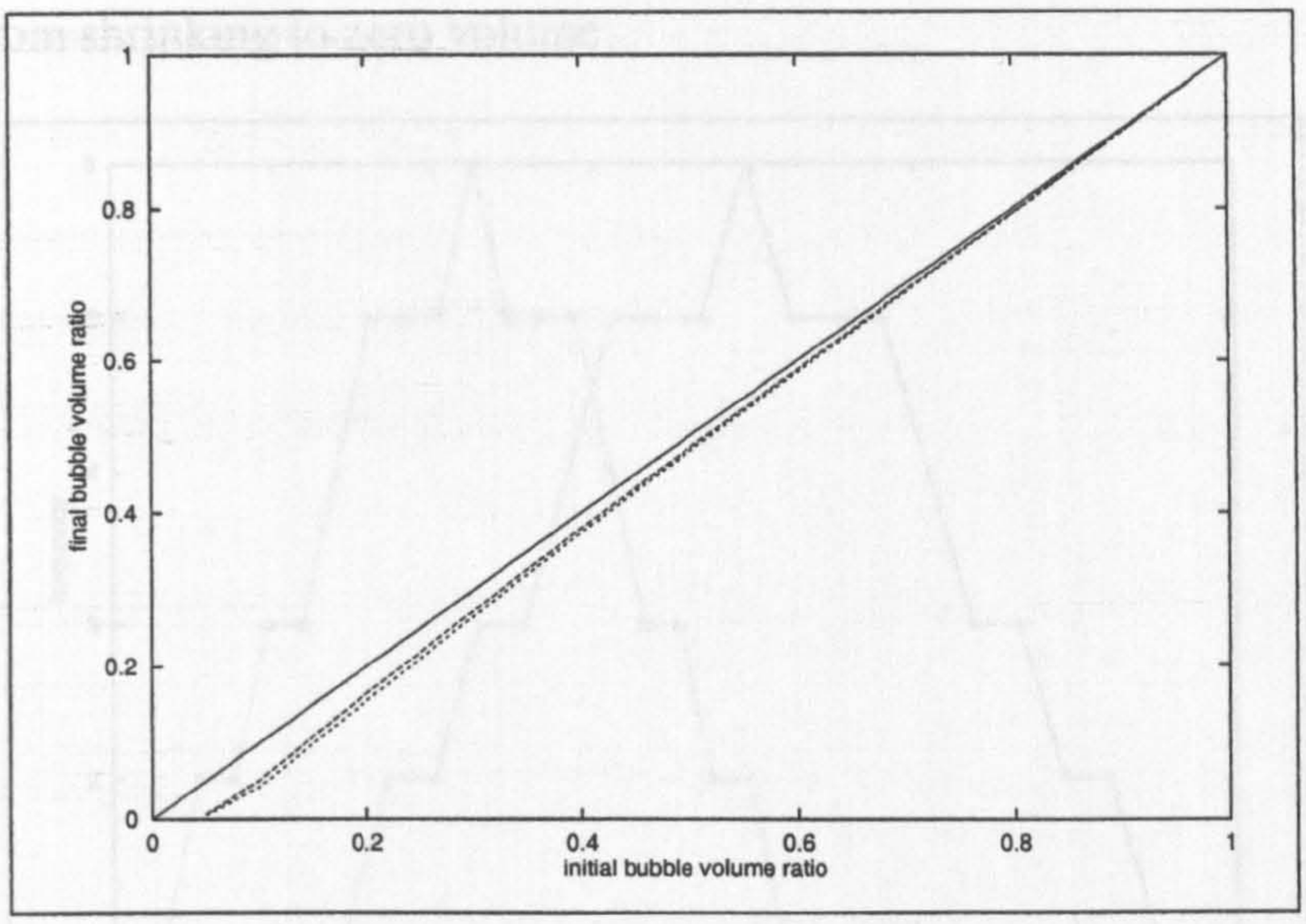


Figure 5.3: Diagram showing the effect of viscoelasticity on the final bubble volume ratio as a function of initial volume ratio in the limit of large capillary number. Solid line: Newtonian liquid, $\gamma = 0$ (here the final volume ratio equals the initial volume ratio); dashed line: viscoelastic liquid $\gamma = 5$; dotted line: viscoelastic liquid $\gamma = 10$.

volumes of all the bubbles are reduced. This effect is greater for large bubbles and so the final bubble volume distribution is reduced as the reaction rate is increased. Figure 5.4 compares the final bubble volume distributions for a high and a low reaction rate in the limit of infinite capillary number. Here 66 bubbles are initially normally distributed with mean 1 and variance 0.03. The values of the mean and variance at $t = 20$ are 13.9 and 5.9 respectively for a reaction rate $c_\alpha = 1$, and 10.5 and 3.5 for $c_\alpha = 10$. The effect of increasing the reaction rate reduces the dimensionless numbers $M$ and $\gamma$ by the same factor.

Gelation is able to quench the system before the effects of Ostwald ripening are seen, figure 5.5 shows the expansion of two bubbles with an initial bubble volume ratio of 0.5 and reaction rate $c_\alpha = 10$. Here the dimensionless numbers $M = 0.9$ and $\gamma = 73.8$. We can see that for an inverse capillary number of $1/\Gamma = 0.2$ the reaction rate is sufficiently high to freeze the bubble volumes before the small bubble starts to shrink and for an inverse capillary number of $1/\Gamma = 0.5$ the small bubble starts to shrink but gelation

prevents it from shrinking to zero volume.

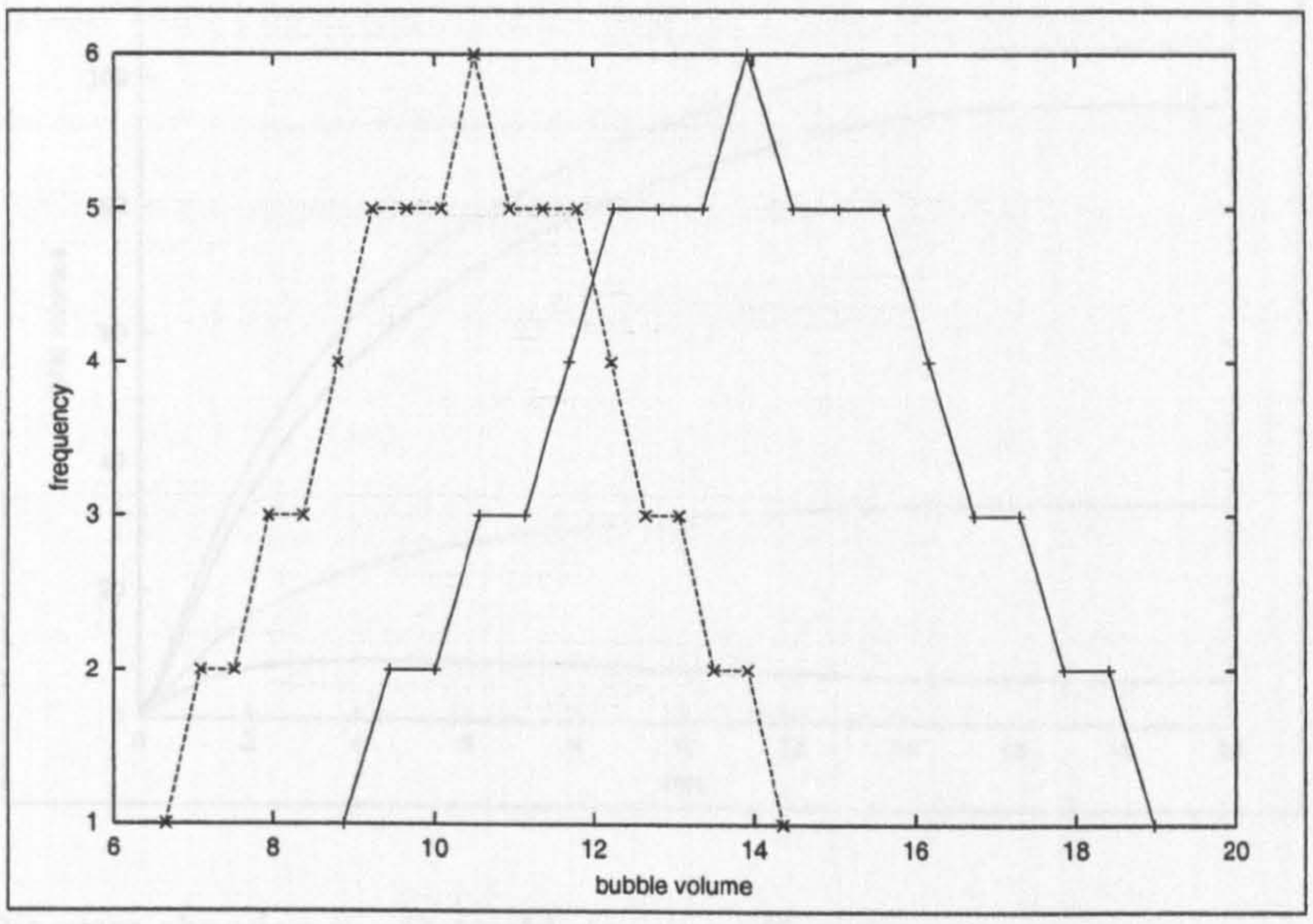


Figure 5.4: Histogram of final bubble volumes for a normal distribution of 66 bubbles with initial mean=1, variance=0.03. Solid line = low reaction rate ($c_\alpha = 1$); dashed line = high reaction rate ($c_\alpha = 10$).

### 5.1.2 Expansion Viscosity

In order to provide a measurable bulk property of the foam we can define an expansion viscosity based on the definition provided by Batchelor [4] for a Newtonian liquid. Batchelor defines an expansion viscosity for gas bubbles expanding in a Newtonian liquid by considering the viscous dissipation in the liquid phase. The rate of dissipation per unit volume of the foam as a homogeneous fluid is $\kappa\Delta^2$ where $\Delta$ is the (uniform) rate of expansion and $\kappa$ is the effective expansion viscosity. The expansion of the foam is due to the change in volume of the gas bubbles and so

$$\Delta = \frac{1}{V}\sum \frac{d}{dt}\left(\frac{4}{3}\pi R^3\right)$$

where $R$ is the bubble radius. The rate of dissipation per unit volume at a distance $r$ from the centre of a bubble is given by $2\mu\mathbf{E} : \mathbf{E}$ where $\mathbf{E}$ is the deformation gradient tensor.

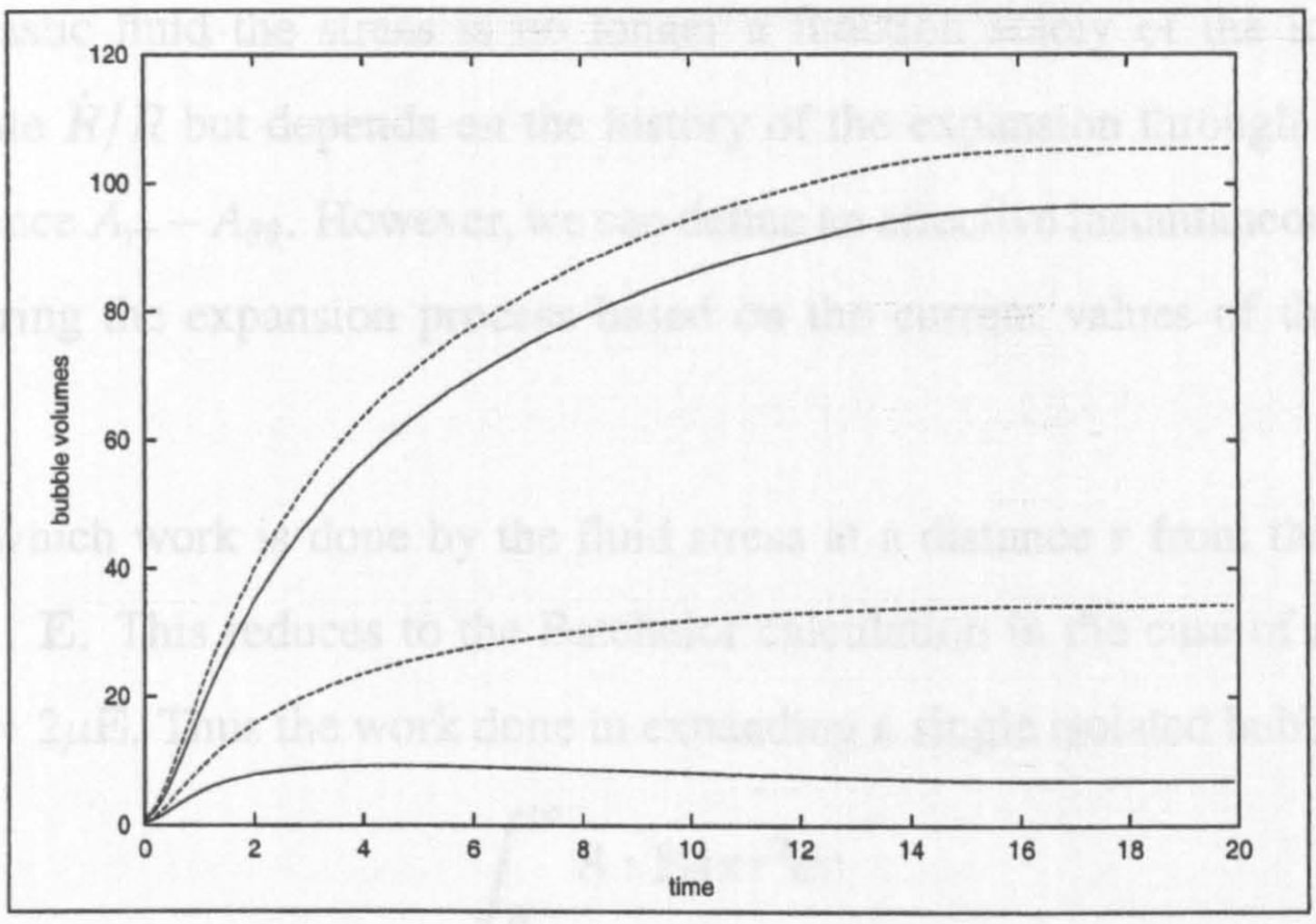


Figure 5.5: Diagram showing the Ostwald ripening effect for a reaction rate $c_\alpha = 10$ and initial bubble volume ratio 0.5. Solid line = $1/\Gamma = 0.2$; dashed line = $1/\Gamma = 0.5$.

For an isolated spherical bubble expanding in an infinte Newtonian liquid

$$2\mu\mathbf{E}:\mathbf{E} = 12\mu\frac{R^4\dot{R}^2}{r^6}.$$

Thus the total rate of dissipation in the liquid due to one bubble is

$$\int_R^\infty 12\mu\frac{R^4\dot{R}^2}{r^6}4\pi r^2 dr.$$

Evaluating the integral over the fluid volume and summing over all the bubbles gives the total rate of dissipation as $16\pi\mu\sum R\dot{R}^2$. Hence the effective expansion viscosity is

$$\kappa = \frac{16\pi\mu\sum R\dot{R}^2}{V\left(\frac{4\pi}{V}\sum R^2\dot{R}\right)^2}$$

$$= \frac{\mu}{\pi}\frac{V\sum R\dot{R}^2}{\left(\sum R^2\dot{R}\right)^2}.$$

Thus, for a dilute foam consisting of $n$ equal sized bubbles the expansion viscosity per unit volume is

$$\frac{\mu}{n\pi u}.$$

In a viscoelastic fluid the stress is no longer a function solely of the instantaneous expansion rate $\dot{R}/R$ but depends on the history of the expansion through the polymer stress difference $A_{rr} - A_{\theta\theta}$. However, we can define an effective instantaneous expansion viscosity during the expansion process based on the current values of the polymeric stress.

The rate at which work is done by the fluid stress at a distance $r$ from the centre of a bubble is $\mathbf{S} : \mathbf{E}$. This reduces to the Batchelor calculation in the case of a Newtonian liquid as $\mathbf{S} = 2\mu\mathbf{E}$. Thus the work done in expanding a single isolated bubble is

$$\int_R^\infty \mathbf{S} : \mathbf{E} 4\pi r^2 dr$$

$$= \int_R^\infty \left( 12\mu \frac{R^4\dot{R}^2}{r^6} - 2\frac{R^2\dot{R}}{r^3} G(A_{rr} - A_{\theta\theta}) \right) 4\pi r^2 dr$$

$$16\pi\mu R\dot{R}^2 - 8\pi R^2 \dot{R} G \int_R^\infty \frac{A_{rr} - A_{\theta\theta}}{r} dr.$$

Hence we can define an effective instantaneous expansion viscosity as

$$\kappa_{eff} = \frac{16\pi\mu \sum R\dot{R}^2 - 8\pi \sum R^2\dot{R} G \int_R^\infty \frac{A_{rr} - A_{\theta\theta}}{r} dr.}{V\left(\frac{4\pi}{V}\sum R^2\dot{R}\right)^2}$$

Using the Lagrangian fluid volume, $r^3 = u + x$, for the distance, $r$, from the bubble centre gives

$$\kappa_{eff} = \frac{V}{\pi(\sum \dot{u})^2}\left(\mu \sum \frac{\dot{u}^2}{u} - \frac{1}{2} G \sum \dot{u} \int_0^\infty \frac{A_{rr} - A_{\theta\theta}}{x + u} dx\right).$$

For a foam consisting of equal sized bubbles the expansion viscosity per unit volume reduces to

$$\kappa_{eff} = \frac{1}{n\pi}\left(\frac{\mu}{u} - \frac{1}{2}\frac{G}{\dot{u}} \int_0^\infty \frac{A_{rr} - A_{\theta\theta}}{x + u} dx\right).$$

For a Newtonian liquid ($G = 0$) the expansion viscosity decreases like $1/u$. For a viscoelastic liquid ($G > 0$) the effective expansion viscosity increases for a time as the bubbles increase in volume, then decrease as the elastic stress relaxes. Figure 5.6 show the expansion viscosity for a non-reactive, viscoelastic ($\gamma = 5$), foam consisting of 100 bubbles with a normal distribution of initial volumes (mean=5, variance=1).

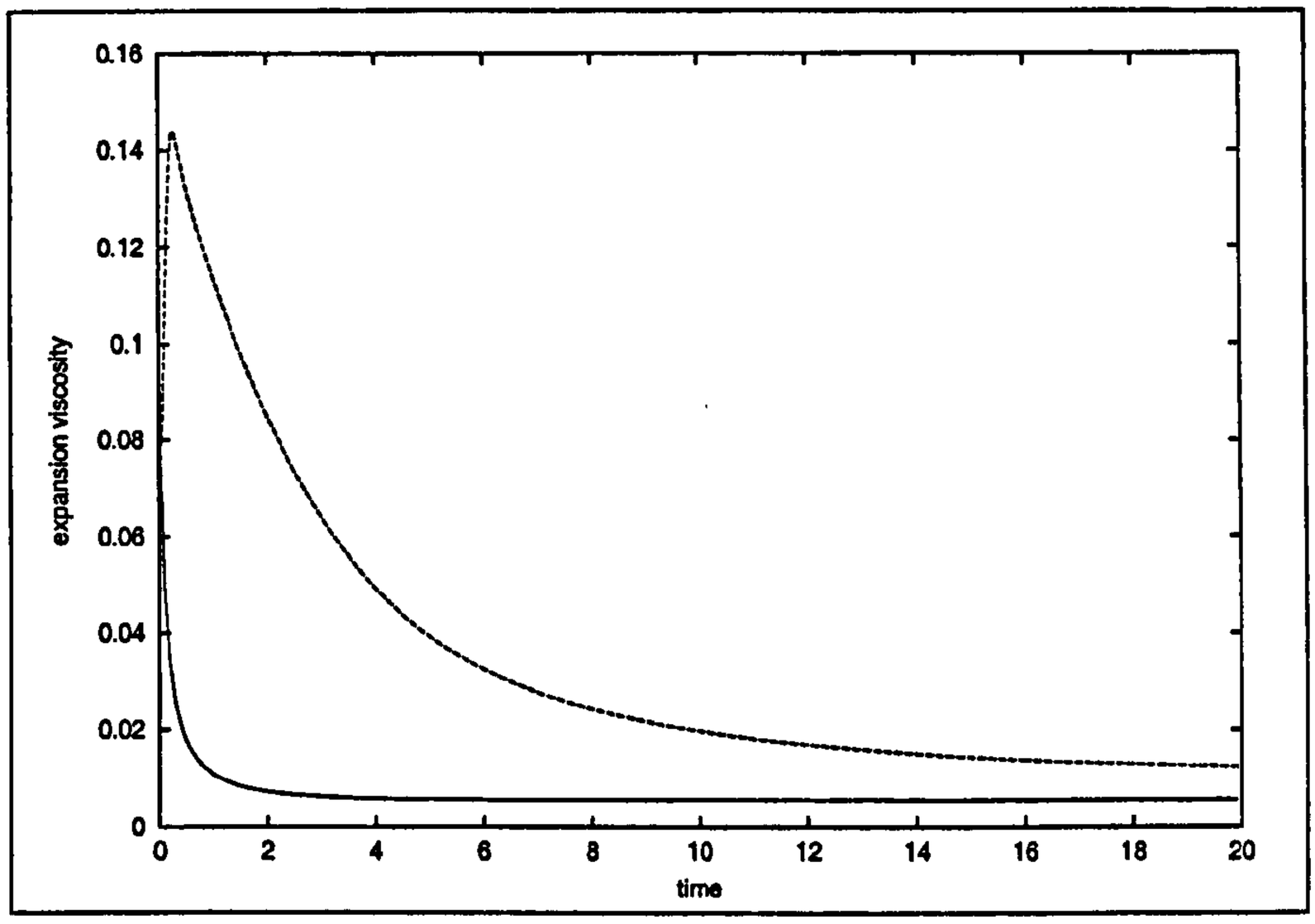


Figure 5.6: Expansion viscosity for Newtonian ($\gamma = 0$) and viscoelastic foam ($\gamma = 5$) consisting of 100 bubbles initially normally distributed with mean=5, variance=1.

## 5.2 Non-Spherical Bubbles

In this section we extend the two-dimensional hexagonal geometry considered in chapter 4 to include bubbles of two different sizes. Bubbles of two different sizes can be arranged in the ratio 2:1 by surrounding each cell containing a bubble of size 1 by cells containing a bubble of size 2. Thus each size 1 bubble has six neighbouring bubbles of size 2, while each size 2 bubble has three neighbouring size 1 bubbles and three neighbouring size 2 bubbles. The computational region is now made up in effect from three of the computational regions considered in chapter 4 - see figure 5.7. We assume that the bubbles are initially circular with a uniform initial gas concentration profile so that the initial gas pressures in the bubbles are equal. We also assume that the polymers in the liquid are unstretched at $t = 0$.

The method of solution is very similar to that described in section 4.1.1 with changes to account for the presence of an extra bubble and an extra edge in the fluid domain. The

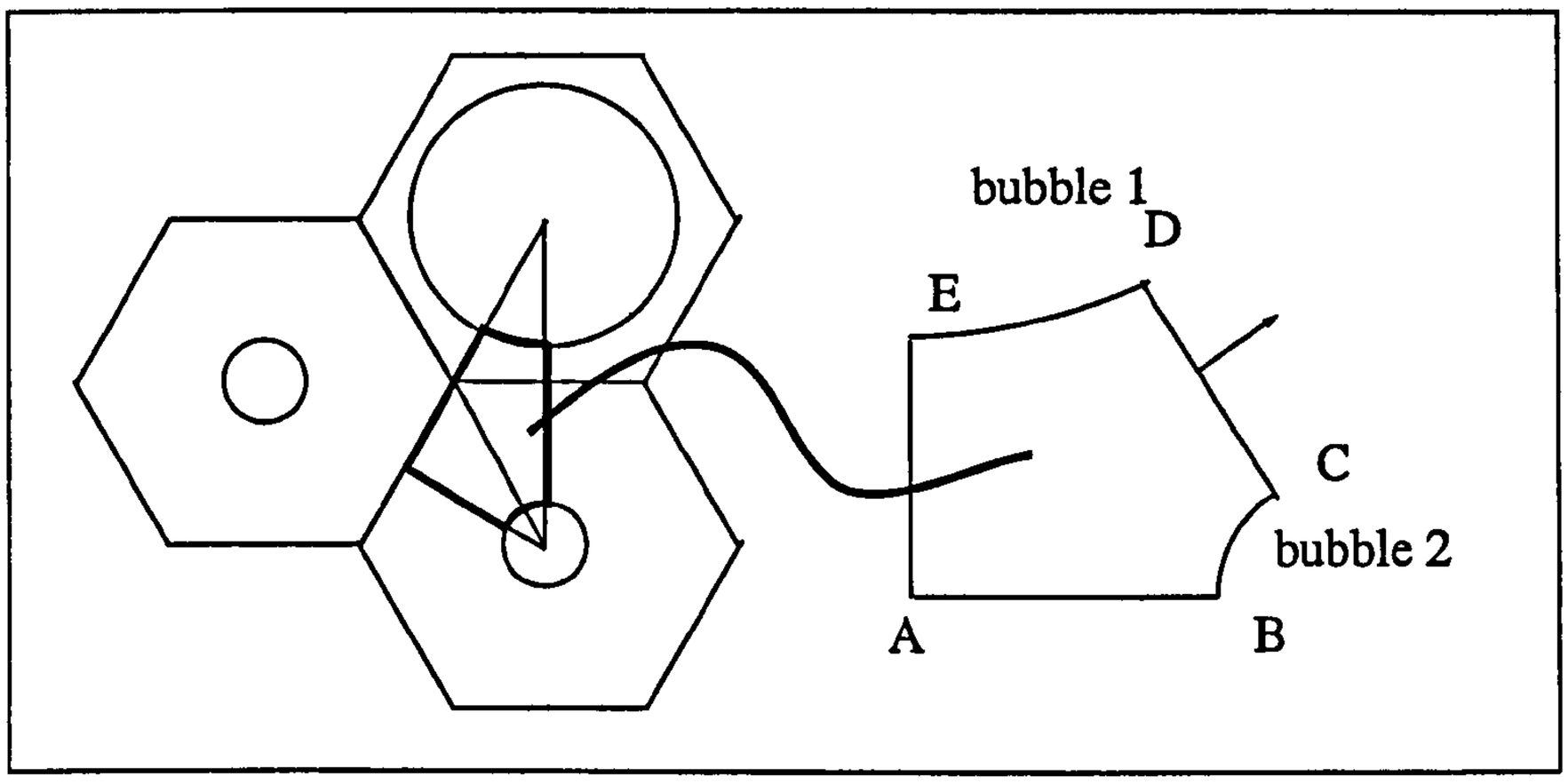


Figure 5.7: Diagram showing the two dimensional arrangement of bubbles.

boundary conditions for the gas diffusion equation 4.7 are now:

$$\begin{aligned}
c &= \frac{\Phi(p_a + (p_{g0} - p_a)P_{g1})}{p_{g0}} && \text{at bubble 1 interface (DE in figure 5.7)} \\
c &= \frac{\Phi(p_a + (p_{g0} - p_a)P_{g2})}{p_{g0}} && \text{at bubble 2 interface (BC)} \\
\hat{\mathbf{n}} \cdot \nabla c &= 0 && \text{on the three symmetry lines (AB, CD and AE).}
\end{aligned} \tag{5.3}$$

The subscripts 1 refer to quantities in bubble 1 and subscripts 2 refer to those in bubble 2. Here we scale gas pressure differences $p_{g1} - p_a$ and $p_{g2} - p_a$ with the initial pressure difference $p_{g0} - p_a$ so that

$$P_{g1} = \frac{p_{g1} - p_a}{p_{g0} - p_a},$$
$$\text{and} \quad P_{g2} = \frac{p_{g2} - p_a}{p_{g0} - p_a}.$$

Conservation of mass across the surface of the bubble allows the gas pressure in each bubble to be calculated from the flux of gas across the surface:

$$\begin{aligned}
(p_a + (p_{g0} - p_a)P_{g1})u_1 &= p_{g0}\left(u_{01} + N\int_t\int_{C_1} \nabla c \cdot \hat{\mathbf{n}}\, dC_1\, dt\right) \\
(p_a + (p_{g0} - p_a)P_{g2})u_2 &= p_{g0}\left(u_{02} + N\int_t\int_{C_2} \nabla c \cdot \hat{\mathbf{n}}\, dC_2\, dt\right).
\end{aligned} \tag{5.4}$$

The increase in bubble areas is calculated from the normal velocity relative to the bubble centres. Defining $\dot{\epsilon}$ as the normal velocity $\mathbf{q} \cdot \mathbf{n}$ on the edge CD, the bubble centres have velocities $(0, 2\dot{\epsilon})$ and $(2\dot{\epsilon}/\sqrt{3}, 0)$ respectively, so that

$$\frac{du_1}{dt} = \int_{C_1} (\mathbf{q} - (0, 2\dot{\epsilon})) \cdot \mathbf{n} dC_1 \tag{5.5}$$

$$\frac{du_2}{dt} = \int_{C_2} \left(\mathbf{q} - \left(\frac{2}{\sqrt{3}} 2\dot{\epsilon}, 0\right)\right) \cdot \mathbf{n} dC_2.$$

The polymer stress equation (4.10) and momentum equations (4.14) and (4.15) are solved for the shape of the fluid region, polymer stress and fluid pressures using the method described in section 4.1.1 for a given value of $\dot{\epsilon}$. The work equation (4.6) is then used to adjust the expansion rate $\dot{\epsilon}$ in the manner described in section 4.1.1 for $\dot{L}$. We then solve the gas diffusion equation with new boundary conditions, equation (5.3) as described in section 4.1.1 and calculate the new gas pressures and bubble volumes from equations (5.4) and (5.5).

### 5.2.1 Results and Discussion

For the non-reacting system we have found, in chapters 3 and 4, that the rate of diffusion of gas through the liquid phase and the ratio of polymer to solvent contributions to the zero shear rate viscosity, $\gamma$, affect the dynamics of the expansion and the shape, but not the final size, of the bubble. The extension of the two-dimensional hexagonal geometry to include bubbles of two different sizes now allows us to investigate the effects of diffusivity and viscoelasticity on the relative sizes of the bubbles as well as the shape of the gas-liquid interface.

We begin by considering the expansion of bubbles in a Newtonian fluid, $\gamma = 0$, and consider the effects of gas diffusivity and surface tension. For large capillary number the timescale associated with the late, surface tension driven, phase of the expansion is much larger than the timescales associated with the viscous expansion and so the system expands to a quasi-equilibrium state before Ostwald ripening occurs causing the smaller bubble to shrink to zero.

In section 5.1 we showed that, for well separated bubbles in the limit of infinite diffusion and infinite capillary number, bubbles of different sizes grow at the same rate so that the ratio of bubble volumes remains the same. However, this equality does not hold at higher bubble volume fractions where bubbles are no longer expanding in an infinite fluid domain. For circular bubbles expanding in a Newtonian fluid at infinite capillary number the conservation of momentum equation (4.21) simplifies to

$$\mu \frac{\dot{u}}{u} \frac{X}{X+u} = p_g - p_a \tag{5.6}$$

where $X$ is the liquid area. Thus in the limit of infinite diffusion, where gas pressures are equal, bubbles will expand faster for larger values of $u/X$. Consequently the larger bubbles will expand faster resulting in a wider bubble size distribution at higher bubble concentrations.

At early times the bubble volume increases as

$$u = u_0 \left( 1 + \frac{(p_{g0} - p_a)}{\mu} \left( 1 + \frac{u_0}{X} \right) t \right) + O(t^2) \tag{5.7}$$

and so, with no diffusion the bubble gas pressure becomes,

$$p_g - p_a = \frac{p_{g0} - p_a}{1 + \frac{(p_{g0} - p_a)}{\mu} \left( 1 + \frac{u_0}{X} \right) t}. \tag{5.8}$$

Thus, small bubbles maintain a higher gas pressure than large ones. In figure 5.8 we show the effects of diffusivity on the expansion of bubbles in a ratio of two large to one small bubbles and compare the growth rate to that predicted in this early time limit.

In figure 5.9 we have attempted to compare the full two-dimensional simulation of the hexagonal array with the limit of infinite diffusion for perfectly circular bubbles analogous to the spherical model described in section 5.1. In section 5.1 the bubbles expand in an infinite fluid domain but in the hexagonal array there is a specific quantity of fluid between the bubbles. Therefore in the comparison in figure 5.9 we compare the hexagonal simulation ($N = 500$) for bubbles in the ratio one large to two small bubbles with the circular approximation with fluid partitioned proportional to the initial bubble areas; and partitioned proportional to the initial bubble circumferences. It can be

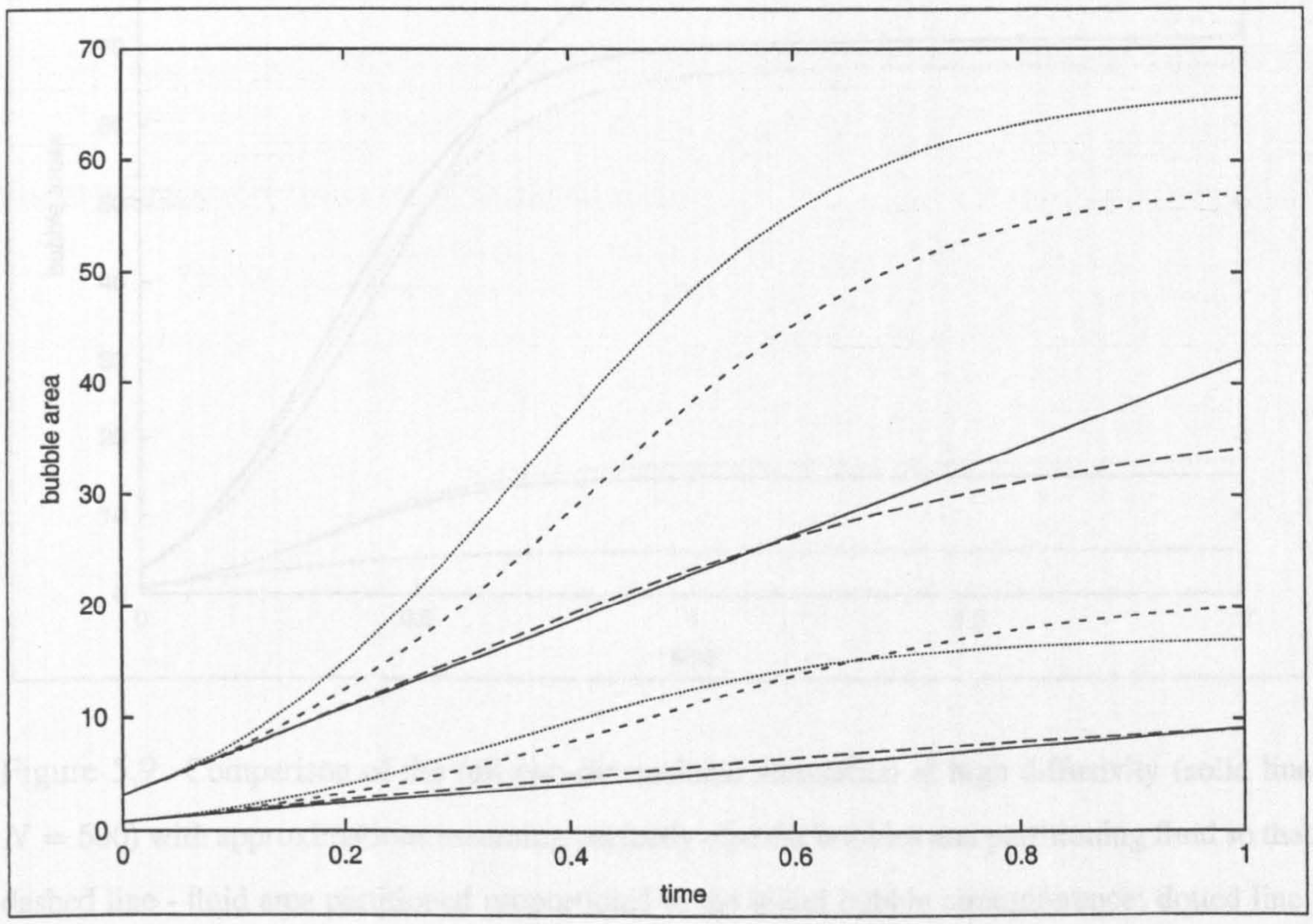


Figure 5.8: Comparison of the early time bubble areas from two-dimensional simulations (long dashed line: $N = 0.1$; short dashed line: $N = 1$; dotted line: $N = 10$). Solid lines show the initial growth rate. Upper curves represent the area of bubble 1, initially $u_1 = \pi$ and lower curves represent the area of bubble 2, initially $u_2 = \pi/4$.

seen that, while the partitioning by bubble area gives the nearest prediction, the circular approximation can only give qualitative predictions.

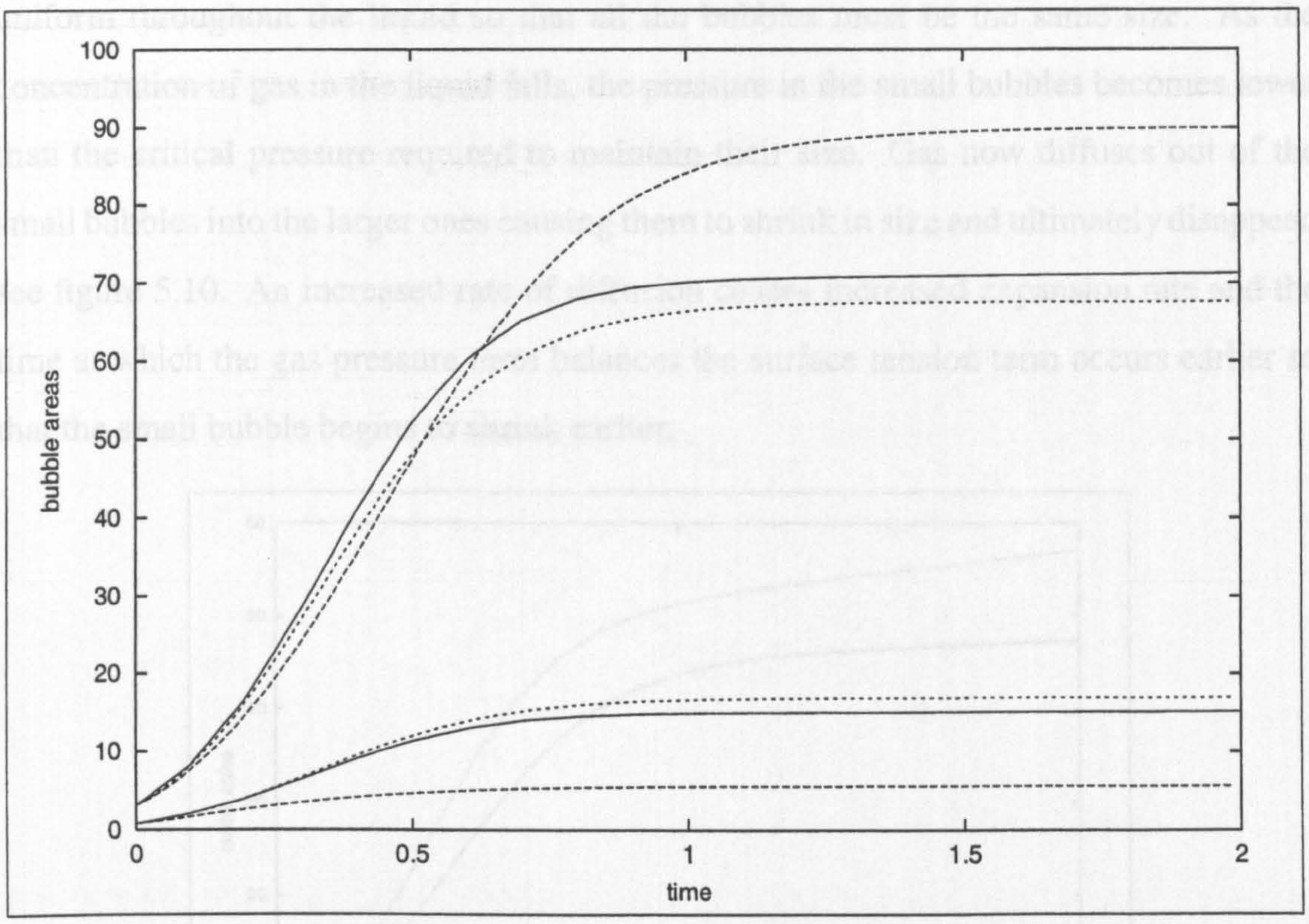


Figure 5.9: Comparison of the full two-dimensional simulation at high diffusivity (solid line: $N = 500$) with approximations assuming perfectly circular bubbles and partitioning fluid so that: dashed line - fluid area partitioned proportional to the initial bubble circumference; dotted line - fluid area partitioned proportional to the initial bubble area. Upper curves represent the area of bubble 1, initially $u_1 = \pi$ and lower curves represent the area of bubble 2, initially $u_2 = \pi/4$.

When bubbles are identical, as in chapter 4, surface tension acts to limit the final bubble size by modifying the equilibrium gas pressure and imposes a circular bubble-liquid interface (or circular arcs connected by black films). When bubbles of different sizes are present Ostwald ripening causes small bubbles to shrink while large bubbles continue to expand. When there is no interaction between bubbles the final gas pressure difference in a bubble of volume $u_\infty$ is

$$P_{g\infty} De = \frac{1}{\Gamma u_\infty^{1/3}}.$$

Thus, small bubbles would have a larger final gas pressure than large bubbles. However, if the gas can diffuse through the liquid then the gas concentration profile becomes uniform throughout the liquid so that all the bubbles must be the same size. As the concentration of gas in the liquid falls, the pressure in the small bubbles becomes lower than the critical pressure required to maintain their size. Gas now diffuses out of the small bubbles into the larger ones causing them to shrink in size and ultimately disappear, see figure 5.10. An increased rate of diffusion causes increased expansion rate and the time at which the gas pressure term balances the surface tension term occurs earlier so that the small bubble begins to shrink earlier.

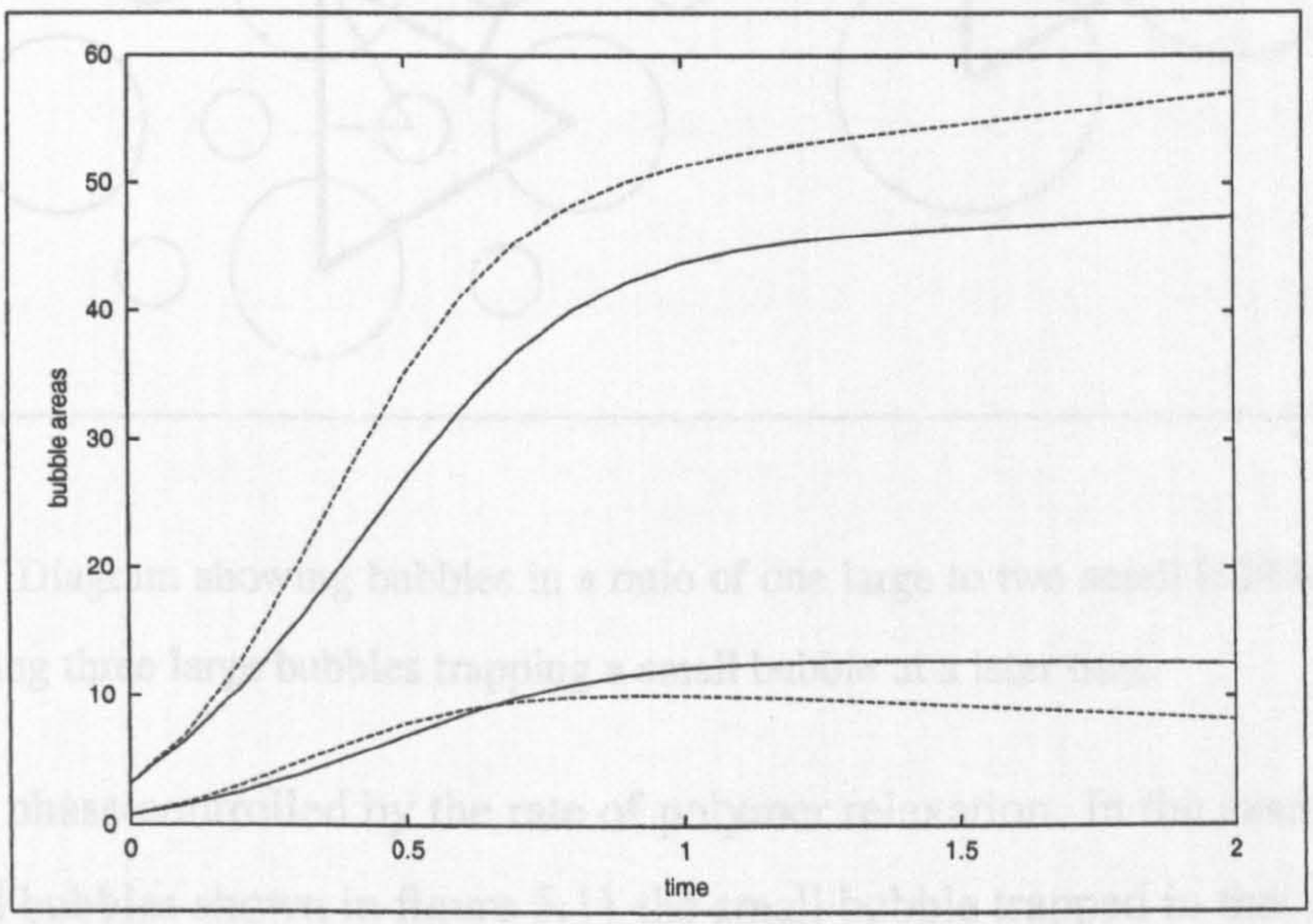


Figure 5.10: Ostwald ripening demonstrated by the evolution of two bubbles in a Newtonian liquid with initial radii 1 and 0.5. Inverse capillary number, $1/\Gamma = 1$. Solid line: $N = 1$; dashed line: $N = 10$.

In section 5.1 we saw that at infinitesimal bubble concentrations viscoelasticity widens the bubble size distributions. However, in the finite concentration array we find that the affect of viscoelasticity on the relative bubble size depends upon the bubble configuration, in particular whether the smaller bubbles are in the minority or majority in the array. When the ratio of the number of large to small bubbles is 1:2 the small bubbles become trapped in the corner region between three surrounding large bubbles

as shown in figure 5.11. In the opposite ratio of two large to one small bubble, each small bubble is surrounded by six large bubbles as in figure 5.12. Here the large bubbles restrict each other's size, allowing the small bubbles to expand in the hexagonal space between them. The expansion is again divided into two phases: an initial rapid viscous

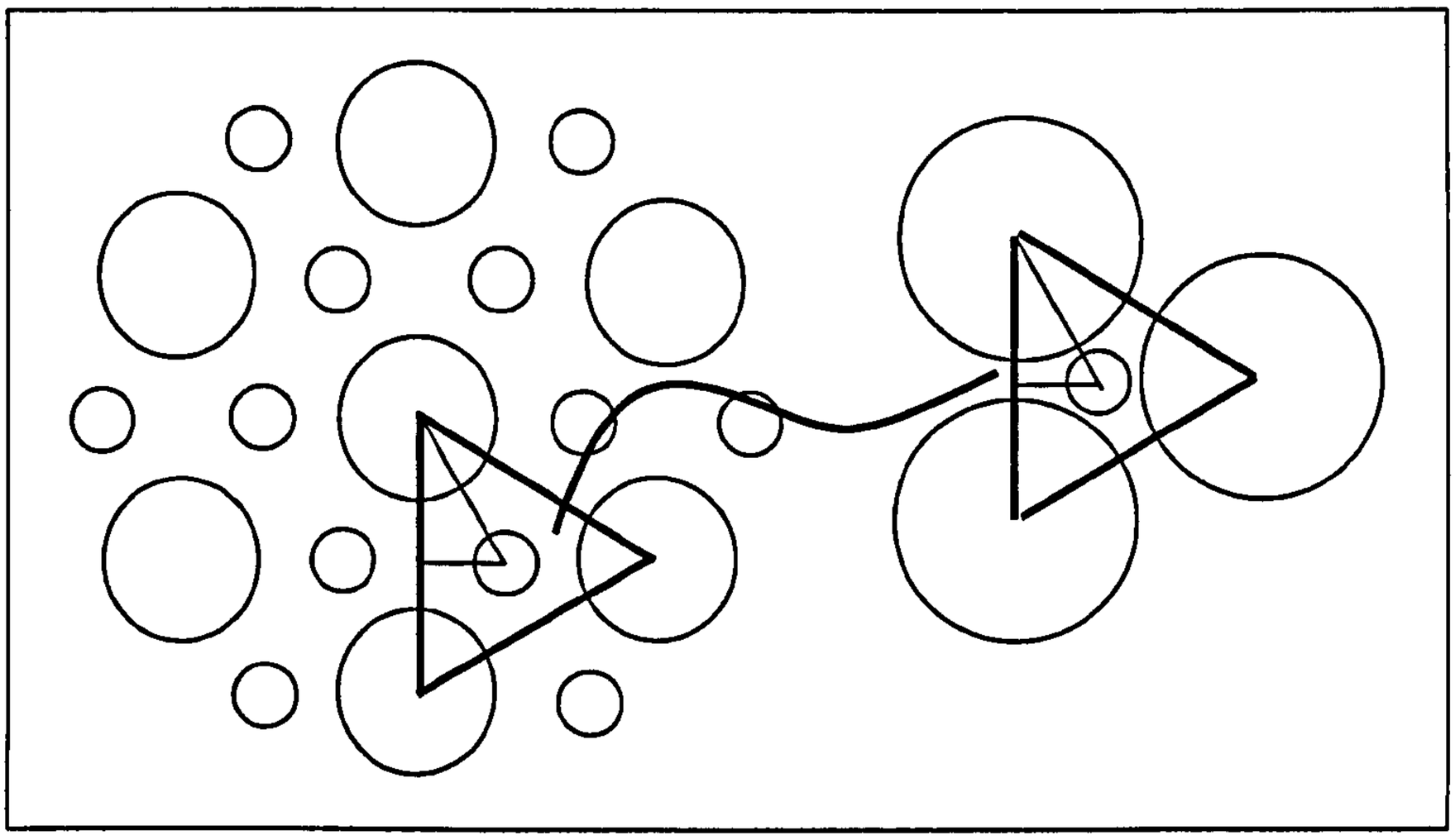

Figure 5.11: Diagram showing bubbles in a ratio of one large to two small bubbles. Triangular section showing three large bubbles trapping a small bubble at a later time.

phase and a phase controlled by the rate of polymer relaxation. In the case of one large to two small bubbles shown in figure 5.11 the small bubble trapped in the corner region is prevented from expanding by the high elastic stresses in the windows between the large and small bubbles resulting in a wider distribution of bubble sizes in viscoelastic liquids than in Newtonian liquids. The evolution of the bubble area is shown in figure 5.13 while snapshots of the stress in the liquid phase are shown in figure 5.14. In the opposite configuration the region of highest elastic stress is between two large bubbles. When diffusivity, and hence the expansion rate, is high the large bubbles grow rapidly producing high elastic stresses in the thin liquid regions between them. These elastic stresses both restrict the expansion of the large bubbles and also pull the liquid from the region surrounding the small bubble resulting in a bubble size distribution that is narrower for viscoelastic liquids than for Newtonian liquids. This can be seen in

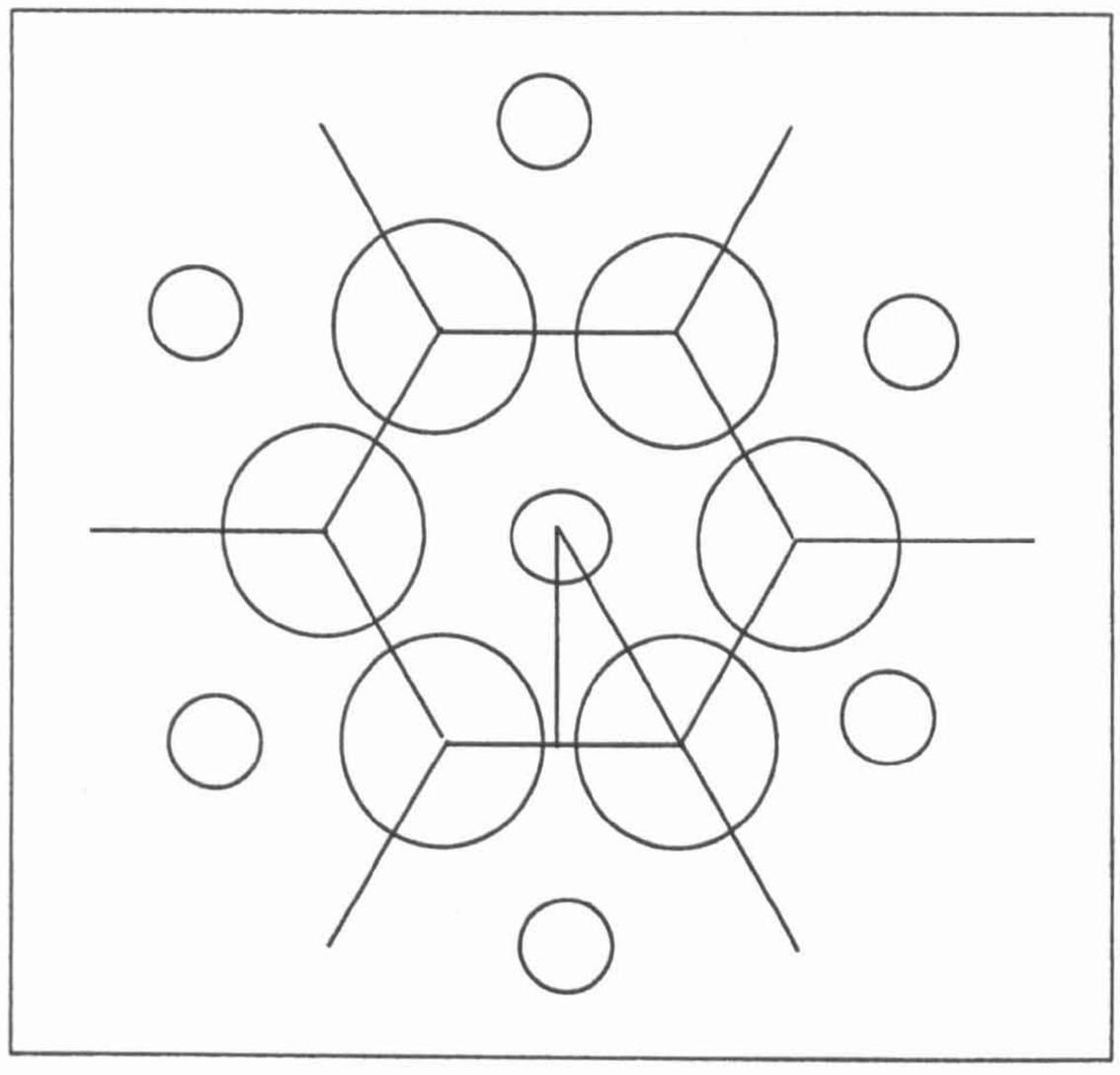

Figure 5.12: Diagram showing bubbles in a ratio of two large to one small bubble.

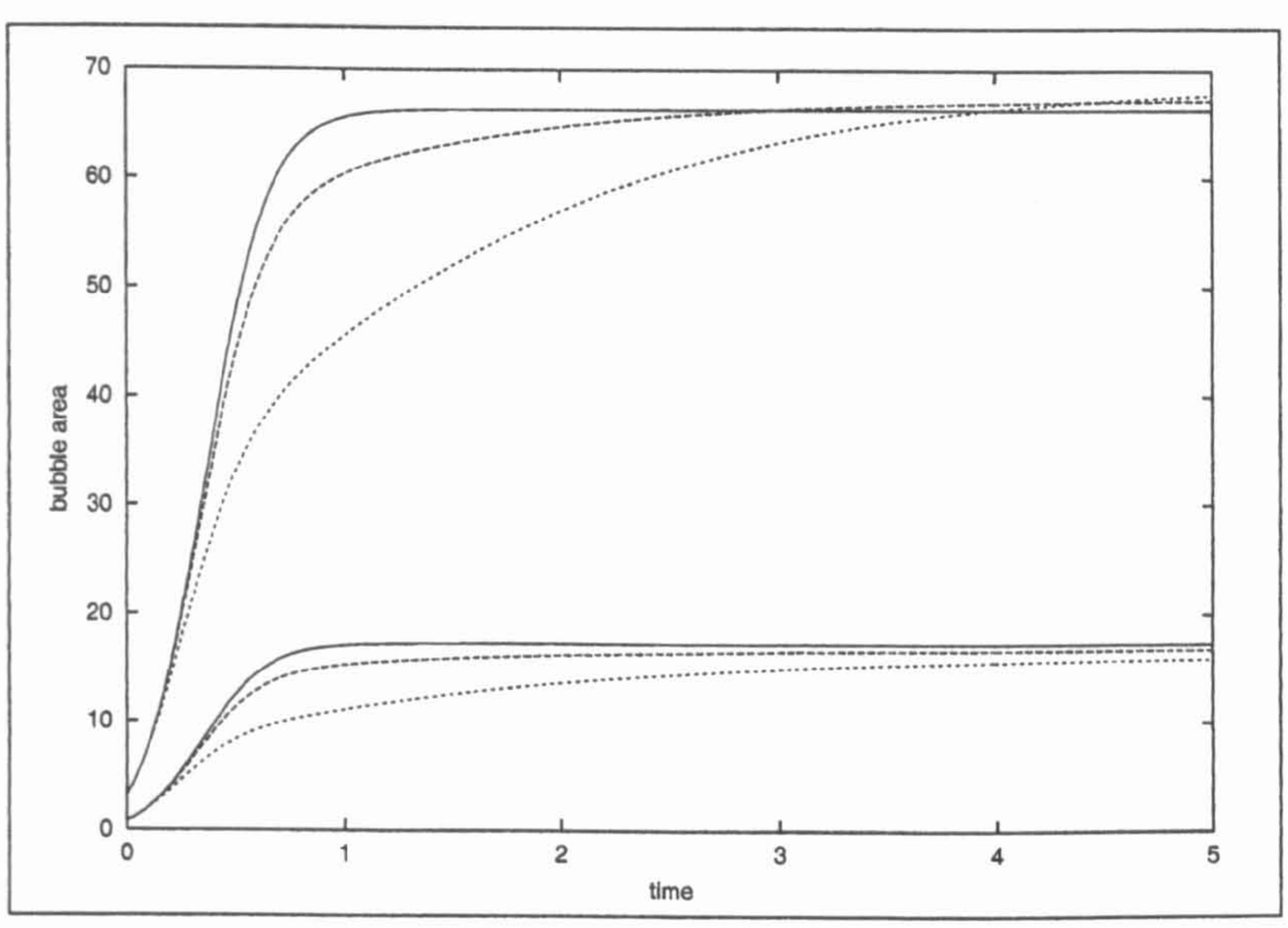


Figure 5.13: Evolution of bubble area for bubbles in a ratio of one large to two small bubbles when diffusivity, $D = 10$ and solvent viscosity $\mu = 1$. Upper curves represent the area of bubble 1, initially $u_1 = \pi$ and lower curves represent the area of bubble 2, initially $u_2 = \pi/4$. Solid lines are bubbles expanding in a Newtonian liquid; dashed lines bubbles expanding in a viscoelastic liquid with $\gamma = 0.2$; and dotted lines bubbles expanding in a viscoelastic liquid with $\gamma = 1$.

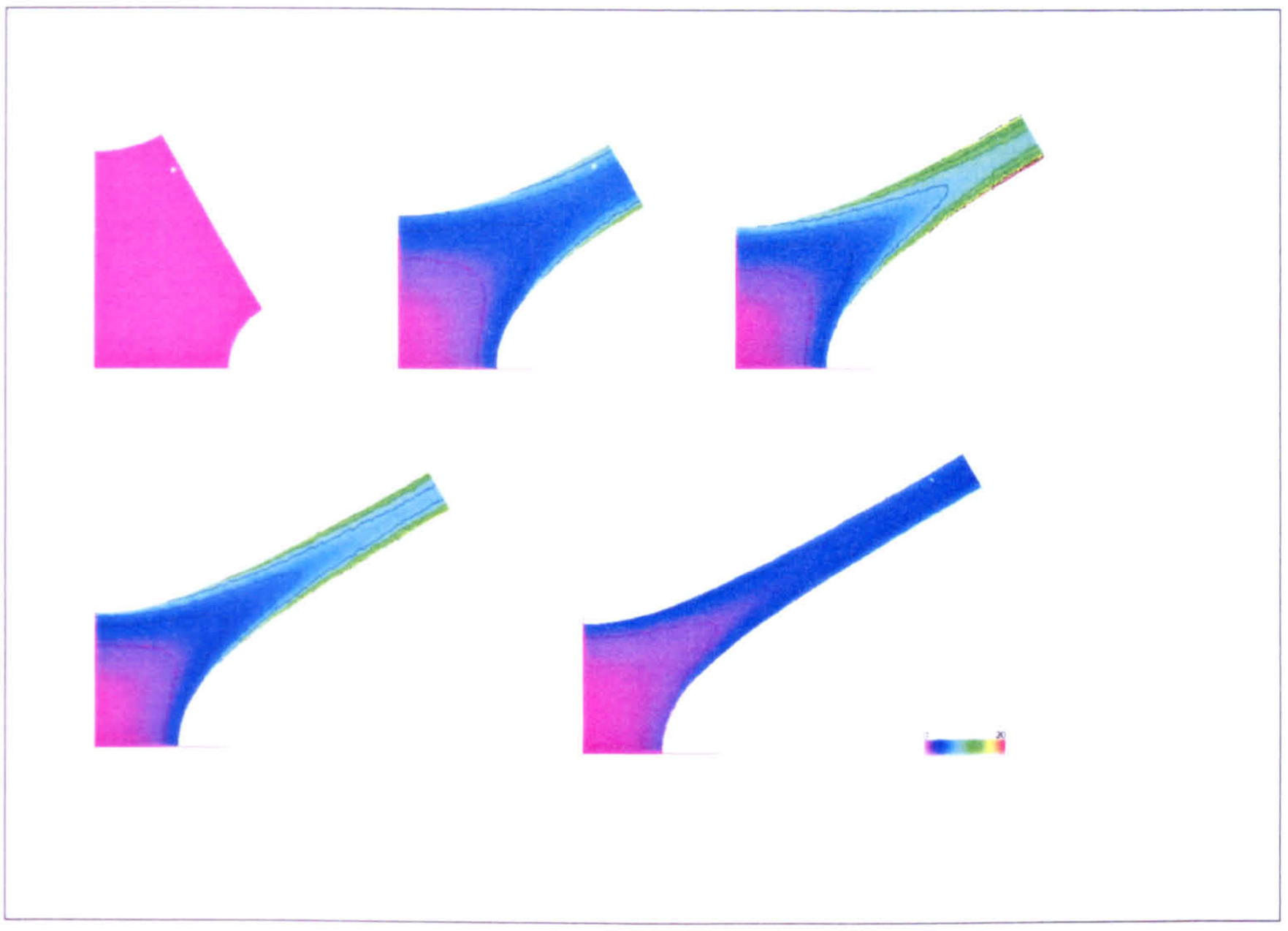

Figure 5.14: Snapshots of the elastic stress in the liquid for a configuration of one large to two small bubbles. Here the colouration indicates the magnitude of the difference in the eigenvalues of $\mathbf{A}$ and $\gamma = 1$. Contours are in intervals of 2.

figure 5.15 where we compare the evolution of the bubble areas between Newtonian and viscoelastic liquids and in figure 5.16 where we show snapshots of the elastic stress in the liquid. It should be noted here that the maximum magnitude of the difference in the eigenvalues of **A** for this configuration of bubbles is approximately double that of the case of the one large to two small bubble configuration. In figure 5.17 we show the bubble gas pressures for the expansion of bubbles in a ratio of two large to one small bubble. Here we see that, as the large bubbles become restricted by other large bubbles and viscoelasticity allows the small bubbles to continue to expand, the gas pressures in the small bubbles become less than that of the large bubbles. This can be seen most clearly on the $\gamma = 0.2$ curves.

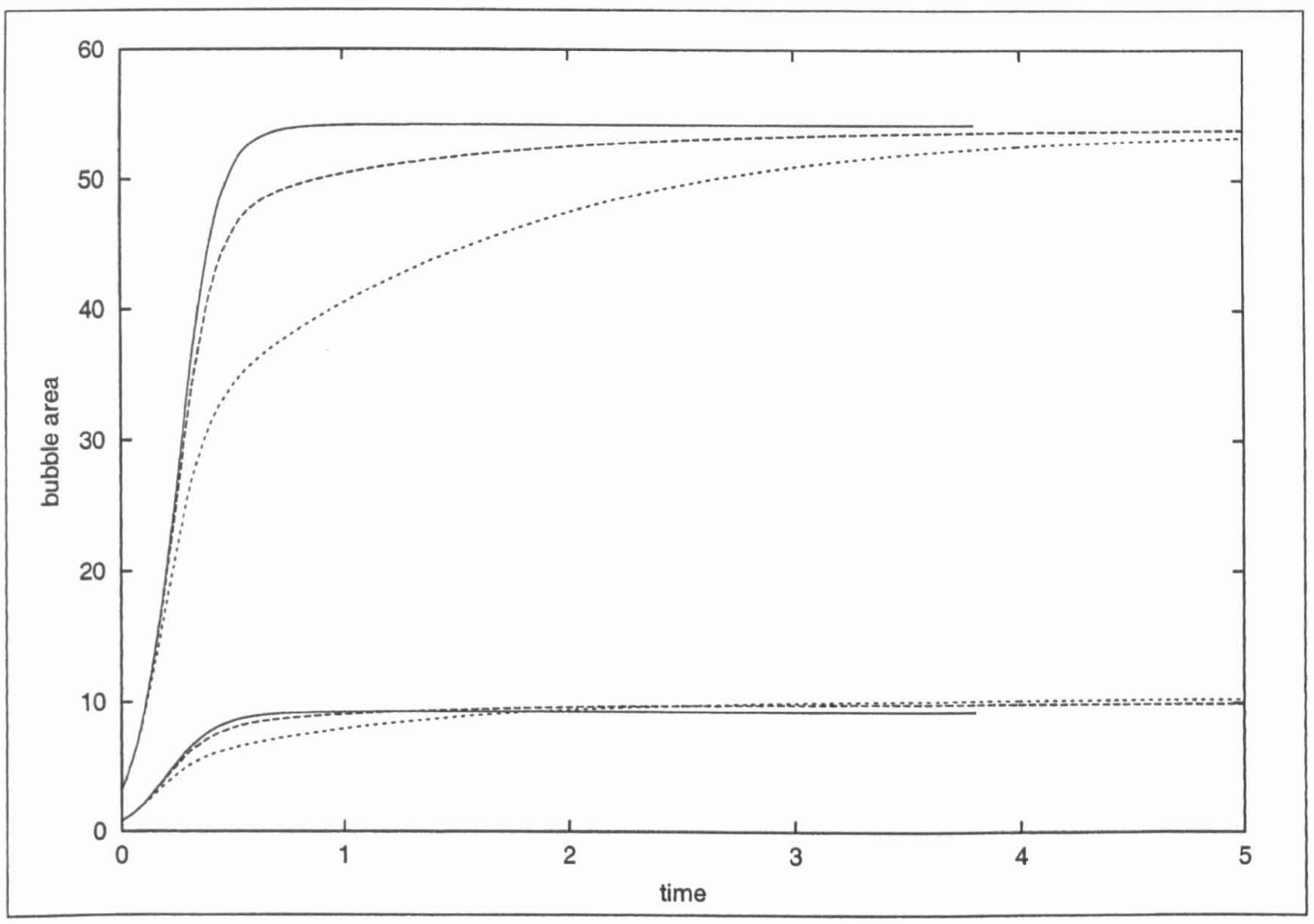


Figure 5.15: Evolution of bubble area for bubbles in a ratio of two large to one small bubble when diffusivity, $D = 10$ and solvent viscosity, $\mu = 1$. Upper curves represent the area of bubble 1, initially $u_1 = \pi$ and lower curves represent the area of bubble 2, initially $u_2 = \pi/4$. Solid lines are bubbles expanding in a Newtonian liquid; dashed lines bubbles expanding in a viscoelastic liquid with $\gamma = 0.2$; and dotted lines bubbles expanding in a viscoelastic liquid with $\gamma = 1$.

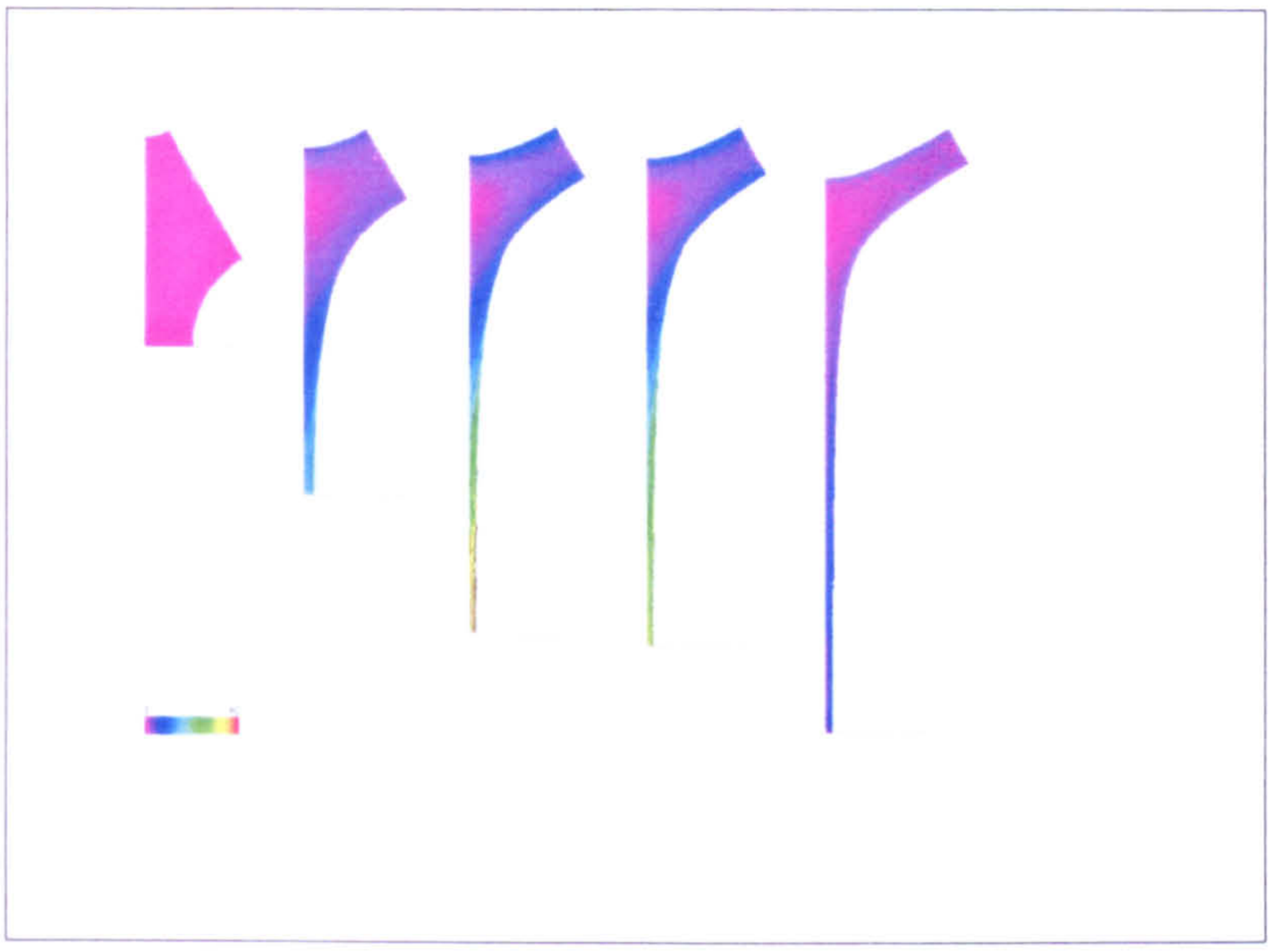

Figure 5.16: Snapshots of the elastic stress in the liquid for a configuration of two large to one small bubble. Here the colouration indicates the magnitude of the difference in the eigenvalues of $\mathbf{A}$, $\gamma = 1$ and diffusivity, $N = 90$. Contours are in intervals of 4.

When the diffusivity is small the bubbles expansion during the viscous phase is slower and the large and small bubbles are closer in size than in the high diffusivity case described in figures 5.15, 5.16 and 5.17. The windows between neighbouring large bubbles are thicker and windows between large and small bubbles are thinner than in the high diffusion case. Consequently, while the elastic stresses throughout the fluid are smaller due to the lower expansion rate the most signifcant reduction is in the stress levels between the large bubbles. As with the case of isolated bubbles, the higher curvature of the smaller bubbles means that the resultant force from the polymer stress in the liquid surrounding the bubbles restricts the size of *the small bubble more* than the larger ones resulting in a wider distribution of bubble sizes in viscoelastic liquids compared to Newtonian fluids for both bubble configurations. Figure 5.18 shows snapshots of the elastic stress in the liquid for the two large to one small bubble configuration, plotted as the difference in the eigenvalues of $\mathbf{A}$.

In figures 5.19 and 5.20 we compare snapshots of part of the developing foam in each

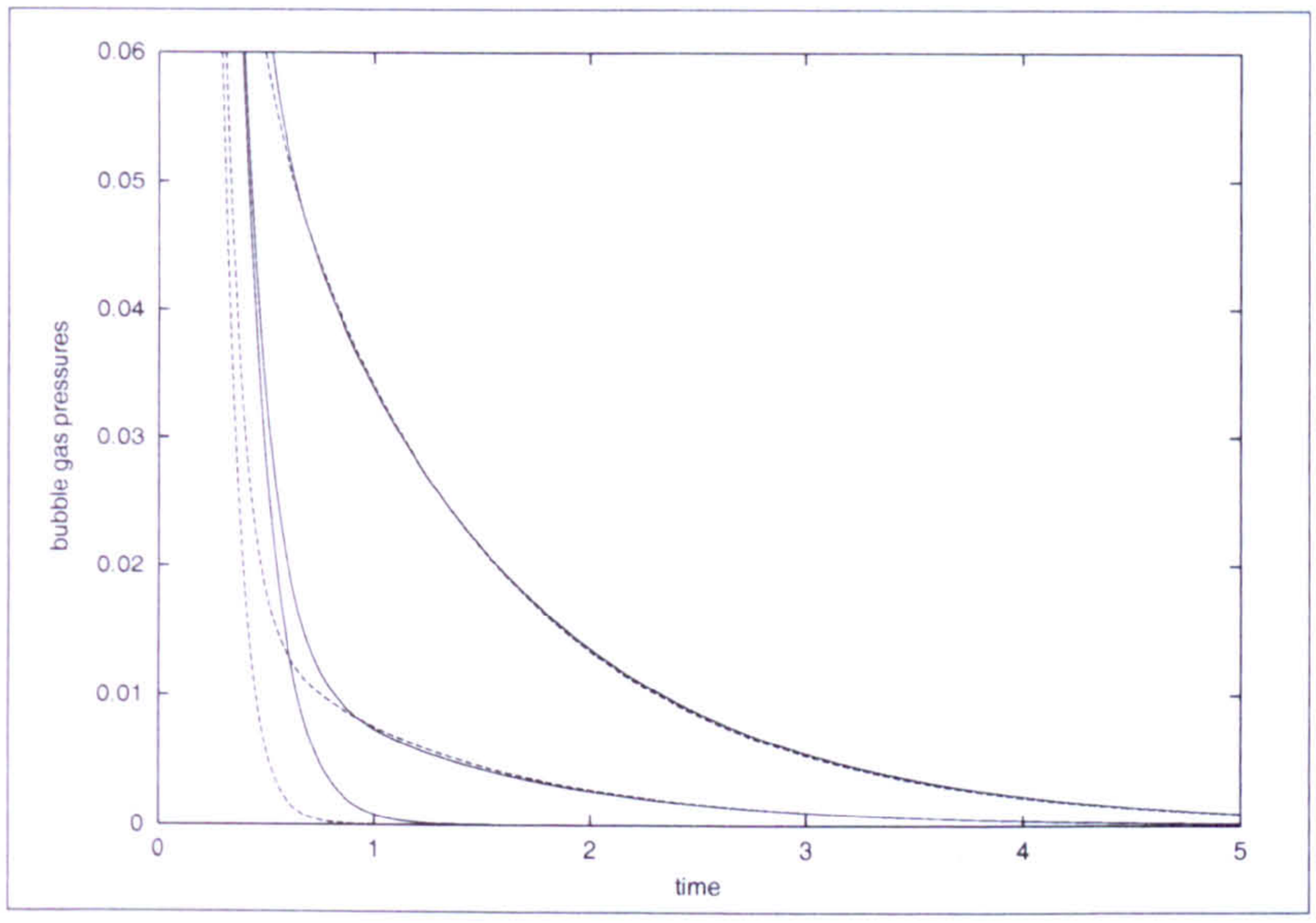


Figure 5.17: Comparison of the bubble gas pressures for bubbles in the ratio of two large to one small bubble between Newtonian liquids and viscoelastic liquids. Solid lines: small bubble; dashed lines: large bubble. Lower curves: Newtonian liquid; middle curves: viscoelastic liquid, $\gamma = 0.2$; and upper curves: viscoelastic liquid, $\gamma = 1$.

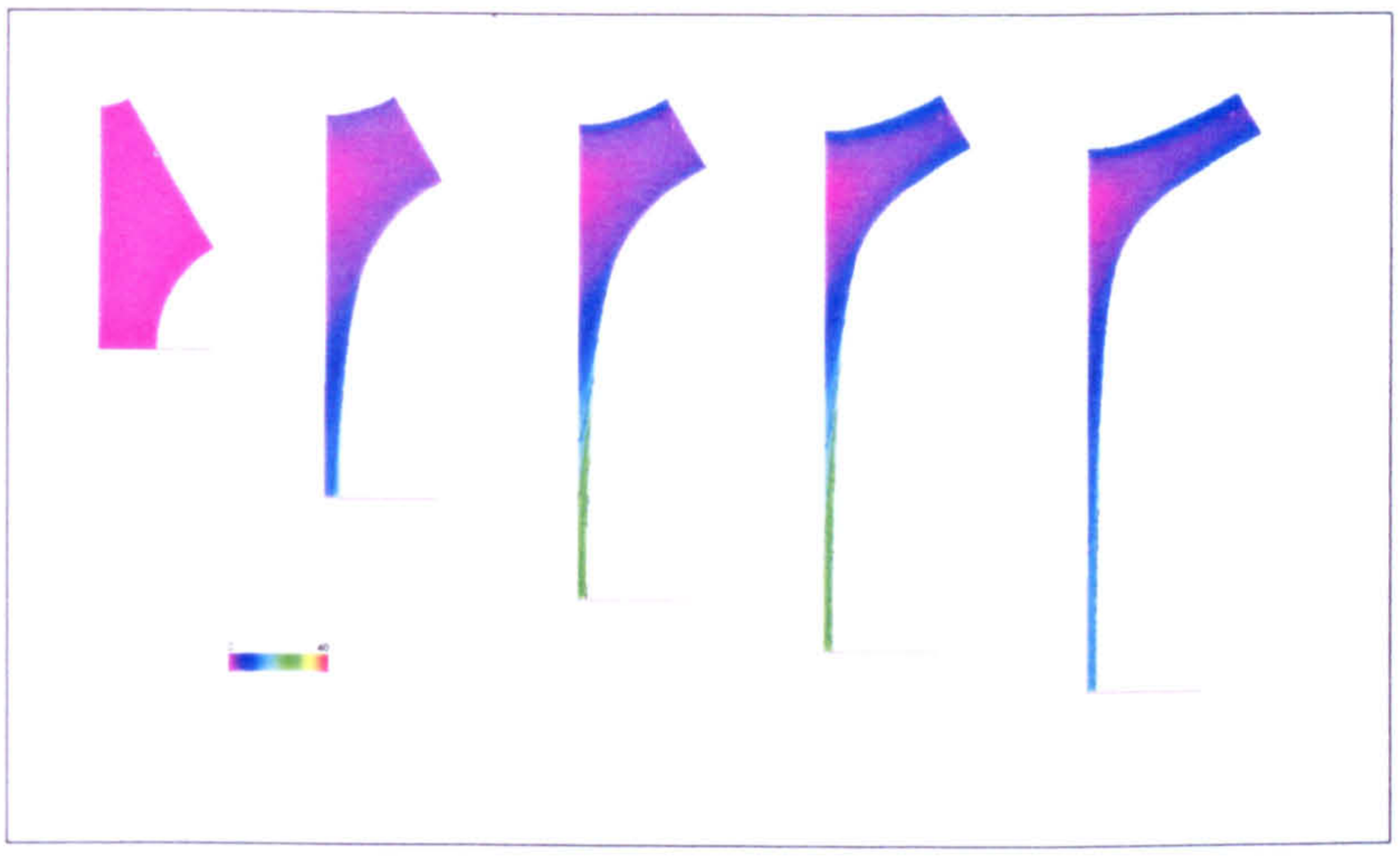

Figure 5.18: Snapshots of the elastic stress in the liquid for a configuration of two large to one small bubble. Here the colouration indicates the magnitude of the difference in the eigenvalues of $\mathbf{A}$, $\gamma = 1$ and diffusivity, $N = 0.9$. Contours are in intervals of 4.

configuration of bubbles. The colours shows the elastic stress difference in the liquid, plotted as the difference in the eigenvalues of A. In either configuration the majority bubble is pulled into a triangular shape.

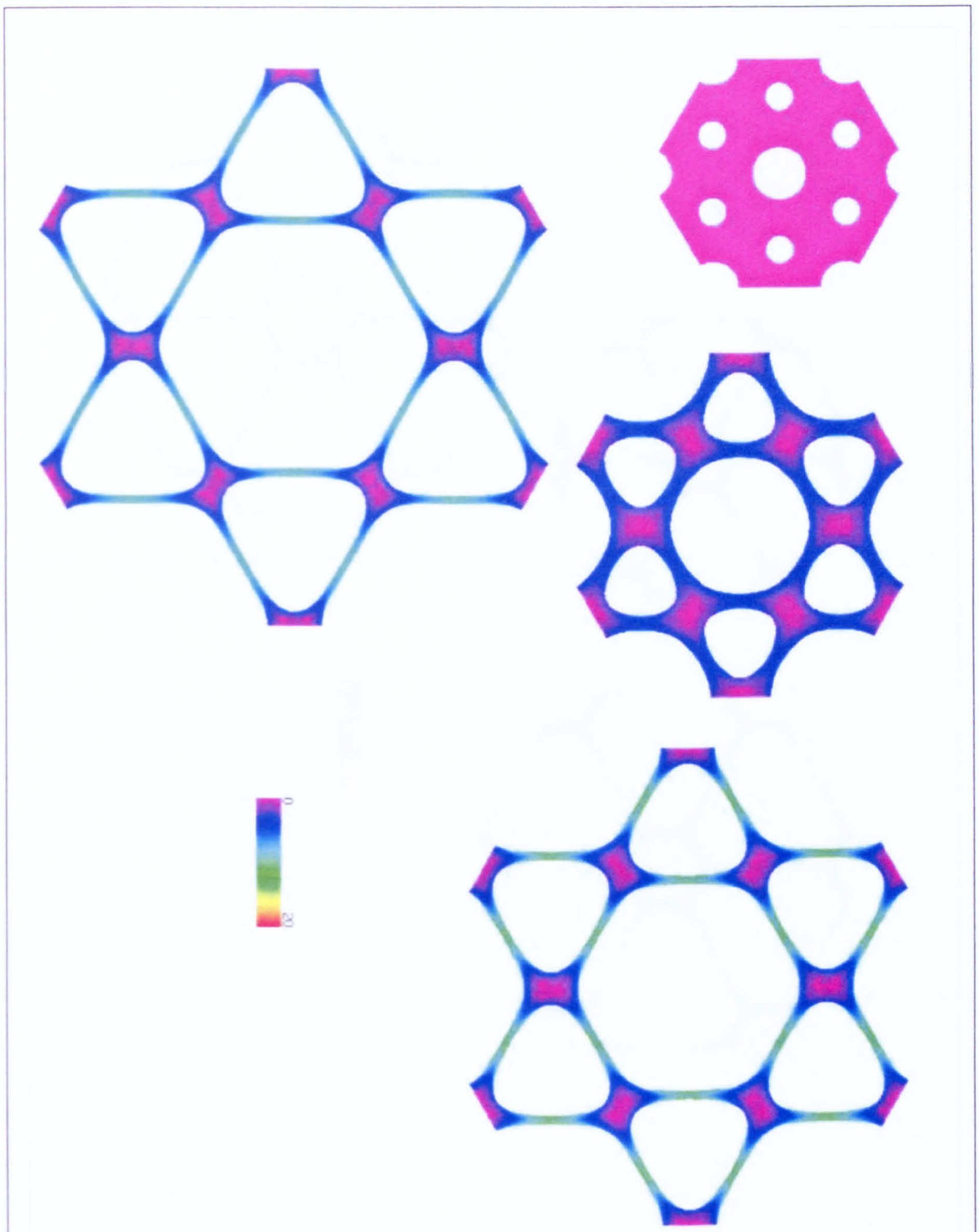


Figure 5.19: Snapshots of the developing foam for a configuration of one large to two small bubbles. Colouration indicates the magnitude of the difference in the eigenvalues of $\mathbf{A}$ and $\gamma = 1$.

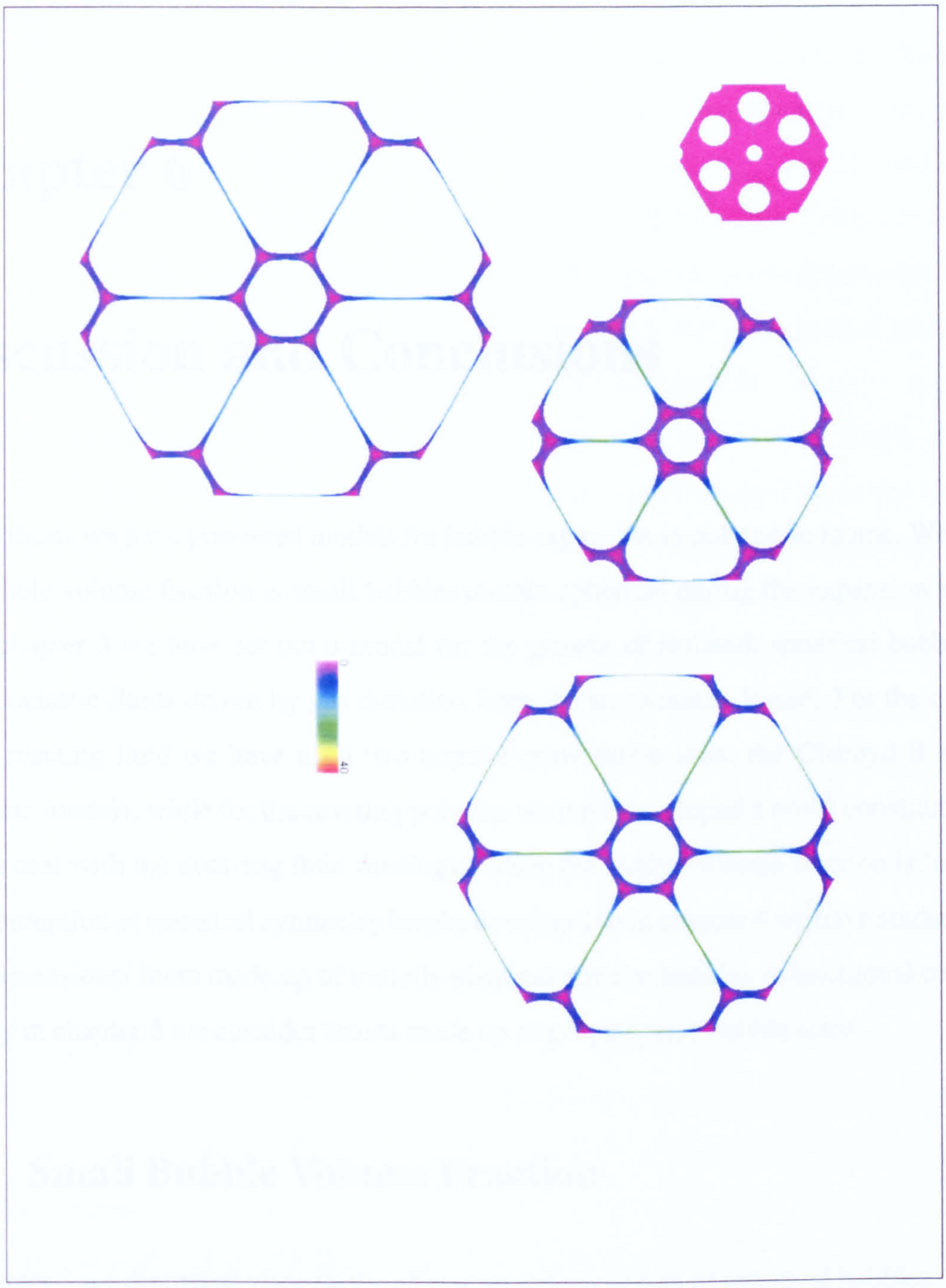

Figure 5.20: Snapshots of the developing foam for a configuration of two large to one small bubble. Colouration indicates the magnitude of the difference in the eigenvalues of $\mathbf{A}$ and $\gamma = 1$.

# Chapter 6

# Discussion and Conclusions

In this thesis we have presented models for bubble expansion in polymeric foams. When the bubble volume fraction is small bubbles remain spherical during the expansion and so in chapter 3 we have set out a model for the growth of isolated, spherical bubbles in viscoelastic fluids driven by gas diffusion from the surrounding liquid. For the case a non-reacting fluid we have used two popular constitutive laws, the Oldroyd B and Pompom models, while for the reacting polymer we have developed a novel constitutive law to deal with the evolving fluid rheology. When the bubble volume fraction is large the assumption of spherical symmetry breaks down and so in chapter 4 we have studied a two-dimensional foam made up of initially identical circular bubbles in hexagonal cells. Finally in chapter 5 we consider foams made up of polydisperse bubble sizes.

## 6.1 Small Bubble Volume Fraction

In chapter 3 we discussed viscoelastic effects on the expansion of spherical bubbles. We used Oldroyd B and Pompom constitutive models to describe foaming in a non-reacting fluid during the thermoplastic injection moulding process. We also extended the linear viscoelastic rheological model of Rubinstein, Colby and Gillmor [43] to a non-linear, multimode Oldroyd B constitutive equation to describe a reacting fluid as a model of the

reaction injection moulding process.

For a non-reacting polymer in which the liquid rheology remains constant there are three important time scales that characterise bubble growth: the polymer relaxation time; a characteristic time for bubble growth in a viscous liquid; and gas diffusion time. For viscoelastic effects to be important the polymer relaxation time must be larger than the expansion timescale, i.e. $De > 1$. Provided that this condition is satisfied, bubble growth can be divided into two classes: diffusion limited growth, where the growth rate is controlled by the diffusive transport of gas from the liquid; and stress limited growth, where the expansion rate is determined by the polymer relaxation rate.

For high Deborah number expansions where the expansion rate is much larger than the polymer relaxation rate, the expansion is divided into two phases: an initial rapid viscous phase during which polymer stress increases; and a later phase controlled by the relaxation of polymer stress. Surface tension restricts the final size of the bubble by modifying the difference between gas pressure inside the bubble and ambient pressure outside the system. Simulations using Oldroyd B and Pompom constitutive models give similar results, as both models incorporate the extension hardening of the polymer with strain that restricts the expansion.

In a reacting polymer system there is a fourth timescale: the reaction time. This sets both the rate of gas production and the onset of gelation where the polymer relaxation time diverges. Most of the gas is produced in the early phase of the reaction, whereas the changes to the rheology are most significant when the reaction is near completion. If the reaction rate is fast relative to the timescale for bubble growth (set either by diffusion or fluid rheology) then gelation will freeze the structure before the stresses have relaxed or pressure decayed.

At low reaction rates a simple generalized Newtonian liquid model, or a combination of a generalized Newtonian and Oldroyd B model, with increasing relaxation time, give reasonable predictions for bubble growth in a gelling liquid. However, at high reaction rates the material properties change so rapidly that the large elastic stresses caused by the bubble expansion make a fluid model such as the one presented necessary.

## 6.2 Large Bubble Volume Fraction

In chapters 4 and 5 we have considered the effects of large gas volume fraction on the expansion of gas bubbles in a viscoelastic fluid. Initially the bubbles are effectively isolated, but as they expand the liquid surrounding them becomes stretched into thin films separating neighbouring bubbles. In chapter 4 our two-dimensional calculations capture this changing structure for identical planar bubbles in a hexagonal array. Although this is not the geometry found in real three-dimensional foams, the results of section 4.3, suggest that the effects of viscoelasticity are qualitatively similar between two and three dimensions.

Viscoelasticity controls the bubble growth when the gas diffusion is sufficiently rapid to allow the bubbles to expand at a rate faster than the polymer relaxation time. In this regime we see the same two stage expansion found previously for isolated spherical bubbles. The bubbles initially grow rapidly until they reach a size where the elastic polymer stress balances the pressure difference. Beyond this time the bubbles continue to grow at the polymer relaxation rate as the stress relaxes. During the initial phase the polymers become most extended in the mid sections of the windows where the fluid layer is thinnest. Once stretched, the polymers resist further extension and draw fluid back from the corners during the relaxation phase. The result is that polymeric foams have a more even thickness of fluid surrounding the gas bubbles than Newtonian foams, provided that the system is quenched before surface tension restores the interface to circular arcs. The extension hardening of the polymer acts to stabilise the fluid interfaces against breakage.

As well as the full two-dimensional calculation we also considered two one-dimensional approximations: a circular model valid at low gas area fractions, and a thin film model valid at high gas area fractions. Both of these simplified models give accurate predictions of the bubble area over a wide range of parameter values, suggesting that gas area is not particularly sensitive to the detailed flow in the films. This suggests that models of three-dimensional foams that assume spherical symmetry should give accurate predictions of

bubble volumes to quite high gas volume fractions. However, these approximate models only captured the detailed shape of the fluid films over a much more restricted range of parameters, although the thin film model does give the correct qualitative behaviour. Thus for high gas volume fractions three-dimensional foams could be investigated using an analogue of the thin film model to avoid having to compute the full three dimensional flow.

### 6.2.1 Polydisperse Bubbles

In chapter 4 we assumed that the bubbles were identical and evenly spaced on a hexagonal array. In practice foams are disordered with a wide range of bubble sizes. In foams with bubbles of different sizes neighbouring bubbles compete unevenly for the available gas. In chapter 5 we first studied how well-separated bubbles compete for the available gas in the limit of high gas diffusivity. We then considered the expansion of bubbles of two different sizes in a two-dimensional hexagonal array.

Surface tension limits the size of each bubble and influences the shape of the bubble by restoring circular arcs. When bubbles are unequal in size Ostwald ripening causes large bubbles to grow at the expense of small ones.

When gas diffusion is faster than the viscous expansion rate bubble growth is limited by the fluid rheology. In this case viscoelasticity affects the bubble size distribution in two ways depending on the configuration of bubbles. In the limit of large capillary number we again see a two-phase expansion. By the end of the viscous phase the bubbles have expanded such that the difference between their sizes is large. When the ratio of large to small bubbles is 1:2 the small bubbles become trapped in the corner region between three large bubbles. During the relaxation phase relaxation of the elastic stress pulls liquid from the corner region into the windows between the large bubbles reducing the size of the corner region and limiting the size of the small bubbles. Thus, in this configuration increasing viscoelasticity results in a wider bubble size distribution. In the opposite ratio of two large to one small bubble the small bubble is surrounded by six

large bubbles. Fluid pulled into the windows between large bubbles now comes from the fluid surrounding the small bubble causing the small bubble to expand more than if it was surrounded by Newtonian liquid. Thus, increasing viscoelasticity now results in a narrower bubble size distribution. Consequently, whether viscoelasticity increases or decreases the bubble size distribution depends upon the details of the configuration. Anecdotal experimental observations suggest that foams made of extension hardening polymers have a more even size distribution. However, this may in part be due to the prevention of film breakage and bubble coalescence.

## 6.3 Discussion

In order to maintain simplicity in a highly complex system we have chosen to ignore many additional complications that arise in reaction injection moulding. We assumed a single species of reactant, whereas in many cases there are at least two. Our analysis assumes isothermal conditions, whereas in practice the synthesis reaction is often highly exothermic. Also, in addition to chemical gelation due to branching there may be phase separation that is thought to produce a physical gel [29, 31]. This occurs before chemical gelation and so gives a gel point earlier in the reaction. These latter two effects could be incorporated into the model and would be expected to modify the quantitative results. However, our model is able to capture the qualitative dependence of this highly complex system on the various parameters.

Throughout chapters 4 and 5 we have chosen to use the Oldroyd B fluid to model the polymeric fluid. Although this simple model reproduces the extension-hardening characteristic of polymeric fluids it has several shortcomings. In particular it has a constant viscosity in shear and has infinite extensibility. However, these shortcomings are not very important in the flow considered here. The flow is almost shear free and the extensions are limited by the growth of the bubble which is determined by the available supply of gas. In the spherical geometry of chapter 3 we justified its use by

investigating the effects of using the Pompom model which shear thins and has a stretch relaxation time that increases as the molecule is stretched near its maximum and found no qualitative change in behaviour.

For foams produced by reaction injection moulding the gelling model described in 2.5 would be appropriate. Implementation of this model into the thin film approximation indicates that the onset of gelation acts to inhibit the equilibrium bubble area, freezing gas pressure and polymer stress into the system. It also freezes the shape of the bubble-liquid interface before surface tension is able to restore circular arcs.

While our two-dimensional foam models assume a highly simplified geometry with bubbles being either identical or of two different sizes evenly spaced in a symmetrical array they are able to capture some of the key features exhibited by expanding polymeric foams. We are able to predict a two phase expansion at high Deborah number; simulate two-dimensional foams in which viscoelasticity produces thicker, flatter fluid windows and surface tension enforces circular arcs connected by black films; and capture the effects of competition for gas between bubbles of different sizes in bi-disperse two-dimensional arrays.

The thin film approximation of section 4.1.3 predicts the evolution of the bubble area so closely that a three-dimensional foam model might be constructed from these one dimensional fluid elements.

This thesis has considered the expansion of gas bubbles in a foam that is otherwise at rest. However, in injection moulding the foam is subjected to shear flow. Consequently another extension of this work would be to model such a foam under shear flow. A first step would be to study isolated bubbles, then the two-dimensional geometries of chapters 4 and 5, in shear flow. The effects of viscoelasticity, bubble area fraction, relative bubble sizes and bubble shape on the flow could be analysed as well as the effects of the flow on the deformation of the bubbles.

# Bibliography

[1] M Amon and C Denson, *A Study of the Dynamics of Foam Growth: Analysis of the Growth of Closely Spaced Spherical Bubbles*, Polymer Engineering and Science **24** (1984), 1026–1034.

[2] A Arafmanesh and SG Advani, *Diffusion Induced Growth of a Gas Bubble in a Viscoelastic Fluid*, Rheologica Acta **30** (1991), 274–283.

[3] A Arafmanesh and SG Advani, *Non-Isothermal Bubble Growth in Polymeric Foams*, Polymer Engineering and Science **35** (1995), 252–260.

[4] GK Batchelor, *An Introduction to Fluid Dynamics*, Cambridge University Press, Cambridge, 1967.

[5] RB Bird, RC Armstrong, and O Hassager, *Dynamics of Polymeric Fluids, Volume 1*, John Wiley and Sons, 1987.

[6] G Bishko, TCB McLeish, OG Harlen, and RG Larson, *Theoretical Molecular Rheology of Branched Polymers in Simple and Complex Flows*, Physical Reveiw Letters **79** (1997), 2352–2355.

[7] Graeme Brian Bishko, *Implementing Molecular Rheology in Complex Flow Fields: A Lagrangian Simulation*, Ph.D. thesis, Applied Mathematics, 1997.

[8] R Blackwell, TCB Mcleish, and OG Harlen, *Molecular Drag-Strain Coupling in Branched Polymer Melts*, Journal of Rheology **44** (2000), 121–136.

[9] BV Boger and K Walters, *Rheological Phenomena in Focus*, Elsevier, Amsterdam, 1993.

[10] F Chambon and HH Winter, *Linear Viscoelasticity at the Gel Point of a Cross-linking PDMS with Imbalanced Stoichiometry*, Jounal of Rheology **31** (1987), 683–697.

[11] TJ Chung, *Finite Element Analysis in Fluid Dynamics*, McGraw-Hill, 1978.

[12] PG de Gennes, *Scaling Concepts in Polymer Physics*, Cornell University Press, Ithaca, 1979.

[13] ME De Rosa, M Mours, and HH Winter, *The Gel Point as Reference State: A Simple Kinetic Model for Crosslinking Polybutadiene via Hydrosilation*, Polymer Gels and Networks **5** (1997), 69–94.

[14] M Doi and SF Edwards, *Theory of Polymer Dynamics*, Oxford Science Publications, Clarendon Press, Oxford, 1986.

[15] VM Entov and EJ Hinch, *Effect of a Spectrum of Relaxation Times on the Capillary Thinning of a Filament of Elastic Liquid*, Journal of Non-Newtonian Fluid Mechanics **72** (1997), 31–53.

[16] SL Everitt, OG Harlen, HJ Wilson, and DJ Read, *Bubble Dynamics in Reacting and Non-Reacting Polymer Foams*, Jounal of Non-Newtonian Fluid Mechanics **114** (2003), 83–107.

[17] JH Ferziger, *Numerical Methods for Engineering Applications*, John Wiley and Sons, 1998.

[18] RJ Fisher and MM Denn, *A Theory of Isothermal Melt Spinning and Draw Resonance*, AIChE Journal **22** (1976), no. 2, 236–246.

[19] PJ Flory, *Principles of Polymer Chemistry*, Ithaca, 1953.

[20] JC Gimel, T Nicolai, D Durand, and JM Teuler, *Structure and Size Distribution of Percolating Clusters. Comparison with Gelling Systems*, European Physical Journal B **12** (1999), 91–97.

[21] CJ Han and HJ Yoo, *Studies on Structural Foam Filling. IV Bubble Growth During Mould Filling*, Polymer Engineering and Science **21** (1981), 518–533.

[22] OG Harlen, JM Rallison, and P Szabo, *A Split Lagrangian-Eulerian Method for Simulating Transient Viscoelastic Flows*, Journal of Non-Newtonian Fluid Mechanics **60** (1995), 82–104.

[23] AW Hodgson, *Homogeneous Nucleation*, Advances in Colloid and Interface Science **21** (1984), 303–327.

[24] KH Huebner, *The Finite Element Method for Engineers*, John Wiley and Sons, 1942.

[25] NJ Inkson, TCB Mcleish, and OG Harlen, *Predicting Low Density Polyethylene Melt Rheology in Elongational and Shear Flows with Pompom Constitutive Equations*, Journal of Rheology **43** (1999), 873–896.

[26] RJ Koopmans, JCF den Doelder, and N Paquet, *Modelling Foam Growth in Thermoplastics*, Advanced Materials **12** (2000), 1873–1880.

[27] AM Kraynik, *Foam Flows*, Annual Review of Fluid Mechanics **20** (1988), 325–357.

[28] RG Larson, *Analysis of Isothermal Fiber-Spinning with the Doi-Edwards Constitutive Model*, Journal of Rheology **27** (1983), no. 5, 475–496.

[29] CW Macosko, *Fundamentals of Reaction Injection Molding*, Hanser Publishers, 1989.

[30] TCB McLeish and RG Larson, *Molecular Constitutive Equations for a Class of Branched Polymers: The Pompom Polymer*, Journal of Rheology **42** (1998), 81–110.

[31] E Mora, LD Artavia, and CW Macosko, *Modulus Development During Reactive Polyurethane Foaming*, Journal of Rheology **35** (1991), 921.

[32] M Mours and HH Winter, *Relaxation Patterns of Nearly Critical Gels*, Macromolecules **29** (1996), 7221–7229.

[33] N Orbey and JM Dealy, *Determination of the Relaxation Spectrum From Oscillatory Shear Data*, Jounal of Rheology **35** (1991), 1035–1049.

[34] N Phan-Thien, *Understanding Viscoelasticity: Basics of Rheology*, Springer, 2002.

[35] C Pozrikidis, *Expansion of a Two-dimensioanl Foam*, Engineering Analysis with Boundary Elements **26** (2002), 495–504.

[36] WH Press, BP Flannery, SA Teukolsky, and WT Vetterling, *Numerical Recipes in Fortran 77: The Art of Scientific Computing*, Cambridge University Press, 1986.

[37] F Prochazka, D Durand, and T Nicolai, *Dynamic Mechanical Properties of Linear and Crosslinked Polyurethane*, Journal of Rheology **43** (1999), 1511–1524.

[38] F Prochazka, T Nicolai, and D Durand, *Dynamic Viscoelastic Characterization of a Polyurethane Network Formation*, Macromolecules **29** (1996), 2260–2264.

[39] F Prochazka, T Nicolai, and D Durand, *Molar Mass Distribution of Linear and Branched Polyurethane studied by Size Exclusion Chromatography*, Macromolecules **33** (2000), 1703–1709.

[40] JM Rallison and EJ Hinch, *Do We Understand the Physics in the Constitutive Equation?*, Journal of Non-Newtonian Fluid Mechanics **29** (1988), 37–55.

[41] NS Ramesh, DH Rasmussen, and GA Campbell, *Numerical and Experimental Studies of Bubble Growth During the Microcellular Foaming Process*, Polymer Engineering and Science **31** (1991), 1657–1664.

[42] H Randrianantoandro, T Nicolai, D Durand, and F Prochazka, *Slow Dynamics in Gels*, Journal of Non-Newtonian Fluid Mechanics **67** (1996), 311–323.

[43] M Rubinstein, RH Colby, and JR Gillmor, *Space-time Organisation in Macromolecular Fluids, editors: F Tanaka, M Doi, T Ohta*, ch. Dynamic Scaling For Polymer Gelation, Springer, Berlin, 1989.

[44] E Ruckenstein and B Nowakowski, *A Kinetic Theory of Nucleation in Liquids*, Journal of Colloid and Interface Science **137** (1990), no. 2, 583–592.

[45] LW Schwartz and RV Roy, *Interim Report: Theoretical and Numerical Modelling of an Expanding Foam*, Tech. report, January (2000, ).

[46] MA Shafi and RW Flumerfelt, *Initial Bubble Growth in Polymer Foam Processes*, Chemical Engineering Science **52** (1997), 627–633.

[47] MA Shafi, K Joshi, and RW Flumerfelt, *Bubble Size Distribution in Freely Expanded Polymer Foams*, Chemical Engineering Science **52** (1997), 635–644.

[48] VK Shen and PG Debenedetti, *A Kinetic Theory of Homogeneous Bubble Nucleation*, Journal of Chemical Physics **118** (2003), no. 2, 768–783.

[49] SH Spiegelberg, DC Ables, and GH McKinley, *The Role of End-effects of Measurements of Extensional Viscosity in Filament Stretching Rheometers*, Jounal of Non-Newtonian Fluid Mechanics **64** (1996), 229–267.

[50] D Stauffer and A Ahaony, *Introduction to Percolation Theory (Revised second edition)*, Taylor and Francis, London, 1994.

[51] D Stauffer, A Coniglio, and A Adam, *Gelation and Critical Phenomena*, Advances in Polymer Science **44** (1982), 103–158.

[52] JR Street, *The Rheology of Phase Growth in Elastic Liquids*, Transactions of the Society of Rheology **12** (1968), 103–131.

[53] P Szabo, *Transient Filament Stretching Rheometer 1: Force Balance Analysis*, Rheologica Acta **36** (1997), 277–284.

[54] I Tanasawa and W Yang, *Dynamic Behavior of a Gas Bubble in Viscoelastic Fluids*, Journal of Applied Physics **41** (1970), 4526–4531.

[55] R Ting, *Viscoelastic Effect of Polymers on Single Bubble Dynamics*, AIChE Journal **21** (1975), 810–813.

[56] D Vaynblat, JR Lister, and TP Witelski, *Rupture of Thin Viscous Films by Van der Waals Forces: Evolution and Self-similarity*, Physics of Fluids **13** (2001), no. 5, 1130–1140.

[57] A Wathen and D Silvester, *Fast Iterative Solution of Stabilised Stokes Systems Part 1: Using Simple Diagonal Preconditioners*, SIAM Journal on Numerical Analysis **30** (1993), no. 3, 630–649.

[58] HH Winter and F Chambon, *Analysis of Linear Viscoelasticity of a Cross-linking Polymer at the Gel Point*, Journal of Rheology **30** (1986), 367–382.

[59] HH Winter and M Mours, *Rheology of Polymers Neär Liquid-Solid Transitions*, Advances in Polymer Science **134** (1997), 165–234.

[60] WW Zhang and JR Lister, *Similarity Solutions for Van der Waals Rupture of a Thin Film on a Solid Substrate*, Physics of Fluids **11** (1999), no. 9, 2454–2462.